PB98-117658

Information is our business.

FRP-CONCRETE COMPOSITE COLUMN AND PILE JACKET SPLICING
PHASE II

31 AUG 97

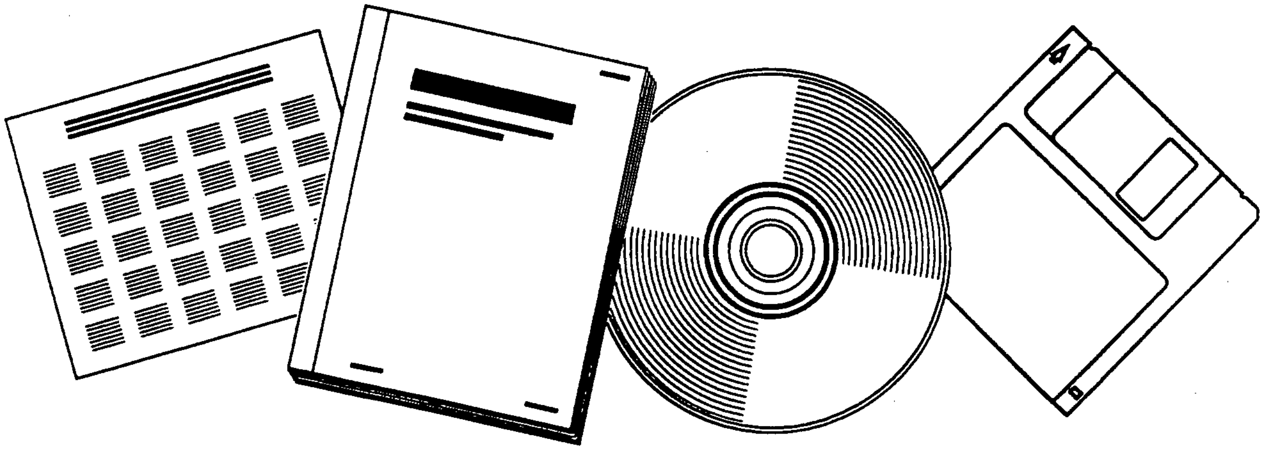

U.S. DEPARTMENT OF COMMERCE
National Technical Information Service

FINAL REPORT

for

PB98-117658

FRP-CONCRETE COMPOSITE COLUMN AND PILE JACKET SPLICING
PHASE II

WPI 0510700
Contract B-9895
State Job 99700-7604-119

Prepared for
Dr. Mohsen Shahawy, Director
Structural Research Center
The Florida Department of Transportation
Tallahassee, Florida

Prepared by
Dr. Amir Mirmiran, P.E.
Department of Civil & Environmental Engineering
University of Central Florida
Orlando, Florida

August 31, 1997

REPRODUCED BY: NTIS
U.S. Department of Commerce
National Technical Information Service
Springfield, Virginia 22161

FINAL REPORT

for

FRP-CONCRETE COMPOSITE COLUMN
AND
PILE JACKET SPLICING
PHASE II

WPI 0510700
Contract B-9895
State Job 99700-7604-119

Prepared for
Dr. Mohsen Shahawy, Director
Structural Research Center
The Florida Department of Transportation
Tallahassee, Florida

Prepared by
Dr. Amir Mirmiran, P.E.
Department of Civil & Environmental Engineering
University of Central Florida
Orlando, Florida

August 31, 1997

Technical Report Documentation Pa

1. Report No.
0510700

2. Government Accession No.

3. Recipient's Catalog No.

4. Title and Subtitle
FRP-Concrete Composite Column and Pile Jacket Splicing - Phase II

5. Report Date
8/31/97

6. Performing Organization Code

7. Author's
DR. Amir Mirmiran, P.E.

8. Performing Organization Report No.

9. Performing Organization Name and Address

Dr. Amir Mirmiran, P.E.
Department of Civil & Environmental Engineering
University of Central Florida
4000 Central Florida Blvd.
Orlando, FL 32816-2450
Tel. (407) 823-3592 Fax: (407) 823-3315

10. Work Unit No. (TRAIS)

11. Contract or Grant No.
B-9895

12. Sponsoring Agency Name and Address

Florida Department of Transportation
605 Suwannee Street
Tallahassee, FL 32399-0450

13. Type of Report and Period Covered
Final Report
8/22/95 - 8/31/97

14. Sponsoring Agency Code

15. Supplementary Notes
Prepared in cooperation with the US Department of Transportation and Federal Highway Administration

16. Abstract

A new and innovative use of fiber composites has been introduced which consists of concrete-filled FRP tubes as structural columns, piles and piers. The tube acts as the pour form, protective and confining jacket, shear stirrups, and flexural reinforcement. Feasibility of this system was shown under Phase I of this project. Phase II has been focused on several issues including; shear capacity of hybrid columns, effect of cross-section shape and column length and construction bond on the strength and ductility of column, optimization of hybrid columns, and acoustic emission testing of hybrid systems. Results of extensive tests and analytical work have been reported in detail.

17. Key Words
Composites, Columns, Concrete, FRP, Piles Optimization, Shear, Slenderness, and Bond.

18. Distribution Statement
No restriction
This report is available to the public through the National Technical Information Service, Springfield, VA 22161

19. Security Classif. (of this report)
Unclassified

20. Security Classif. (of this page)
Unclassified

21. No. of Pages
151

22. Price

Form DOT F 1700.7 (8-72)

Reproduction of completed page authorized

TABLE OF CONTENTS

ACKNOWLEDGEMENTS

The author would like to thank his Project Manager, Dr. Mohsen Shahawy, Director, Structural Research Center for his help, time, and encouragements during the course of this project. His valuable and timely suggestions helped avoid many pitfalls that are often parts of any research project. The author takes this opportunity to also thank the personnel of Florida Department of Transportation, Structural Research Center, and in particular, Tom Beitelman.

This project was made possible by generous donations of Marine Muffler Corp. of Apopka, Florida in the form of materials and labor. For this, the author is grateful to Mr. David Parks and his associates. Partial student support was also received from the University of Central Florida Division of Sponsored Research and the Department of Civil and Environmental Engineering.

Special thanks are due to graduate assistants at the University of Central Florida, Ph.D. candidate Michel Samaan, M.S. graduates Mike Scherer, Suramy Cabrera, Odell Pico, Hazem El Echary, and Juan Carlos Mastrapa. Portions of this report correspond to the theses and dissertations of these students.

List of Tables

List of Figures

EXECUTIVE SUMMARY

Problem Statement

Issues of corrosion and deterioration of steel reinforcement have led to the use of fiber reinforced plastics (FRP) in infrastructure. Florida DOT has been in the forefront of using FRP for the repair of existing bridges. A new and innovative use of fiber composites has been introduced by Mirmiran and Shahawy that consists of concrete-filled FRP tubes as structural columns, piles and piers. The tube acts as the pour form, protective and confining jacket, shear stirrups, and flexural reinforcement, all at the same time. It further allows removing conventional reinforcement from the column. Feasibility of this method of construction was clearly demonstrated under Phase I of this research project. Phase I also resulted in a new model for confined concrete, and new methods of fabricating hybrid beam-columns. Phase II of this research has been focused on several issues including; shear capacity of hybrid FRP-concrete columns, effect of cross-sectional shape on the degree of confinement provided by the FRP shell, effect of length and slenderness of hybrid columns on their strength and ductility, effect of bond between the concrete core and the FRP shell on the strength and ductility, and finally optimization of hybrid columns.

Objective

The following objectives were identified for Phase II:

1. Evaluate the shear capacity of hybrid columns and develop methods to increase shear transfer between the tube and the concrete core.
2. Study the effect of cross-sectional shape, length or slenderness of the column, and bond between the tube and the core, on the strength and ductility of hybrid columns.
3. Develop procedures for optimization of hybrid FRP-concrete columns, and perform parametric studies to establish the effects of basic variables on the cost of the system.

Findings

The experimental and analytical studies of Phase II led to several findings as outlined below:

1. Shear tests on a total of 16 hybrid beams indicated that unless shear ribs are provided, hardly any bond would exist naturally between the FRP jacket and the concrete core. As a result, slippage would not allow shear to be transferred at the concrete-FRP interface. The tube, however, still somewhat increases the shear strength of concrete by simply containing the cracked section. With the shear connectors, the slippage problem was corrected, and the tube increased the strength by at least 6 times the shear strength of unjacketed beams of the same cross section. Also, the ribbed FRP tubes proved effective in inhibiting shear failure of the beams.

2. Uniaxial compression tests on a total of 9 composite specimens with square section demonstrated that square sections are not as effective as circular sections in confining the concrete core, as the strength of concrete is increased only marginally and rather independent of the jacket thickness. However, a post-peak ductility can be expected. Failure of the square FRP-encased

specimens is accompanied by white patches around the corners, showing stress concentration at the edges. As the corner radius is increased, the confinement effectiveness and the behavior of confined concrete become closer to circular sections. The over-riding parameter in controlling the confinement was shown to be the product of the corner radius and the confining pressure.

3. Uniaxial compression tests on a total of 24 composite columns with various lengths and jacket thicknesses indicated that length-to-diameter ratios of up to 5:1 would not alter the general behavior of confined concrete such as its mode of failure or dilation characteristics. No slenderness effect in the form of buckling was observed during the tests. Further analysis indicated that the maximum eccentricity was within 10-12% of the section width. Noting that ACI 318-95 considers a minimum eccentricity of 10% and a strength reduction of 20% for tied columns, the amount of eccentricity and the strength reductions that were noticed for L/D ratios of 2:1 to 5:1 seemed acceptable. It was therefore, concluded that the 12" cylinders should be considered adequate to represent the confinement of concrete sections. Longer specimens possess an inherent eccentricity that results in lower values of the ultimate load. However, the eccentricity is well within the acceptable range, and does not qualify for any slenderness effect.

4. Uniaxial compression tests on a total of 24 composite specimens with and without construction bond and with various jacket thicknesses indicated that the effect of construction bond on confined concrete is not significant, as long as the biaxial stresses in the jacket are considered properly for the bonded specimens.

5. Optimization studies for a variety of jacket thicknesses and core diameters indicated that adding hoop fibers at low axial loads does not increase the capacity of the section. For a specific core diameter, there is only one particular combination of axial and hoop fibers that provides the optimum solution. A penalty function was introduced to determine the significance of weight on the total cost of a hybrid column. When weight becomes a significant factor, the optimum solution shifts to a lower core diameter and higher hoop and axial fiber reinforcement ratios.

6. Acoustic emission (AE) was shown to be an efficient nondestructive evaluation technique for concrete-filled FRP tubes. Of the various AE parameters, AE energy and number of AE counts both proved to be effective measures for the response of confined concrete. It was shown that while Kaiser effect was not present for hybrid columns even at low levels of axial load, Felicity effect during loading and unloading was apparent as one would expect from fiber composites.

Conclusions

A series of beam and column tests with a variety of design parameters helped quantify the response of hybrid FRP-concrete columns as related to shear strength, confinement, cross-section, slenderness, and construction bond. It was shown that design of hybrid columns can be optimized for any load combination and core diameter. Finally, effective use of nondestructive methods for FRP-concrete columns was demonstrated. Phase III of this project will focus on field testing of concrete-filled FRP piles.

CHAPTER 1

INTRODUCTION

1.1 Problem Statement

Issues of corrosion and deterioration of steel reinforcement have led to the use of fiber composites in infrastructure. A new and innovative use of fiber composites was introduced by Mirmiran and Shahawy (1995) that consisted of concrete-filled fiber reinforced plastics (FRP) tube as structural columns, piles and piers. This idea was supported by the Florida Department of Transportation under Phase I of a research effort which was completed in 1996. Details of the construction technique, its benefits, and a multitude of useful information are provided in the Final Report of Phase I (Mirmiran 1997). That report forms the basis (or Volume I) of this document, and rather than unnecessary duplication of the materials, multiple references to that report have been made throughout this document.

Phase I of this research was focused more towards investigating the feasibility of the construction method, modeling of confined concrete, and methods of fabricating hybrid beam-columns. There were, however, several other issues that remained to be studied before the proposed system could be fully implemented. Those issues include the following:

1. Shear capacity of hybrid FRP-concrete columns.
2. Effect of cross-sectional shape on the degree of confinement provided by the FRP shell.
3. Effect of length and slenderness of hybrid columns on their strength and ductility.
4. Effect of bond between the concrete core and FRP shell on the strength and ductility.
5. Design procedures, optimization, and cost-benefit analysis for hybrid columns.
6. Field tests of hybrid columns and piles.
7. Design issues such as connections, long-term performance, environmental effects, etc.

Of the above items, the first five have been investigated under Phase II, and will be addressed in this report. Item 6 is the main focus of Phase III, which undertakes the driving of a hybrid pile at a selected site. The issue of long-term performance under item 7 is the topic of a parallel project with the National Science Foundation and the Florida Department of Transportation.

1.2 Research Objectives

The objectives of Phase II may be listed as follows:

1. Evaluate the shear capacity of hybrid columns and develop methods to increase shear

transfer between the tube and the concrete core.
2. Study the effect of cross-sectional shape, length or slenderness of the column, and bond between the tube and the core, on the strength and ductility of hybrid columns. It was intended to quantify these effects and make necessary modifications in the confinement model that was developed under Phase I.
3. Develop procedures for design and cost optimization of hybrid FRP-concrete columns, and perform necessary parametric studies to establish the effects of basic parameters on the cost of the system.

1.3 Report Outline

This report consists of nine chapters including this introduction. This Phase of the project consisted of the following program:

1. Beam Shear Tests: to establish the contribution of the FRP tube to the shear strength of the hybrid FRP-concrete beam.
2. Square Column Tests: to evaluate the effect of cross-sectional shape on the confinement provided by the FRP tube.
3. Length Effect Tests: to determine the effect of column length on the strength and ductility of concrete confined in FRP tube.
4. Bond Effect Tests: to compare the confinement effectiveness of fiber-wrapping mechanism versus concrete-filled FRP tubes.
5. Cost Optimization: to develop an analytical technique for design optimization of hybrid columns.
6. Acoustics Emission Tests: to develop a non-destructive testing method for predicting the strength of concrete-filled FRP tubes.

Of these, items 1, 4 and 6 were in the original proposal, while others were added during the course of the project. The next six chapters cover the various elements of this research as outlined above. Each chapter contains a section on literature review, experimental work (except for the chapter on cost optimization) and analysis and discussion (except for the chapter on Acoustics Emission). Chapter 8 summarizes the conclusions and discusses various recommendations. A list of all disseminated information is presented in Chapter 9. References are categorized for convenience of the reader. In this report, as in that of Phase I (Mirmiran 1997) the terms FRP-encased concrete, concrete-filled FRP tubes, hybrid FRP-concrete columns, and composite FRP-concrete columns are used interchangeably to mean the same system.

CHAPTER 2

SHEAR STRENGTH OF CONCRETE-FILLED FRP TUBES

2.1 Literature Review

Fiber reinforced plastics (FRP) sheets and plates have often been used for repair or strengthening of beams and slabs. Bonding of FRP sheets was used in Lucerne, Switzerland to repair the Ibach Bridge when it was accidentally damaged resulting in a decreased load carrying capacity for the bridge. It was estimated that 175 kg of steel plates would have been needed to repair the bridge. Instead, only 6.2 kg of carbon fiber sheets were needed for the same repair (McKenna and Erki 1994). It was also reported that the Kattenbusch bridge in Germany was repaired with both steel and glass fiber reinforced plastic (GFRP) plates. In addition, it was noted that the GFRP plates provided the same increase in strength as the steel plates (Nanni 1995). Saadatmanesh and Eshani (1991) investigated strengthening of beams with externally bonded GFRP plates. Tests were conducted on five rectangular beams and one T-beam. Of the five beams, one was under-designed for shear and the rest were over-designed in shear according to ACI code. The flexural reinforcement included steel bars of three different reinforcement ratios. All beams were strengthened with FRP plates externally bonded to their tension sides. The test indicted that FRP plates significantly increased the flexural strength of the beams, reduced the crack size of the beams, and slightly reduced ductility. It was also noted that the greatest increase in flexural strength occurred in the beams with lower steel reinforcement ratio. Similar to this experiment was one conducted by Philip et al. (1991). There too, the results indicated an increase in strength and stiffness. None of the beams in this test, however, showed ductile behavior.

Al-Sulaimani et al. (1994a) conducted tests on the strengthening of damaged beams. Tests were conducted on ten reinforced concrete beams. The beams were under-reinforced in flexure and over-designed in shear to avoid a brittle shear failure of the damaged beams after repair. The beams were initially loaded to 85% of their ultimate load. They were then repaired by plate bonding. The beams were divided into four categories depending on the repair technique. The four categories were as follows:

1. Beams repaired by bonding a plate to the beam soffit.
2. Beams repaired with plate bonded and anchored by steel bolts to the beam soffit.
3. Beams repaired by bonding a plate to the beam soffit and additional plates bonded to the sides of the beam.

4. Beams repaired with an I-jacket bonded to the sides and soffit of the beam.

The beams were loaded until failure. Overall, the results indicated that the beams repaired with the bonded I-jacket provided the best anchorage system to eliminate plate separation and diagonal tension failure, and developed the flexural strength of the repaired beams. They also found that beams did show adequate ductility while developing their flexural capacity.

Al-Sulaimani et al. (1994b) later conducted an experiment on the effectiveness of FRP plate bonding on the shear capacity of reinforced concrete beams. In this test, sixteen reinforced concrete beams were deliberately designed to be deficient in shear capacity. As with the previous test, the beams were then loaded to a predetermined load. The damaged beams were then divided into four groups according to the form of repair. The four repair categories were as follows:

1. Control beams having no shear repair.
2. Beams repaired by shear strips.
3. Beams repaired by shear wings.
4. Beams repaired by U-jackets.

Within these four groups, the beams were further divided into two subgroups, beams having no flexural repair and beams repaired in flexure by FRP plate bonding. The beams were then loaded until failure. In general, the beams repaired with the U-jacket showed the best shear performance. The shear strength was so high that even the U-jacketed beams that were strengthened with additional FRP plates failed in flexure.

Chajes et al. (1995) conducted an experiment on the shear strength of reinforced concrete beams using externally applied composite fabrics. In this study, 12 T-beams were tested. Eight of the beams were wrapped with externally bonded composite fabrics, two were reinforced with woven aramid, E-glass, and graphite fabrics with the weave direction along and perpendicular to the beams' longitudinal axis, and two beams had plain-weave graphite fabric bonded with the weave directions rotated ± 45° from the beams' longitudinal axis. The beams were tested in a four-point loading test. All beams failed in shear with the beams reinforced with composite fabric failing at the highest loads. The externally wrapped beams displayed an increase in load carrying capacity of 60% to 150% over the control beams. The beams wrapped with the fabric oriented at ±45° showed the highest increase in strength. It was also noted by the authors that the composite fabric had only a minor effect on the flexural stiffness of the wrapped beams.

In all the research presented, the common conclusion was that the use of fiber composite as a material to reinforce concrete members is a desirable one. Advantages of fiber composites include (Mallick 1988):

1. The high strength-to-weight ratio of FRP helps reduce the weight of the structure, making FRP a more economical choice.
2. Fibers have a lower coefficient of thermal expansion than most metals, giving fibers better

stability over a wider temperature range.
3. The unique anisotropic properties of fibers allow one to design for stresses in a specific direction, and effectively uncouple the axial and hoop directions.
4. The tensile stress-strain response of fibers is linear-elastic, while steel yields plastic deformations.
5. Fiber composites can be used to enhance shear strength of concrete beams.

2.2 Experimental Work

An experimental study was performed to evaluate the contribution of FRP to the shear strength of concrete-filled tubes. The proposed study was to test 8 beams under a 4-point loading setup. Two unconfined (un-jacketed) beams were used as control beams. These beams were lacking in any form of shear reinforcement so as to ensure a shear failure. The shear strength of the 6 jacketed specimens was then compared to the shear strength of the 2 control specimens. The effect of slippage was not considered to be of great consequence in the beam shear tests. However, it was, and a second series of tests was devised and carried out with beams containing shear connectors. The details of both series of tests are discussed below.

Series 1

Series 1 consisted of eight 6"x6"x22" beams tested under a 4-point loading setup. The specimens were designed to ensure a shear failure if no FRP jacket was provided. Therefore, the control beams were designed with a flexural strength of about 9 times their shear strength. Clear cover for the compression and tension bars was 0.5 inch and 0.75 inch, respectively (Figure 2.1). The jacketed specimens were reinforced identical to the control beams against flexure, the only difference being the enhanced shear strength provided by the FRP jacket. The jacket was expected to increase the shear strength by over 9 times, changing the failure mode from shear to flexural, assuming full bond with the concrete core.

Specimen Layout

Table 2.1 shows the test matrix for Series 1. Eight specimens were divided into four groups with two identical samples from each group for repeatability verification. Two 6"x12" cylinders were also made to determine the average compressive strength of the concrete mix. The characteristics of the four groups are as follows:

1. Group A consisted of the control specimens with no shear reinforcement.
2. Group B specimens were the same as control specimens with the addition of the FRP tube.
3. Group C specimens were FRP jacketed with an additional layer of carbon fiber glued to the inside of the tube prior to casting of concrete to increase flexural strength of the beam.
4. Group D specimens were the same as Group C except that at the time of testing, the top face of the tube was cut and removed, to eliminate the continuity in the fibers.

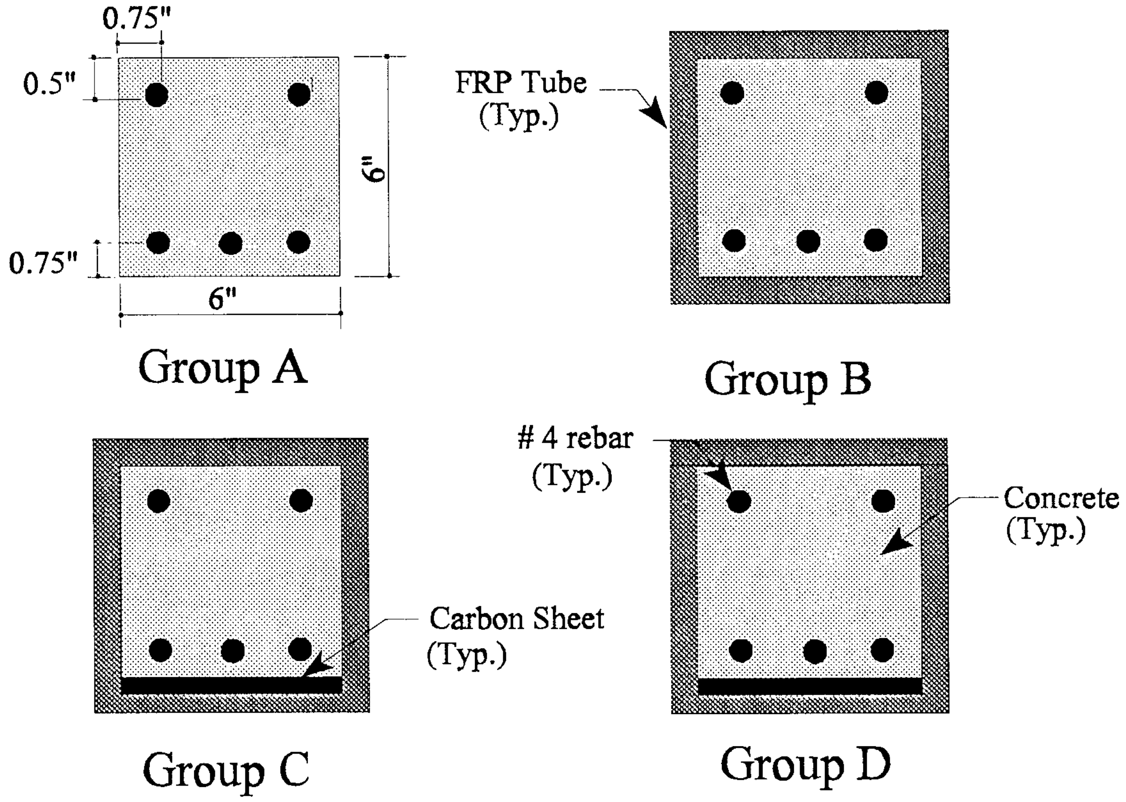

Figure 2.1 Specimen cross sections for Series 1

Table 2.1 Test matrix for Series 1

Group No.	Longitudinal Reinforcement		Shear Reinforcement
	Compression	Tension	
A	2#4 Steel Rebars	3#4 Steel Rebars	None
B	2#4 Steel Rebars	3#4 Steel Rebars	FRP Tube [7 Layers]
C	2#4 Steel Rebars	3#4 Steel Rebars Carbon Fiber Sheet	FRP Tube [7 Layers]
D	2#4 Steel Rebars	3#4 Steel Rebars Carbon Fiber Sheet	FRP Tube [7 Layers] (Top face removed prior to testing)

Tubes were made by Marine Muffler Corporation, Apopka, Florida, and consisted of 7 filament-wound ±15° angle-plies. Material properties of the DION 6692T polyester resin, E-glass R099-660 Roving, and the Thornel T-300 carbon sheet are presented in Table 2.2 from manufacturer's data. The aggregates were provided by the Orlando Paving Company, Winter Park, Florida. Sand was natural silica with a fineness modulus of 2.2, specific gravity of 2.64, dry rodded weight of 101 pcf, and moisture absorption of 2.0%. Gravel was crushed limestone with a specific gravity of 2.82, dry rodded weight of 101pcf, and moisture absorption of 5.4%. Type II Portland Cement from Rinker Materials, Winter Park, Florida was used for concrete.

Table 2.2 Mechanical properties of glass fibers, polyester resin, and carbon sheet

Property	450-Yield E-Glass	Polyester Resin	Thornel Carbon Fiber T-300 12k
Specific Gravity	2.58	1.41	1.77
Tensile Strength, (ksi)	317	10.4	530
Tensile Modulus, (ksi)	10,100	630	33,500
Shear Modulus, (ksi)	4,370	232	700
Poisson's Ratio	0.22	0.36	0.20

Figures 2.2 and 2.3 show the placement of re-bars and preparation of the specimens. Re-bars were affixed to the inside of the FRP tubes with wires that were pulled through small holes drilled in the sides of the tubes 0.5 inches from the compression face and 0.75 inches from the tension face. The re-bars were tightly wound with the wires to ensure they would not slip. The bottom of the beams were sealed with a double layer of plastic sheet taped to the bottoms to prevent the concrete from seeping out. Placement of rebars in the control beams required small U-shaped seats made of steel wire on which the tension re-bars could rest at the required distances. The compression re-bars

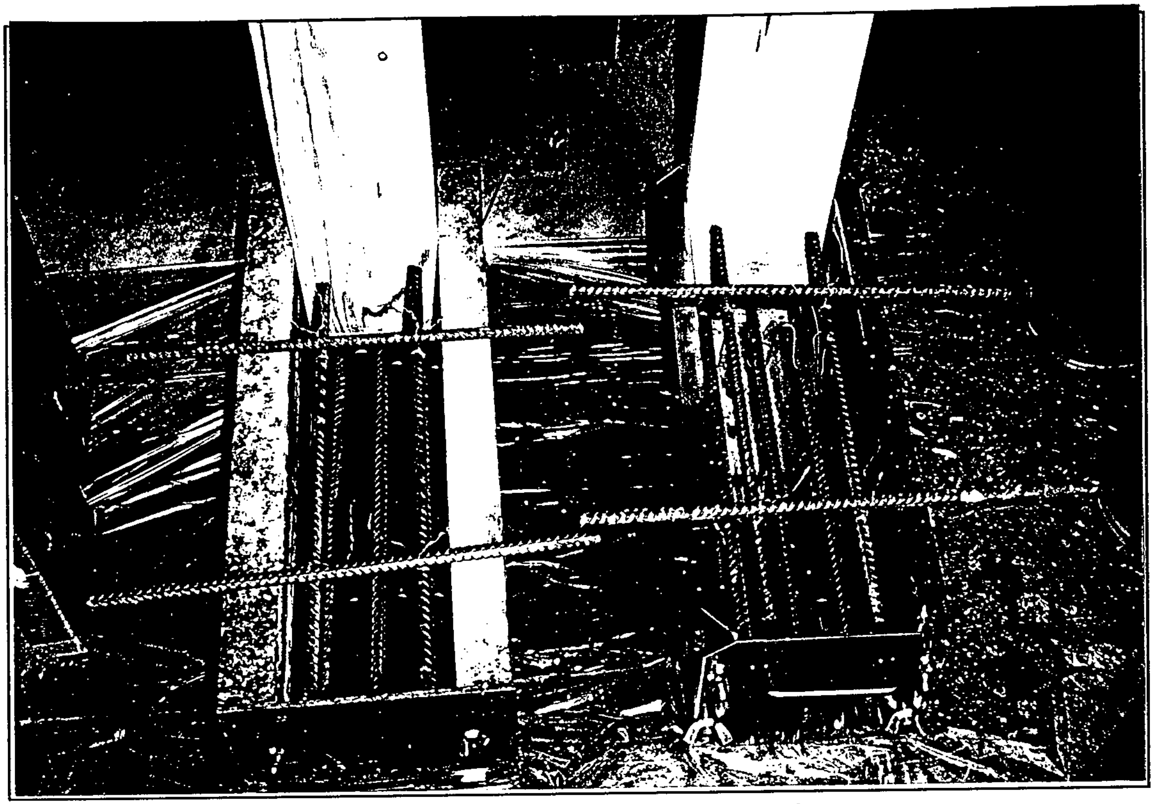

Figure 2.2 Control beams prior to casting of concrete

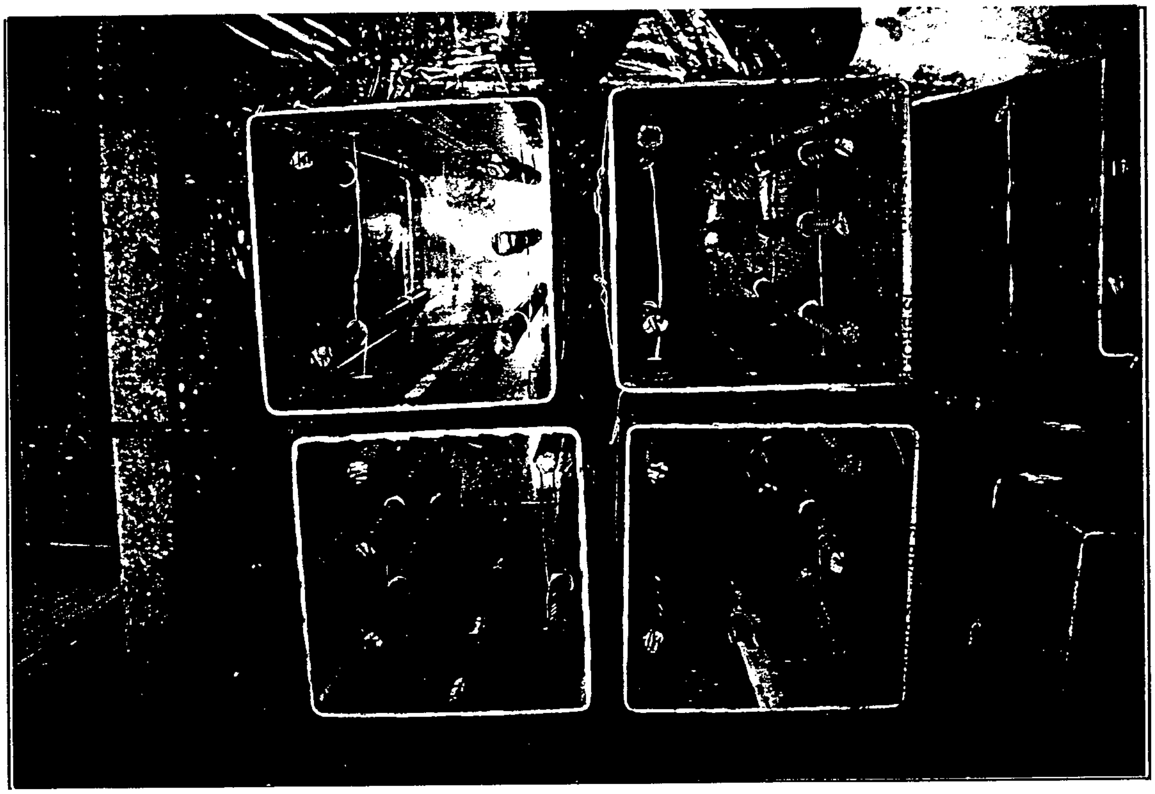

Figure 2.3 FRP tubes with re-bars prior to casting of concrete

were hung with wire at the required height.

The concrete mix was designed with a water-to-cement ratio of 0.52 (by weight) for a 28-day compressive strength of 4000 psi. The quantity of materials per cubic yard of the mix was: 665.6 lb cement, 344.7 lb water, 1034.1 lb sand, and 2078.6 lb gravel. No additives were used. Concrete was cast on November 2, 1995 at UCF using a single batch made in a 9 cubic-foot rental mixer. Exposed surface of the specimens were wetted daily for three days. After 1 week of curing outdoors, specimens were brought inside the lab. All control cylinders were sulfur capped prior to testing.

Instrumentation

All specimens were instrumented with rosettes at mid-height on both sides of the specimens on a 45° line between the support and the point of load application (see Figure 2.4). The rosettes measured strain in the horizontal and vertical directions. Strain gauges were also placed on the top face of the beams centered vertically and horizontally. All gauges were glued onto the surface of the tube or concrete. The beams were additionally instrumented with three LVDTs at the mid-span and under the points of load application. The two control cylinders were instrumented with horizontal strain gauges placed 180° apart at mid-height of the specimen.

Test Procedure

Testing took place on December 9 and 10, 1995 at the FDOT Structural Laboratory, using the MTS and MegaDAQ. Test setup for the beams is shown in Figure 2.5. It consisted of two half cylinders affixed at 18" spacing as beam supports and two rollers as loading points at 3" on either side of the midspan. A metal plate was used to transfer the load onto the two rollers. Testing was carried out in a displacement control mode. Rate of loading was 0.05 inch per minute for Specimens A1, B1, B2, and C1, and 0.125 inch per minute for Specimens A2, C2, D1, and D2.

Observed Behavior

Throughout testing, significant popping and cracking could be heard. Some of the noises may be attributed to the de-bonding of the tube and cracking of concrete. It was possible to see the concrete slipping out of the tube. At the time of failure, an average of ¼ to ½ inch of concrete had slipped out of the tube at either end (Figure 2.6). This indicated very little bond between concrete and the tube. Square chunks of concrete at the end of some specimens completely broke off and fell out. Looking in at the ends of the specimens, it was possible to see bulging of the tube (Figure 2.7). The vertical sides of the tube also buckled outward as can be seen on the front face of specimen B2 (Figure 2.8). As the loading progressed, white lines developed in the tube indicating cracking of the tube and flow of resin. Specimens of Group C were the only ones to show flexural cracking. These specimens were even further reinforced with a carbon sheet to increase the flexural strength above that of other specimens. It is possible that the weave of the carbon sheet helped inhibit slippage on the tension face of concrete resulting in a more successful transfer of load between concrete and the tube. Generally, failure of the tube occurred on a line at the same orientation as the fibers in the tube, i.e., at ±15° from the vertical axis (Figure 2.9). After removing the tube from the failed specimens, one could clearly see extensive shear cracking in the concrete. The tube did not increase the shear strength of the beams beyond their flexural strength. However, the shear strength was increased

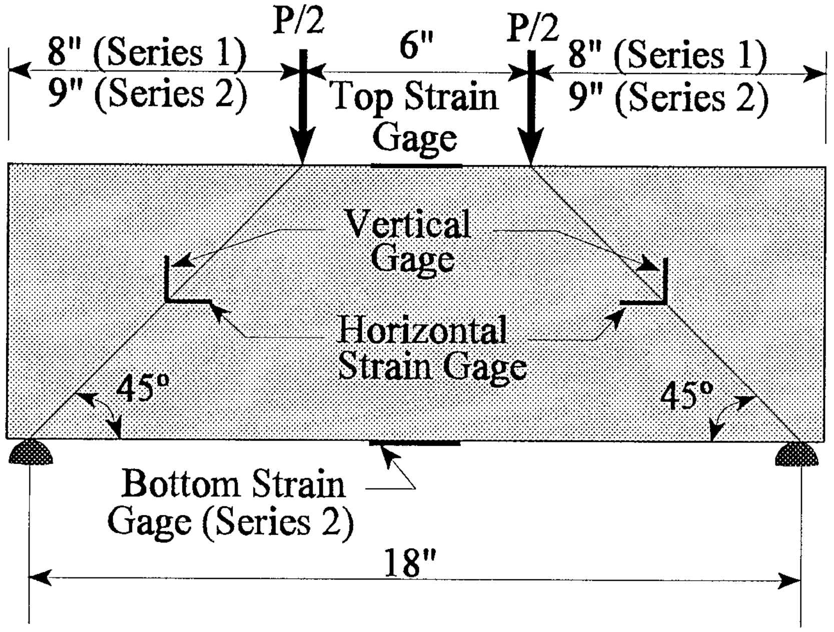

Figure 2.4 Instrumentation of beam specimens

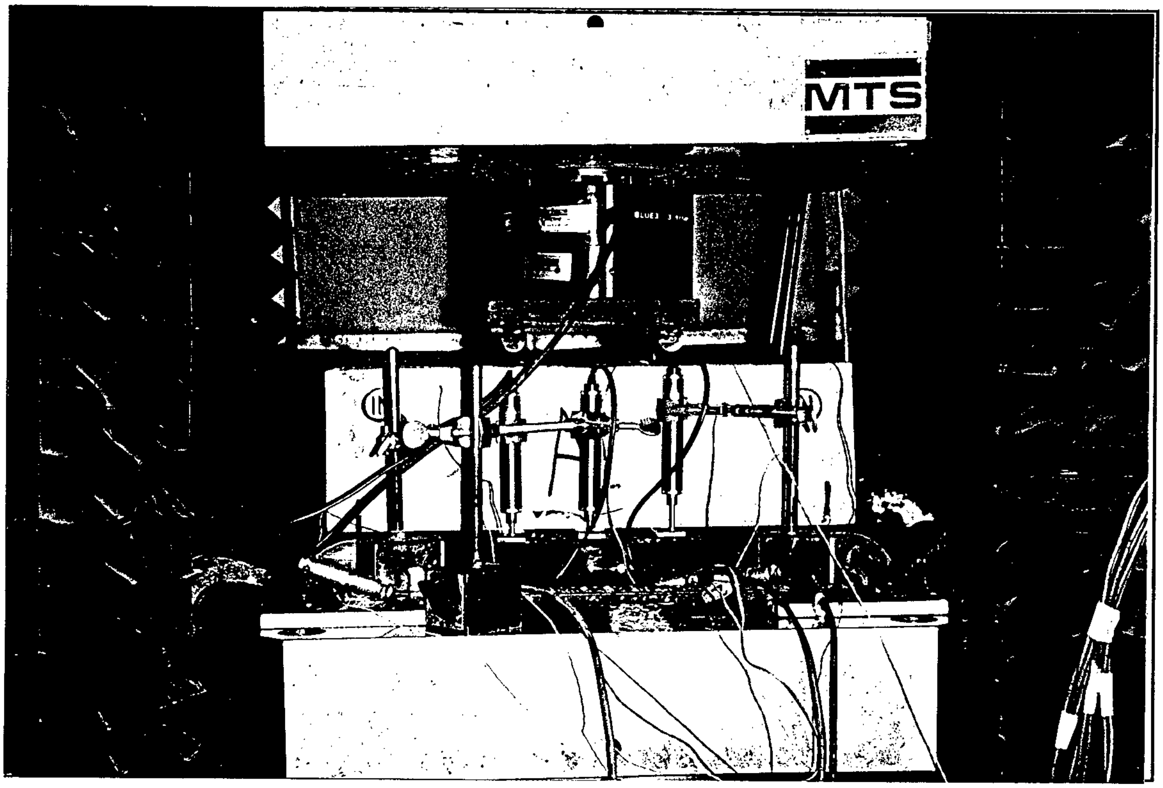

Figure 2.5 Beam shear test setup

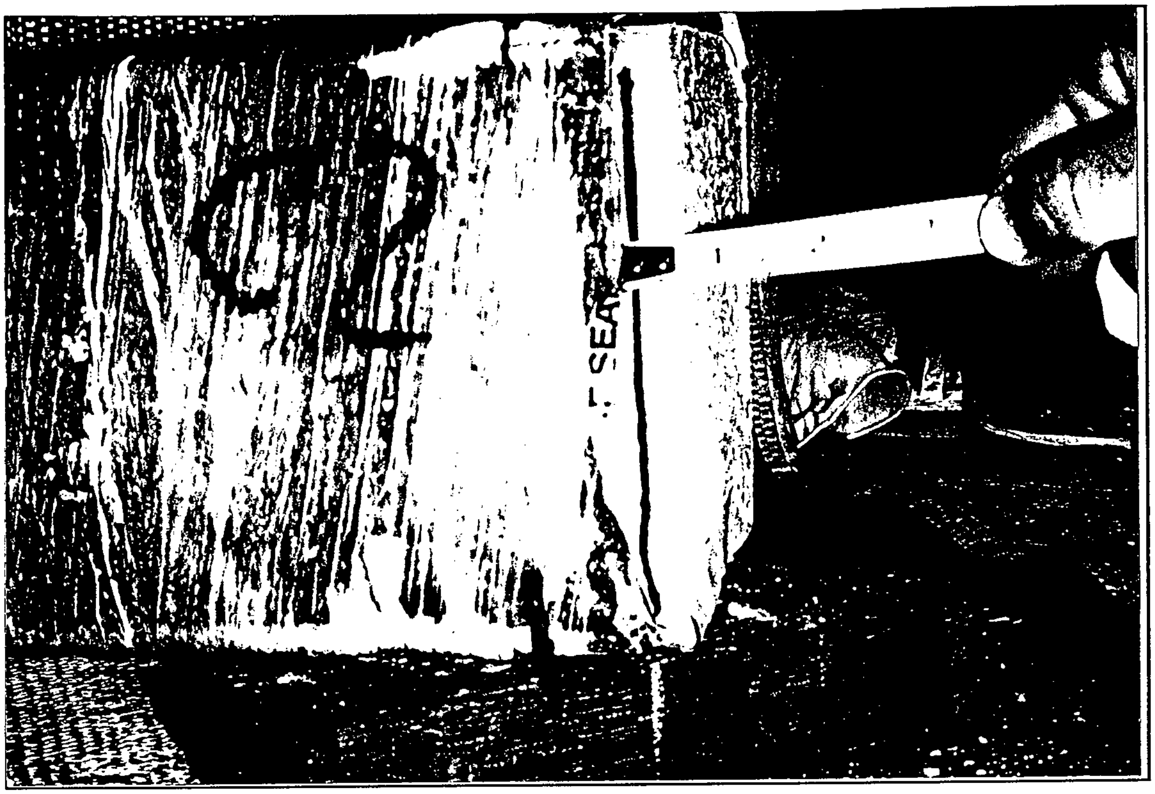

Figure 2.6 Beam C2 after failure showing extreme slippage

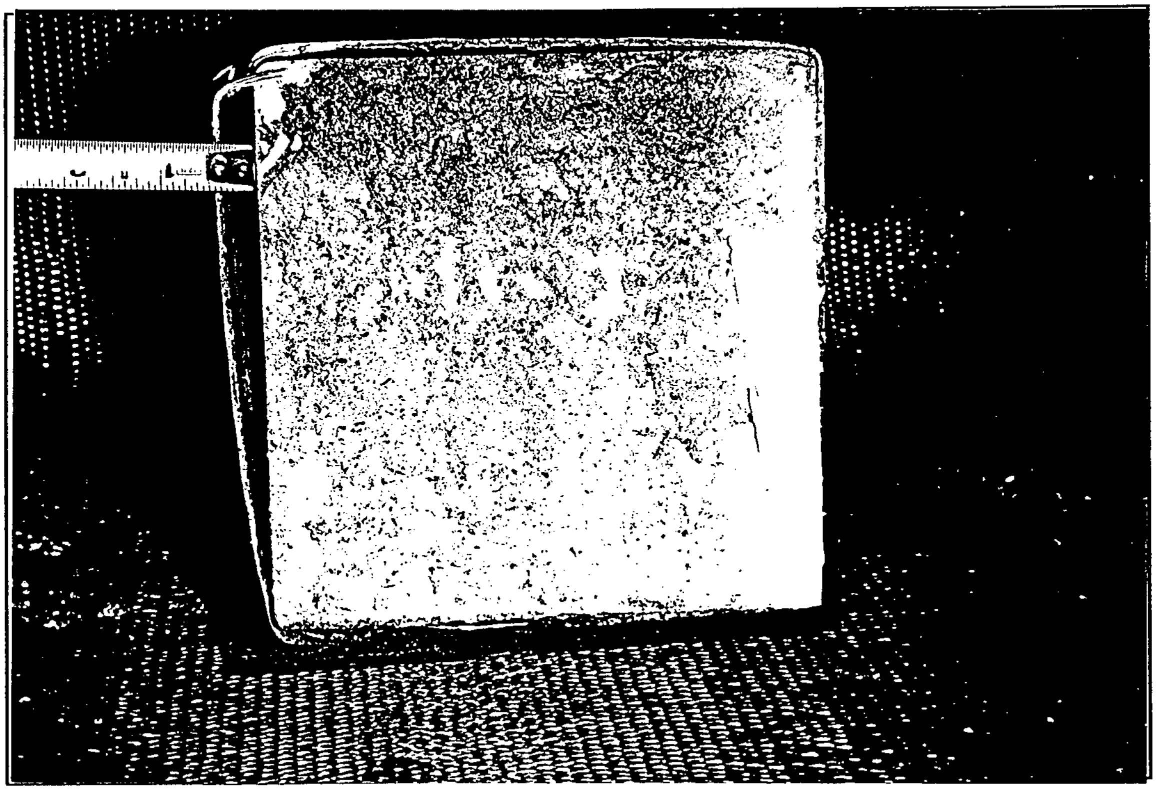

Figure 2.7 Beam C2 with bulged and separated jacket

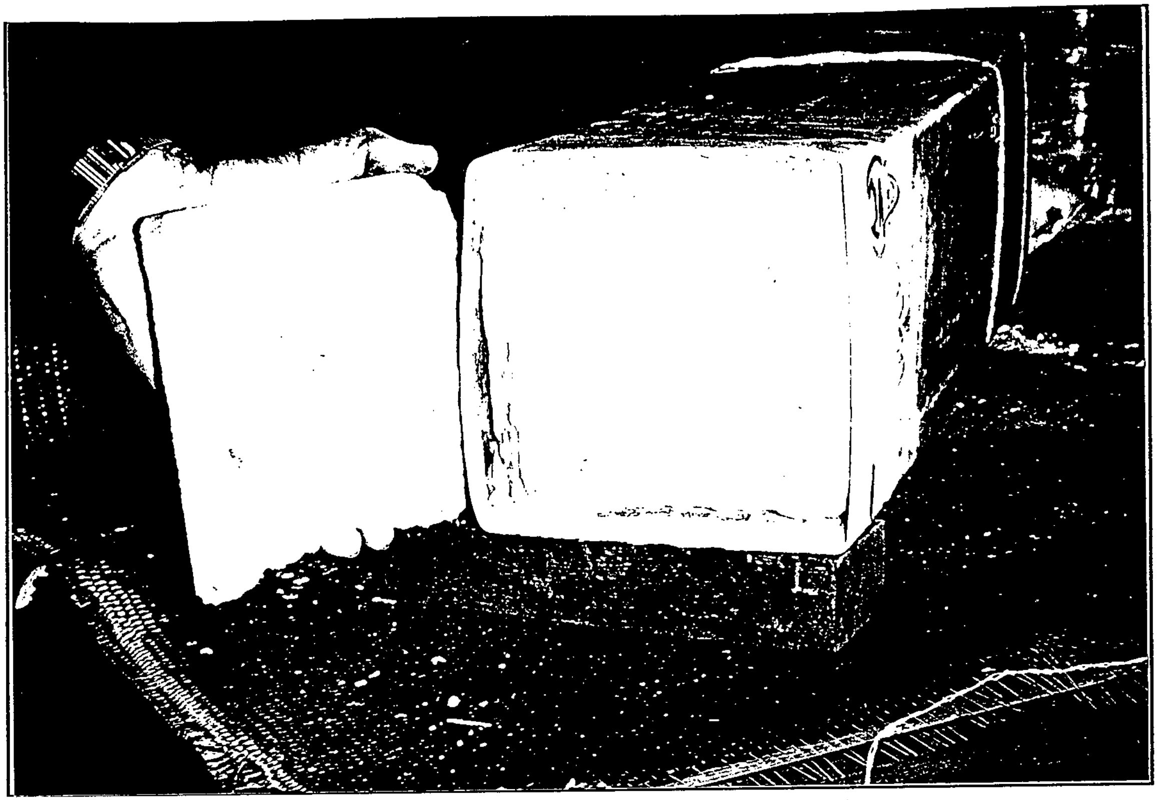

Figure 2.8 Beam C2 after failure (side view)

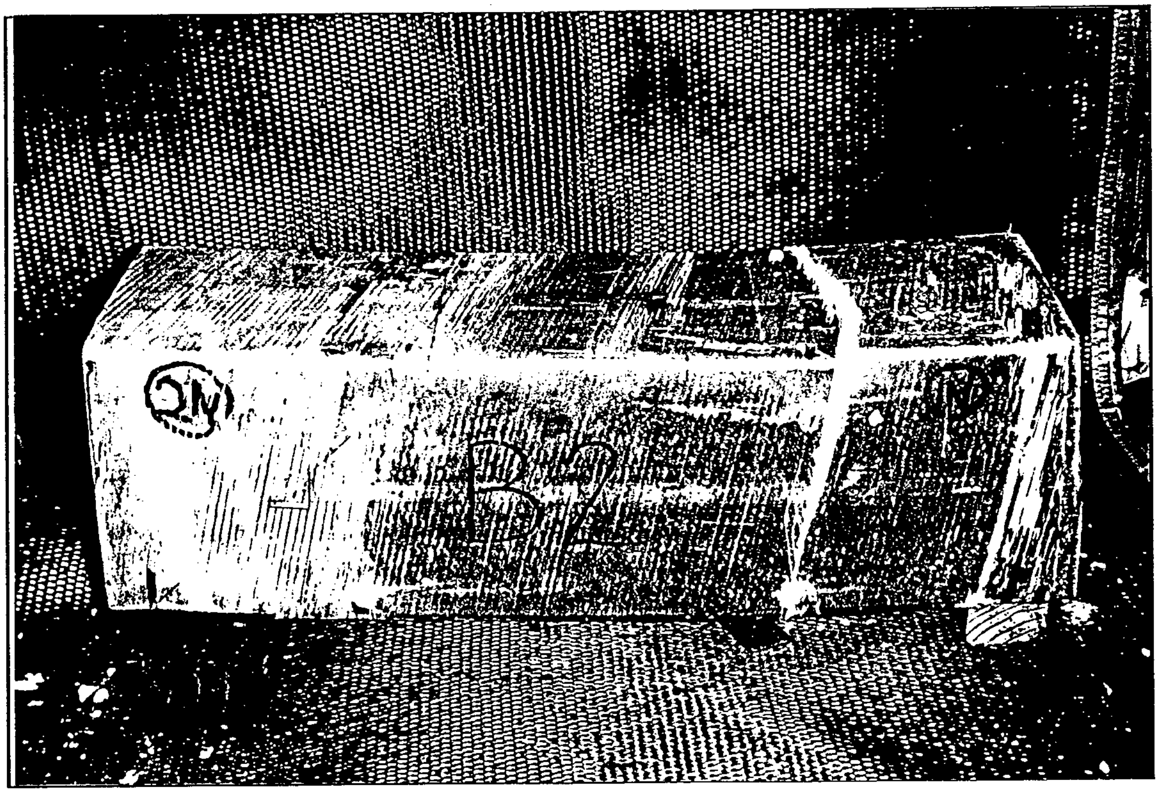

Figure 2.9 Beam B2 after failure showing crack inclination at fiber orientation

considerably due to crack containment. Thus, the expected and actual failure of the control specimens was from shear. The theoretical shear strength of the jacketed specimens was calculated (from equations developed in Section 2.3 and assuming a 45° angle of crack) to be nearly double the flexural strength. Thus the failure for the jacketed specimens was expected to be flexural. However, no flexural failure was observed in any of the specimens. It is believed that the excessive amount of slippage was of great consequence to the lack of shear enhancement provided by the jacket. In order for the jacket to increase the shear strength of the beams, efficient load transfer needed to occur at the onset of the first shear crack in the concrete. However, the extensive amount of slipping indicated that very little or no transfer of load could have occurred until the concrete had completely failed. At this point, the concrete was severely damaged and large voids may have been present in the concrete. It can be seen in specimen B2 (Figure 2.10) that a chunk of the concrete broke off at the end. The jacket for that same specimen (Figure 2.11) failed along a crack near the point where the chunk of concrete broke off. At this point, concrete offered no internal support for the jacket and the jacket failed prematurely. The same was true for specimen B1. Specimens of Group C behaved similar to those of Group B with the exception of some flexure cracking. These specimens were reinforced with a woven carbon sheet on the tension face between the concrete and the glass jacket. It was noted earlier that these specimens were the least likely to show flexural damage since they had the highest flexural strength. Upon removing the jacket from the tested beams, it was noticed that the tension face of the concrete was impressed with the weave pattern from the carbon sheet (Figure 2.12). The woven carbon sheet may have served as a mechanical bond between concrete and the tube aiding the transfer of tensile loads at the interface. Specimens of Group D behaved very similar to the control specimens. Since the jacket was provided only on three faces of the beam (no top), concrete was not confined as it was for the other specimens. It is evident from Group D that part of the enhancement in the shear strength seen for Groups B and C came form the ability of the tube to contain (rather than confine) concrete allowing it to withstand higher loads. Since the top of the jackets had been removed for specimens of Group D, the load was applied directly onto the concrete. This, and the fact that the jacket for these specimens showed no cracks, further supports the theory that no load was transferred to the jacket by concrete.

Test Results

The strain readings from the rosettes were not consistent, possibly because the tube surface where the rosettes were placed was uneven. This unevenness made it difficult to thoroughly glue the entire rosette onto the tube surface. Therefore, the strain readings will not be included in this section. As was mentioned earlier, the control specimens were designed with a flexural strength nearly nine times their shear strength. Table 2.3 shows the increase in the shear strength for the jacketed specimens over the control specimens. Also tabulated, is a comparison of the theoretical shear strength to the experimental results. The theoretical values are calculated according to equations of Section 2.3. Having learned that in order to fully utilize the shear strength of the jacket, some bond needs to be provided between the concrete and the jacket, a second series of test was devised (Series 2) where shear connectors were provided inside the jacket.

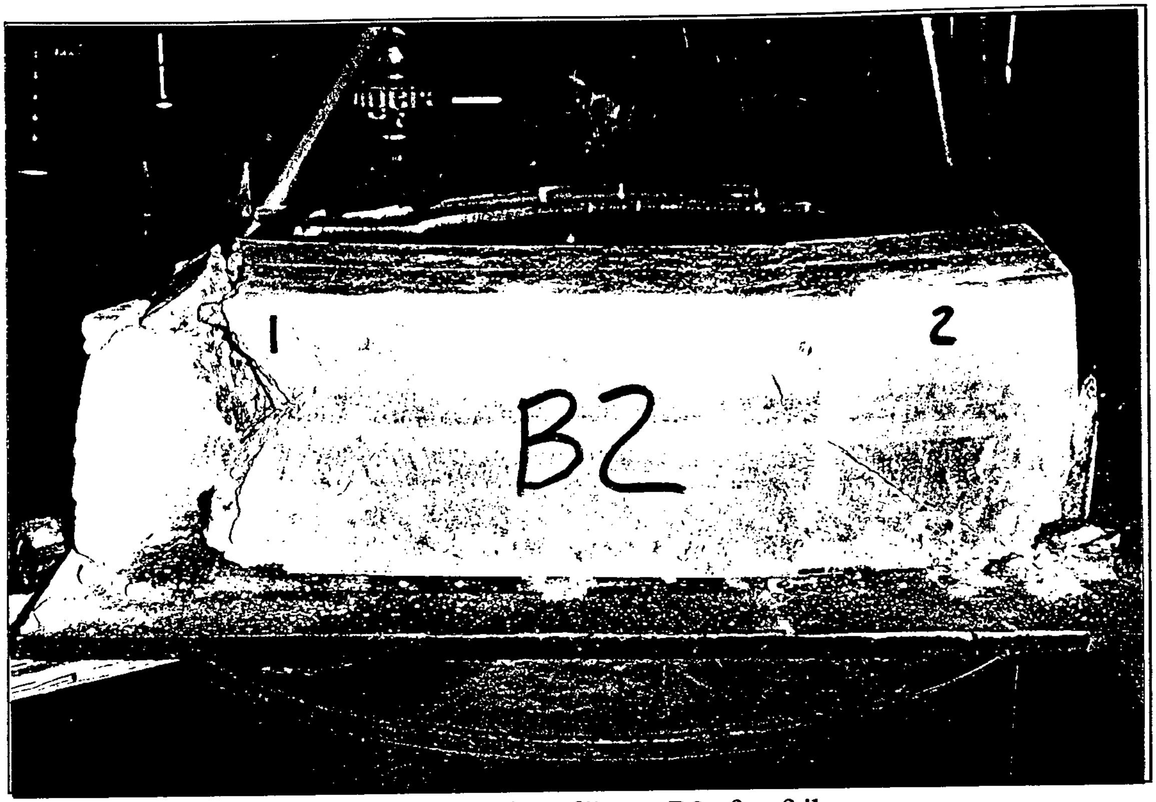

Figure 2.10 Interior of Beam B2 after failure

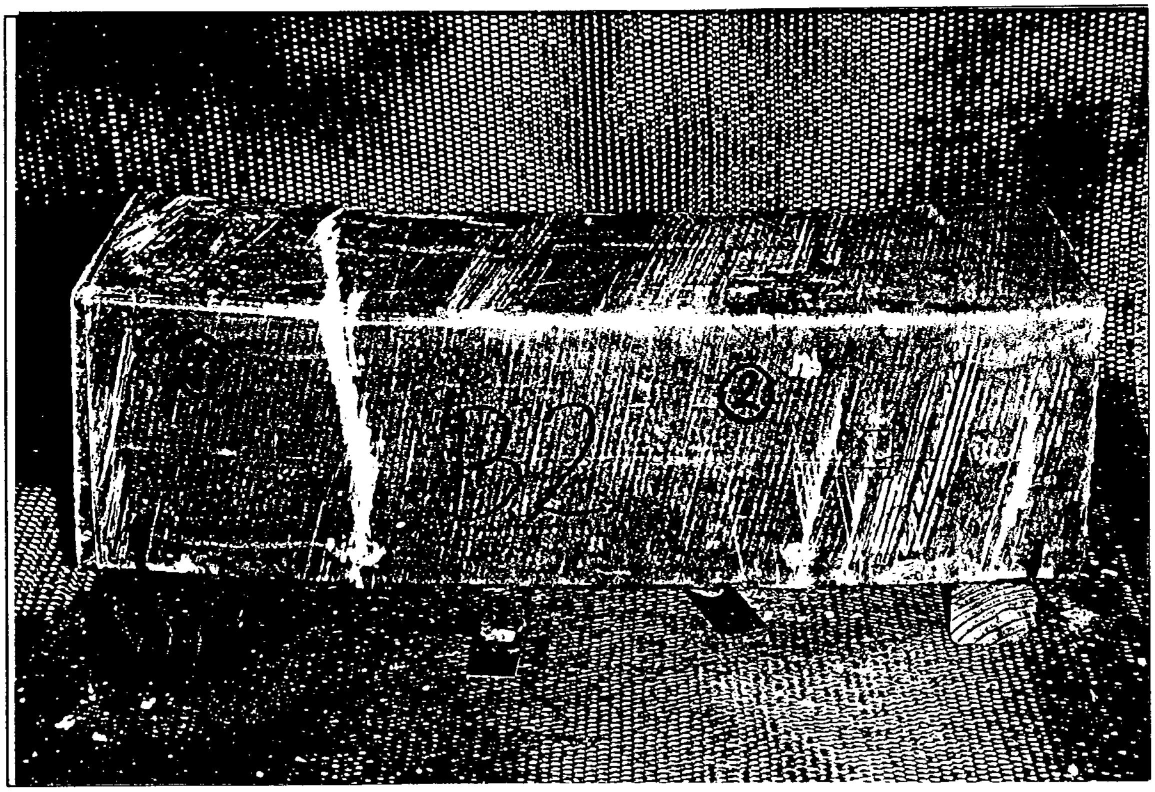

Figure 2.11 Beam B2 after failure

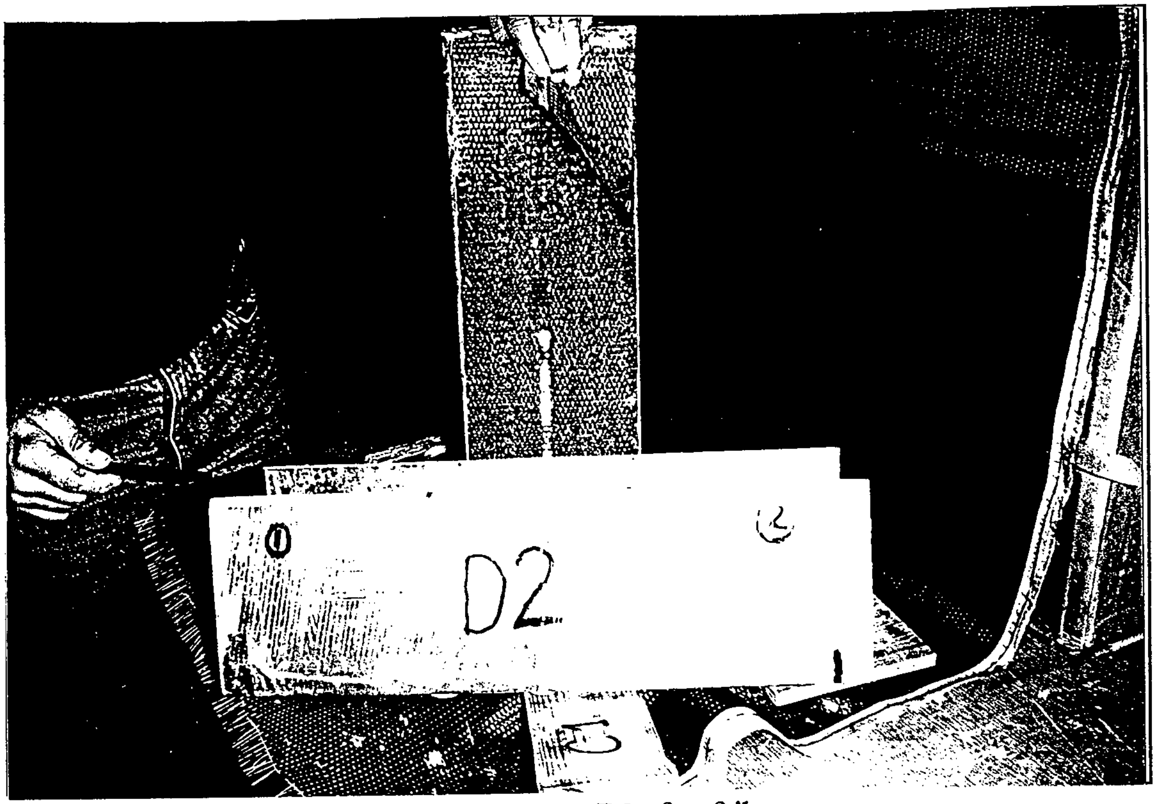

Figure 2.12 Beam D2 after failure

Table 2.3 Test results for Series 1

Specimen	Experimental P_{max} (kips)	Percent increase over control beams	Theoretical P_{max} (kips)	P_{Theo}/P_{Exp}
A1	9.96	-	4.82	0.5
A2	11.93	-	4.82	0.4
B1	20.74	89.49	62.27	3.0
B2	25.55	133.44	62.27	2.4
C1	23.74	116.90	62.27	2.6
C2	19.12	74.69	62.27	3.3
D1	14.18	29.56	62.27	4.4
D2	17.45	59.43	62.27	3.6

* Average strength of concrete cylinders was 4.476 ksi.

Series 2

In order to correct the slippage problem encountered with the beams of Series 1, a new type of beam was manufactured with shear connectors on all four interior faces. Series 2 beams, however are not comparable to Series 1 beams since no steel re-bars were included in these beams. A total of 8 beams were fabricated and tested for Series 2. Fabrication of the tubes and the mandrel were discussed in the Final Report of Phase I (Mirmiran 1997), and will not be repeated here. The differences between the tubes of this study and the one reported under Phase I are as follows; (1) tubes of Group H were made with 6 layers of angle plies while all other tubes and the tubes of Phase I were all made of 15 layers, and (2) no roving was used in the construct of the tube for shear tests, and only for the tubes of series G, a chopped glass fiber mat was glued after the mixture hardened and before the outside jacket was wound on.

Specimen Layout

Table 2.4 shows the test matrix for Series 2. Eight specimens were divided into four groups with two identical samples from each group for repeatability verification. All specimens were approximately 24 inches long. Figure 2.13 shows the schematics of the specimens of each group. Four 6" x 12" concrete cylinders were also cast to determine the average strength of concrete core. The characteristics of the four groups are as follows:

1. Group E consisted of the control specimens with a glass sheet glued onto the tension side as flexural reinforcement. No other type of reinforcement was provided for the control specimens.
2. Group F specimens were reinforced with a 0.135 inch thick FRP jacket made of 15 layers of fibers. No glass sheet was provided as additional reinforcement for these specimens.
3. Group G specimens were also reinforced with a 15-layer FRP jacket. However, they differed from specimens of Group F in that a chopped glass sheet was provided as additional reinforcement on all 4 sides of the inside jacket.
4. Group H specimens consisted of a 6-layer FRP jacket with 0.054 inch thickness and no glass sheet.

Table 2.4 Test matrix for Series 2

Group No.	Longitudinal Reinforcement		Shear Reinforcement
	Compression	Tension	
E	None	Glass Fiber Sheet	None
F	None	None	FRP Tube [15 Layers]
G	Chopped Glass Fiber Mat on all Sides	Chopped Glass Fiber Mat on all Sides	FRP Tube [15 Layers]
H	None	None	FRP Tube [6 Layers]

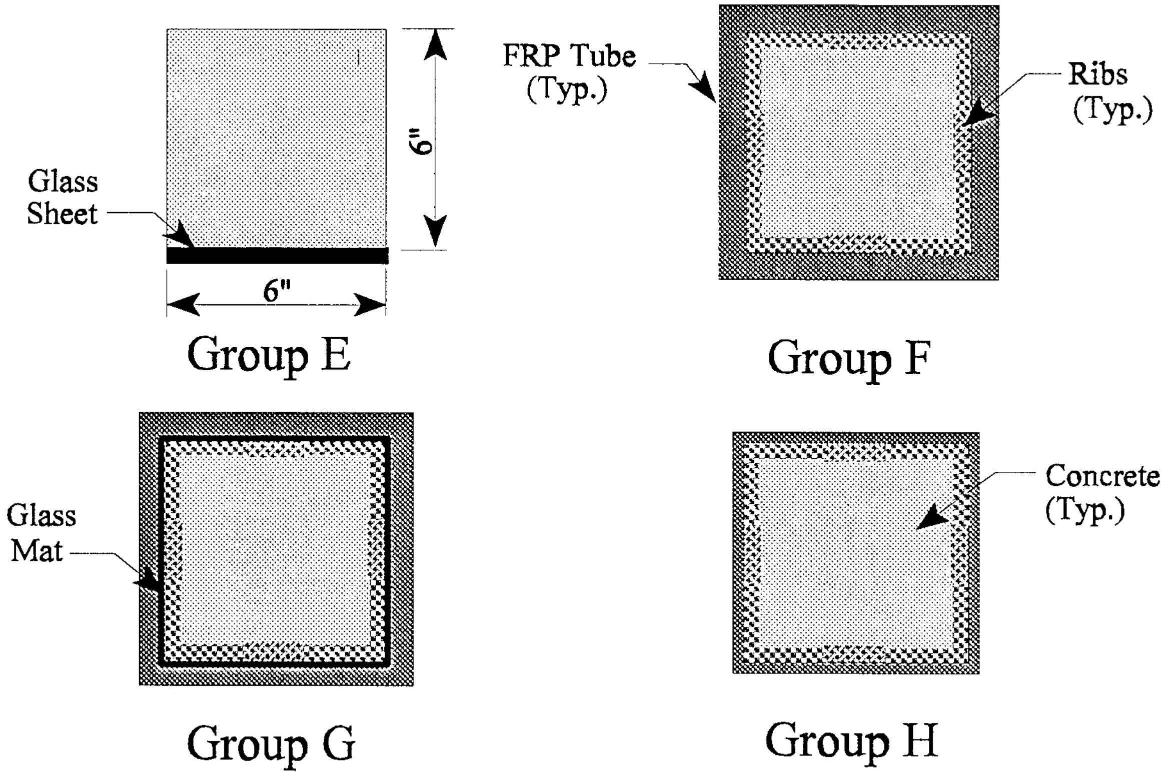

Figure 2.13 Specimen cross sections for Series 2

Materials were the same as those reported earlier for the specimens of Series 1, with the exception of the specific gravity of crushed limestone being 2.321. The concrete mix was designed based on a volume method with a water-to-cement ratio of 0.515 (by weight) for a 28-day compressive strength of 4000 psi. No additives were used in the mix. One cubic yard of the mix consisted of 597.7 lb cement, 308.23 lb water, 1080.87 lb sand, and 1804.15 lb gravel. Casting was done at UCF on July 1, 1996, using a 9-cubic foot rental mixer. Concrete was compacted using an electric vibrator. Other preparation tasks were the same as for Series 1.

Instrumentation

For beams E2, F2, G2, and H2, rosettes were attached at both vertical faces on the center of a 45° line between the support and the load. The rosettes measured horizontal, vertical and the strain along the 45° line (see again Figure 2.4). For all the beams, strain gauges were also placed centered vertically and horizontally on the top and bottom faces. The beams were also instrumented with three LVDTs one at the mid-span, and two under the points of load application.

Test Procedure

Specimens were tested on July 31 and August 1, 1996 at the Florida Department of Transportation. Test setup and equipment were the same as for Series 1.

Observed Behavior

As with Series 1, cracking and popping noises were heard while testing the FRP beams. Although a glass sheet was provided as reinforcement against bending and no shear reinforcement was provided, the control specimens did not fail in shear. The reason for this is that the glass fiber sheet glued to the tension face of the beams de-bonded while loading as can be seen in Figure 2.14. It was later noted that in order to prevent bond failure, it is necessary to sandblast the face of concrete and extend the glass sheet about 2 inches up the front and back face of the beam. However, the objective of Series 2 was to prevent the slippage between the concrete and the FRP jacket, and this was clearly accomplished. Beams F1, H1, and H2 failed in flexure at the midspan. Beams G1, G2, and F2 failed from excessive flexural cracks which developed under the point of load application. It should be noted that the jackets for the specimens contained some unevenness. It is suspected that the unevenness of the jacket surface for these beams prohibited even distribution of the load at both points resulting in the extreme cracking and eventual failure under the loading point (Figure 2.15). No slippage was evident for any of the beams. As a result, flexural cracking was clearly visible in most of the specimens (again see Figure 2.15). Upon removal of the jackets, there was no evidence of the extensive shear cracking present in the concrete as with the specimens for Series 1. The shear connectors had effectively retarded slippage and allowed for the concrete and the jacket to act effectively as one composite section.

Test Results

Since none of the beams failed in shear, it was not possible to make a quantitative comparison of the increase in shear strength provided by the jacket. Therefore, the theoretical values from Section 2.3 clearly overestimate the failure load of the specimens since they all failed in flexure. Table 2.5 presents the percent increase in the load carrying capacity of the beams. Because

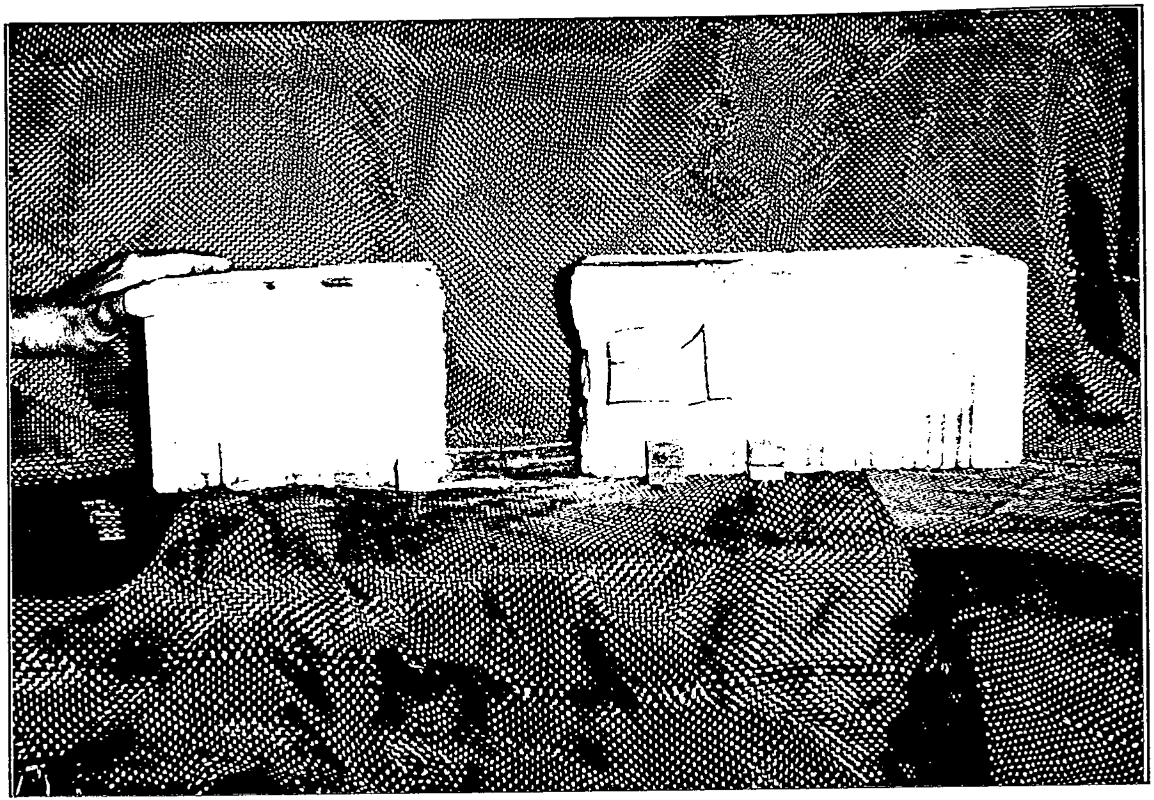

Figure 2.14 Control Beam E1 after failure

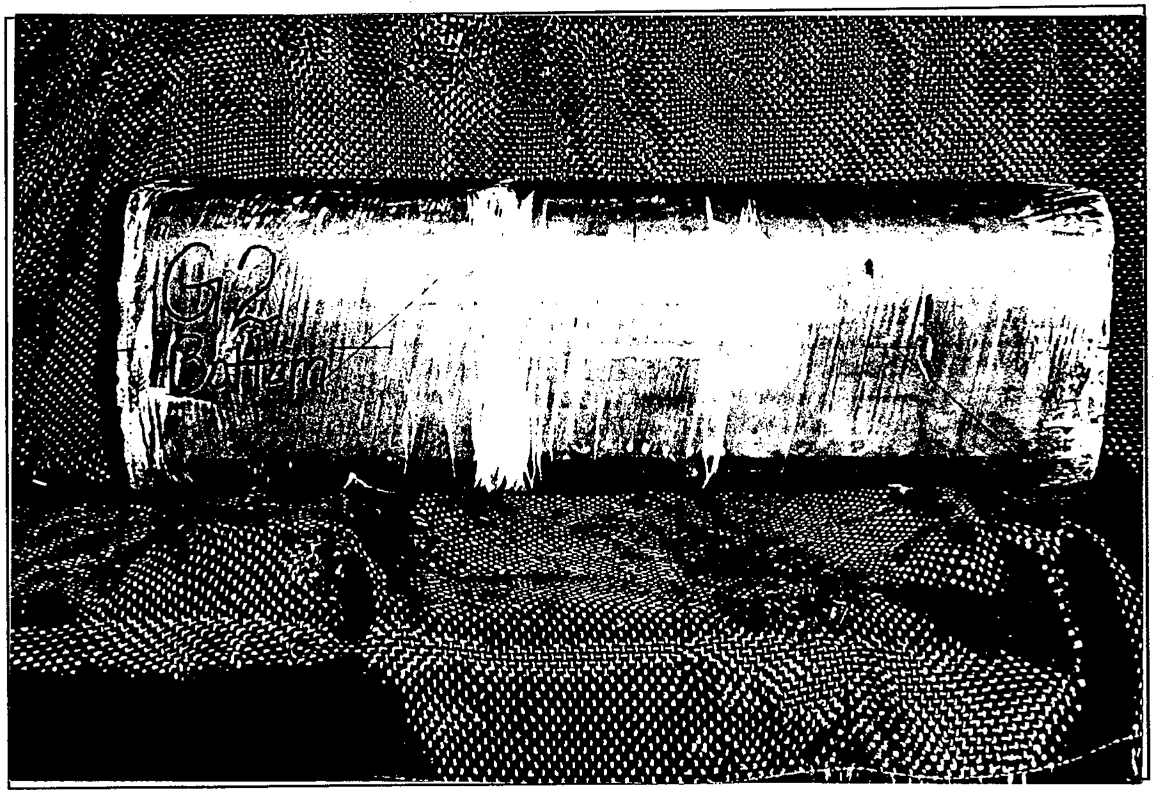

Figure 2.15 Beam G2 after failure

none of the jacketed beams failed in shear, it is known that the shear strength of the jacketed beams was greater than the load at failure. Since the load at failure was anywhere between 2 and 6 times the strength for unjacketed specimens as given by ACI, we may conclude that the jacket enhanced the shear strength by more than 2 to 6 times the theoretical shear strength of unjacketed beams.

Table 2.5 Test results for Series 2

Specimen	Experimental P_{max} (kips)	Percent increase over control beams	Theoretical P_{max} (kips)	P_{Theo}/P_{Exp}
E1	4.54	-	4.95	1.1
E2	4.11	-	4.95	1.2
F1	27.55	537	155.61	5.6
F2	19.85	359	155.61	7.8
G1	10.64	146	155.61	14.6
G2	10.80	150	155.61	14.4
H1	24.68	471	54.20	6.3
H2	24.32	462	54.20	6.4

* Average strength of concrete cylinders was 4.722 ksi.

Graphs of load versus top and bottom strains are also provided for these specimens (Figures 2.16 and 2.17). Also, Figure 2.18 shows the moment-curvature for all specimens. The curvature is calculated by dividing the algebraic difference between the top and bottom strains by the depth of the section (6"). The latter graph shows considerable ductility for jacketed specimens. It can be seen in all three graphs that the strain and load capacity for all jacketed beams are considerably increased. The beams which clearly failed in flexure at midspan show the greatest increase. It is also of interest to note that the jacketed specimens exhibit the same behavior as the unjacketed specimens up to the point where the plain concrete fails. From this point on, a clear change in the slope occurs. All jacketed beams except G2 show the same second slope in the load-strain curve. No such behavior was evident for Series 1. As with Series 1, however, the unevenness of the jacket combined with the relatively short length of the rosettes is suspected responsible for the inconsistent strain readings from the rosettes. For this reason, no charts of these readings are provided here. It is apparent from the results from Series 2 that the shear connectors successfully corrected the slippage problem encountered in Series 1. With slippage no longer a problem, the jacket acted effectively to increase the shear strength of the beams. However, fabrication of the square jackets needs to be improved to ensure a smooth, level surface.

2.3 Analysis and Discussion

Because of the sudden and often catastrophic nature of shear failures, it is necessary to develop a way of adequately predicting the shear strength of FRP-encased beams. In this section,

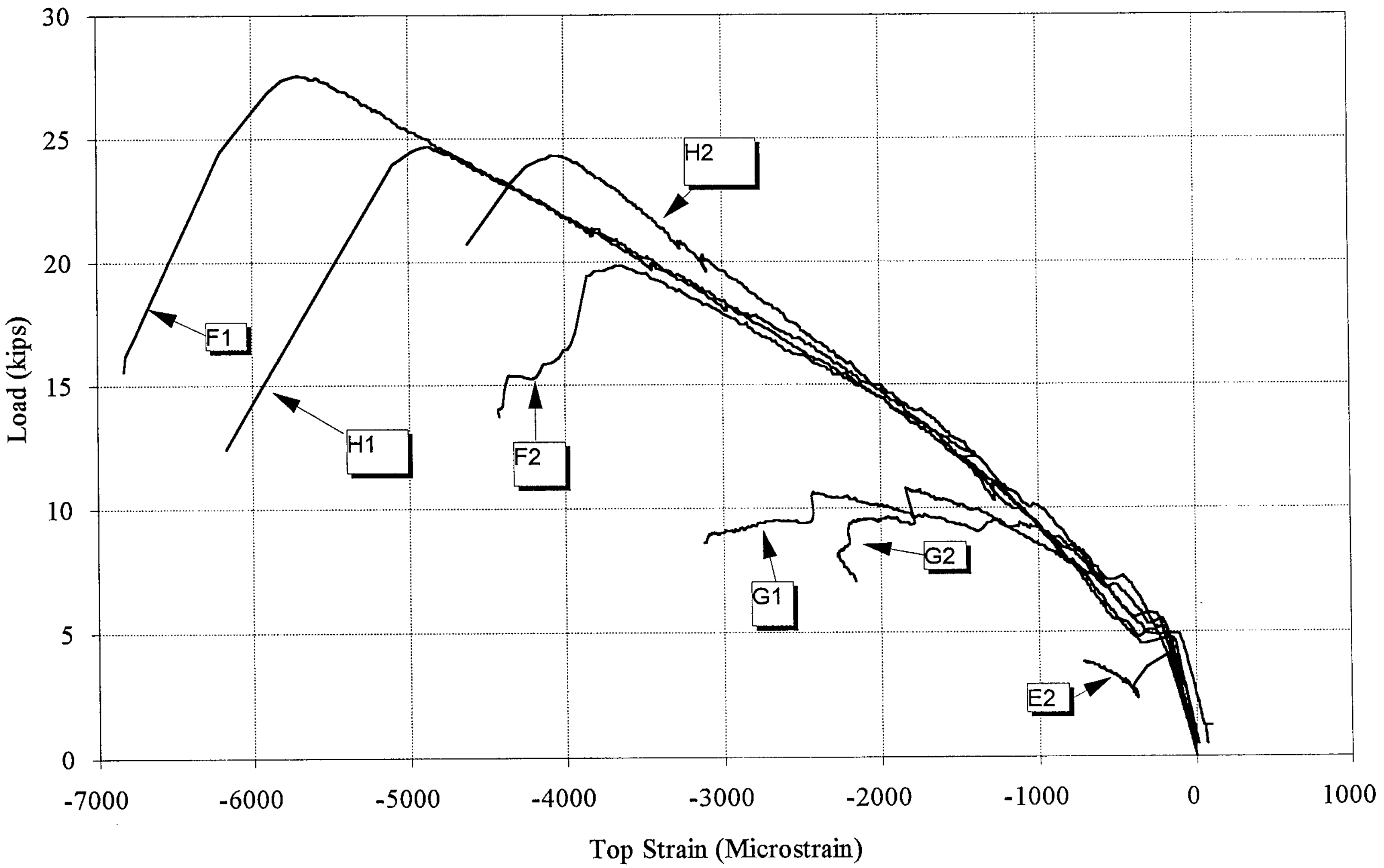

Figure 2.16 Load versus top strain for specimens of Series 2

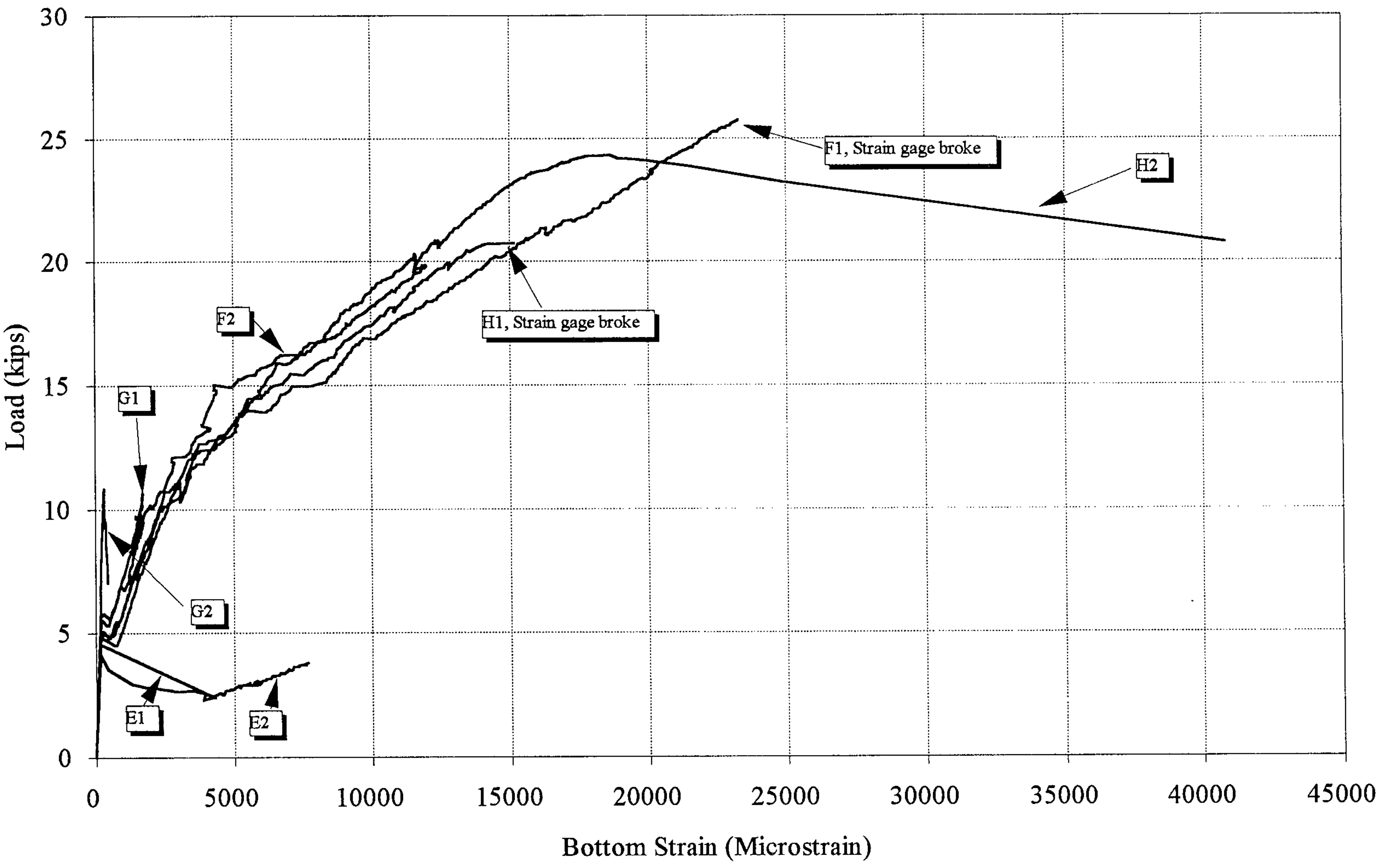

Figure 2.17 Load versus bottom strain for specimens of Series 2

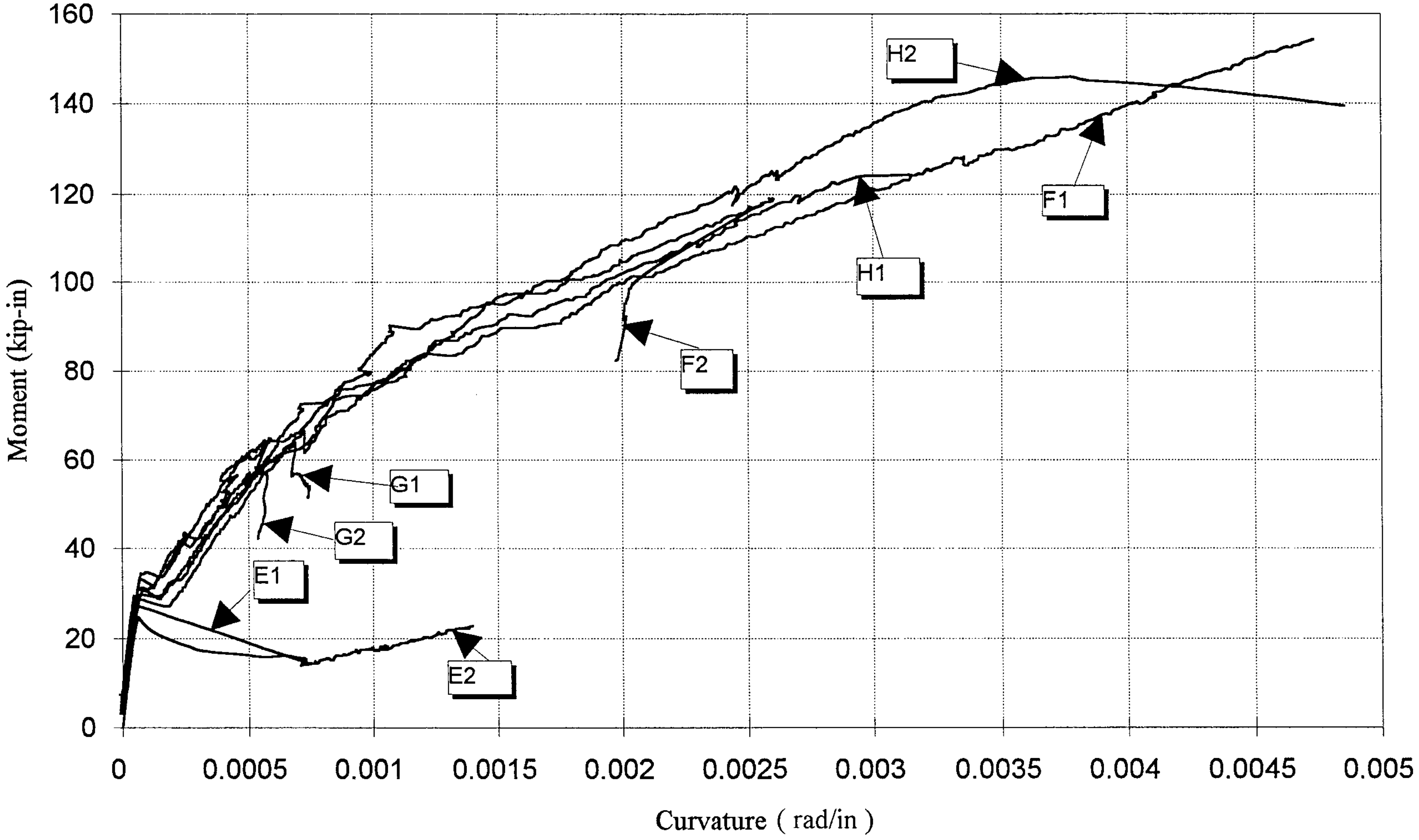

Figure 2.18 Moment-curvature for specimens of Series 2

shear strength of FRP-encased concrete beams will be discussed. The truss analogy will be used to establish the shear strength formulas. The theoretical study concentrated on members of both rectangular and circular cross sections, even though experimental work was only conducted on square sections. The underlying assumption in the derivations of shear strength is the full bond between the tube and the concrete core, and the shear failure of the cross section.

Rectangular Sections

In order to aid in developing the equation for the shear strength provided by the FRP jacket, first, the simplest case was undertaken. That is, it was assumed that the fibers in the jacket were oriented only in the vertical direction. When concrete cracks, the crack traverses a distance *c* along the jacket. Figure 2.19 is an illustration of the cracked beam and the forces developed in the jacket. The forces in the jacket exposed by the crack are given by

$$V_j = f_j A_j \tag{2.1}$$

where f_j is the strength of the jacket. Let *p* be the horizontal projection of the crack, and t_j the thickness of the jacket, the jacket area traversed by the crack will then be

$$A_j = 2\, p\, t_j \tag{2.2}$$

Substituting the above equation in Equation (2.1), V_j becomes:

$$V_j = 2\, f_j\, p\, t_j \tag{2.3}$$

Let *d* be the depth of the beam, and *q* the angle that the crack makes with the horizontal axis, the crack length in terms of the beam depth will then be

$$p = \frac{d}{\tan\ \theta} \tag{2.4}$$

and the expression for the maximum force in the jacket in its final form becomes

$$V_j = \frac{2\, f_j\, t_j\, d}{\tan\ \theta} \tag{2.5}$$

The case of vertical fibers is only a special case of the more general equation for inclined fibers (fiber inclination = 0°). Letting ϕ denote the fiber inclination, the fibers are equally oriented at $\pm\phi$ from the vertical axis. Figure 2.20 shows the forces developed in the jacket. The vertical component of the force exposed by the crack is

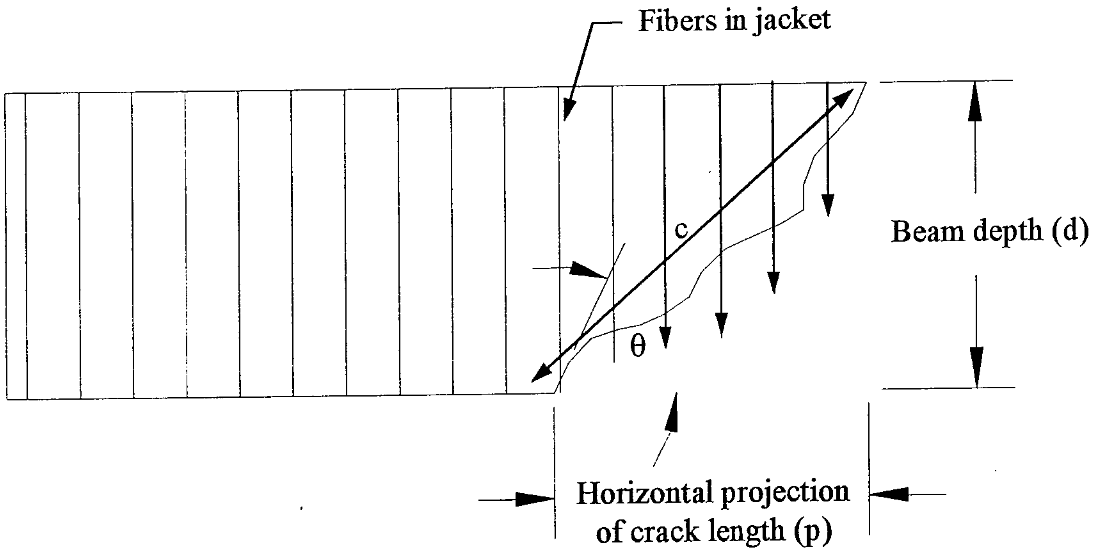

Figure 2.19 Shear crack in a rectangular FRP beam with only hoop fibers

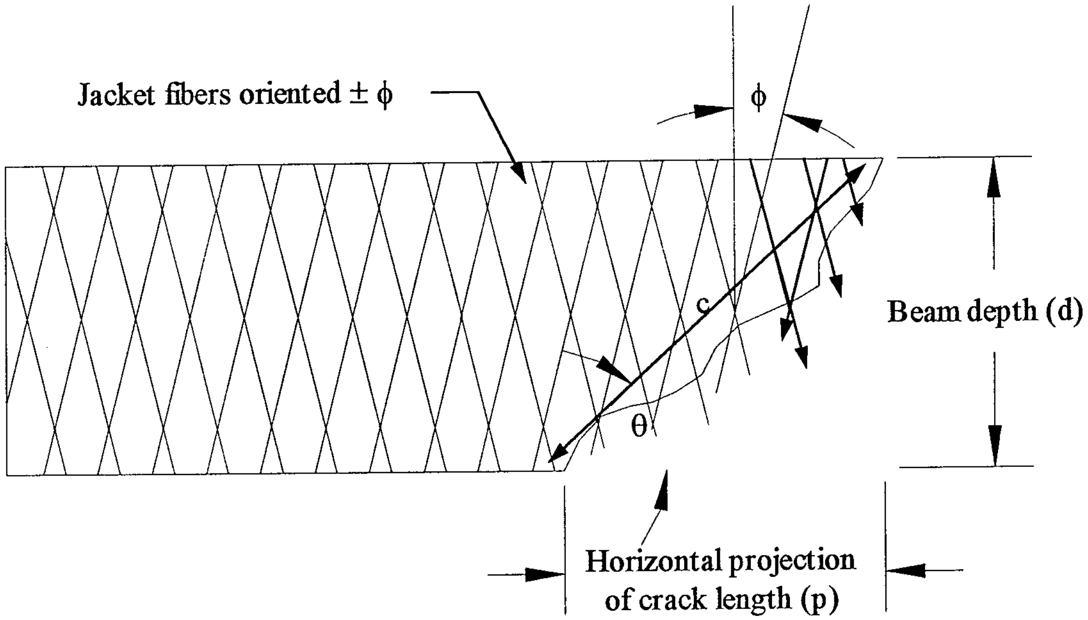

Figure 2.20 Shear crack in a rectangular FRP beam with ± ϕ angle plies

$$V_j = f_j A_j \cos \phi \tag{2.6}$$

Substituting Equation (2.2) in Equation (2.6) and relating the crack length to the dimensions of the beam, the equation for the maximum force that can be taken by the jacket becomes

$$V_j = \frac{2 f_j t_j d}{\tan \theta} \cos \phi \tag{2.7}$$

which is the general expression for the shear strength provided by the jacket in a rectangular cross section.

Circular Sections

Developing the shear strength provided by the jacket for a circular cross section requires a somewhat different approach. Chai (1991) addressed the shear strength of circular retrofitted columns with steel jackets. The same approach is taken here with slight modification to account for the possibility of fiber inclination within the jacket. Figure 2.21 shows the forces exposed by the shear failure plane. The fibers in the jacket are equally inclined at ±ϕ from horizontal and θ is the angle that the shear failure plane makes with the vertical axis. For an infinitesimal jacket height, *dz*, the shear force resisted by the jacket is

$$dV_j = 2 f_j t_j \cos \phi \sin \alpha \, dz \tag{2.8}$$

where cosϕ represents the horizontal component of the fibers in the jacket. The total shear force would then be given by

$$\int dV_j = \int 2 f_j t_j \cos \phi \sin \alpha \, dz \tag{2.9}$$

In order to solve the equation, a relationship between *dz* and the angle α is needed, as below

$$\begin{aligned} y &= r' \cos \alpha \\ y &= - z \tan \theta \end{aligned} \tag{2.10}$$

z may be expressed as

$$z = \frac{r' \sin \alpha}{\tan \theta} d\alpha \tag{2.11}$$

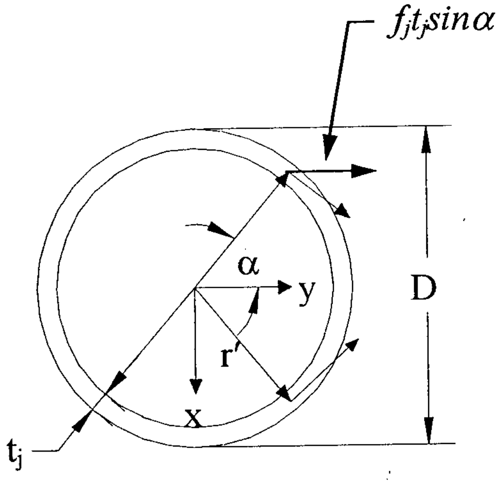

Plan

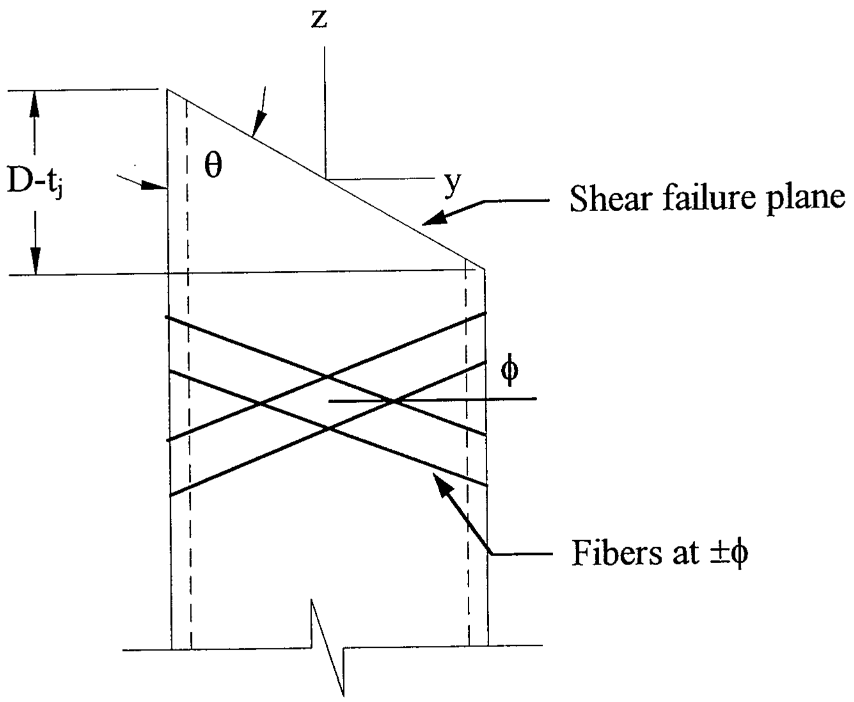

Elevation

Figure 2.21 Shear crack in a circular FRP beam with ± ϕ angle plies from which

$$dz = \frac{r' \sin \alpha}{\tan \theta} \, d\alpha \tag{2.12}$$

which is the desired relationship. Substituting Equation (2.12) into Equation (2.10), the equation for the shear force becomes

$$V_j = \frac{2 \, f_j \, t_j \, r' \cos \phi}{\tan \theta} \int_o^{\Pi} \sin^2 \alpha \, d\alpha \tag{2.13}$$

Noting that $r' = \dfrac{D - t_j}{2}$ and evaluating the integral, the final expression for the shear strength of the jacket is arrived at and is given by

$$V_j = \frac{\Pi \, f_j \, t_j \, (D - t_j) \cos \phi}{2 \tan \theta} \tag{2.14}$$

This equation is the most general case allowing for any fiber inclination and any crack angle.

Shear Strength of Concrete

The shear strength of the concrete core would also contribute to the total shear strength of the member. According to ACI 318-95 (1995), the shear strength provided by concrete is $2\sqrt{f'_c}\,bd$ where b is the width and d is the depth of the member and f'_c is the 28 day compressive strength of concrete. The total shear strength of the member, as provided by the FRP jacket and the concrete is then given by

$$V = V_j + V_c \tag{2.15}$$

where V_j is the jacket strength and V_c is the concrete strength.

Although the strength of the jacket is expected to considerably increase the shear strength of the members, the confinement provided by the jacket also enhances the shear strength of the member. At the first onset of a crack in the concrete, the load would be transferred to the jacket. The jacket would retard any further increase in the width of the crack since the concrete would have nowhere to move to (assuming no slip). An unconfined beam would not be as efficient in crack containment. The narrower cracks would allow for a greater interface force, hence, further increasing the shear strength of the beam.

CHAPTER 3

EFFECT OF CROSS SECTION ON CONFINEMENT

3.1 Literature Review

It is well known that lateral confinement of concrete increases its strength and ductility. In conventionally reinforced concrete columns, confinement is provided by transverse steel stirrups or hoops. Generally, building codes such as ACI 318-95 (1995) specify the spacing and bar size requirements for the transverse steel to allow for ductile failure of the columns under overload conditions. Another method of confining concrete is by encasing concrete in a steel tube. Concrete-filled steel tubes have in recent years attracted a growing interest in the construction industry. As a result, researchers too have investigated several aspects of their performance. Ge and Usami (1996) evaluated the inelastic behavior of concrete-filled steel box columns under cyclic loading. Hijjar and Gourley (1996) developed a polynomial strength equation to represent the moment-thrust interaction diagram of concrete-filled steel tubes. Lu and Kennedy (1994) determined that concrete-filled steel tubes increased the flexural strength of hollow steel tubes by up to 30%. Prion and Boehme (1994) showed that confinement effectiveness of the tube is greatest for slenderness ratios of less than 15.

Confining of concrete columns is also advantageous for strengthening of existing columns. One such method was developed by researchers at the University of California, San Diego for the California Department of Transportation (Caltrans). In this technique two half cylinders of steel are placed around the existing column, and then welded together. The gap between the jacket and the existing column is filled by grout. Priestley et al. (1994) have shown that steel jacketing not only improves flexural strength of the column but also increases the shear capacity somewhat similar to transverse steel ties.

Another method of confinement that has been developed during the last ten years is fiber-wrapping. The wrapping of unidirectional fiber composite sheets around concrete columns offers a promising technique to strengthen and repair existing bridge structures. Demers and Neale (1994) tested several circular and square specimens with fiber-wrapping made of glass or carbon fibers. They concluded that increases in strength of up to 70% are possible and that the ultimate failure strain can be of the order of seven times that of a plain concrete specimen. Extensive studies at the University of Sherbrooke have shown that circular sections are more effectively confined than rectangular sections (Picher 1995, Rochette 1997). For rectangular sections, it is the corner radius that controls the confinement effectiveness. As the corner radius increases, the behavior of the column becomes closer to a circular column confined by fiber composites.

For the last three years, the Florida Department of Transportation has sponsored a detailed investigation of concrete-filled FRP tubes. Pilot tests by Kargahi (1995) showed the feasibility of the proposed method. Scherer (1996) extended the experimental studies and developed a framework for modeling of concrete confined by fiber composites. He also studied the optimization of the tube thickness and concrete section. Cabrera (1996) studied the shear strength and seismic performance of the hybrid system. Samaan et al. (1997) developed a confinement model for circular FRP tubes. Collective studies of the last three years at UCF have proved the advantages of the proposed system as follows:

1. High strength-to-weight ratio of fiber composites reduces the necessary thickness of the tube and results in lighter and more slender sections.

2. Poisson ratio of fiber composites is more compatible with concrete as compared with steel tubes.

3. Anisotropic properties of fiber composites allow for uncoupling of the design in the axial and hoop directions.

4. Fiber composites can effectively contain the dilation tendency of concrete. This is mainly due to the linear-elastic response of fiber composites. Also, this is in contrast to the behavior of steel-encased concrete columns in which, upon yielding of steel, dilation of the concrete core becomes unstable.

Despite advances in the use of fiber composites in hybrid construction with concrete, theoretical work has often been limited to simple extension of the models developed for steel and concrete composite systems. Of great importance in concrete-filled tubes is the accurate prediction of the strength and ductility of the column as the result of confinement. The first to propose a model for confinement was Richart et al.(1929) who suggested a relation in the following form

$$f'_{cc} = f'_{co} + 4.1\, f_r \tag{3.1}$$

where f'_{cc} is the maximum stress of confined concrete, f'_{co} is the peak stress of unconfined concrete, and f_r is the confining pressure.

The many models that followed the above work have all been developed for confinement with transverse steel. However, most have been applied to steel tubes, steel jackets, and even fiber-wrapped columns. Perhaps one of the most known models is the one developed by Mander et al. (1988). Recent studies by Mirmiran and Shahawy (1997) and Demers and Neale (1994) have shown that Mander's model overestimates the strength while underestimating the ductility of FRP-encased concrete. Specifics of the problems associated with Mander's model as related to fiber composites have been elaborated by Kargahi (1995), Scherer (1996), and Harmon and Wang (1996). The latter indicated that since Mander's energy-balance technique only uses the strain energy of the steel confinement to compute the internal energy and neglects the energy stored in the concrete as a simplifying assumption, it fails to predict the behavior of FRP-encased concrete where the energy of fiber composites may account for only one fifth of the total strain energy with concrete accounting for the remaining 80%. Therefore, the strain energy of the concrete core can not be neglected.

The only model specifically developed for fiber composites is that of Fardis and Khalili (1981) which uses Equation (3.1) for estimating the maximum stress f'_{cc} of confined concrete. The failure strain is given by

$$\epsilon_{cu} = 0.002 + \frac{0.0005\ f_r}{\epsilon_{ru}\ f'_{co}} \tag{3.2}$$

where ϵ_{ru} is the ultimate strain of fiber composites in the hoop direction. They further suggest a hyperbolic relation for the stress-strain response of FRP-encased concrete as follows

$$f_c = \frac{E_c\ \epsilon_c}{1 + \epsilon_c \left(\frac{E_c}{f'_{cu}} - \frac{1}{\epsilon_{cu}} \right)} \tag{3.3}$$

where ϵ_c and f_c are the strain and stress in confined concrete, and E_c is the modulus of elasticity of unconfined concrete. Experimental studies by Demers and Neale (1994), however, showed that this model underestimates the ductility of the column. Moreover, it is not applicable for square sections. Most recently, Samaan, Mirmiran and Shahawy (1997) developed a simple, yet accurate, mathematical model to predict the stress-strain response of cylindrical FRP-encased concrete both in the axial and lateral directions. In this chapter, an attempt will be made to extend the model to square cross sections.

3.2 Experimental Work

In order to investigate the effect of cross-section on the confining behavior of FRP tubes, a series of tests was carried out on a total of fifteen specimens, including nine 6"x6"x12" concrete-filled square FRP tubes, three control cylinders (unconfined) with 6" diameter and 12" height, and three 6"x6"x12" control squares (unconfined). Three groups of tubes with jacket thicknesses of 6, 10, and 14 plies (layers) were used. For each group, three specimens of the same thickness were prepared for repeatability verification. Each specimen was labeled with SQ for square or CYL for cylinder, number of plies (6, 10, or 14, and 0 for controls), and sample number (A, B, or C). For example, SQ6B is a 6-ply square tube. All specimens were made of the same concrete batch with a target strength of 4000 psi. Table 3.1 presents the test matrix. All tubes had a ¼-inch corner radius. Also, unlike the square columns tested under Phase I, these tubes had a smooth inside edge with no shear ribs. FRP square tubes were made of the same resin and fibers as described in Chapter 2. Also, the aggregates and cement were the same as those described for Series 1 in Chapter 2.

Table 3.1 Test matrix *

Group and Specimen No.	Cross Section	Type of Specimens	No. of Layers	Tube Thickness	Size of Specimens	Number of Samples
SQ6A, B, C	Square	Composite	6	0.083"	6" x 6" x 12"	3
SQ10A, B, C	Square	Composite	10	0.1248"	6" x 6" x 12"	3
SQ14A, B, C	Square	Composite	14	0.1617"	6" x 6" x 12"	3
SQ0A, B, C	Square	Control	-	-	6" x 6" x 12"	3
CYL0A, B, C	Circular	Control	-	-	6" (Dia.) x 12"	3

* Design strength for concrete core was 4,000 psi.

In order to make the square FRP tubes, a collapsible mandrel was designed with aluminum angles. Four (4) aluminum angles of 2½" x 2½" x ⅜" were connected with two end plates and an intermediate interior support plate, and placed on a 1-inch diameter driving shaft. There was a ½" gap between the angles that was covered with masking tape. The mandrel was constructed at the UCF machine shop. However, the filament-winding process was performed at Marine Muffler Corp., Apopka, Florida. A winding angle of ±15° was maintained for all specimens to match the winding angles of the circular tubes. For more details, regarding the mandrel, see Final Report of Phase I (Mirmiran 1997). It should be noted that since no internal shear ribs were desired, all wooden plates were removed from the mandrel prior to the filament winding process.

The bottom of each tube was sealed with nylon to contain the concrete mix. The square control specimens were prepared using metal molds, with a wooden divider to allow for a 6" x 6" x 12" casting area. A concrete mix of 4000 psi with a 5 inch slump was designed using the volume method for a 28-day curing period. The quantities of materials per cubic yard of the mix were as follows: 610.48 lb cement, 315.51 lb water, 1055.66 lb sand, and 1800.22 lb gravel. The water-cement ratio by weight was 0.517. No additive was used in the preparation of concrete specimens. The casting of all specimens was performed using a 9 cubic feet capacity rental mixer at UCF on September 5, 1996.

The top surface of each specimen was wetted daily for 5 days, to avoid any cracking of the exposed surface of concrete. Seven days after casting, the specimens were taken indoors. A 3/16" thick groove was cut from each FRP specimen around its perimeter. This groove was cut at the top and bottom of each specimen, ¾" from each end. This was done to ensure that the FRP jacket acted only as confinement for the concrete core. Figure 3.1 shows the grooving process with an electric sander. To attain a purely uniaxial load and even stress distribution, all specimens were capped with sulfur mortar. A hand-made capping device was used for square sections, as can be seen in Figure 3.2. Nonetheless, the capping process is the same as the one for cylindrical specimens. The alignment guides ensure verticality of the specimen with respect to its both end surfaces.

Instrumentation

A total of 8 PL-60 strain gauges were attached to each tube, a vertical and a horizontal gauge on each side of the tube at its mid-height. The surface where the gauges would be placed on was first

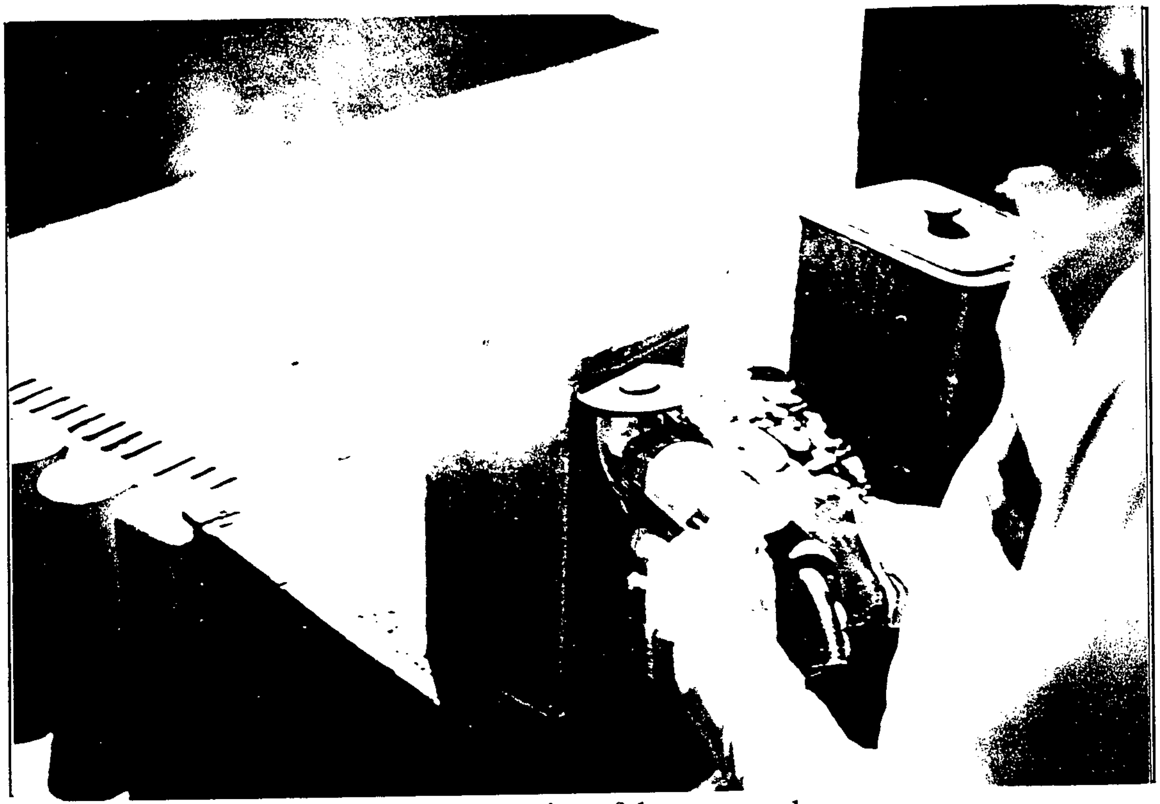

Figure 3.1 Grooving of the square tubes

Figure 3.2 Capping device for square sections

sanded and cleaned with acetone. Cyanocrylate adhesive was applied onto the surface, and the gauge oriented in the vertical (axial) direction was pressed against the glued surface. The gauge oriented in the horizontal (hoop) direction was then glued on top of the axial gauge. The control specimens were not instrumented with any strain gauges. In addition to the strain gauges, four LVDTs were used, one opposite each side of the specimen. Only three LVDTs were used for cylindrical control specimens. Figure 3.3, shows a specimen with full instrumentation prior to loading.

Test Procedure

Testing of the specimens was conducted at the FDOT Structural Research Lab on October 16, 1996, at the age of 41 days. Tests were performed using an MTS machine with a 550-kip capacity, and were recorded with a MegaDAQ data acquisition system (Figure 3.3). Each specimen was loaded at a constant rate of 0.22 inch per minute in a displacement control mode.

Observed Behavior

As predicted, control specimens (both square and circular) failed in a shear cone mode. However, composite specimens failed in a different mode. On these, the four vertical edges began to turn white at about 50%-60% of the ultimate load. The white patches began to appear at the mid-height, and then slowly spread along the entire edge, as can be seen in Figure 3.4. This was due to the plastic flow of the resin, leaving the fiberglass strands to resist the load. Then, low cracking sounds would be heard, at which point the load significantly dropped, but then stabilized. Some of the specimens hardly showed any visible signs of significant distress during loading. The only warning these delivered were the white patches and the low cracking noises, followed immediately by failure. The first composite specimen that was tested was SQ6C. It was noted that the specimen failed at a load not much higher than the failure load of the unconfined square specimens. The specimen failed very quietly, and remained intact, except for some white patches at the edges. Therefore, it was decided to reload the specimen. Upon reloading, it failed at 131 kips, compared to the initial 221 kip load. At this point, the specimen showed obvious signs of failure as the FRP tube cracked open along one of its edges (Figure 3.4). It was later concluded that this was due to the square shape of the cross-section and the stress concentration at the corners. Nonetheless, the rest of the confined specimens failed in a similar fashion, with the thickness of the jacket having little or no effect on the added strength to the concrete core. Figures 3.5 and 3.6 show the failure modes of the FRP-encased specimens with 10 and 14 plies, respectively. Note how most of the specimens appear intact, with the white patches barely visible. This clearly shows that the FRP tubes are not fully utilized as hoop tension bands. The average strength for the unconfined square specimens was 202 kips, while the average strength for the FRP-encased specimens was 233 kips. This resulted in a strength increase of only 15%, which was rather independent of the jacket thickness. For the 6-layer specimens, the average strength was 228 kips. Both the 10 and 14-layer specimens had average strengths of about 236 kips. Recalling that the average strength of all FRP-encased specimens was 233 kips, it can be seen that perhaps any thickness larger than 10 layers might be unnecessary, as the tube would be under-utilized. It should be noted, however, that for cylindrical FRP-encased specimens, strength increases of about 300% had been obtained (Mirmiran 1997). Another aspect to be noted was the duration of each test, since this was an indication of the straining capacity of the FRP-encased specimens. The average duration for the unconfined specimens was about 95 seconds,

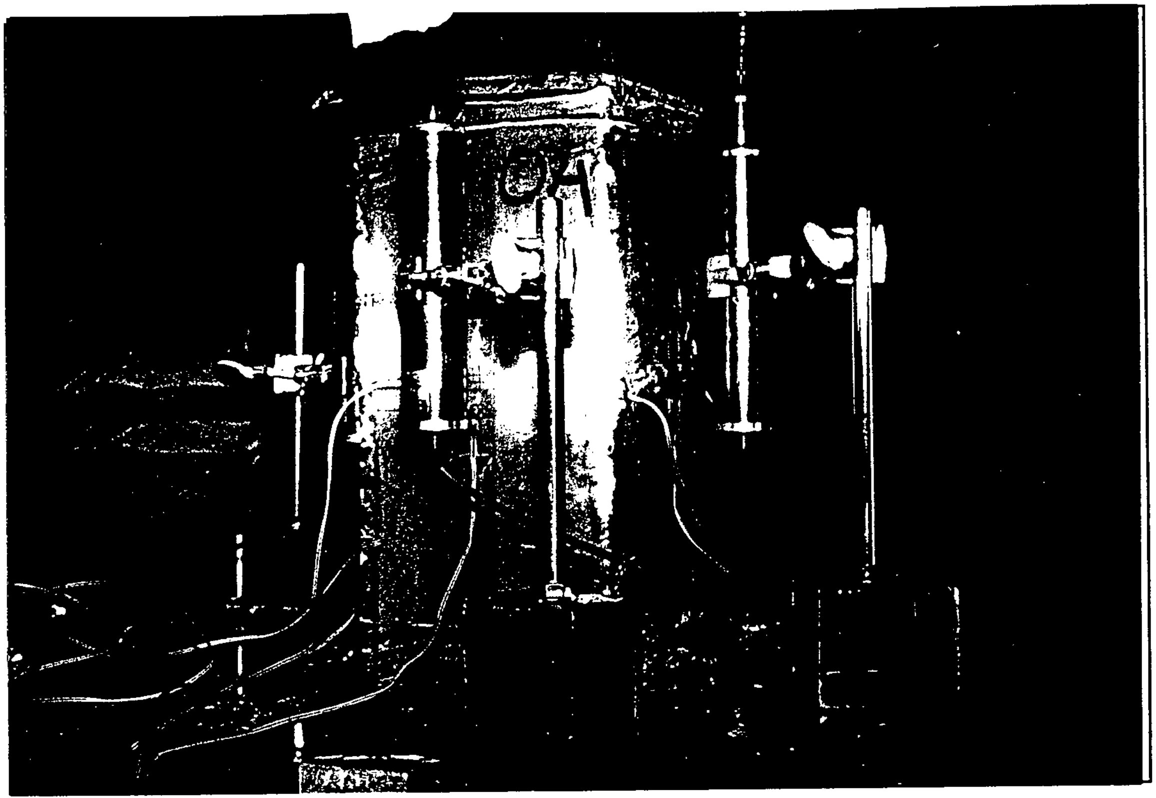

Figure 3.3 Instrumentation for a square tube

Figure 3.4 Specimen SQ6C after reloading

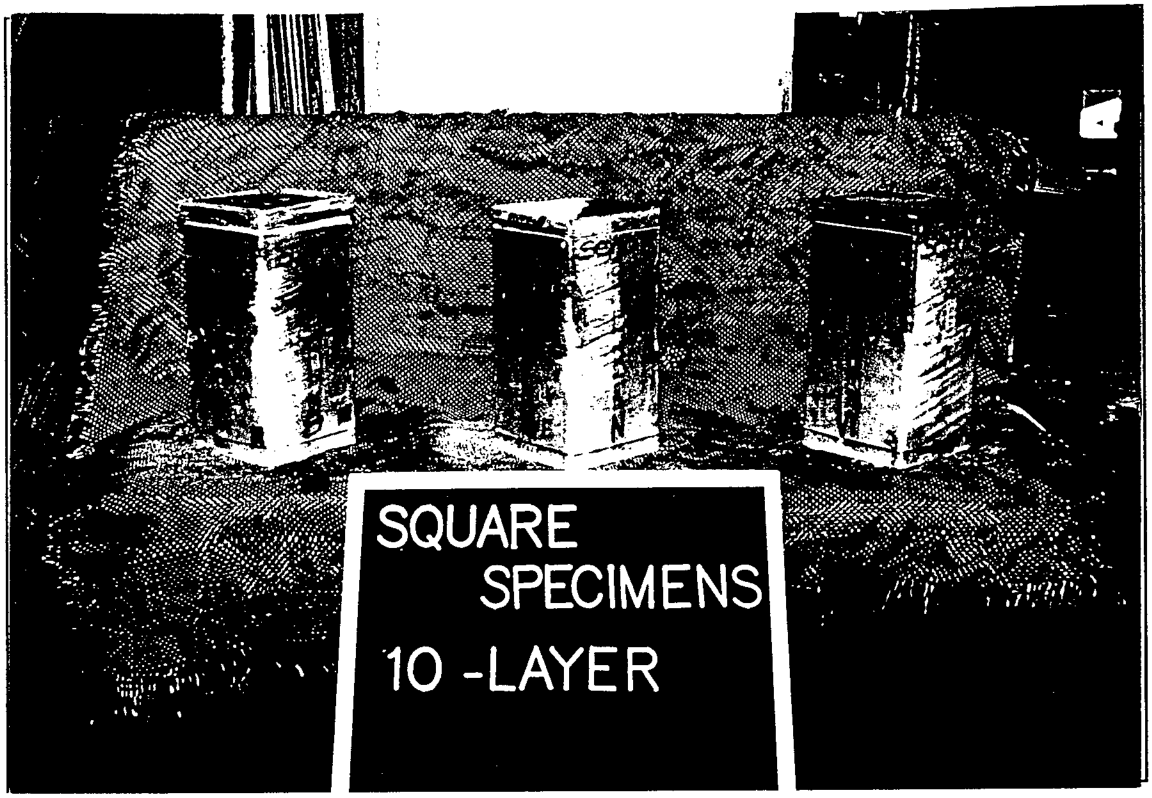

Figure 3.5 10-ply specimens after failure

Figure 3.6 14-ply specimens after failure

compared with 103 seconds for the FRP-encased specimens. Specimens SQ10C and SQ14A lasted longer than the average, failing at 153 and 136 seconds after the start of loading, respectively. If these two specimens were counted out, then the average duration for the fiber reinforced specimens would be about the same value as for the control specimens. Generally, failure of the jacketed specimens was quite passive and ductile, lacking any violent or explosive failure such as concrete pieces being shot at high speeds. Finally, three issues regarding the accuracy of test results, and the task of data reduction should be mentioned:

1. It was noticed that due to the uneven surface of FRP tubes, a few of the strain gauges were partially detached from the tube during the test. This may have also been due to inadequacy of the glue used for affixing the gauges. Since four gauges were used in each direction, and since four LVDTs were also present, the gauges with non-consistent readings were discarded. All in all, since the strain gauges were considerably long (60mm gauge length), the partial detachment did not seem to affect but the few gauges that were noticed during the tests.

2. It was noticed that due to uneven surface of the tube and the capping plate, some eccentricity was present in a few of the tests. This non-verticality resulted in slight tilting of the loading platens. However, due to the short height of the specimens, this did not appear to have affected any of the test results.

3. An initial strain hardening was noticed in almost all specimens which was attributed to the soft capping materials. This was corrected in all stress-strain curves as outlined in the Final Report of Phase I (Mirmiran 1997).

Test Results

Tables 3.2 and 3.3 show a summary of the test results. The tables show the peak strength and strain of unconfined concrete (f'_{co} and ϵ_{co}), as well as the peak strength, ultimate strength and strain of confined concrete (f'_{cc}, f'_{cu}, and ϵ_{cu}). The value of the lateral pressure f_r from the tube is determined as

$$f_r = \frac{2\, f_j\, t_j}{D} \tag{3.4}$$

where f_j= hoop strength of the jacket, t_j= jacket thickness, and D = inside dimension of the tube.

Figure 3.7 and 3.8 show the stress-strain response of control cylindrical and square specimens, respectively. Both graphs are drawn based on the LVDT readings, as none of the control specimens were instrumented with strain gauges. It is clear that neither the peak strength nor the corresponding strain are significantly affected by the cross-sectional shape of unconfined concrete. However, the elastic modulus of cylindrical specimens is on the average about 15% higher than that of square specimens. Also, regardless of the cross-sectional shape, the descending post-peak branch shows a fast drop of strength, since not much ductility could be expected from unconfined concrete.

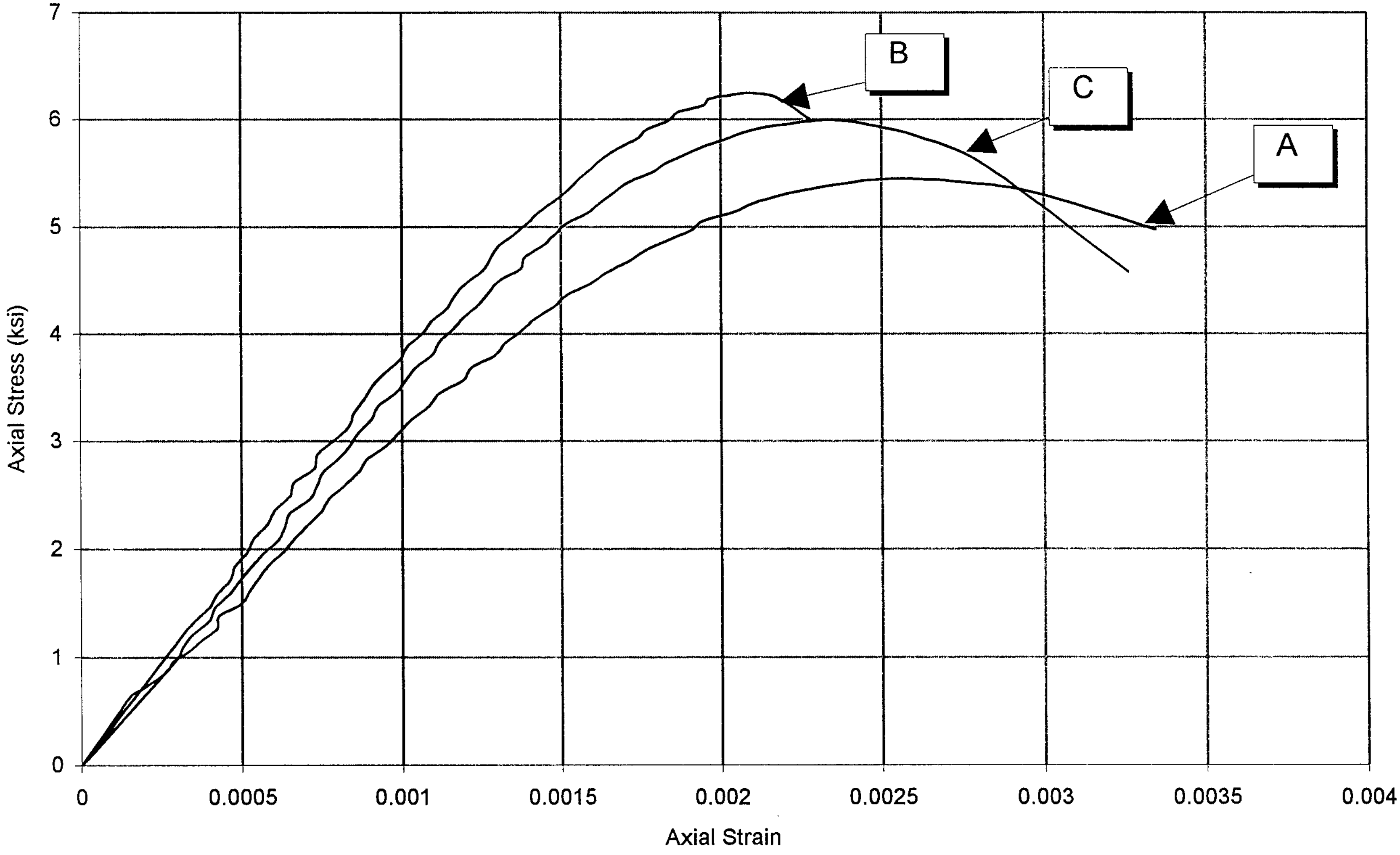

Figure 3.7 Stress-strain curves for plain concrete cylindrical (control) specimens

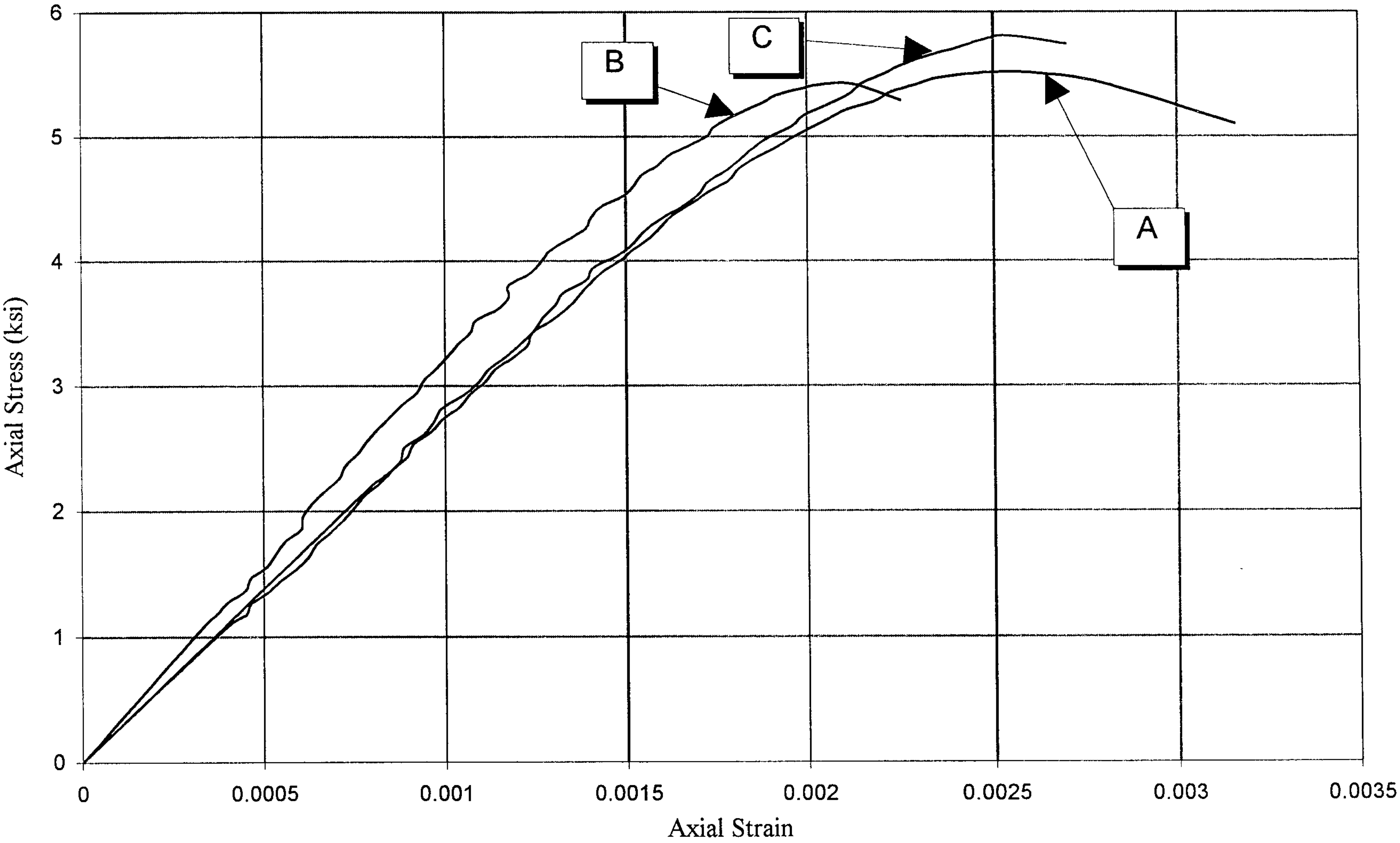

Figure 3.8 Stress-strain curves for plain concrete square (control) specimens

Table 3.2 Summary of results for unconfined specimens

Cross Section	Specimen No.	Peak Strength, f'_{co} (ksi)	Peak Strain, ϵ_{co}
Square	SQ0A	5.51	0.0025
	SQ0B	5.41	0.0021
	SQ0C	5.80	0.0025
Circular	CYL0A	5.44	0.0026
	CYL0B	6.24	0.0021
	CYL0C	5.99	0.0023

Table 3.3 Summary of results for confined specimens

Specimen No.	Peak Strength, f'_{cc} (ksi)	Ultimate Strength, f'_{cu} (ksi)	Ultimate Strain, ϵ_{cu}*
SQ6A	6.93	3.3	0.0080
SQ6B	5.83	3.7	0.0100
SQ6C	6.21	3.8	0.0076
SQ10A	6.56	3.9	0.0150
SQ10B	6.74	5.0	0.0165
SQ10C	6.28	5.0	0.0165
SQ14A	6.08	4.5	0.0106
SQ14B	6.55	5.5	0.0085
SQ14C	6.95	4.8	0.0105

* Since some of the tests were stopped soon after the load stabilized and not at subsequent load drops, the ultimate strain is to be treated as a lower bound value.

Biaxial stress-strains curves for the 6, 10, and 14-ply concrete-filled FRP tubes are shown in Figures 3.9-3.11, respectively. Figure 3.12 shows curves with the average for each specimen type, including the unconfined square specimens. As can be seen from this figure, the slope of the unconfined concrete is the same as the slope for the confined concrete. This shows that as the load is applied, concrete is taking most of the axial load in the elastic region. Upon careful observation, the stress-strain curves for all specimens depart from their linear shapes and begin to curve at about the point where the unconfined concrete nears its peak strength. This means that the specimens have entered into a transition zone. At this point, the concrete core has significantly cracked, and the FRP tube becomes effective as a hoop tension band, and the only restraint against catastrophic failure. Although increase in strength is not considerable, it is quite obvious that confinement by FRP tube provides significant ductility for concrete, as the descending branch of the curves for the FRP-encased specimens show plastic deformations not seen for any of the unconfined specimens. As mentioned in test observations, tube thicknesses of above 10 plies appear to be unnecessary for strength enhancements. From Figure 3.12, it can be seen that this is true for the peak strength of confined concrete, as the curves for the 10 and 14-ply specimens peak at about the same value.

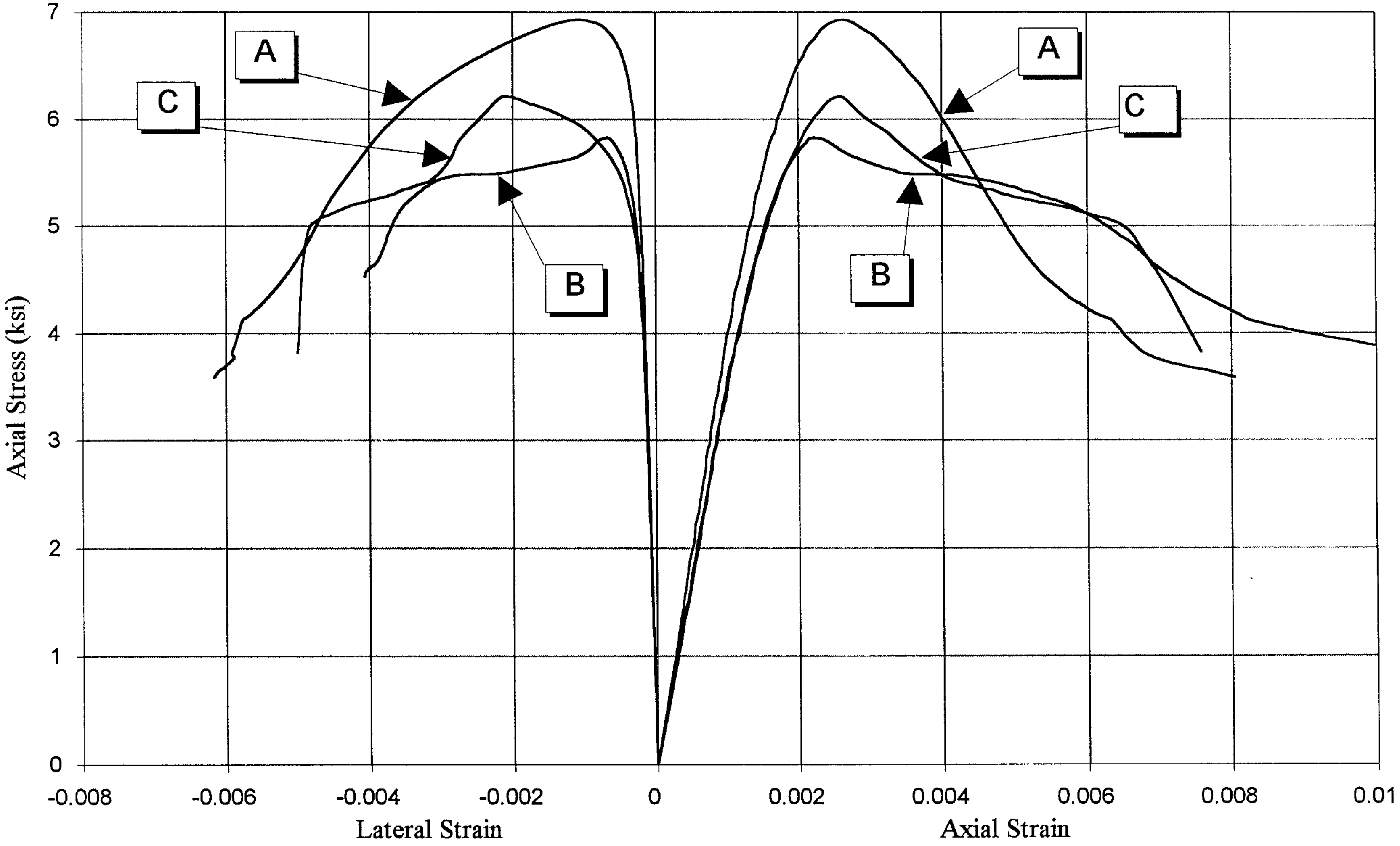

Figure 3.9 Biaxial stress-strain for 6-ply concrete-filled square FRP tubes

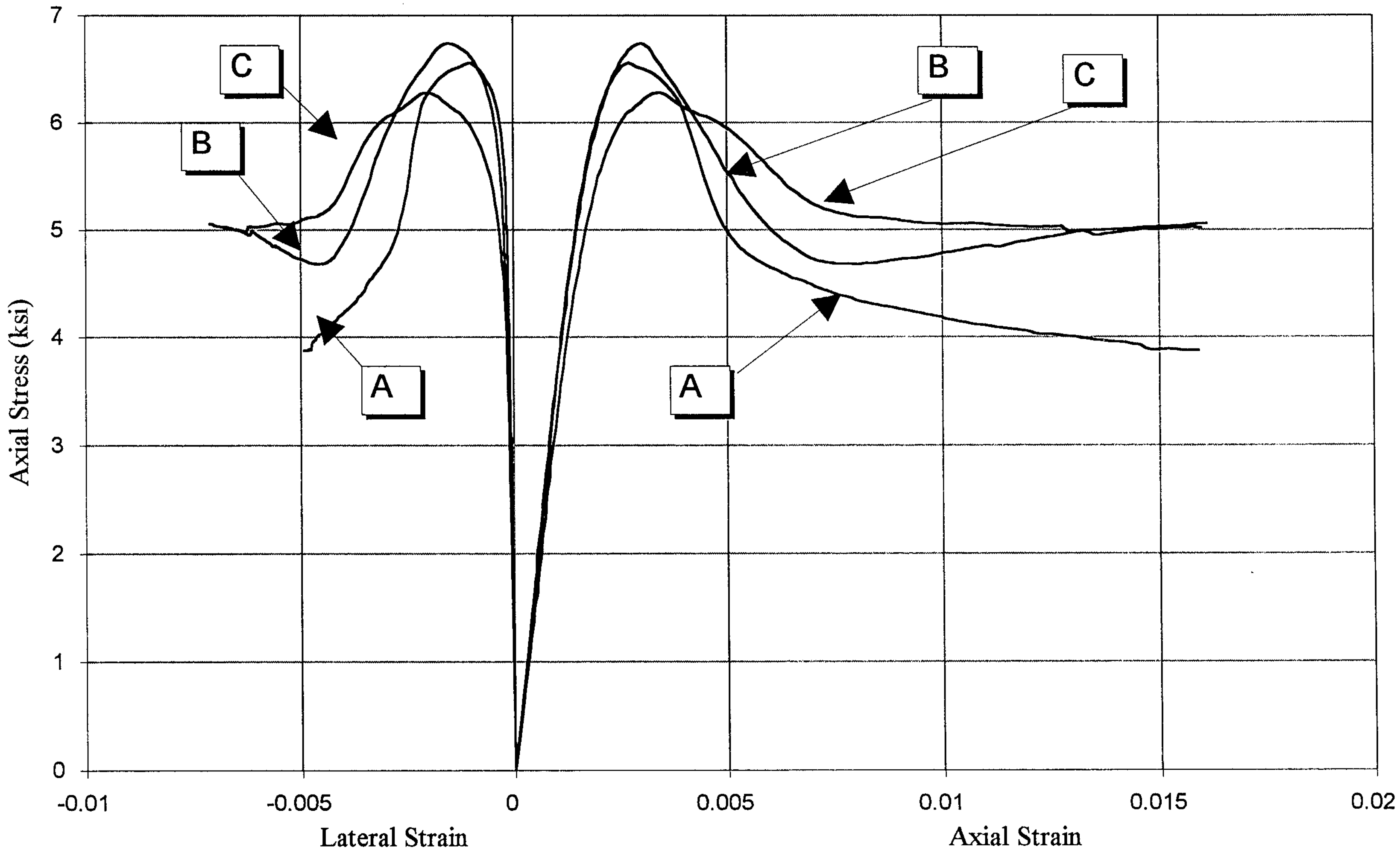

Figure 3.10 Biaxial stress-strain for 10-ply concrete-filled square FRP tubes

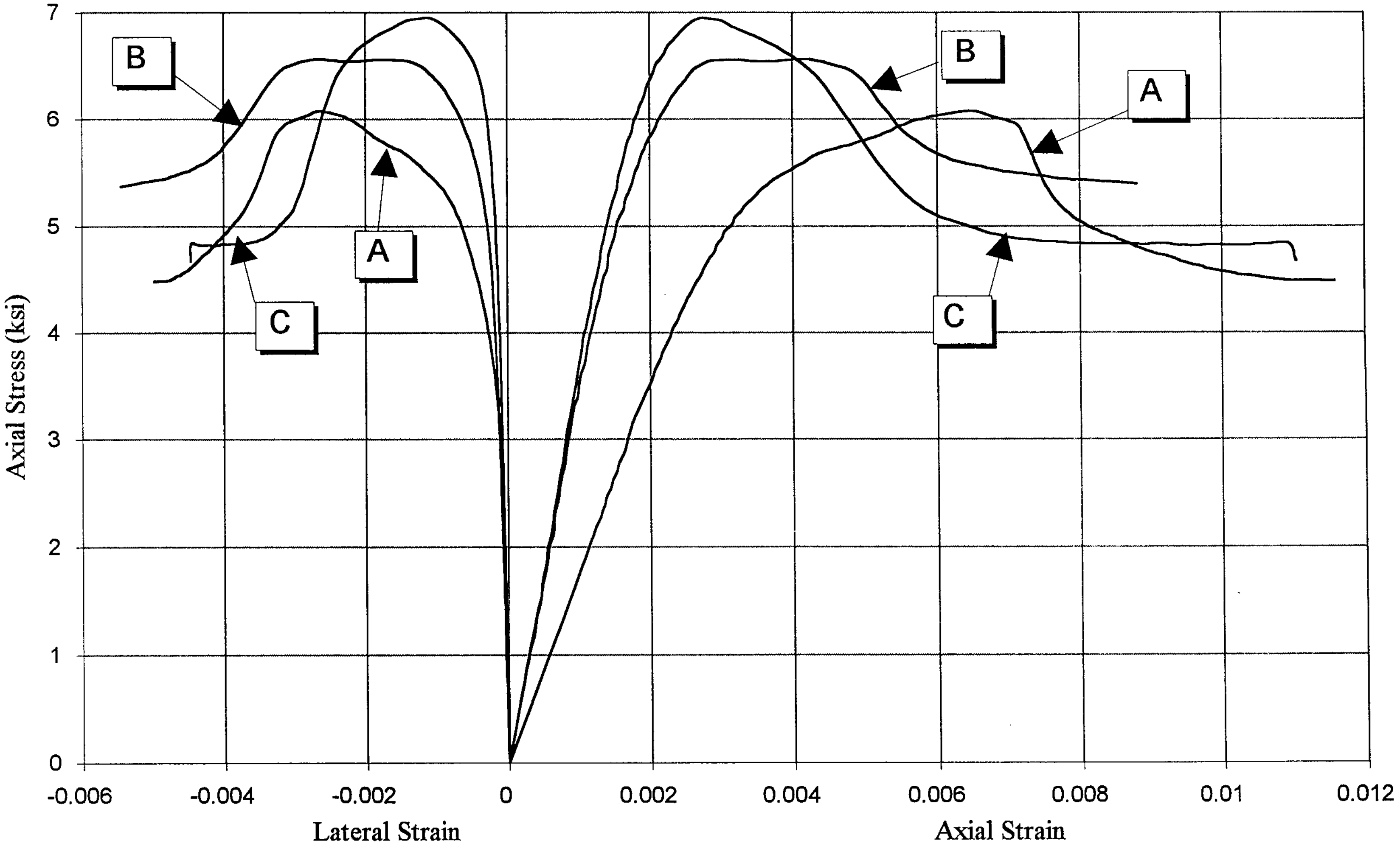

Figure 3.11 Biaxial stress-strain for 14-ply concrete-filled square FRP tubes

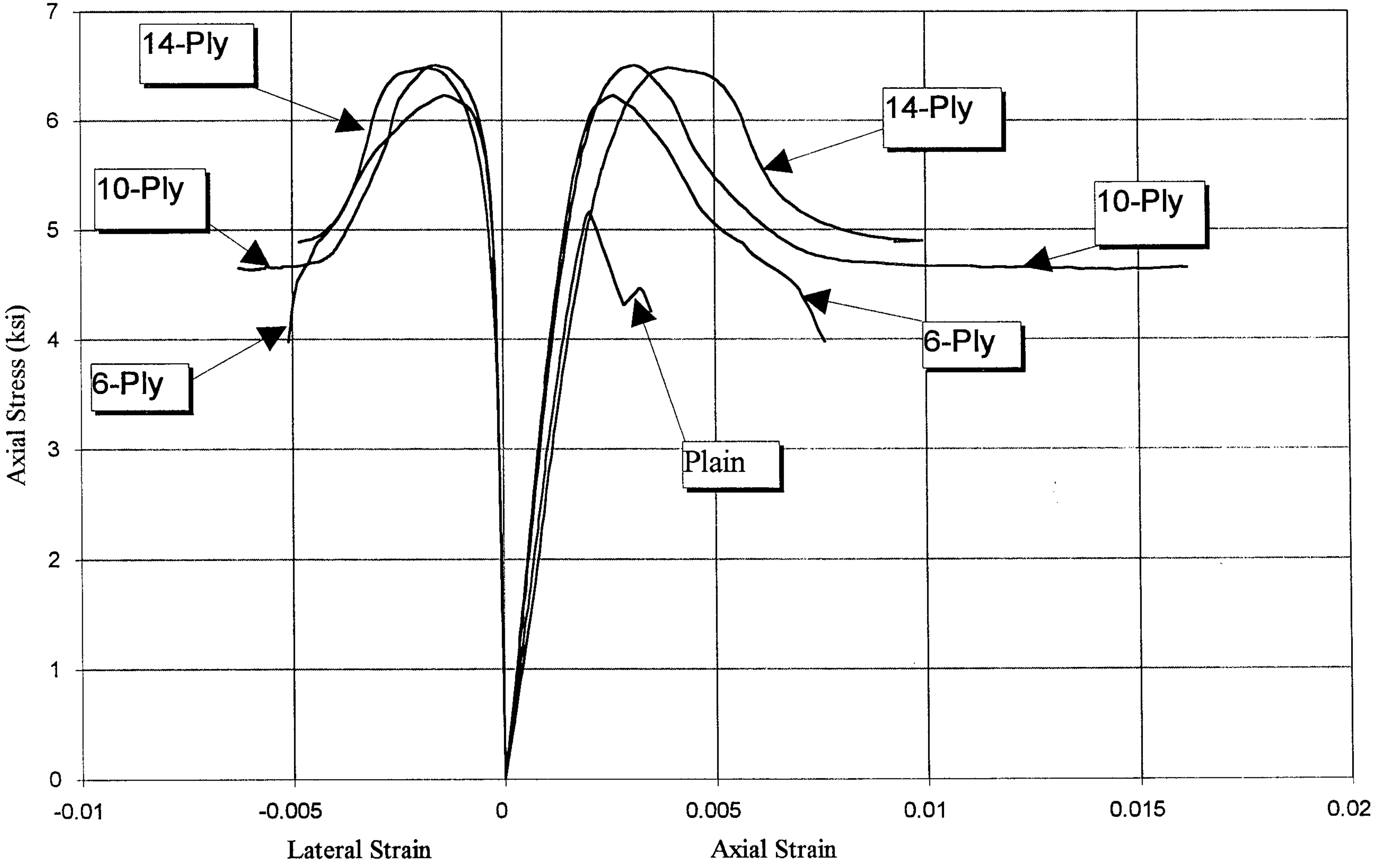

Figure 3.12 Average biaxial stress-strain for concrete-filled square FRP tubes

However, the thickness of the tube seems to have a direct effect on the descending branch. The curve for the 6-ply specimens shows complete failure shortly after the peak. The specimens with 10-ply tubes show a rather long plastic zone and a higher plastic strength. The plastic strength is further increased for the 14-ply tubes, indicating the effectiveness of the tube thickness when the concrete core is practically crushed.

Plots of lateral strains versus axial strains are shown in Figure 3.13. Each curve represents an average of the three similar specimens. It should be noted that the slope of these curves is a representative of the Poisson's expansion (or dilation) of the concrete core. The curves for all three thicknesses begin with a Poisson's ratio of about 0.15 to 0.22, which is the characteristic of plain concrete. At about an axial strain of 0.002, i.e., peak strain of plain concrete, the curves begin to shift to a higher slope, indicating that concrete has considerably cracked and become unstable. Between axial strain values of 0.002 and 0.006, lateral strains increase at a non-linear rate, while at about halfway in this range they transition through an inflection point indicating a maximum slope, and a tendency to control further dilation of concrete. This is the point when the tube becomes actively involved as a hoop tension band. After strain value of 0.008, the relationship becomes linear again, with the thinner jackets displaying a higher slope. Another observation that can be made is that thicker jackets have lower lateral strains in relation to their axial strains. This indicates that specimens with thicker jackets will take longer to reach their lateral failure strains.

There is another variable known as dilation rate that can be determined from the previous curves. Dilation rate is the rate of change of lateral strains with respect to axial strains. In mathematical terms, it is the slope or the first derivative of the lateral-axial strain plots. The experimental dilation rate, μ_{exp} is calculated for every two consecutive readings as follows:

$$\mu_{exp} = \frac{\Delta \epsilon_r}{\Delta \epsilon_1} = \frac{\epsilon_{r\,new} - \epsilon_{r\,old}}{\epsilon_{1\,new} - \epsilon_{1\,old}} \tag{3.5}$$

where ϵ_r and ϵ_1 represent the lateral and axial strains, respectively.

Figure 3.14 shows the average plots of dilation rates versus axial strains. Each curve represents an average of the three similar specimens. The dilation curves show three distinct regions. The first region indicates a gradual increase in the dilation rate from a starting point of about 0.15 to 0.20, which is the Poisson's ratio for plain concrete. As concrete begins to crack, the curve becomes steeper, resulting in a rapid increase in the dilation rate. The dilation rate keeps increasing until it reaches a peak. Thicker jackets have lower peaks, since they provide more confining pressure. It appears that the peak dilation rate occurs at an axial strain of about 0.004, which is the ultimate strain of unconfined concrete. After the peak, dilation rate decreases rapidly, indicating that the jacket is effectively containing the crack openings. Eventually, dilation rate stabilizes around a constant value. At this point, the concrete has reached its maximum lateral straining rate and the jacket is effectively containing the internal cracks of the concrete core.

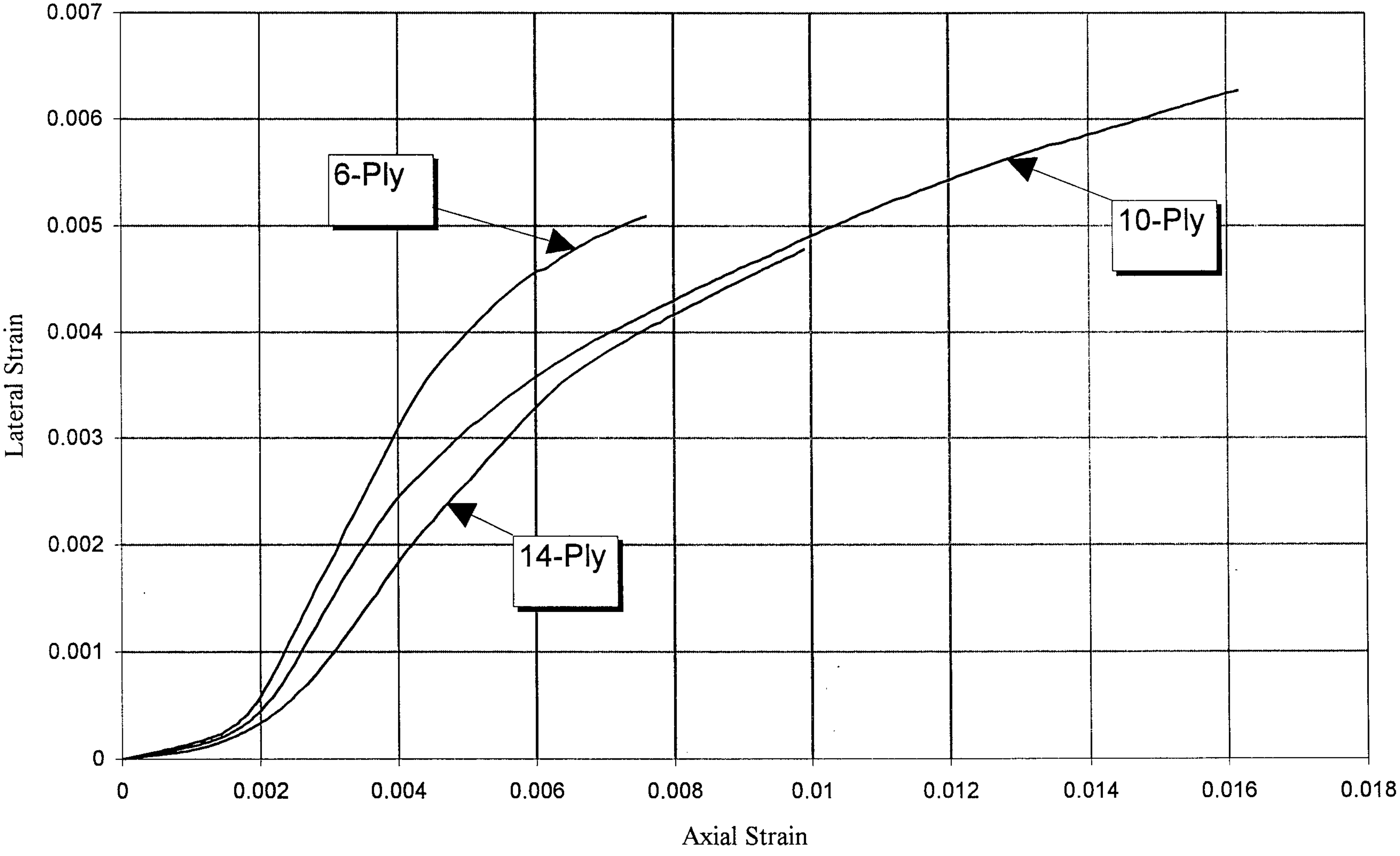

Figure 3.13 Average lateral strain versus axial strain for concrete-filled square FRP tubes

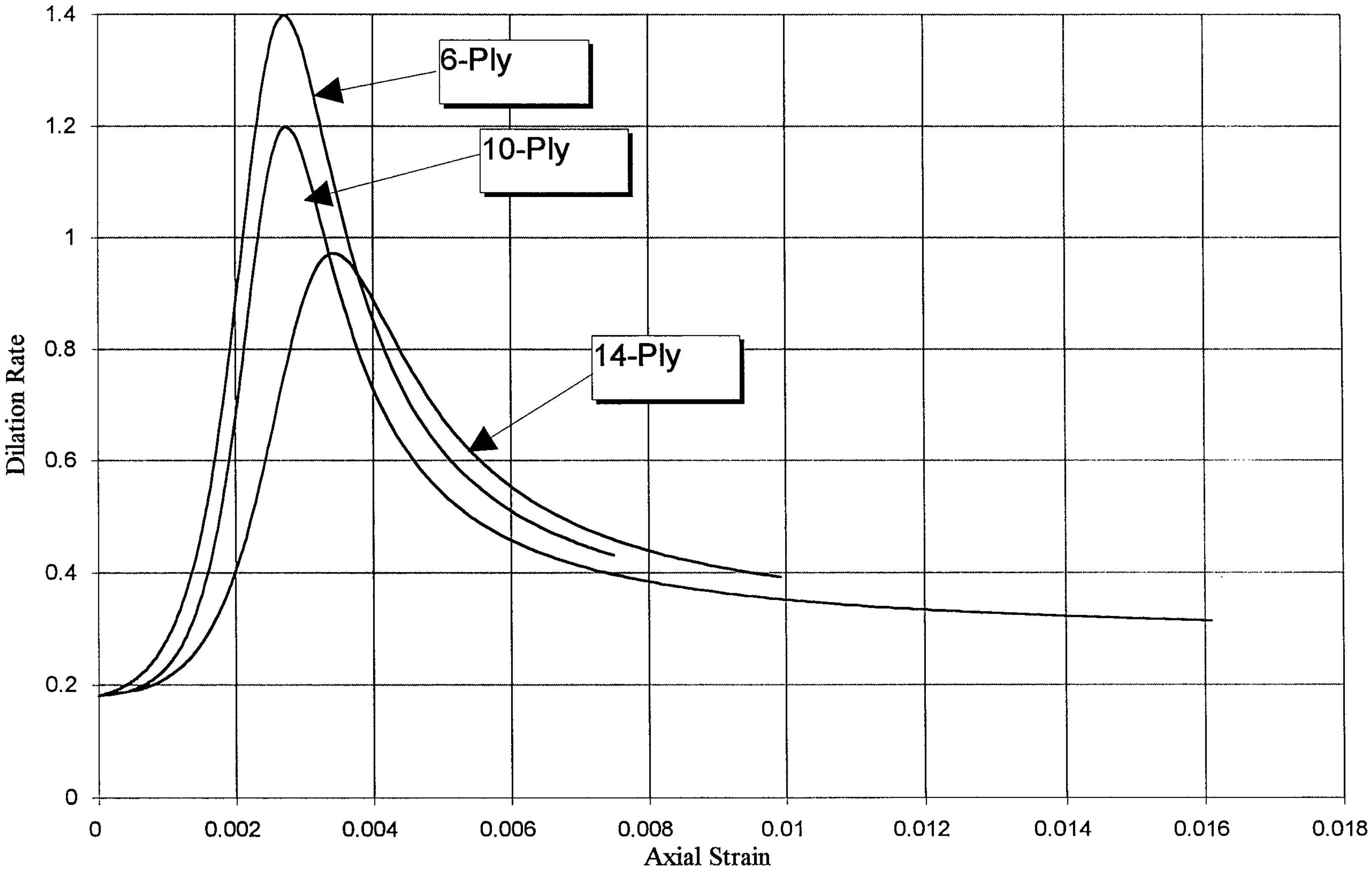

Figure 3.14 Average dilation rates for concrete-filled square FRP tubes

The plastification of FRP-encased concrete in the descending branch can also be looked at in terms of its volumetric strain. Figure 3.15 show the average plots of axial stress versus volumetric strain for each tube thickness. The horizontal axis in all these figures represents the change in volume per unit volume of concrete. This is calculated by adding the axial and lateral strains as

$$\frac{\Delta V}{V} = \epsilon_v = \epsilon_1 + 2\ \epsilon_r \tag{3.6}$$

where ϵ_v = volumetric strain, ϵ_1 = axial strain, and ϵ_r = lateral strain. Sign convention is negative for lateral strains which are tensile strains. Also, positive volumetric strains represent volume reduction while negative values indicate volume expansion (dilation). Referring back to Figure 3.15, all specimens begin to gradually decrease in volume until they reach a point of maximum compaction. At this point, the specimens enter a zone of expansion until failure happens. As can be seen in the figure, specimens with thicker jackets have a lower slope in the volume reduction zone, indicating better confinement than specimens with thinner jackets. One important point that should be discussed is how these plots compare with the ones obtained from cylindrical specimens of Phase I (Mirmiran 1997). Although both circular and square sections appear to effectively contain the dilation of concrete core, and leading the specimen to the compaction (or volume reduction) zone, the reversal occurs at higher stresses for circular sections as compared to square sections. That is why plastification of the section takes place within the post-peak response of the square sections.

From the standpoint of plasticity in concrete, plots of octahedral shear stresses versus octahedral normal stresses indicate the true loading surface of the specimen, and its deviation from the pure uniaxial compression. Figure 3.16 shows the average octahedral loading surfaces for each tube thickness. These plots were derived using the following relations

$$\begin{aligned} \tau_{oct} &= \frac{\sqrt{2}}{3}\left(f_c - f_r\right) \\ \sigma_{oct} &= \frac{1}{3}\left(f_c + 2\ f_r\right) \end{aligned} \tag{3.7}$$

where τ_{oct} = octahedral shear stress, σ_{oct} = octahedral normal stress, f_c = axial stress, and f_r = lateral stress. The lateral stress is determined from the following equation:

$$f_r = \frac{2\ E_j\ t_j}{D}\ \epsilon_r \tag{3.8}$$

where E_j = modulus of elasticity of the tube in the hoop direction. The straight line with the slope of √2:1 represents the pure uniaxial compression test with no confining pressure. As confining pressure increases, deviation from this line becomes more significant. Referring back to Figure 3.16,

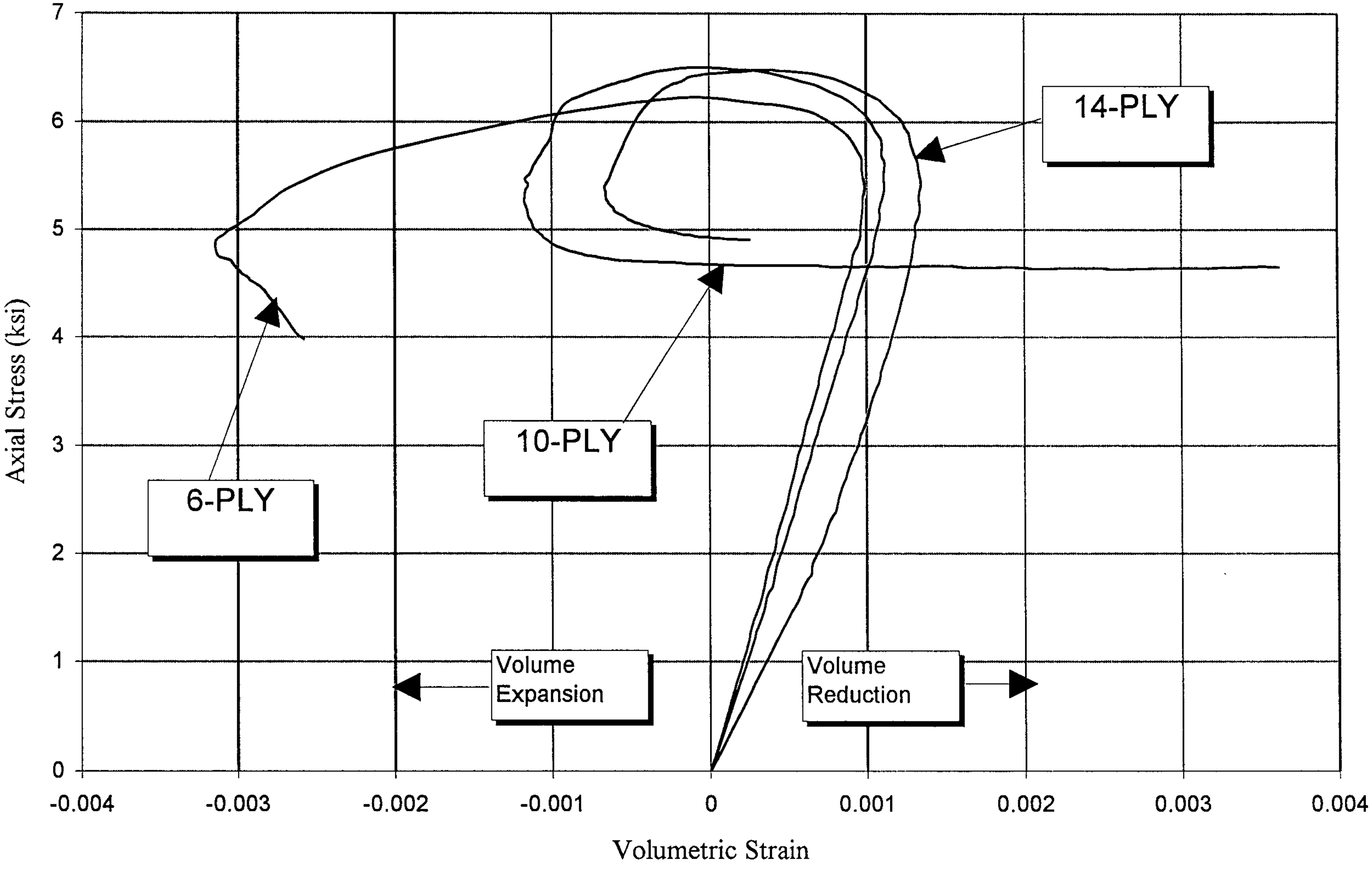

Figure 3.15 Average axial stress versus volumetric strain for concrete-filled square FRP tubes

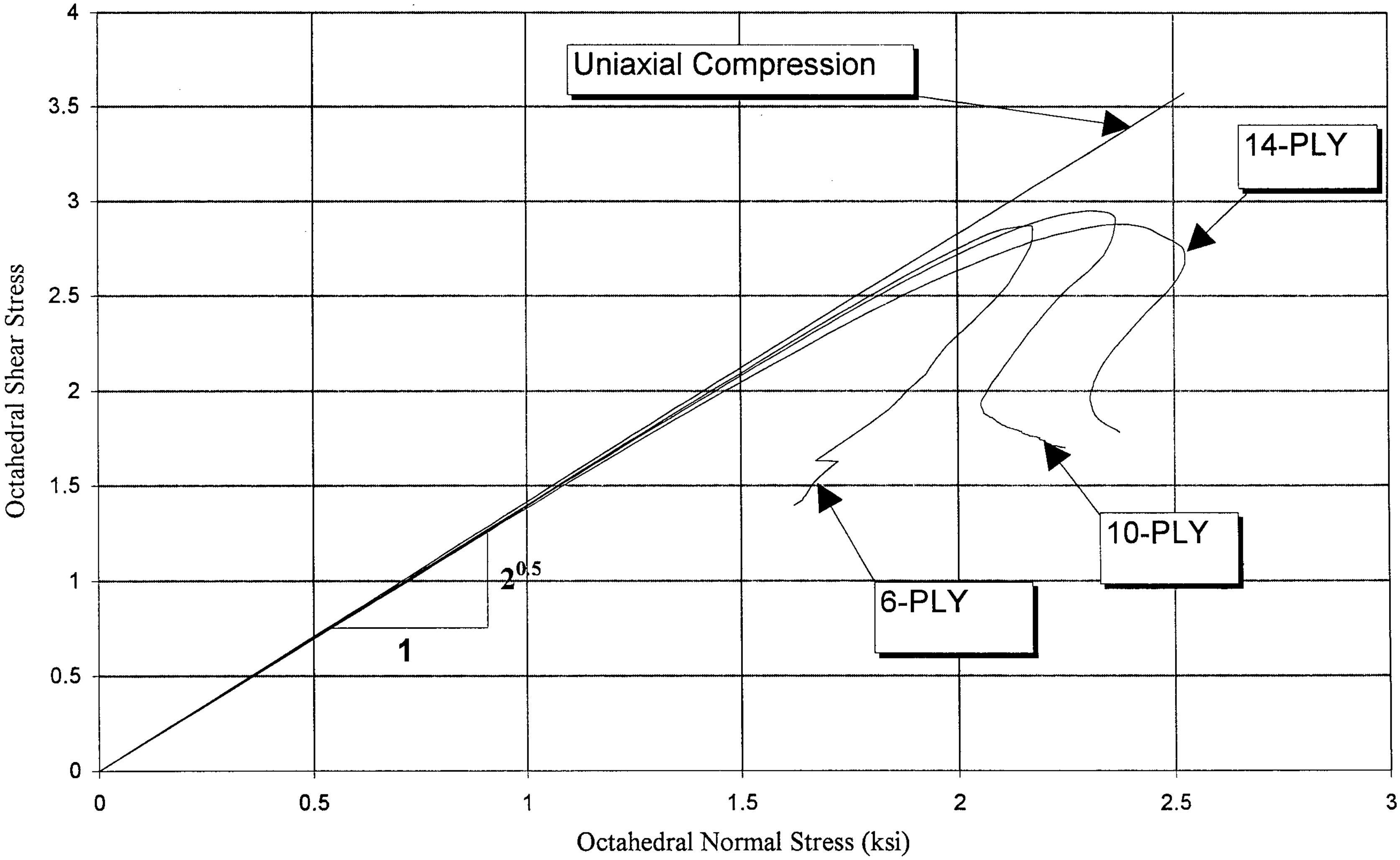

Figure 3.16 Average octahedral loading surfaces for concrete-filled square FRP tubes

it is clear that this deviation occurs earlier for the thicker tubes, indicating that thicker tubes become activated as hoop tension bands sooner than thinner tubes. The peak octahedral shear strength, however, does not appear to depend very much on the tube thickness. On the other hand, the octahedral shear and normal stresses, around which some level of plasticity occurs, seem to be a function of jacket thickness. These are indicative of post-peak response of square sections. Results of Phase I (Mirmiran 1997) indicate that for circular sections the octahedral loading surfaces have a totally different pattern, as no peak stress nor descending branch is present in their response.

3.3 Analysis and Discussion

In this section, an attempt is made to model the true response of FRP-confined concrete sections. First, experimental results of the square sections are compared with those of circular sections tested under Phase I (Mirmiran 1997). To shed more light on the reasons for the observed behavioral differences, results of extensive tests at the University of Sherbrooke on fiber-wrapped square and circular concrete specimens are analyzed next (Rochette 1997). Finally, an equation is proposed for confinement with square tubes.

Comparison of the Responses of Circular and Square Sections

Under Phase I, 24 6"x12" concrete-filled FRP cylinders were tested as Series D, in 3 batches of concrete and with 3 different jacket thicknesses, equivalent of 6, 10, and 14 plies (layers). These tests were part of the total 52 concrete cylinders under uniaxial compression. Results were modeled in the Final Report (Mirmiran 1997). Figure 3.17 shows the average axial stress-strain curves for circular tubes of Series D, Batch C of Phase I together with the average curves for the square tubes of Phase II. Notice that the number of plies in both studies were kept the same. As the figure clearly shows, there are two major differences between the responses of circular and square sections:

> (1) Confinement effectiveness of circular sections is much higher, resulting in a strain hardening behavior after the peak strength of unconfined concrete, while square sections show a descending post-peak response, with little or no increase in their peak strength over that of unconfined concrete.
>
> (2) Ductility of circular sections is considerably higher by a factor of 6 to 7. While square sections reach their crushing ultimate strain at about 0.005 to 0.007, circular sections extend the ultimate strain of concrete to 0.03-0.045.

The figure, however, can not truly reveal the effect of cross-sectional shape, because the compressive strengths of the concrete core for the two experiments are different. Therefore, to eliminate the effect of unconfined concrete strength and to isolate the effect of cross sectional shape, the curves of Figure 3.17 are normalized and shown in Figure 3.18 by dividing values of each curve by the peak stress and strain of their corresponding unconfined concrete core. The figure shows that while jacket thickness greatly affects the response of circular tubes, for square sections, this effect is minimal. It appears that the descending branch of the response is stabilized at about 70% of the peak strength of unconfined concrete, irrespective of the tube thickness. Of course, there seems to be a threshold thickness between 6 to 10 layers, below which little or no post-peak plasticity occurs.

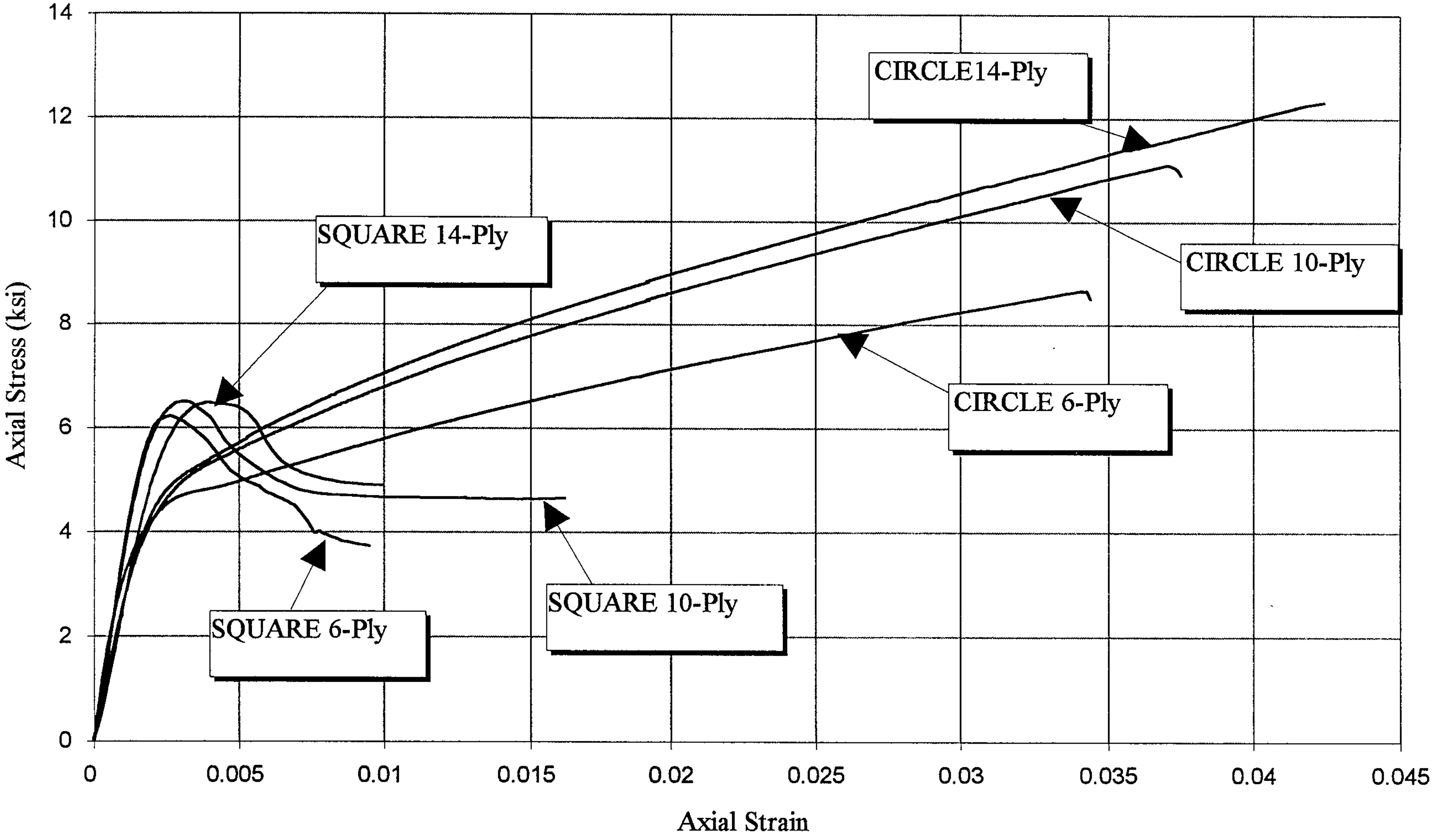

Figure 3.17 Average stress-strain curves for circular and square FRP tubes

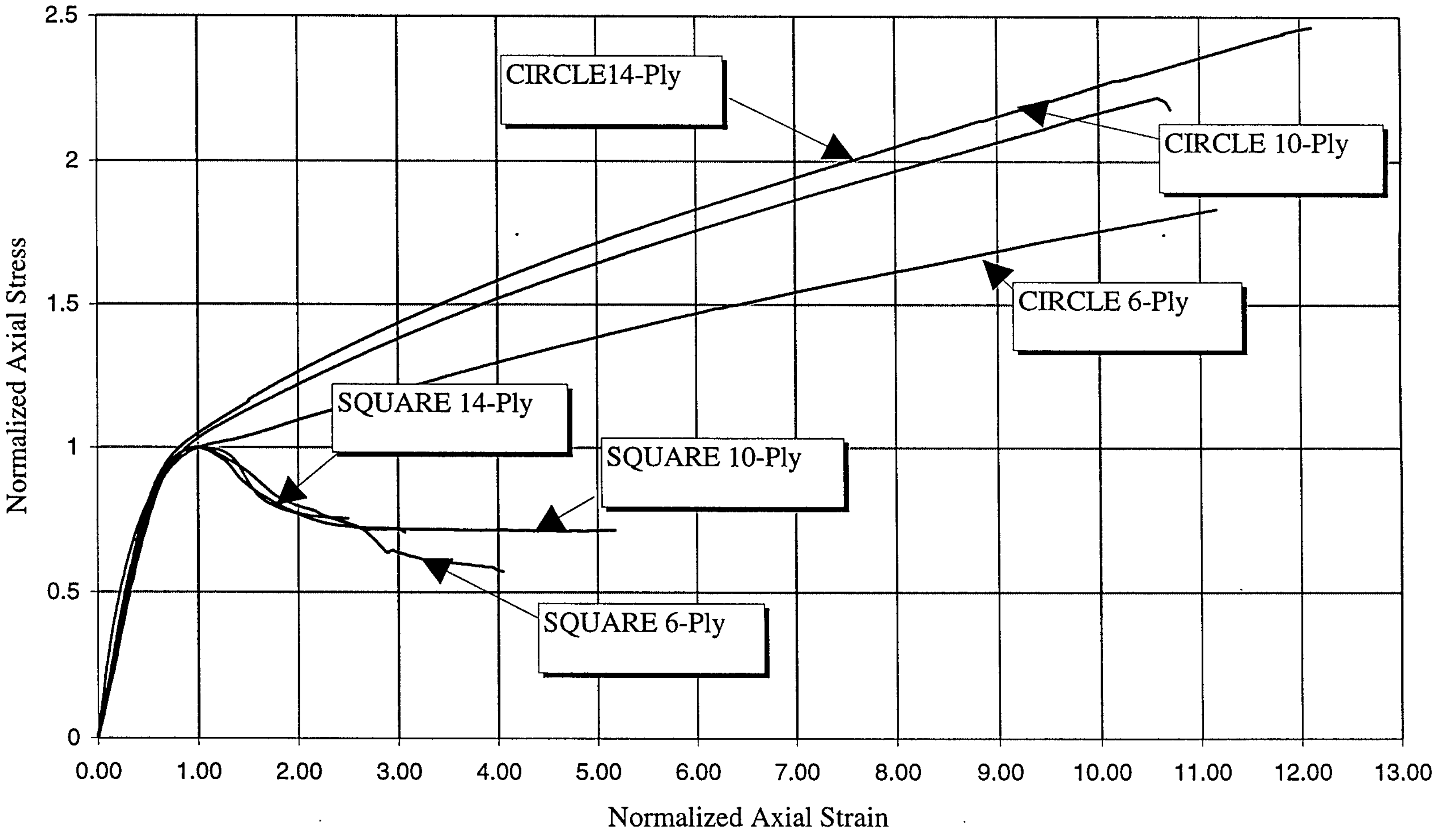

Figure 3.18 Normalized stress-strain curves for circular and square FRP tubes

Another important comparison between the square and circular sections is in their volumetric responses. Figure 3.19 shows the axial stress versus volumetric strain for the circular specimens of Series D, Batch C of Phase I, along with the square tubes of Phase II. The curves are again normalized in both directions to eliminate the effect of different concrete batches. As shown in the figure, circular sections tend to effectively curtail the dilation tendency of concrete while continually increasing the strength of the cross section. On the other hand, square sections achieve some level of crack dilatancy containment. However, in this process, strength of the cross sections does not increase, and is only stabilized after considerable post-peak strength degradation. The figure clearly shows that even though square sections are not as effective in confining the concrete core as circular sections, presence of FRP-materials contains the crack dilatancy of concrete much in the same fashion. When compared with steel-encased concrete, FRP materials reverse the direction of volumetric strains, and do not result in unstable dilation.

Finally, comparison of dilation rates for the circular and square sections can clarify some aspects of the behavioral differences between the two types of cross-sections. Figure 3.20 shows the average dilation rates for the 6, 10, and 14-ply circular tubes of Series D, Batch C of Phase I, and the square sections of Phase II. It is clear that the general shape of dilation curves is the same for both circular and square FRP sections, indicating that dilation response is a function of material properties of the tube rather than the cross-sectional shape. One needs to recall the dilation rate for an unconfined concrete which becomes unstable and approaches very large values at about the peak strength. Also, it should be noted that for steel-encased concrete, dilation rate, although initially contained, becomes unstable and approaches very large values as soon as the steel tube yields. There are however some differences in the dilation curves of the square and circular FRP tubes. First, it is clear that the peak dilation rate is higher for the square sections. This points to the fact that activation of the crack containment is delayed for square tubes. This may be explained by the distribution of lateral pressure in the circular and square sections.

Figure 3.21 shows the lateral pressure buildup in square and circular sections. This schematic diagram is modified after the work of Saatcioglu and Razvi (1992) on the confining effect of steel hoops. Passive confinement pressure exerted by a tube depends on the restraining force developed within the tube. For circular sections, maximum confining pressure can be developed because the tube can effectively act as a hoop tension band. Moreover, the hoop stresses and the confining pressures are, at least theoretically, uniform around the perimeter of the tube. On the other hand, for square sections, the tube can generate high restraining forces at the corners, where it is supported laterally by the transverse sides, and low restraining action between the corners. The restraining force at the corners depends on the force that can be developed in the transverse sides of the tube, which in turn relates to the thickness and hoop strength of the tube. However, the restraining action of the tube in between the corners is a function of the flexural rigidity rather than membrane action of the plate between the corners. The flexural rigidity of the FRP plate on each side of the tube depends on the thickness and materials of the tube as well as the unsupported length of the plate in the circumferential direction. Therefore, from Figure 3.21 it is clear that most of the confining pressure is built up around the corners of the tube, and as the corner radius is increased, the pressure distribution becomes more uniform. As such, it appears that the corner radius as well as the overall

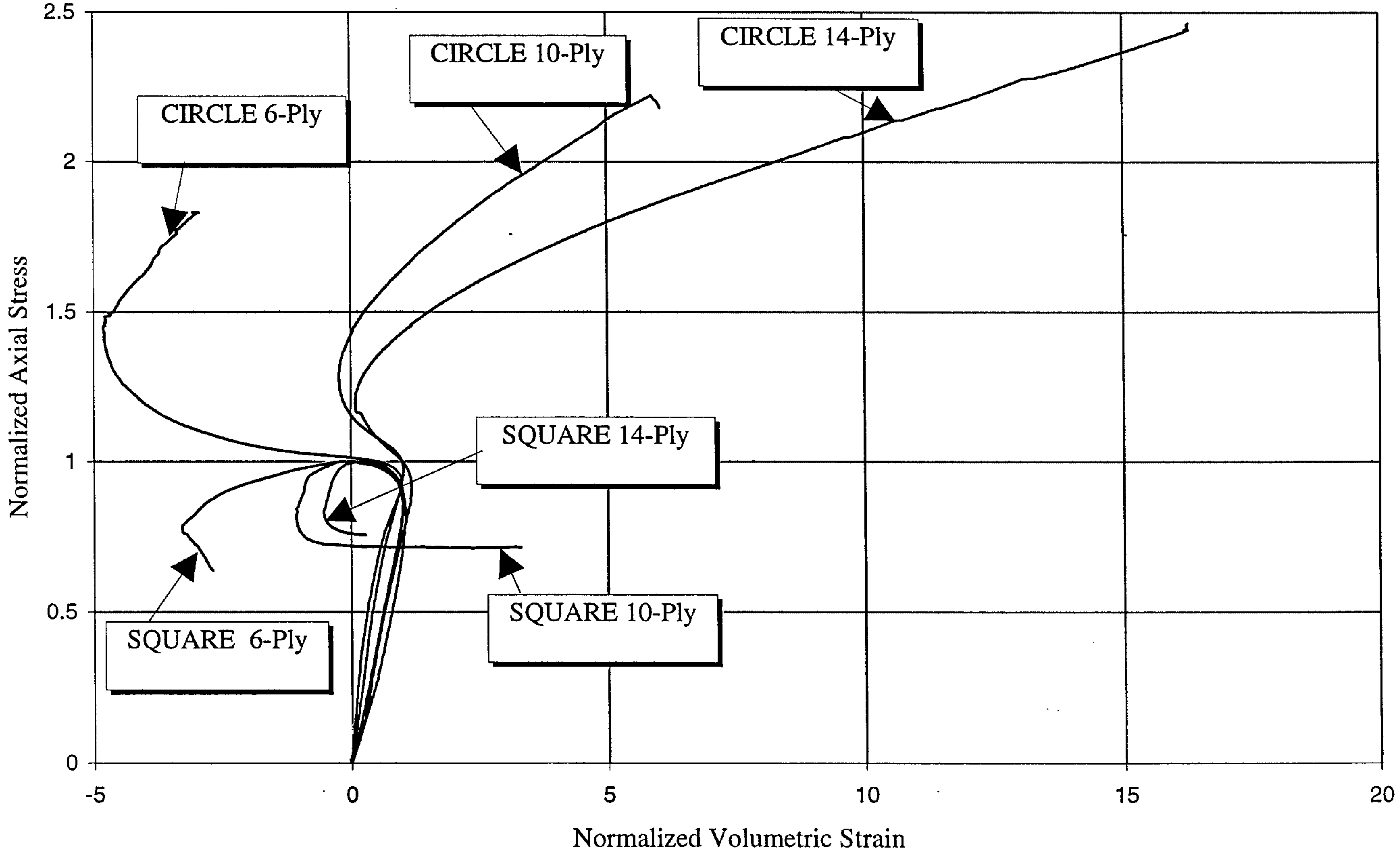

Figure 3.19 Normalized volumetric strain curves for circular and square FRP tubes

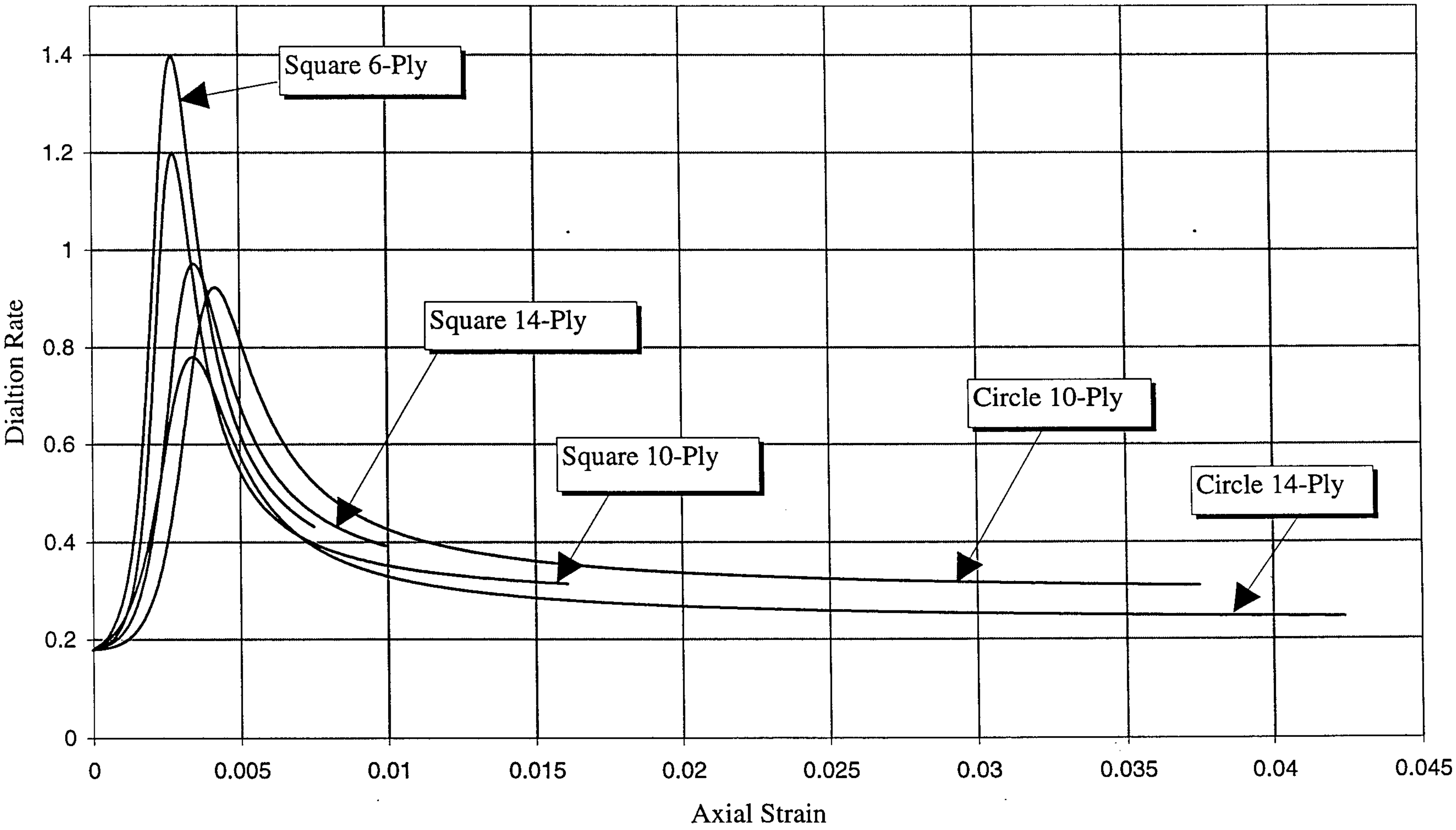

Figure 3.20 Dilation curves for circular and square FRP tubes

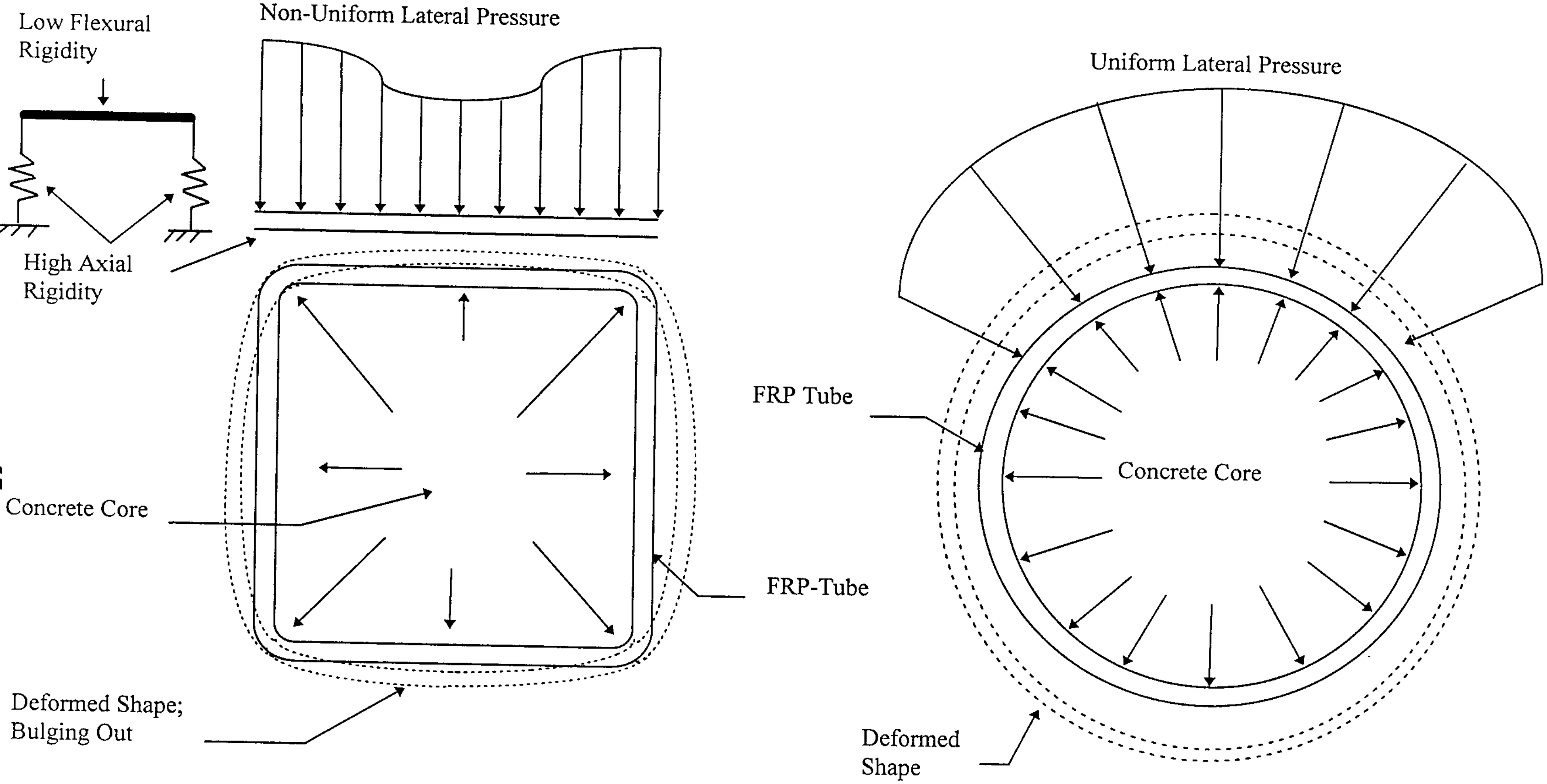

Figure 3.21 Lateral pressure buildup in square and circular sections

dimensions of the section have great impact on the confinement effectiveness of the square section. While the effect of the former can be modeled (as will be discussed at the end of this section), the latter parameter (size of the section) seems to impose an important restriction on the applicability of any such confinement model. In other words, while for circular sections, scale factor is not likely to cause a great impact on the modeling process, the unsupported length of large square sections most likely makes full-scale tests more necessary.

Finally, recalling Figure 3.20, and in light of the above discussion, without any attempt to quantify the dilation rates of the square sections, one notes the following:

1. The peak dilation rate of square sections is up to 20% larger than that of circular sections.
2. The ultimate dilation rate of square sections seems to be independent of the jacket thickness, but about the same as that of circular sections.

Comparison with Fiber-Wrapped Specimens

To shed more light on the reasons for the observed behavioral differences between the circular and square tubes, in this section we shall examine some of the results of the extensive experiments on fiber-wrapped specimens conducted at the University of Sherbrooke in three separate studies (Demers and Neale 1994, Picher 1995, and Rochette 1997). Of these, the one by Rochette (1997) addresses the confinement of short square and rectangular columns with composite materials. It should be noted that there are some differences between the response of fiber-wrapped specimens and concrete-filled FRP-tubes (see Chapter 5). Despite the differences, general behavior of FRP-encased concrete, whether bonded or not, is the same, and therefore, it is reasonably justified to expand the limited database of the present study by tapping into the more extensive set of tests conducted in Canada (Demers and Neale 1994, Picher 1995, and Rochette 1997).

Rochette (1997) tested a total of 33 fiber-wrapped specimens and 5 control (unconfined) specimens. All specimens were tested in uniaxial compression. The parameters studied included cross-sectional shape (circular, square, and rectangular), fiber type (carbon and aramid), corner radius, number of composite layers or wraps (2 to 5 layers for carbon, and 3 to 12 layers for aramid). The concrete strength, although from different batches, generally ranged between 4.2 to 6.4 ksi. Table 3.4 shows the properties of fiber composites as provided by the manufacturer. Table 3.5 shows the test matrix and the results of uniaxial compression tests.

Table 3.4 Material properties for fiber composites (Rochette 1997)

Material	Modulus	Tensile Strength	Tensile Strain	Thickness
	(ksi)	(ksi)	(%)	(in)
Carbon	11993.0	183.5	1.5	0.012
Aramid	1972.2	33.3	1.69	0.016

Table 3.5 Test matrix and results of uniaxial compression tests by Rochette (1997)

Specimen	Section	Specimen Size	t_j * (in)	R * (in)	f'_{co} * (ksi)	No. of Layers	Fiber
1A1	Circle	4"(dia.)x8"	0.02	1.97	6.09	2	Carbon
1A2	Circle	4"(dia.)x8"	0.02	1.97	6.09	2	Carbon
1A3	Circle	4"(dia.)x8"	0.02	1.97	6.09	2	Carbon
2B	Square	6"x6"x12"	0.04	0.20	6.09	3	Carbon
2C	Square	6"x6"x12"	0.06	0.20	6.37	5	Carbon
2D1	Square	6"x6"x12"	0.04	0.98	6.09	3	Carbon
2D2	Square	6"x6"x12"	0.04	0.98	6.09	3	Carbon
2E	Square	6"x6"x12"	0.05	0.98	6.37	4	Carbon
2G1	Square	6"x6"x12"	0.04	1.50	6.09	3	Carbon
2G2	Square	6"x6"x12"	0.04	1.50	6.09	3	Carbon
3B	Square	6"x6"x12"	0.05	0.98	5.19	4	Carbon
3C	Square	6"x6"x12"	0.06	0.98	5.19	5	Carbon
3D	Square	6"x6"x12"	0.05	1.50	5.19	4	Carbon
3E	Square	6"x6"x12"	0.06	1.50	5.19	5	Carbon
4B	Rectangle	6"x8"x20"	0.06	0.20	6.37	5	Carbon
4C	Rectangle	6"x8"x20"	0.04	0.98	6.09	3	Carbon
4D	Rectangle	6"x8"x20"	0.05	0.98	6.37	4	Carbon
4E	Rectangle	6"x8"x20"	0.04	1.50	6.09	3	Carbon
5A	Circle	6"(dia.)x12"	0.05	2.95	6.24	3	Aramid
5B	Circle	6"(dia.)x12"	0.10	2.95	6.24	6	Aramid
5C	Circle	6"(dia.)x12"	0.15	2.95	6.24	9	Aramid
5D	Circle	6"(dia.)x12"	0.20	2.95	6.24	12	Aramid
6A	Square	6"x6"x12"	0.05	0.20	6.24	3	Aramid
6B	Square	6"x6"x12"	0.10	0.20	6.24	6	Aramid
6C	Square	6"x6"x12"	0.15	0.20	6.24	9	Aramid
6D	Square	6"x6"x12"	0.20	0.20	6.24	12	Aramid
6E	Square	6"x6"x12"	0.05	0.98	6.24	3	Aramid
6F	Square	6"x6"x12"	0.10	0.98	6.24	6	Aramid
6G	Square	6"x6"x12"	0.15	0.98	6.24	9	Aramid
6H	Square	6"x6"x12"	0.20	0.98	6.24	12	Aramid
6I	Square	6"x6"x12"	0.10	1.50	6.24	6	Aramid
6J	Square	6"x6"x12"	0.15	1.50	6.24	9	Aramid

* t_j = jacket thickness, R = corner radius, f'_{co} = strength of unconfined concrete.

Rochette (1997) indicated that there are two variables that affect the response of fiber-wrapped specimens; corner radius and the thickness of the jacket. Our evaluation of test results indicate that these variables can best be described by $\left(\frac{2\ R}{D}\right)\frac{f_{ru}}{f'_{co}}$, where R is the corner radius, D is the inside dimension of the tube, f'_{co} is the compressive strength of unconfined concrete (concrete core) and f_{ru} is the ultimate confining pressure as given below

$$f_{ru} = \frac{2\ f_{ju}\ t_j}{D} \tag{3.9}$$

where f_{ju} is the ultimate hoop strength of the jacket, and t_j is the jacket thickness. Figure 3.22 shows a plot of $\frac{f'_{cu}}{f'_{cc}}$ versus $\left(\frac{2\ R}{D}\right)\frac{f_{ru}}{f'_{co}}$ for all specimens tested by Rochette (1997) as well as the square tubes tested under Phase II. In this figure, f'_{cu} indicates the ultimate strength of the section, while f'_{cc} is the maximum (peak) strength of the section. Notice that for circular sections, this ratio is always 1.0, while for square and rectangular sections, depending on the degree of confinement and the corner radius, this value may be considerably less than 1.0. Also, notice that the $\left(\frac{2\ R}{D}\right)$ ratio for circular sections is equal to 1.0, and therefore, only the confining pressure is of any consequence. Revisiting Figure 3.22, it becomes clear that the collective parameters of corner radius and confining pressure dictates whether or not a descending branch will be present in the response curve. It appears that for $\left(\frac{2\ R}{D}\right)\frac{f_{ru}}{f'_{co}}$ of less than 10%, the jacket is not very effective in strengthening the concrete core. Although, there will be considerable additional ductility due to crack dilatancy containment, no strength increase should be expected. Low confining effects may be due to thin jackets; i.e., low f_{ru}, or cross-sectional shape; i.e., square or rectangular sections with sharp edges. As the sharp corners are rounded, the jacket becomes more effective. A careful examination of the data in Figure 3.22 reveals that for low confinements and non-circular sections, despite the considerable dispersion, a logarithmic trend can produce a reasonable estimate of the post-peak response. Prior studies on concrete confined with steel indicates that the stress level in a confined concrete zone is not to be dropped below 30% of the confined concrete strength (Yong et al. 1988). Muguruma et al. (1992) proposed that this plateau be at 50% of the confined concrete strength. Bjerkly et al. (1990) have attributed this post-peak minimum stress level to the degree of confinement. Although a logarithmic

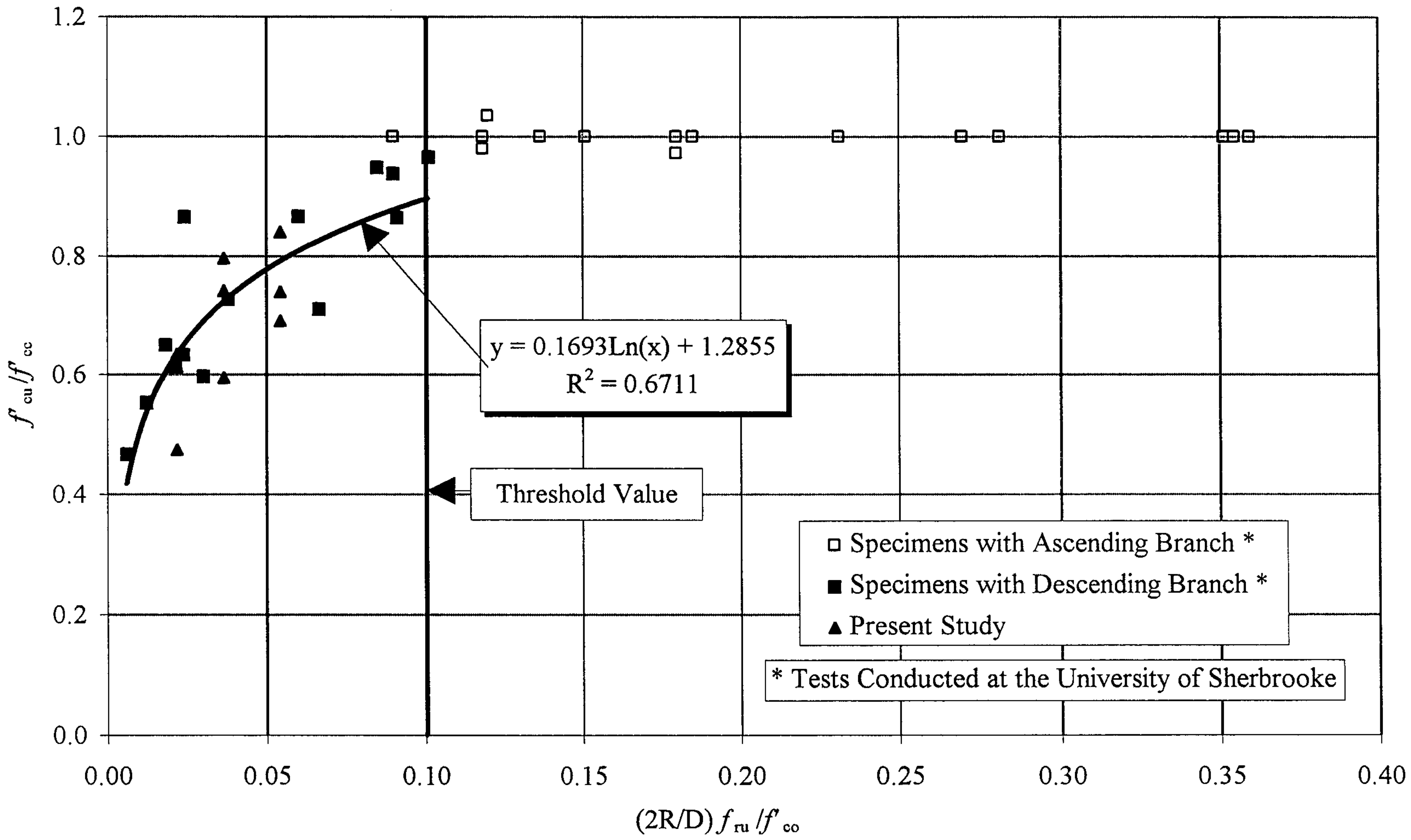

Figure 3.22 Ultimate strength ratio versus $(2R/D)f_{ru}/f'_{co}$

trend does not render a value for $\left(\frac{2\ R}{D}\right)\frac{f_{ru}}{f'_{co}} = 0$, it is not expected that exact sharp corners or zero confinement be of any concern in the confinement analysis. Therefore, the following relationship is proposed for the post-peak minimum stress level:

$$\frac{f'_{cu}}{f'_{cu}} = 0.1693\ Ln\left[\left(\frac{2\ R}{D}\right)\frac{f_{ru}}{f'_{co}}\right] + 1.2855 \qquad (\ R^2 = 67.11\%\ ) \qquad (3.10)$$

where R^2 represents the statistical correlation.

CHAPTER 4

EFFECT OF COLUMN LENGTH ON CONFINEMENT

4.1 Literature Review

Of the main characteristics of FRP-reinforced concrete are the low stiffness and high deformability as compared to conventional steel-reinforced concrete. Therefore, it is necessary to revisit the effect of lateral deflections and secondary moments on the load-carrying capacity of beam-columns reinforced with FRP. Concrete columns may be reinforced internally with FRP reinforcing bars, or externally by encasing concrete in an FRP tube which also serves as the pour form. Even though the confining characteristics of the two reinforcing methods are very different, the slenderness effects can be studied under the same principles.

In contrast with the vast database available on FRP-reinforced beams and slabs, literature on beam-columns is few and limited. The primary concerns for FRP-reinforced concrete columns include: ultimate strength, ductility, confinement, and slenderness. Paramanantham (1993) and Daniali and Paramanantham (1994) studied the behavior of FRP-reinforced concrete columns, and developed equations similar to those in the ACI building code. They tested fourteen 8"x8"x72" columns reinforced with E-glass/vinylester rebars under combined axial and flexural loading, and concluded that FRP rebars in compression would only be stressed up to 20%-30% of their strength. In pure flexure, they noted that the maximum tensile stress in FRP rebars was about 70% of their ultimate strength. Kawaguchi (1993) tested twelve 6"x8"x56" concrete columns reinforced with aramid rebars and subjected to eccentric tension or compression. He noted a rather small ductility for the columns, however, as for the analytical procedure, he did not find any marked difference with the conventional reinforced concrete. Kobayashi and Fujisaki (1995) tested a multitude of 8"x8"x26" concrete columns reinforced with aramid, carbon, or glass rebars under concentric loads, and concluded that ductile failure of concrete columns depends very much on the compressive strength of FRP reinforcement. They also noted that compressive strength of FRP rebars could be as low as 10% of their tensile strength. Amer, et al. (996) tested eight 6"x6"x96" concrete columns reinforced with four 0.3" diameter carbon rebars under various eccentric loads. They noted considerable differences of up to 37% between their theoretical and experimental values for axial loads. Use of concrete-filled FRP tube with no internal reinforcement as a structural column is unique and innovative (Mirmiran and Shahawy 1995). The experimental interaction diagram of five 7"x7"x52" concrete-filled FRP tubes made of E-glass/polyester corresponded to a reinforced concrete column of the same cross section with more than 5% steel rebars (Mirmiran 1997). However, test results indicated that secondary moments could be of great significance due to low stiffness of FRP materials. Therefore, length effects need to be considered.

4.2 Length Effect Tests

To evaluate the effects of length-to-diameter and diameter-to-thickness (L/D and D/t) ratios of the column on confinement of concrete, a series of tests was conducted. It has been stated (Harries 1997) that specimens with L/D ratio of 2:1 can not truly represent confinement of concrete. The reason being the friction zone that is created at each end plate which further prevents lateral expansion of concrete beyond the resistance of the confining jacket. Therefore, the question is the extent of this friction zone, and how it affects the confinement at the mid-height of the specimen. Assuming a 45° distribution angle, for a 12" cylinder a 6" central section still exists that stays free of the effects of the friction zone of the end plates. However, to evaluate the effect of the end plates on the confinement mechanism, and to see if strength or ductility of the member changes with separation of the end plate friction zones, this series of tests was carried out. It is also necessary to evaluate the L/D ratio for which slenderness is not critical. Finally, another objective of this research was to make necessary refinements to the proposed confinement model of Phase I (Mirmiran 1997).

Specimen Layout

A total of 24 composite specimens with three different tube thicknesses (6, 10, and 14 layers) and four different lengths (12", 18", 24", and 30") were tested. Table 4.1 shows the test matrix and instrumentation. For each tube length and thickness two identical samples were prepared for repeatability verification. The tubes were labeled by the character S (for slenderness), number of plies (6, 10, or 14), length (12, 18, 24, or 30), and sample number (1 or 2). The ply arrangement, tube thickness, fibers and resin, and winding angle were all the same as specimens of Series D from Phase I (Mirmiran 1997). Tubes were made of E-glass fibers and polyester resin wound at ±15° with respect to the cross section of the tube, or ±75° with respect to the axis of the mandrel. Thickness of the tubes were 0.057, 0.087, and 0.117 inch for the 6, 10, and 14 layer tubes, respectively. The inside diameter of the tubes was 5.71" as controlled by the diameter of the mandrel making the tubes. Therefore, the diameter-to-thickness (D/t) ratios of the 6, 10, and 14 layer tubes were approximately 100, 65, and 50, respectively. Usually, concrete-filled tubes with D/t ratios of less than 50 are considered stocky, while very slender tubes have a D/t ratio of over 100 (US-Japan Planning Group 1992). According to these definitions, the tubes under study are considered to be in between the stocky and very slender columns. Of course, it should be noted that these definitions are made for steel tubes. As for the L/D ratio of the tubes, a range from approximately 2:1 to 5:1 was selected which still qualifies as short column. Therefore, slenderness and secondary moments were not expected to be an issue in these tests. However, eccentricities and slenderness effects are studied in more detail later in this chapter. In addition, three 6"x12" control cylinders were made to determine the average strength of concrete core.

Casting was performed at UCF on February 19, 1997. Concrete was ready mix as delivered from Rinker with a target strength of 4,000 psi, a slump of 4", and maximum aggregate size of 1" (DOT #57). However, the initial slump taken from the truck was zero. Therefore, 2 gallons of water was added to the 1 cubic yard of concrete in the mixer truck. This resulted in a slump of 4". The zero slump concrete was only used in the S14-24-1, S14-24-2, S14-30-1, and S14-30-2. No control cylinder was taken from the zero slump concrete, and therefore, the results for the above 4 specimens should be looked upon with caution, as it is expected that the concrete core in these specimens may be stronger than the rest. All specimens were grooved near the top and bottom end surfaces, and were capped with sulfur mortar prior to testing, same as specimens of Phase I (Mirmiran 1997). It should be noted that as part of a parallel NSF project, an innovative component was added to this study which was the non-destructive testing, i.e., Acoustic Emission (AE) along with the traditional strain gage and LVDT instrumentation. A discussion of the AE test results are presented in Chapter 7.

Table 4.1 Test matrix for length effect specimens

Specimen Numbers			Length (in.)	L/D Ratio	No. of Strain Gages	No. of LVDTs	No. of AE Sensors*
6 Plies $t_j = 0.057"$ (D/t = 100)	10 Plies $t_j = 0.087"$ (D/t = 65)	14 Plies $t_j = 0.117"$ (D/t = 50)					
S6-12-1 S6-12-2	S10-12-1 S10-12-2	S14-12-1 S14-12-2	12	2 : 1	4	3	2
S6-18-1 S6-18-2	S10-18-1 S10-18-2	S14-18-1 S14-18-2	18	3 : 1	4	3	2
S6-24-1 S6-24-2	S10-24-1 S10-24-2	S14-24-1 S14-24-2	24	4 : 1	12	3	2 (4‡)
S6-30-1 S6-30-2	S10-30-1 S10-30-2	S14-30-1 S14-30-2	30	5 : 1	12	3	2

* See Chapter 7 for more details on AE tests.

‡ Only for S6-24-1, 4 sensors were used.

Instrumentation

All specimens were instrumented with TML (PL-60) strain gages (60 mm gage lengths). Number of gages for each type of specimen is shown in Table 4.1. The 12" and 18" cylinders were only instrumented at their mid-heights with two vertical and two horizontal gages placed at 180° opposite from each other. The horizontal and vertical gages were glued to the surface of the tube with one gage located on top of the other. The 24" and 30" cylinders were instrumented at the top and bottom quarters as well as mid-height with a total of 12 strain gages arranged similar to that described for the 12" and 18" cylinders. Figure 4.1 shows the strain gage arrangements for the tubes. In addition to surface gages, three LVDTs were used for each specimen to measure the average axial strains. Control cylinders were only instrumented with LVDTs.

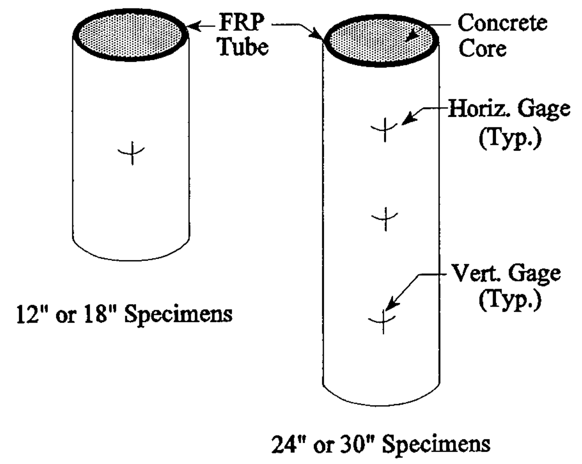

Figure 4.1 Instrumentation of composite tubes

Test Procedure

All specimens of this series were tested on May 13-15, 1997 at the FDOT Structures Lab at the age of 83-85 days. Three of the specimens (S14-18-2, S6-24-2, and S10-24-1) fell on the floor during the handling process, and were slightly damaged. These were then marked for comparison. However, all but one (S6-24-2) failed at about the same ultimate load as others when tested. A monotonic loading at a rate of 0.22 inch per minute as in Series D of Phase I was applied to all specimens. Tests were conducted using a 550-kip MTS machine, and data were recorded by a Mega DAQ data acquisition system. Figure 4.2 shows the test set up and one of the composite specimens with full instrumentation. All specimens were tested under uniaxial compression.

Observed Behavior

General failure mode of composite specimens was not any different from that observed in Phase I. Typical failure was marked by fiber rupture at point of maximum stress concentration, which was preceded by snapping of inner layers of the tube, appearance of white patches, and noises from inside the tube. White patches were indicative of the flow of resin, leaving white glass fibers to take the load. Sounds heard during the early to middle stages of loading were attributed to the micro-cracking of concrete and shifting and settling of aggregates. Snapping of the inner layers of the fiberglass could be heard near the end of the loading process. Failure, while sudden, was physically detectable and predictable. Although some local buckling and waving in the tubes were observed, shear failure was noted as the primary mode of failure for the tubes. It was also noted that specimens typically remained intact after failure. No form of violent failure was observed. Location and extent of fiber rupture for each specimen is indicated in Table 4.2. In the group of the 12" specimens, all but two failed at or around the middle band. One of these two specimens (S14-12-2) failed at the top groove. This specimen was also the only one in the entire series that failed due to the weakness at the groove, and upon its failure, except for the grooved ring that came off, the specimen remained intact. In the group of the 18" specimens, on the other hand, all but two failed at the top or bottom quarters. In the group of the 24" specimens, all but one failed at somewhere away from the mid-height. Finally, in the group of the 30" specimens, no single specimen fractured at mid-height. Slenderness effects in the form of buckling, even if present, was not noticeable during the tests or when photos of failed specimens were being taken. Later, analysis revealed that only minor eccentricities were present. Figures 4.3-4.5 show the 18" (14 layers), 24" (6 layers), and 30" (10 layers) specimens after failure.

Test Results

Recorded data from Mega DAQ was reduced and adjusted for the balance load and the initial straining of the capping materials same as in Phase I (Mirmiran 1997). After careful review of all readings from strain gages and LVDTs, average values were obtained to represent actual strains for each specimen. Test results for the control and composite specimens are summarized in Table 4.2. In this table, t_j is the tube thickness, L is the overall length of the specimen including the capping materials, f'_{cu} is the ultimate strength, f'_{co} is the average strength of concrete core, f_r is the confining pressure provided by the jacket, and ϵ_{cu} and ϵ_{ru} are the ultimate axial and lateral strains, respectively. The table clearly shows that considerable increase in strength and ductility can be achieved regardless of the length of the column, and that length effects are not very significant.

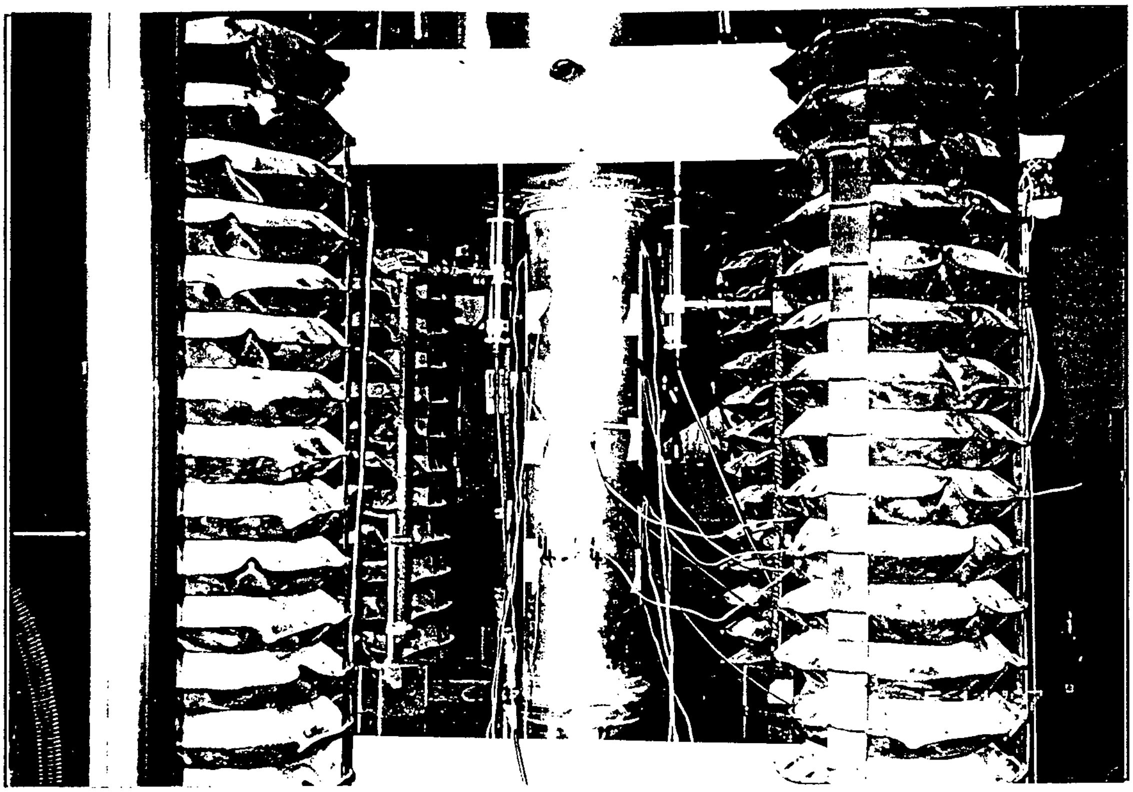

Figure 4.2 Composite specimen with full instrumentation prior to loading

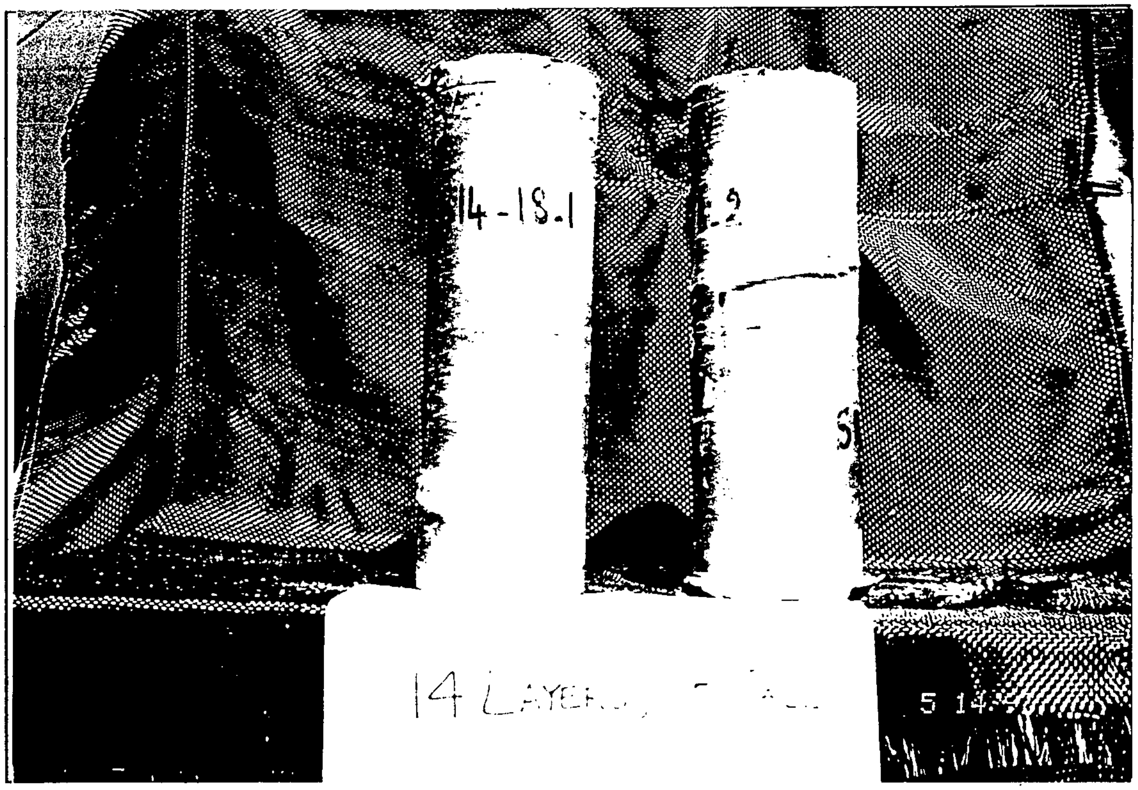

Figure 4.3 14-ply 18" tall specimens after failure

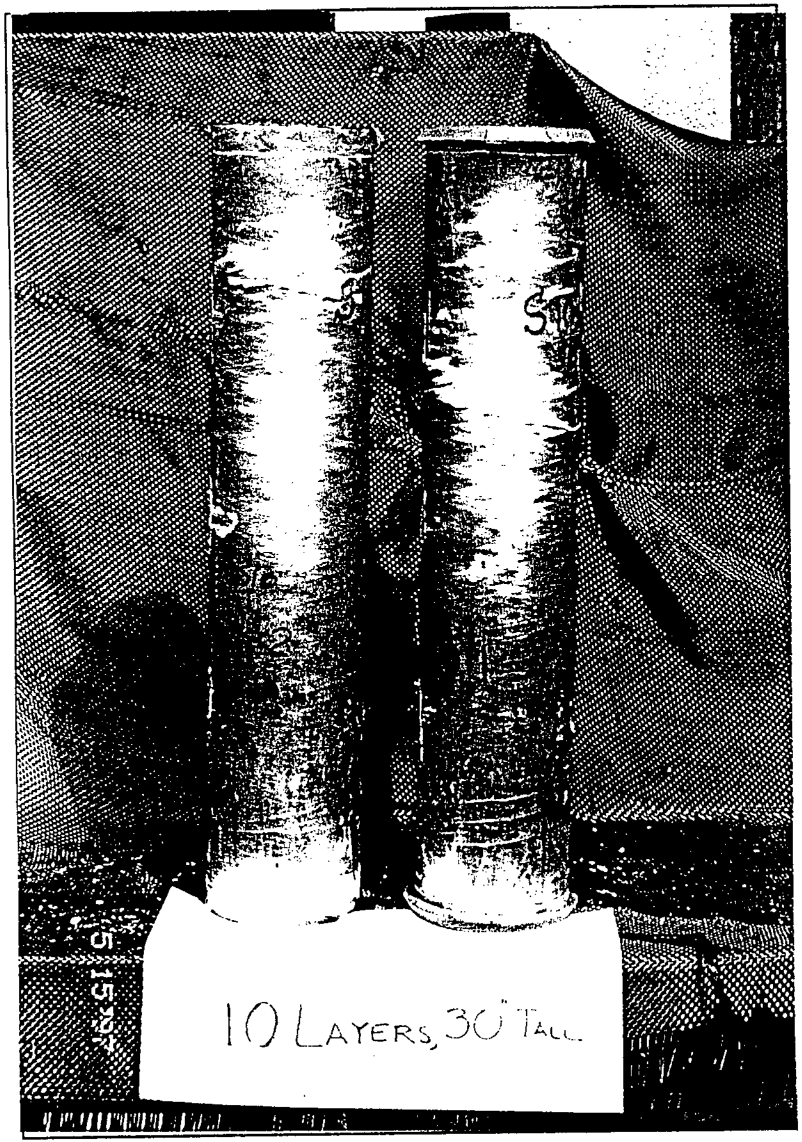

Figure 4.5 10-ply 30" tall specimens after failure

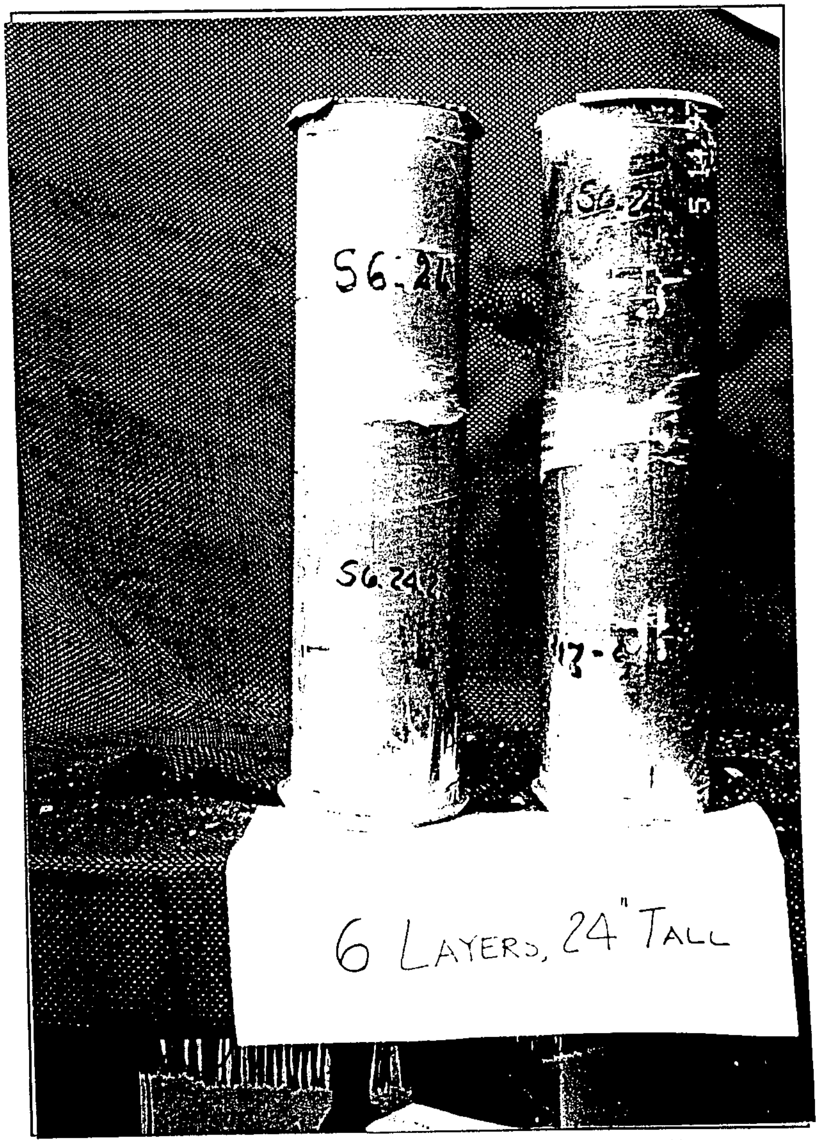

Figure 4.4 6-ply 24" tall specimens after failure

Table 4.2 Test results for length effect specimens

Specimen No.	t_j (in.)	L (in.)	f'_{cu} (ksi)	f'_{cu}/f'_{co}	f_r/f'_{co}	ϵ_{cu}	ϵ_{ru}	Location of Fiber Rupture
Control 1	-		6.67	-	-	0.002	-	-
Control 2	-		6.65	-	-	0.003	-	-
Control 3	-		6.19	-	-	0.003	-	-
S6-12-1	0.057	12.375	9.14	1.41	0.233	0.025	-0.019	all around, middle band
S6-12-2		12.250	8.27	1.27		0.022	-0.014	one side, mid-height
S10-12-1	0.087	12.313	12.07	1.86	0.394	0.029	-0.018	all around, upper quarter
S10-12-2		12.313	10.93	1.68		0.024	-0.014	all around, middle band
S14-12-1	0.117	12.313	15.16	2.33	0.586	0.030	-0.015	all around, middle band
S14-12-2†		12.313	12.91	1.99		0.027	-0.011	premature failure, top groove
S6-18-1	0.057	18.438	7.48	1.15	0.233	0.013	-0.009	one side, mid-height
S6-18-2		18.313	7.09	1.09		0.008	-0.009	one side, 3" above middle
S10-18-1	0.087	18.375	10.10	1.55	0.394	0.021	-0.011	4" above & below middle
S10-18-2		18.250	9.78	1.50		0.020	-0.010	one side, mid-height
S14-18-1	0.117	18.438	12.24	1.88	0.586	0.025	-0.010	all around,6"below middle
S14-18-2*		18.250	12.33	1.90		0.025	-0.012	one side, 6" below middle
S6-24-1	0.057	24.438	7.65	1.18	0.233	0.013	-0.011	one side, mid-height
S6-24-2*		24.250	6.19	0.95		0.008	-0.009	one side,3.5"above middle
S10-24-1*	0.087	24.438	9.37	1.44	0.394	0.016	-0.010	one side,10" below middle
S10-24-2		24.375	9.17	1.41		0.014	-0.009	one side,4" above middle
S14-24-1‡	0.117	24.313	12.88	1.98	0.586	0.026	-0.010	one side,8" above middle
S14-24-2‡		24.313	12.94	1.99		0.023	-0.012	one side,11" above middle
S6-30-1	0.057	30.188	6.93	1.07	0.233	0.011	-0.009	one side, top quarter
S6-30-2		30.313	7.60	1.17		0.013	-0.011	one side, top quarter
S10-30-1	0.087	30.250	9.46	1.46	0.394	0.016	-0.010	one side,6.5"above middle
S10-30-2		30.313	8.30	1.28		0.011	-0.007	one side, top quarter
S14-30-1‡	0.117	30.188	11.93	1.83	0.586	0.019	-0.009	one side, top quarter
S14-30-2‡		30.188	12.25	1.88		0.019	-0.009	one side,13" below middle

* Specimens fell down during handling (only S6-24-2 was affected).

† Lower ultimate load for this specimen is due to premature failure at the top groove.

‡ Specimens cast with the initial zero-slump concrete.

Figures 4.6-4.9 show the stress-strain curves of the 12", 18", 24", and 30" specimens, respectively. In these figures, axial stress is plotted against axial and radial strains. The stress-strain curves have the same bilinear shape as those observed in Phase I. Although the confinement effectiveness in Table 4.2 is determined based on the unconfined strength of 6.50 ksi (average of the

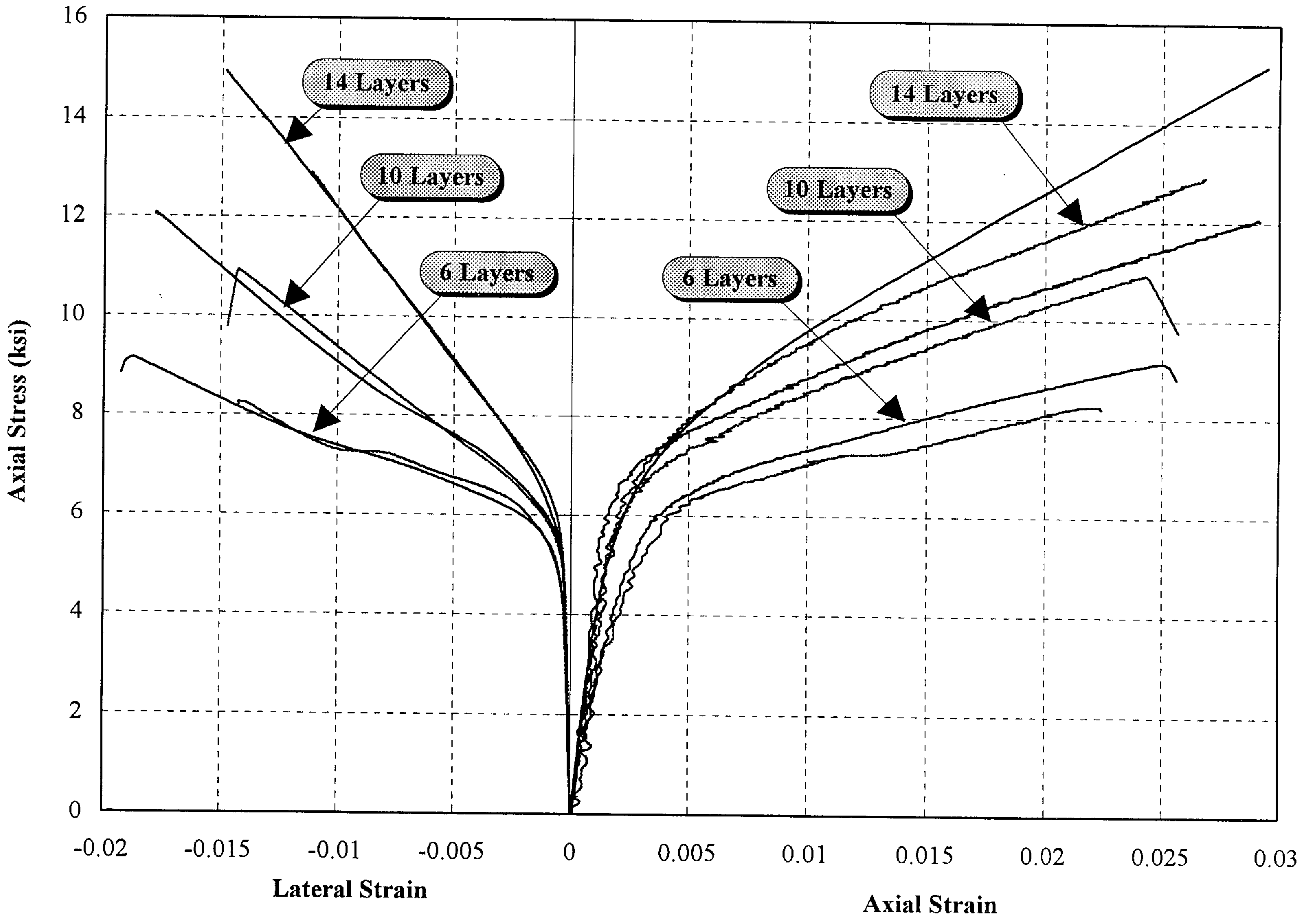

Figure 4.6 Stress-strain curves for 12″ specimens

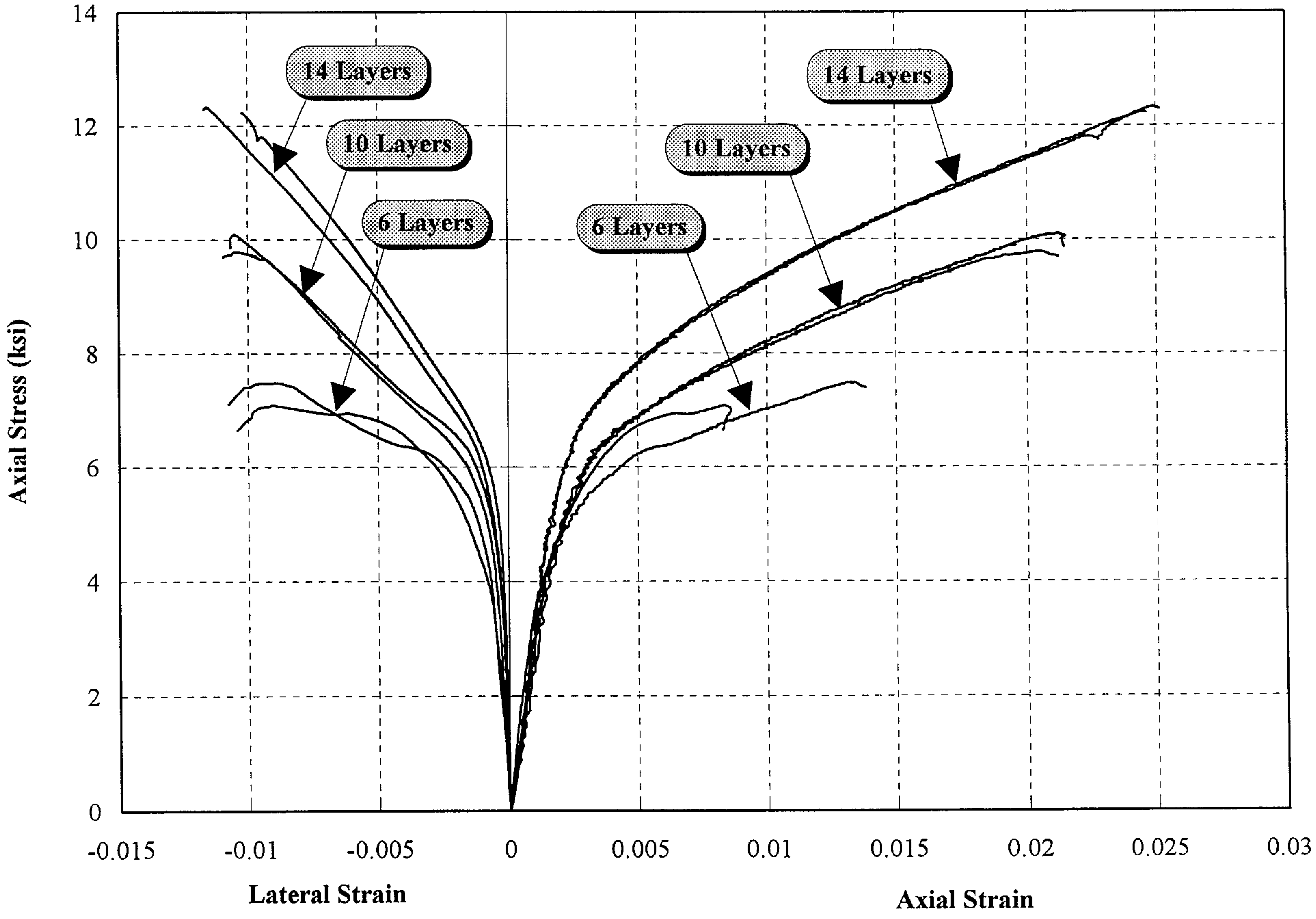

Figure 4.7 Stress-strain curves for 18″ specimens

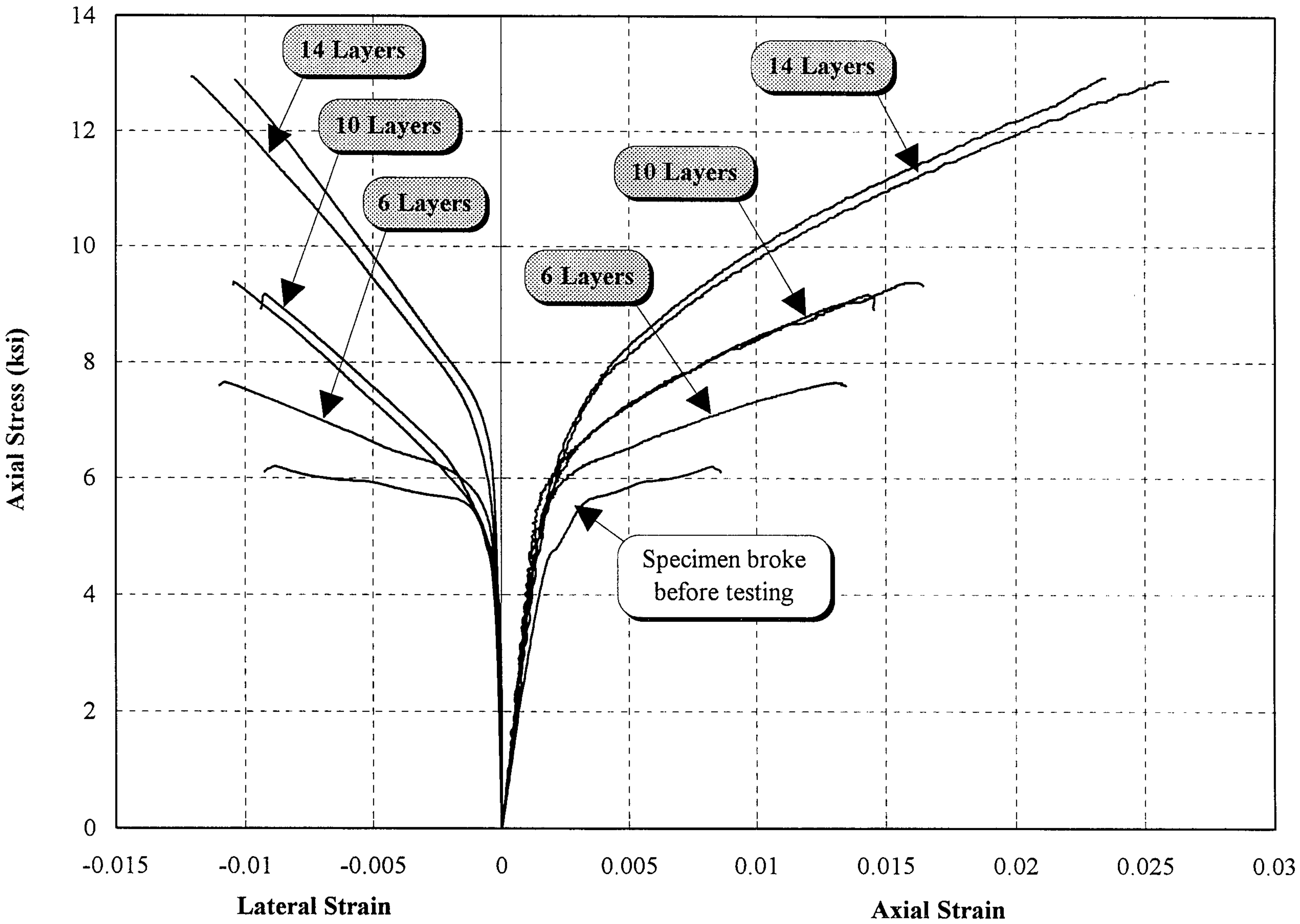

Figure 4.8 Stress-strain curves for 24″ specimens

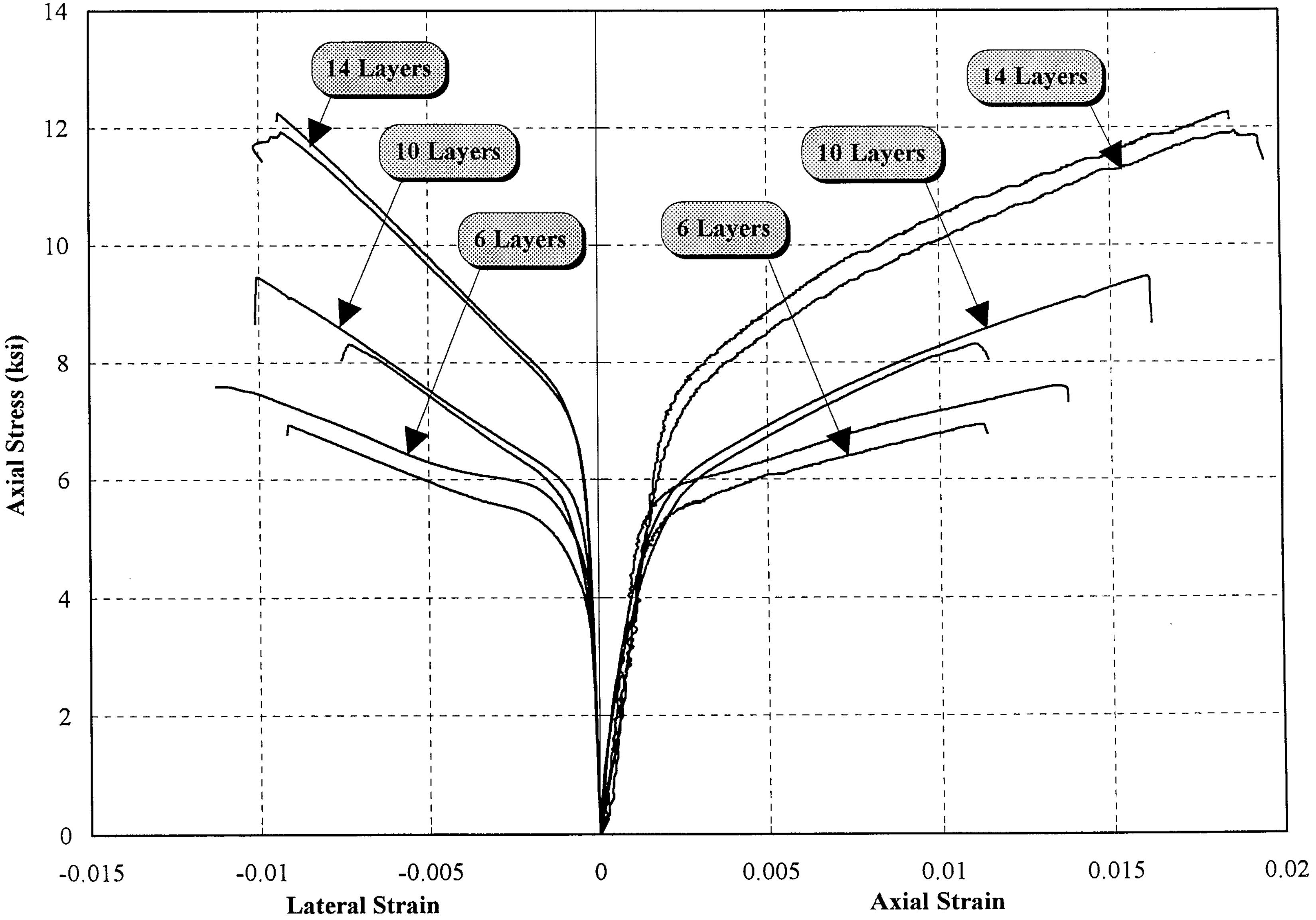

Figure 4.9 Stress-strain curves for 30″ specimens

three control specimens), it is clear from the figures that slight variation exist at the bend points of each specimen. This means that the actual unconfined strength of each specimen may slightly differ from the average value of 6.50 ksi. It further helps to group the stress-strain curves together by the number of layers to examine the effect of column length. Figures 4.10-4.12 show the stress-strain curves for the 6, 10, and 14 layer tubes, respectively. The heavy lines in these figures show the predicted stress-strain curves from the confinement model as discussed in Section 4.3. As clear from these figures, length effects are not significant within the range of 2:1 to 5:1 that has been studied here. There is no difference in the initial and secondary slopes of the response curves for tubes of the same thickness but variable lengths. It appears, however, that the bend and failure points are somewhat affected by the length of the tube. This may be caused by premature fracture of the concrete core or the tube as a result of slenderness of the specimen (see Section 4.3).

Figures 4.13-4.15 show the axial stress versus volumetric strains for the 6, 10, and 14 layer tubes. Again, it is clear that effect of column length on dilation characteristics of confined concrete are not significant within the normal scatter of the results. It appears that the general shape of dilation curves and volumetric change depends on the stiffness and materials of the tube rather than its length or thickness. All composite tubes, regardless of their thickness or length, reverse the dilation tendency of the concrete core in the same fashion as was observed in Phase I (Mirmiran 1997). Similar observations were made for the dilation rates and volumetric strains versus axial strains, which, however, for brevity, are not reported here. For more details, see El Echary (1997).

4.3 Analysis and Discussion

It is of some interest to quantify the length effects on strength and ductility of concrete columns confined by fiber composites. Figure 4.16 shows the normalized ultimate strength of the 24 test specimens versus their L/D ratios. In this figure, the ultimate strengths (f'_{cu}) are divided by the average ultimate strength of the corresponding 12" specimens with the same number of layers (f'_{cu12}). As shown in the figure, the scatter of data and the effect of the L/D ratio are not significant, and the data can be best fit by a parabolic function as below

$$f_{cu} = f_{cu12}\left[0.0288\left(\frac{L}{D}\right)^2 - 0.263\left(\frac{L}{D}\right) + 1.418\right] \tag{4.1}$$

Similarly, Figure 4.17 shows the normalized ultimate strain of the 24 test specimens versus their L/D ratios. Again, the ultimate strains (ϵ_{cu}) are divided by the average ultimate strain for the corresponding 12" specimens with the same number of layers (ϵ_{cu12}). The scatter of the data appears larger for the ultimate strains than for the ultimate strengths. However, a similar parabolic function is derived as below

$$\epsilon_{cu} = \epsilon_{cu12}\left[0.0529\left(\frac{L}{D}\right)^2 - 0.5214\left(\frac{L}{D}\right) + 1.8506\right] \tag{4.2}$$

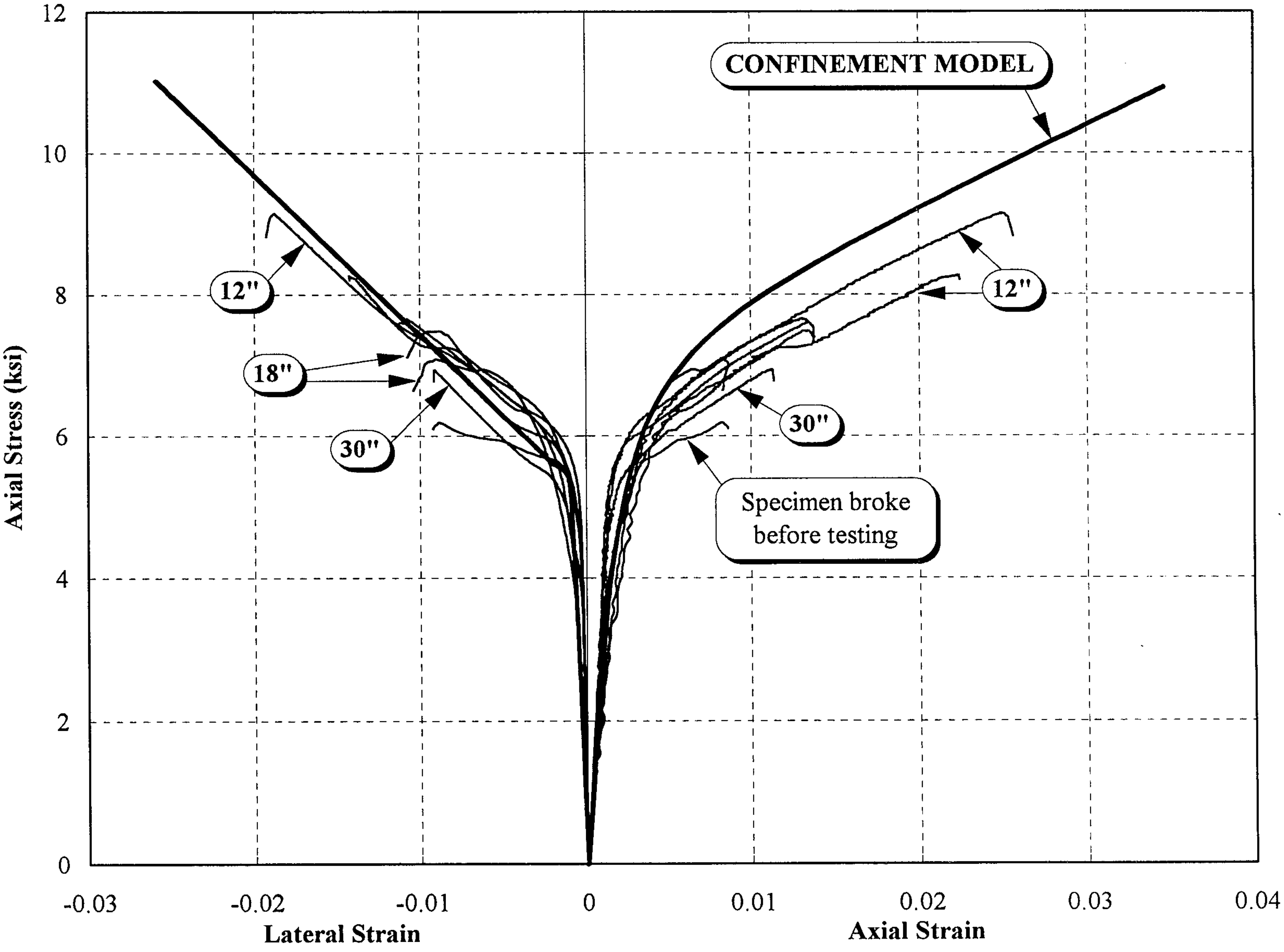

Figure 4.10 Stress-strain curves for 6-layer specimens

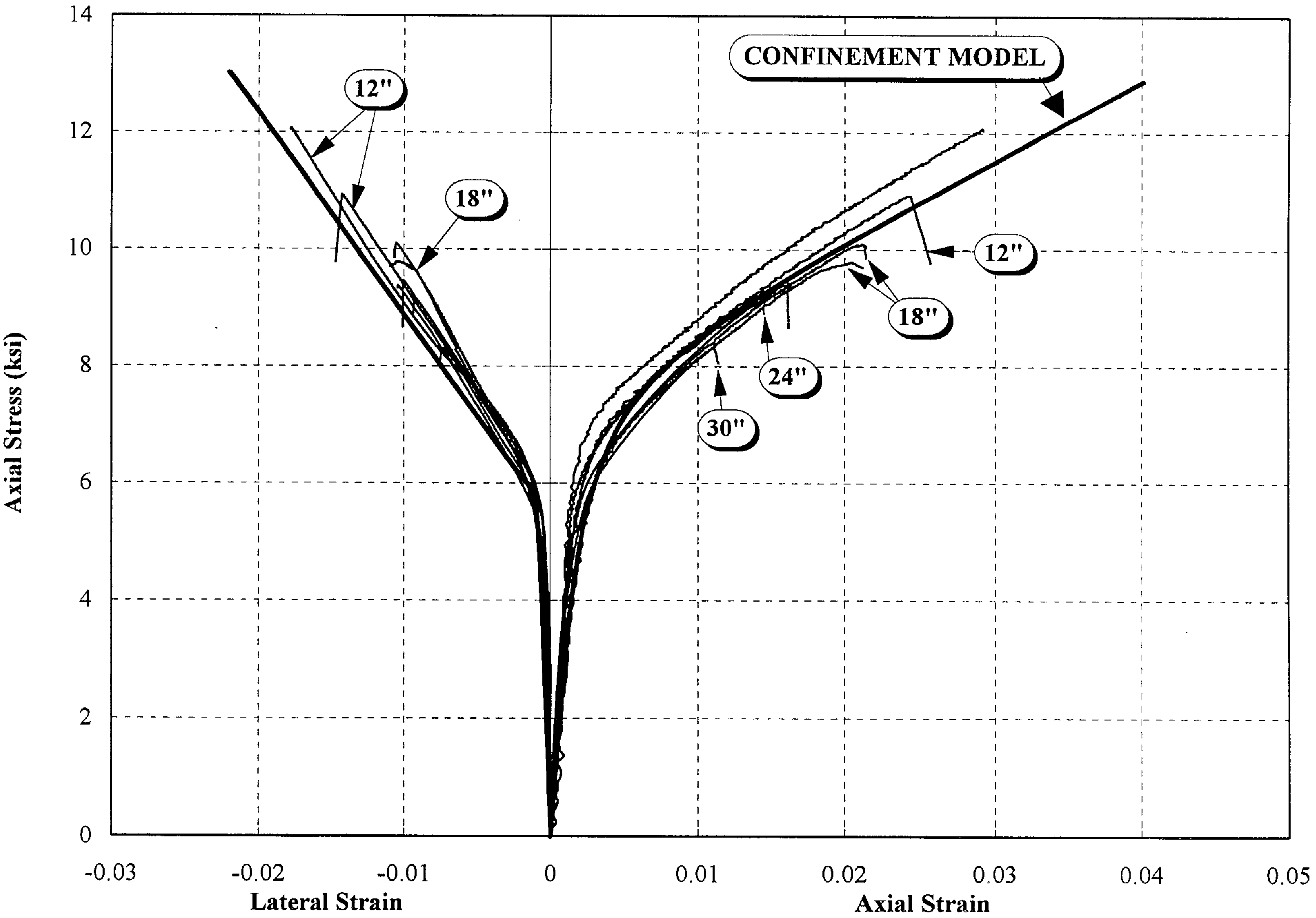

Figure 4.11 Stress-strain curves for 10-layer specimens

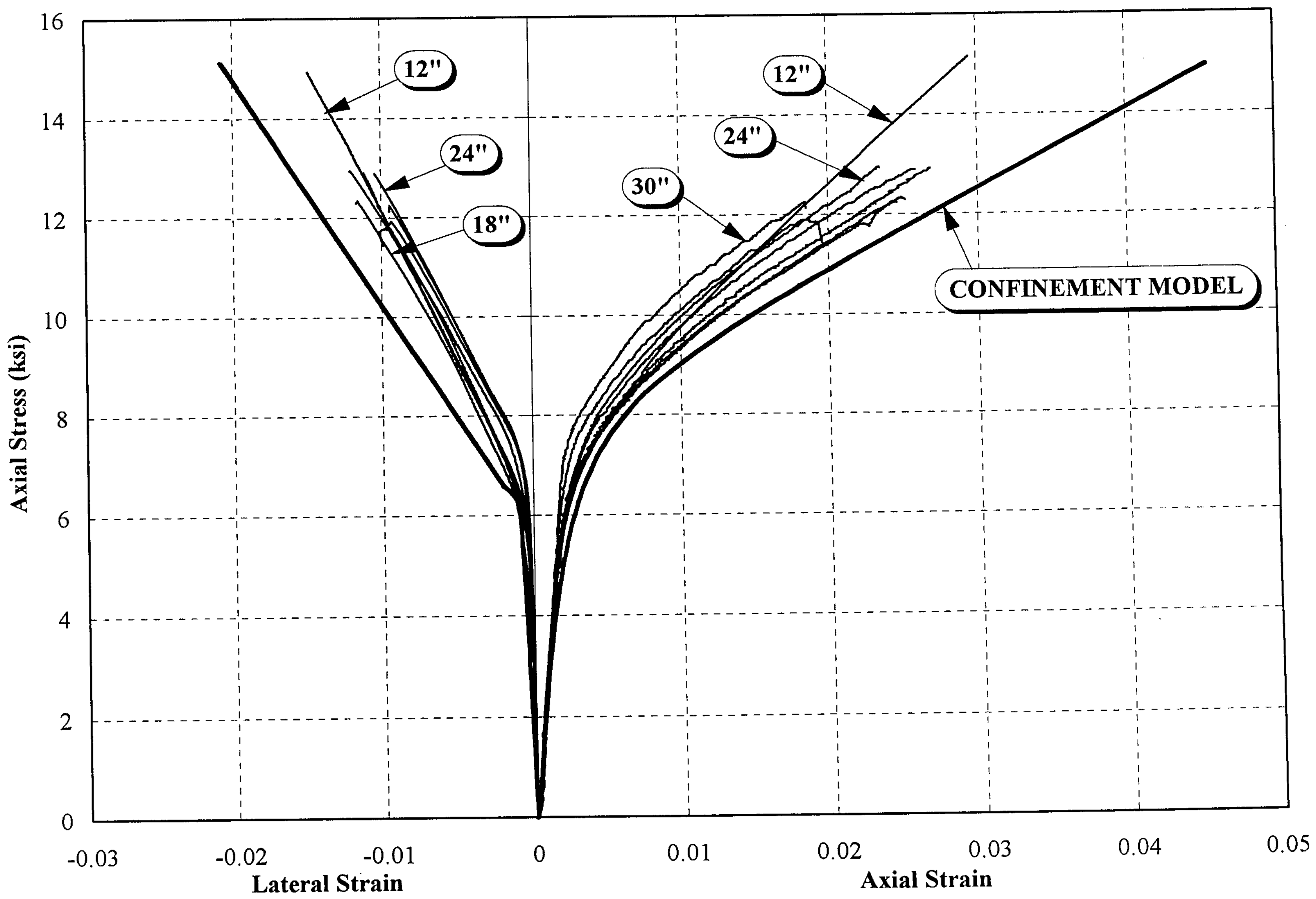

Figure 4.12 Stress-strain curves for 14-layer specimens

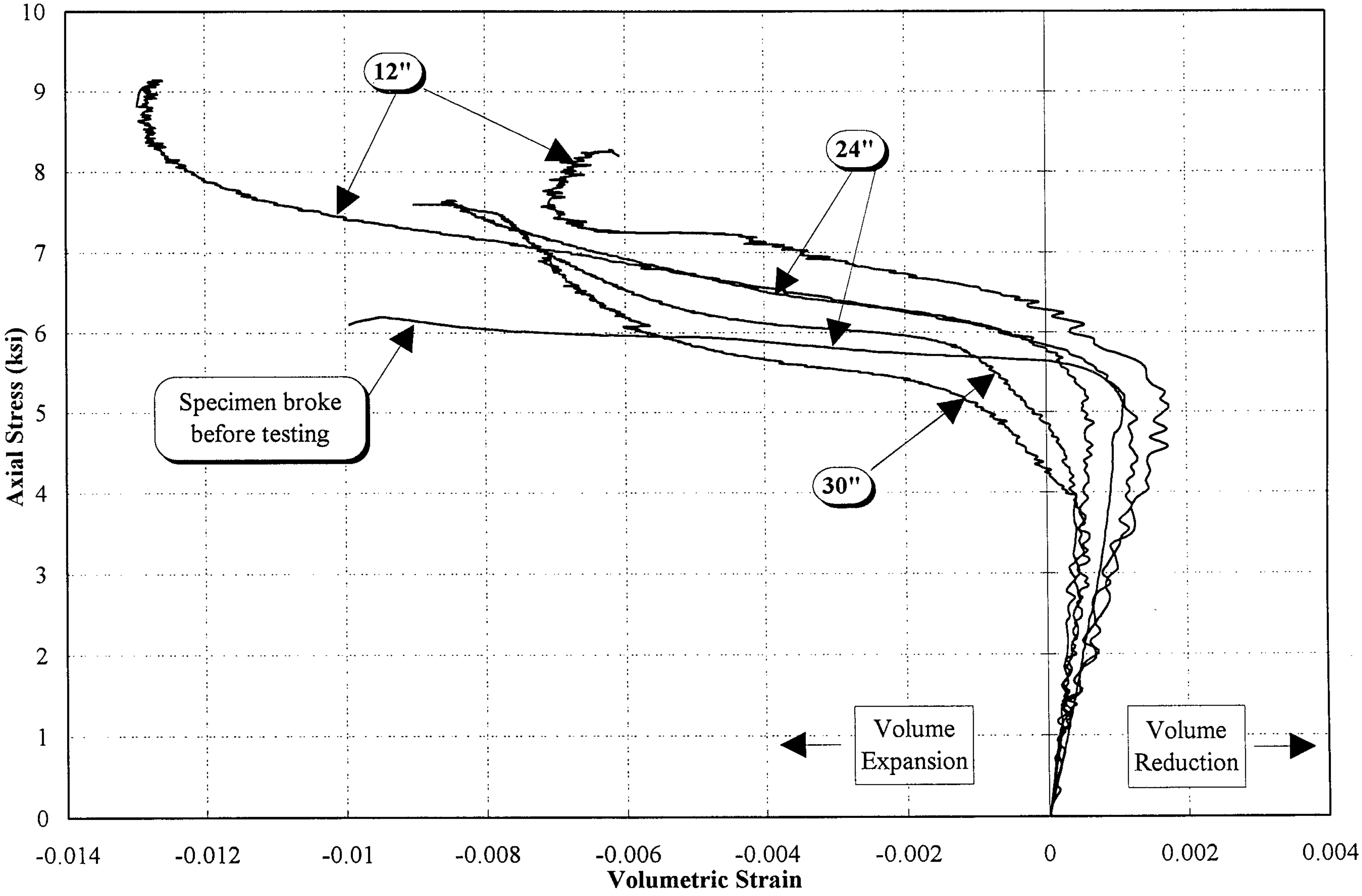

Figure 4.13 Axial stress versus volumetric strain for 6-layer specimens

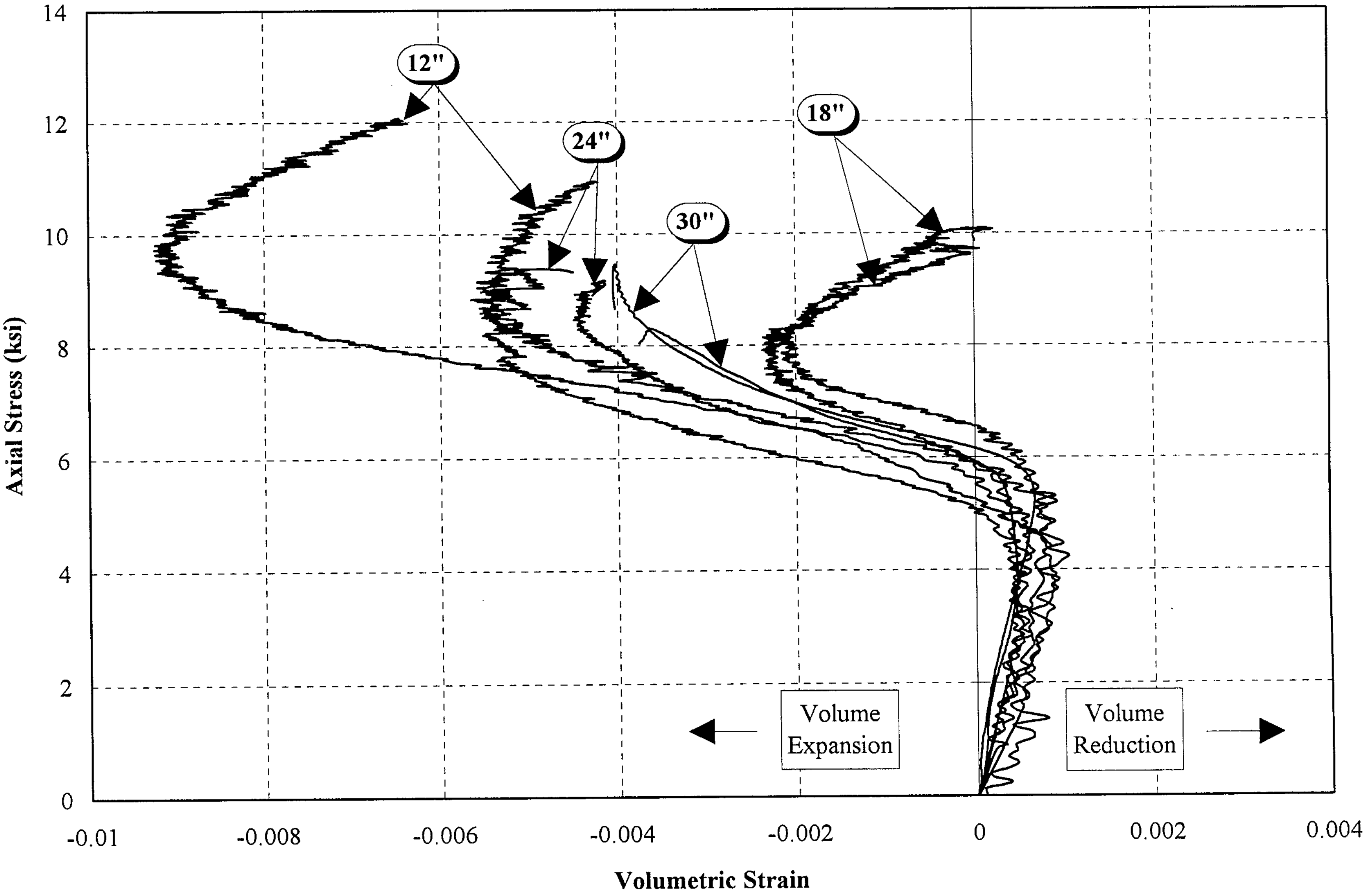

Figure 4.14 Axial stress versus volumetric strain for 10-layer specimens

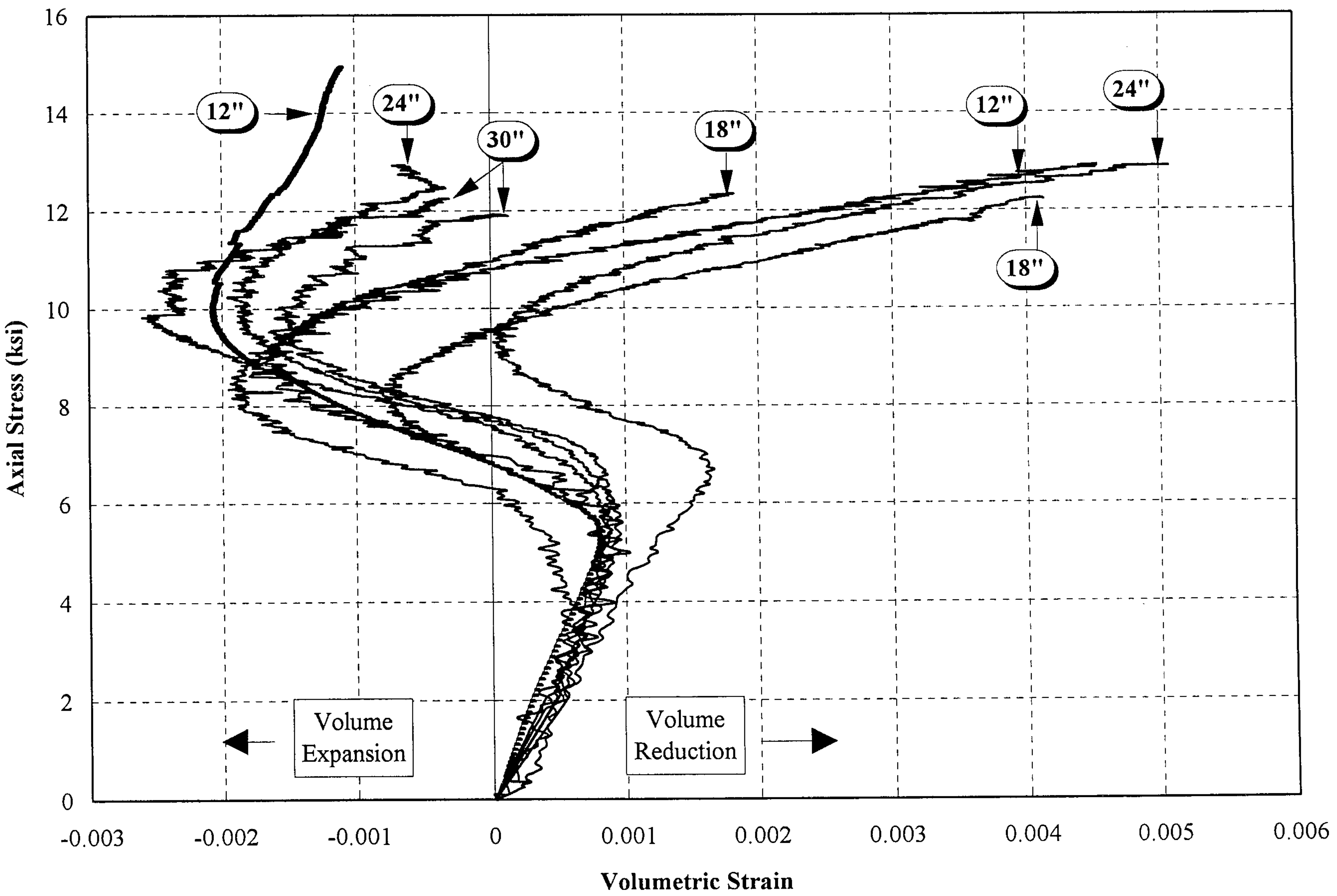

Figure 4.15 Axial stress versus volumetric strain for 14-layer specimens

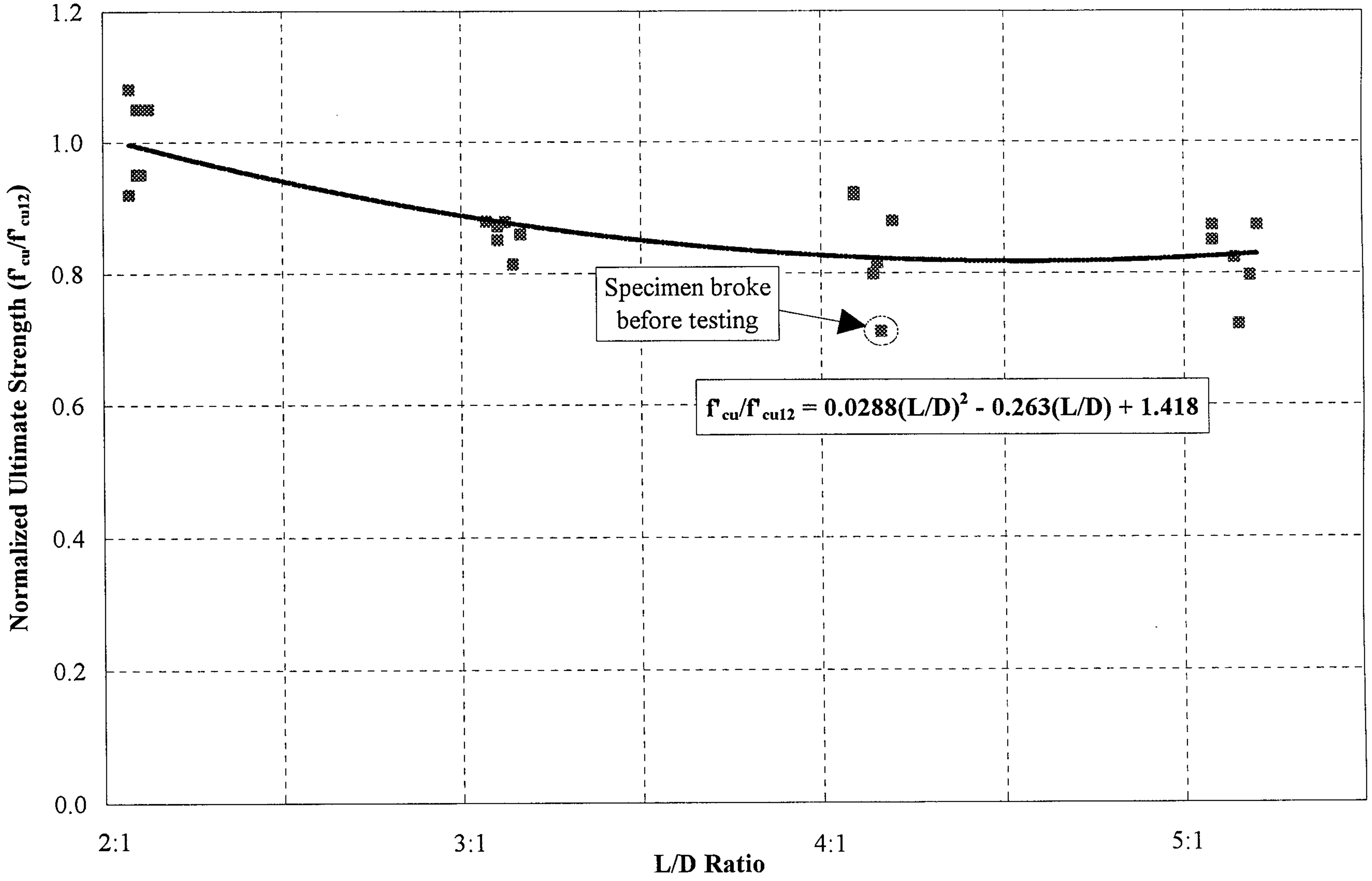

Figure 4.16 Normalized ultimate strength versus L/D ratio

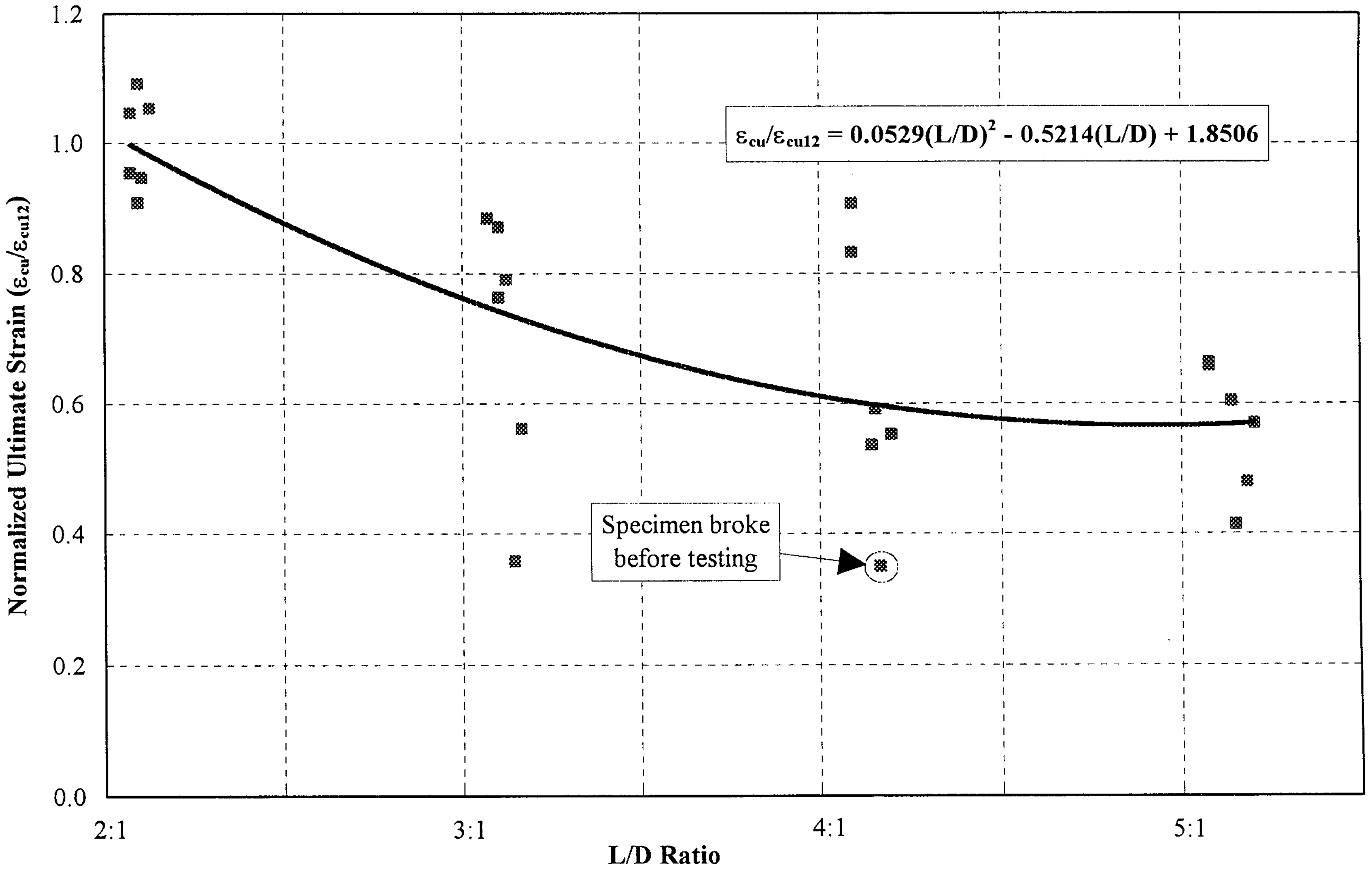

Figure 4.17 Normalized ultimate strain versus L/D ratio

Updated Confinement Model

Next, it is necessary to compare the results of this series with the confinement model developed in Phase I (Mirmiran 1997). It should be noted that some changes were made in that model after the publication of the Final Report. Those changes were reflected in a paper by Samaan, Mirmiran, and Shahawy (1997), and are also presented in this section. The equation for the bilinear stress-strain curve is given by

$$f_c = \frac{(E_{1i} - E_{2i})\epsilon_i}{\left[1 + \left(\dfrac{(E_{1i} - E_{2i})\epsilon_i}{f_{oi}}\right)^{n_i}\right]^{1/n_i}} + E_{2i}\,\epsilon_i \qquad (4.3)$$

where subscript i denotes the direction of stresses and strains. For axial direction, $i = a$, and for lateral (radial) direction, $i = r$. Other parameters are described below. In the axial direction, the initial slope E_{1a} is taken after Ahmad and Shah (1982) as below

$$E_{1a} = 47.586\sqrt{1000\,f'_{co}} \qquad (ksi) \qquad (4.4)$$

E_{2a} is the secondary slope of the stress-strain curve, and is a function of the stiffness of the confining member and the strength of unconfined concrete, as given by

$$E_{2a} = 54.167\,f'^{\,0.2}_{co} + 0.9332\,\frac{E_j\,t_j}{D} \qquad (ksi) \qquad (4.5)$$

for which the goodness of the fit was determined as R^2 is 91.1%. f_{oa} is the intercept stress of the second slope with the stress axis, and is directly related to the confining pressure f_r and the strength of unconfined concrete f'_{co} as below

$$f_{oa} = 0.872\,f'_{co} + 0.371\,f_r + 0.908 \qquad (ksi) \qquad (4.6)$$

for which R^2 is 92.9%. Finally n is a curve-shape parameter which determines the shape of the transition zone between the two slopes. The experiments indicate that a curve shape factor of 1.5 is generally acceptable for the FRP specimens. The ultimate strength of the confined concrete (f'_{cu}) is given by

$$f'_{cu} = f'_{co} + 3.38\,f_r^{\,0.7} \qquad (ksi) \qquad (4.7)$$

for which R^2 is 88.9%. The peak and ultimate dilation rates are

$$\mu_{max} = -0.920 \ Ln \left(\frac{2 \ E_j \ t_j}{f'_{co} \ D} \right) + 4.063 \qquad (4.8)$$

$$\mu_u = -0.176 \ Ln \left(\frac{2 \ E_j \ t_j}{f'_{co} \ D} \right) + 0.906 \qquad (4.9)$$

for which R^2 is 89.8% and 87.4%, respectively. The initial slope in the lateral direction is given by

$$E_{1r} = \frac{E_1}{\mu_o} \qquad (4.10)$$

where μ_o = initial rate of dilation or the Poisson's ratio. The second slope in the lateral direction is given by

$$E_{2r} = \frac{E_2}{\mu_u} \qquad (4.11)$$

for which R^2 is 81.8%. The stress interception point f_{or} has been calibrated similar to f_o, and the following relationship is derived

$$f_{o\,r} = 0.636 \ f'_{co} + 0.233 \ f_r + 0.661 \qquad (ksi) \qquad (4.12)$$

for which R^2 is 79.9%. Finally, the curve shape factor in the lateral direction is estimated as below:

$$n_r = \frac{n_1}{\mu_u} \qquad (4.13)$$

Comparison of Test Results with the Model

Figure 4.18 shows the predicted versus experimental values of ultimate strength for the 24 test specimens. It should be noted that these are the so-called "blind predictions," because the test data are not used in the calibration of the model. It is clear from the figure that the 12" specimens are close to the predicted values. The deviation can be attributed to the variation in the unconfined strength of the concrete core, and also the premature failure of S14-12-2 at its top groove. Furthermore, to avoid total failure of the specimens which might have damaged the AE sensors, the tests of this series were generally stopped as soon as the first fiber rupture was noticed. The lower values for the 18", 24", and 30" specimens can be attributed to the length effects as quantified by Equation (4.1). Finally, referring back to Figures 4.10-4.12, where the heavy lines show the predicted

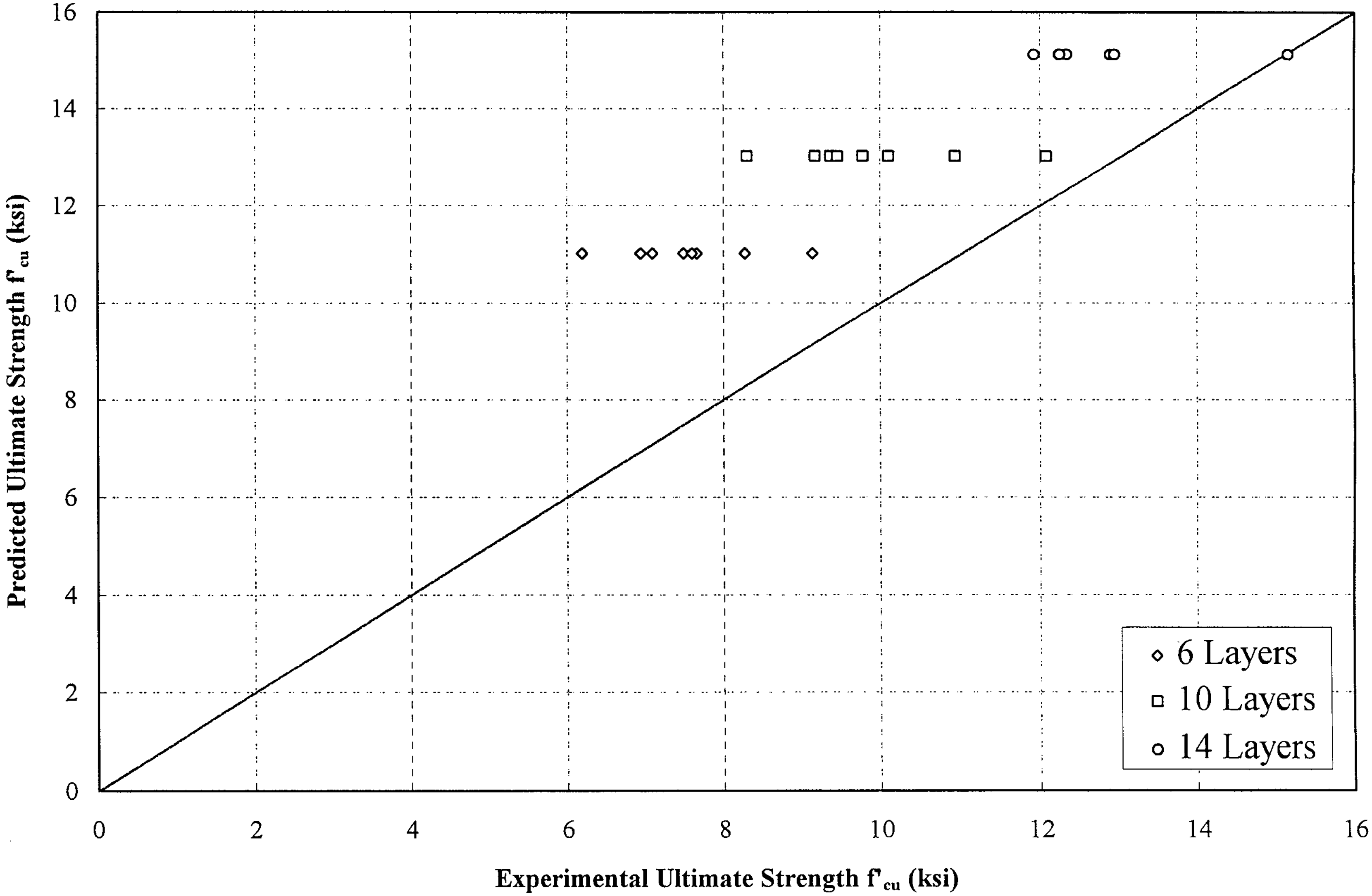

Figure 4.18 Predicted versus experimental values of ultimate strength

stress-strain curves from the model, it is clear that reasonable agreement with the model can be achieved.

Eccentricities and Slenderness Effects

As indicated earlier, the 24" and 30" specimens were instrumented with 6 vertical gauges located at the top quarter, mid-height, and bottom quarter of the specimens. Figures 4.19 and 4.20 show strain distributions along the height of the column for S10-24-2, and S14-30-1, respectively. The graphs to the right of the vertical axis represent readings from the strain gauges on the south side of the specimen, while the graphs to left depict the north side gauge. On each side, four graphs are shown which represent the strain distribution at ¼, ½, ¾, and full ultimate load. As the load increases, some variation in strain readings are observed which reflect bending curvature of the specimen. These two figures represent two of the most severe curvatures. Of the two specimens depicted in these figures, one (S10-24-2) shows a single curvature with maximum strain at the top quarter, while the other (S14-30-1) shows a single curvature with maximum strain at the mid-height.

If the stress resultant (or the applied load) at a section is concentric, strain readings at both sides of the section will be the same. Different strain readings indicates an eccentric load. Figure 4.21 shows the ultimate strain readings on either side of a specimen at a certain height. Noting that the stress-strain relation is linear past the bend point, one can assume the same distribution for the stresses as for the strains. Therefore, the centroid of the trapezoidal area between the two strain readings can in fact show the location of the stress resultant, i.e., the applied load, at that particular section. The distance between that centroid and the centerline of the section is the eccentricity of the load at that section. Table 4.3 shows the eccentricities at various levels calculated for each specimen using the method explained above. In the table, $e_{1/4}$, $e_{1/2}$, and $e_{3/4}$ represent the eccentricities at the top quarter, mid-height, and bottom quarter of the specimen. Note that the 12" and 18" specimens were only instrumented at their mid-heights. One should regard the eccentricities calculated from the difference in strain readings with great caution, since part of the difference in the strain readings is caused by stress concentrations on one side of the specimen, or perhaps a flaw in the construct of the tube. Therefore, the values in Table 4.3 should be considered as the upper bound (maximum) possible eccentricities that were present in the tests. In fact some of the 12" or 18" specimens show somewhat high eccentricities that can be best explained by the above reasons. However, the single most important conclusion from this table is that the maximum eccentricity is within the 10-12% of the section width. Note that ACI 318-95 considers a minimum eccentricity of 10% for all tied columns, and further recommends reducing the ultimate strength of tied columns by 20% to allow for the 10% eccentricity. Using Equation (4.1) that was developed based on 24 test specimens of the present study, the reduction factor is about 18% for a column with L/D ratio of 5:1. It is therefore, concluded that the 12" cylinders should be considered adequate to represent the confinement of concrete sections. Also, longer specimens possess an inherent eccentricity that result in lower values of the ultimate load. However, these eccentricities are within the reasonable range of about 10% of the section width, and do not necessarily qualify for any slenderness effect.

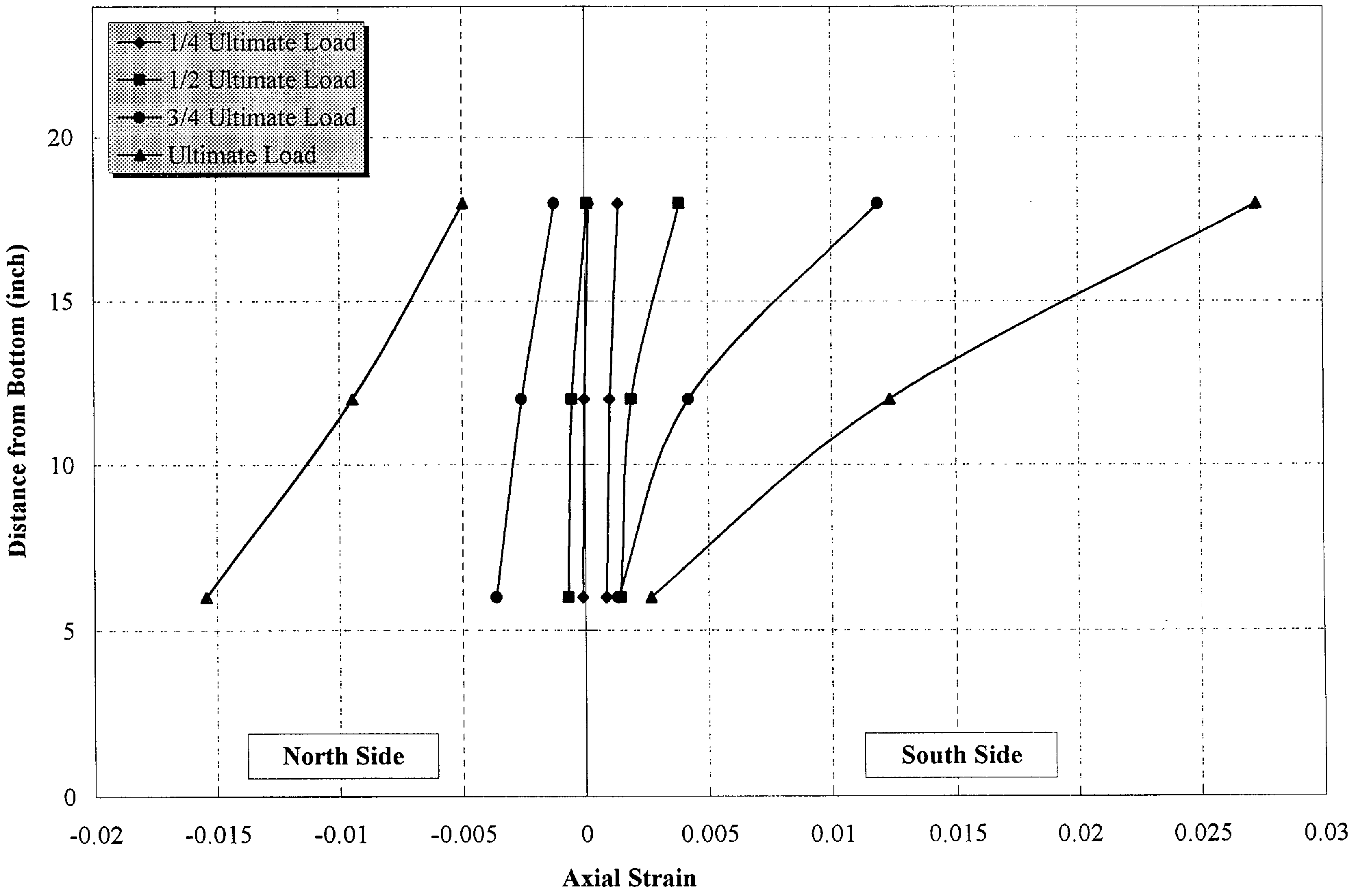

Figure 4.19 Strain distribution along height of S10-24-2

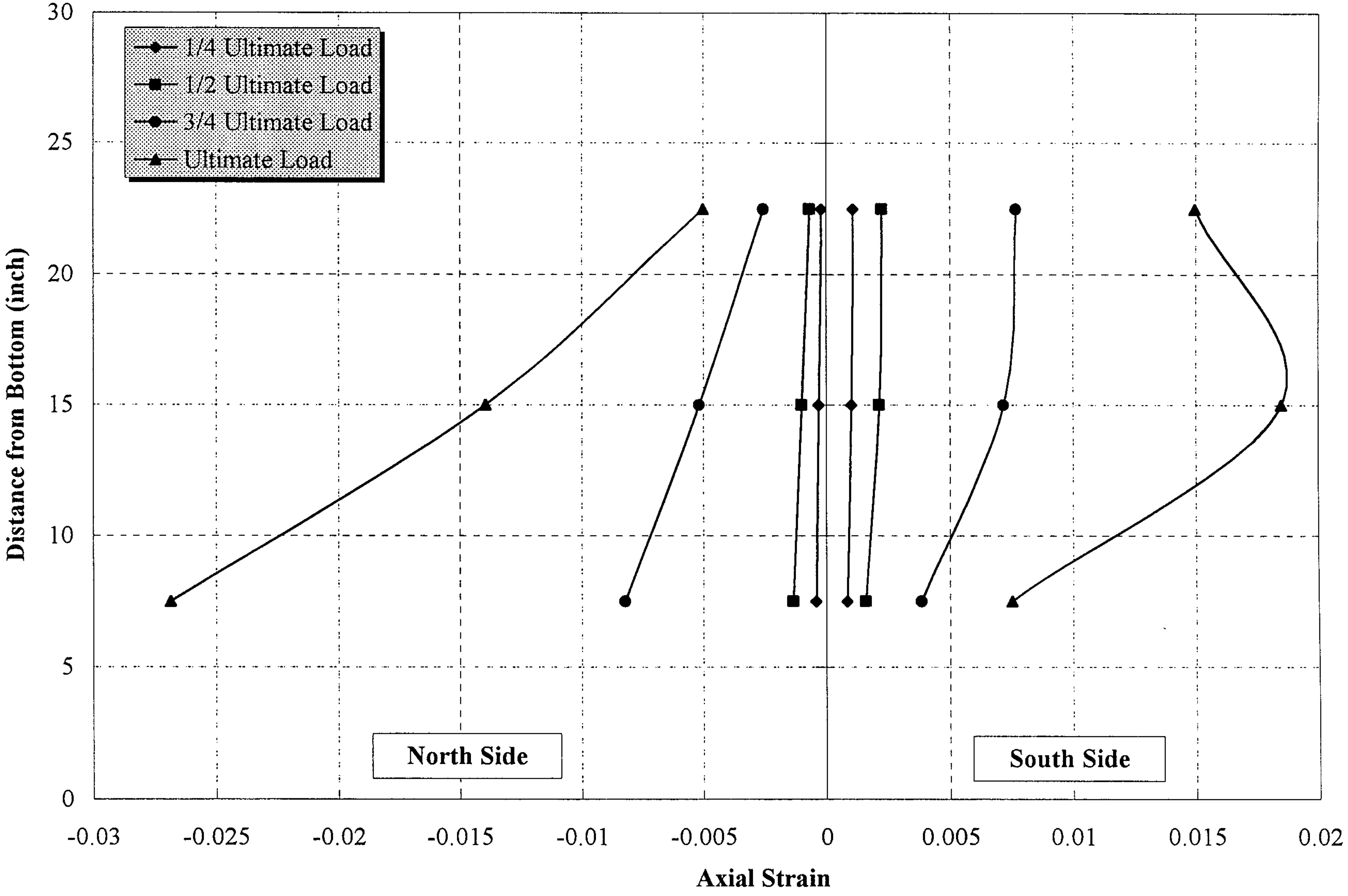

Figure 4.20 Strain distribution along height of S14-30-1

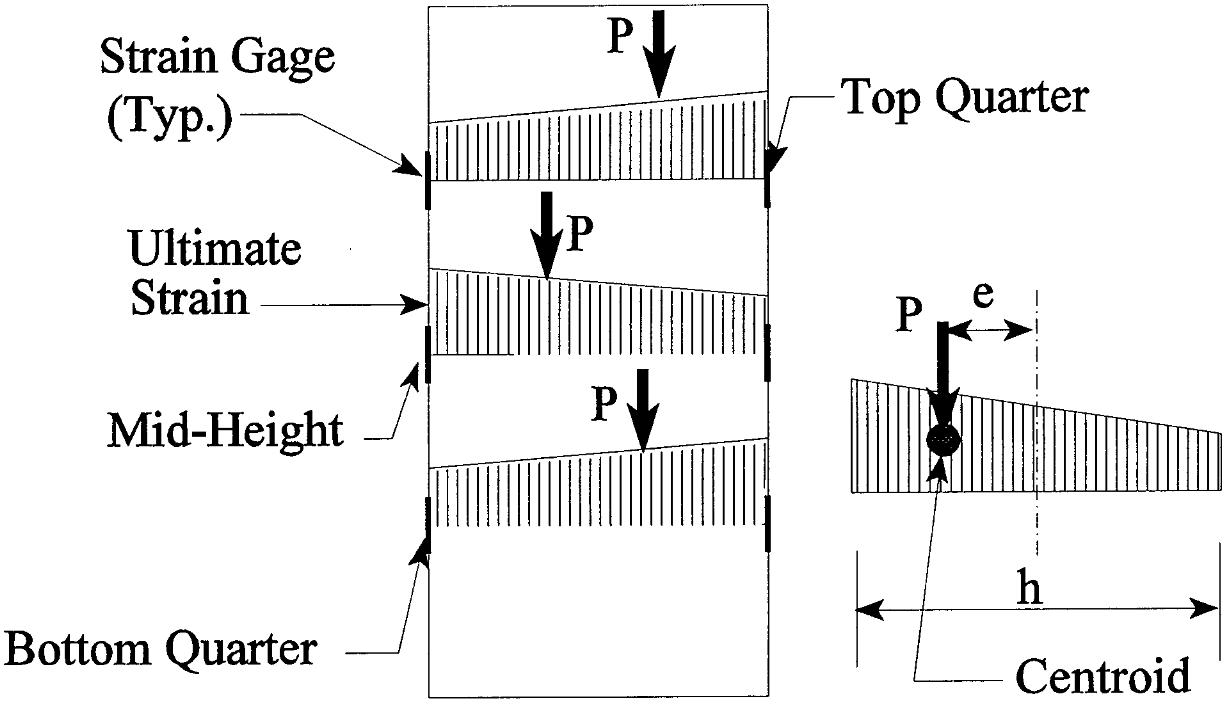

Figure 4.21 Defining eccentricities based on strain variations

Table 4.3 Calculated eccentricity ratios for length effect specimens

Specimen No.	L/D	Eccentricity, e (in)			Eccentricity Ratio (e/h)		
		¼L	½L	¾L	¼L	½L	¾L
S6-12-1	2.1248	-	0.1446	-	-	2.48%	-
S6-12-2	2.1034	-	-0.0415	-	-	-0.71%	-
S6-18-1	3.1658	-	0.1430	-	-	2.46%	-
S6-18-2	3.1443	-	-0.5338	-	-	-9.17%	-
S6-24-1	4.1960	-0.1206	-0.0360	0.2205	-2.07%	-0.62%	3.79%
S6-24-2	4.1638	-0.2090	0.0424	0.0781	-3.59%	0.73%	1.34%
S6-30-1	5.1833	0.3495	-0.4696	-0.4647	6.00%	-8.06%	-7.98%
S6-30-2	5.2048	0.3533	-0.2168	-0.5294	6.07%	-3.72%	-9.09%
S10-12-1	2.0925	-	*	-	-	*	-
S10-12-2	2.0925	-	-0.1840	-	-	-3.13%	-
S10-18-1	3.1229	-	-0.0727	-	-	-1.24%	-
S10-18-2	3.1016	-	-0.2800	-	-	-4.76%	-
S10-24-1	4.1532	*	-0.0901	-0.1299	*	-1.53%	-2.21%
S10-24-2	4.1426	0.6942	-0.1269	-0.6774	11.80%	-2.16%	-11.51%
S10-30-1	5.1411	0.2678	-0.1284	-0.3637	4.55%	-2.18%	-6.18%
S10-30-2	5.1517	0.3520	-0.3600	-0.5530	5.98%	-6.12%	-9.40%
S14-12-1	2.0714	-	-0.1056	-	-	-1.78%	-
S14-12-2	2.0714	-	-0.0476	-	-	-0.80%	-
S14-18-1	3.1019	-	0.2746	-	-	4.62%	-
S14-18-2	3.0703	-	0.3247	-	-	5.46%	-
S14-24-1	4.0903	*	-0.0172	-0.6342	*	-0.29%	-10.67%
S14-24-2	4.0903	0.0100	-0.3460	-0.3059	0.17%	-5.82%	-5.15%
S14-30-1	5.0787	0.5590	-0.1363	-0.4901	9.40%	-2.29%	-8.24%
S14-30-2	5.0787	0.2969	-0.2513	-0.5718	4.99%	-4.23%	-9.62%

* Strain gauge broke before reaching the ultimate load.

CHAPTER 5

EFFECT OF BOND ON CONFINEMENT

5.1 Background

While tests on concrete-filled tubes are few and mainly limited to those under this research project, there is an abundance of information available on fiber-wrapped columns. A comprehensive survey of literature on the fiber-wrapping technology and its various forms was assembled under Phase I (Mirmiran 1997). Although the same principles of radial pressure and concrete expansion apply to the fiber-wrapped columns as to the concrete-filled tubes, there are two differences between these types of construction which may potentially lead to different degrees of confinement effectiveness. The first and foremost important difference is related to the bond between the concrete core and the fiber composite shell. For the purpose of this discussion, the two methods can be distinguished by the bond (or lack thereof) between concrete and the jacket. Based on the mechanics of fiber composites, the following observations can be made:

1. Unbonded construction such as in concrete-filled tubes is achieved when the shell has a smooth interior surface with no mechanical or chemical bond to concrete. The debonding is further ensured by providing discontinuity with full-depth grooves in the shell near the loading platens (Mirmiran 1997). In this case, the shell is considered to be only loaded as a tension hoop band.

2. Bonded construction such as in fiber-wrapped columns or ribbed tubes is achieved when the shell and the concrete core are bonded together with epoxy or a series of mechanical shear connectors (Mirmiran 1997). In this case, even when the column is subject to uniaxial compression, the shell is biaxially loaded, i.e., in both the hoop and the axial directions. The strength of the shell will then depend on the ratio of the applied loads in the two directions. The biaxial state of stress generally lowers the fracture strength of the jacket.

Another but rather minor difference between these two methods of construction has to do with the curing of the concrete core. In the case of fiber-wrapped specimens, almost always, concrete has already cured and at the least has achieved its 28-day compressive strength before the fiber composite enclosure is placed around it. On the other hand, the concrete core in concrete-filled tubes goes through its curing process while encased in a "capsule", i.e., the composite shell. This affects its normal "breathing" process, and the outcome is generally a longer hydration process, minimal loss of moisture, and a lower shrinkage. The experiments of Phase I and II have both confirmed that some specimens even after two or three months of curing still have some trapped moisture within the core.

Once the confinement model of Phase I (Mirmiran 1977) was applied to the fiber-wrapped specimens of Nanni and Bradford (1995) and Picher (1995), it became clear that some variation of confinement effectiveness may be expected. Hence, it was decided to experimentally investigate the effect of bond on confinement. These tests replaced the pushout tests that were originally planned.

5.2 Bond Effect Tests

To evaluate the effects of construction bond on confinement, two series of compression tests were conducted. The difference between the two series is mainly in the continuity of the layered shell. In Series 1, the shell was made layer by layer with an overlapped splice of approximately 3" per layer which is about 17% of the perimeter of the 6"-diameter cylinders. For multi-layer specimens, the location of splice would vary from one layer to another. Once tested, specimens of Series 1 failed mainly at the splice of the outermost layer before reaching the ultimate strength of the fiber composite. Therefore, a second series of tests on a smaller number of specimens was planned. Two types of coupon tests were also planned; a split disk test accompanied specimens of Series 1, while a uniaxial tension test was chosen for Series 2.

Series 1

A total of 24 composite specimens with two types of construction (bonded and unbonded) and four different number of layers (1, 3, 5 and 7) were tested. For each type of construction and number of layers, three identical samples were prepared for repeatability verification. The specimens were labeled by the number of layers (1, 3, 5, or 7), letter B or UB for bonded or unbonded construction, and the sample number (A, B, or C). All specimens were made of S-glass fabric and polyester resin with a core diameter of 6" and a length of 12". The fabric was SA120 (made by Hexcel) which is a unidirectional stitched S-2 glass yarn (made by Owens Corning) with 15.5 warp per inch, 24" width, 13.0 mils nominal thickness, and 12.2 oz. per square yard aerial weight. Table 5.1 shows the manufacturer's data for the S-2 glass fibers in a unidirectional epoxy composite with 57%-63% fiber volume fraction. The resin was DION 6692T polyester with the following characteristics for clear casting at 77° F (manufacturer data): flexural strength and modulus of 15.6 ksi and 580 ksi, respectively, and tensile strength, modulus, and elongation strain of 10.4 ksi, 630 ksi, and 2.02%, respectively. The fiber volume fraction for the bonded and unbonded tubes were kept the same by calculating the equivalent weight fraction of the fibers and the resin, as below

$$\frac{w_r}{w_f} = \frac{\rho_r (1 - v_f - v_v)}{\rho_f v_f} \tag{5.1}$$

where w_r is weight of the resin, w_f is weight of the fibers, v_f is fiber volume fraction, v_v is the void ratio, ρ_f is specific gravity of the fibers taken as 1.39, and ρ_r is specific gravity of the resin taken as 2.48. The required weight of the resin (including MEKP) was calculated using a 1% void ratio and a 40% fiber volume fraction. These values were only used for the first two tubes (1UBA and 1UBB). Then, it was noticed that the amount of resin was not sufficient for the lay-up process. Also, it became clear that the 1% void ratio was not an accurate estimate. Therefore, for the remainder of the specimens, the fiber volume fraction was reduced to 37% and the void ratio was assumed to be 3%.

Table 5.1 Manufacturer's data for 57%-63% S-2 glass fiber unidirectional epoxy composite

Property	ASTM Standard	Typical Values (72° F, Dry)
Longitudinal Modulus	D3039	7,700-8,500 ksi
Transverse Modulus	D3039	2,300-2,900 ksi
Shear Modulus	D3518	900-1,300 ksi
Poisson's Ratio	D3039	0.26-0.28
Longitudinal Tensile Strength	D3039	230-290 ksi
Longitudinal Compressive Strength	D3410	100-180 ksi
Transverse Tensile Strength	D3039	6-12 ksi
Transverse Compressive Strength	D3410	16-29 ksi
Longitudinal Tensile Strain	D3039	2.7%-3.5%
Density	D792	0.071-0.073 lb/in^3

The unbonded tubes were made by wrapping layers of fabric around a 6" O.D. mandrel that was made at UCF machine shop from a 32"-long aluminum tube. It would allow making two 12" tubes simultaneously. The mandrel was made collapsible by cutting a 6" aluminum pipe into two half cylinders, and placed on a wooden dowel and two wooden disks. The half cylinders were machined to provide a ½" gap in between to facilitate the collapsing mechanism. The half cylinders were tied together by clamps at both ends. The fabrication sequence consisted of cutting the 24"-wide fabric into 12"x22" sheets (12"x21" for the first two tubes, i.e., 1UBA and 1UBB), weighing the resin to the right amount, mixing with 1.5% (by volume) MEKP, placing the sheet on a wax paper, applying and spreading about 85% the resin on the sheet, wrapping the sheet around the mandrel, and finally, applying the remainder of the resin onto the sheet. A roller was used to remove air voids from the sheet before placing the next layer. The procedure was repeated for the desired number of layers. For multi-layer specimens, the location of splice would vary from one layer to another.

Figure 5.1 shows the mandrel with two of the wrapped tubes. The tubes would be left on the mandrel to cure for 24 hours. The mandrel would then be collapsed and the tubes removed. Casting was performed at UCF on April 7, 1997. Concrete was ready mix as delivered from Rinker with a target strength of 4,000 psi, a slump of 4", and maximum aggregate size of 1" (DOT #57). However, the initial slump was only 1". Before the concrete was used in any of the specimens, 2 gallons of water was added to the 1 cubic yard of concrete in the mixer truck. Even then, the final slump that was taken after all specimens were cast was about 1½"-2". Three (3) control specimens were made of the same batch to determine the average strength of concrete core. It was noted that some water was seeping out of the thin 1-layer tubes, indicating the presence of some voids in the construct of the tube. This was not the case for the thicker tubes. The cylinders were wetted for three days, then brought inside the lab. The plastic molds and the nylon sheets were removed after 7 days. The cylinders for the bonded specimens were wrapped with the fabric on May 5-7, 1997 at the age of 28-30 days. Wrapping of the cylinders was performed much in the same way as on the mandrel, except that the surface of concrete was saturated with the resin before the first layer was applied. This was to ensure a proper bond, and to further avoid any loss of resin in the first layer of the wrap.

Only the unbonded specimens were grooved near the top and bottom end surfaces similar to the filament-wound tubes. It was later noticed that a couple of thicker tubes (7UBA) were not grooved deep enough. However, that appeared not to have affected the results. All bonded and unbonded specimens were capped with sulfur mortar prior to testing, the same as the filament-wound tubes. All specimens were instrumented with 4 TML (PL-60) strain gauges (60 mm gauge lengths), two in the horizontal and two in the vertical directions, placed at 180° opposite from each other at mid-height of the specimen. Also, three LVDTs were used for each specimen to measure the average axial strains. Control cylinders were only instrumented with LVDTs. In addition, two AE sensors were placed at mid-height of each specimen, 90° across from the strain gauges, to record the acoustics emission of the specimens. Results of AE tests are presented in Chapter 7.

All specimens of this series were tested on May 20-22, 1997 at the FDOT Structures Lab at the age of 43-45 days. All specimens but 4 of the 7-layers (7BB, 7BC, 7UBB, 7UBC) were subjected to a monotonic uniaxial compression loading at a rate of 0.22 inch per minute. Tests were conducted using a 550-kip MTS machine, and data were recorded by a Mega DAQ data acquisition system. Figure 5.2 shows the test setup and one of the composite specimens with full instrumentation. Once it was noticed that the 7-layer specimens would not fail within the capacity of the testing machine, they were subjected to 3 cycles of loading and unloading at the same rate as the initial loading.

Figures 5.3-5.8 show the failed unbonded and bonded specimens with 1, 3, or 5 layers of the fabric. The failure in almost all specimens initiated by the formation of a narrow band or ring as a result of the shearing off and separation of the fabric in the hoop direction. Some specimens failed with simultaneous band separations rather than a single major one. The band-width was in the order of 1/8" to 2½". The band was formed at the location of maximum stress concentration and the least confinement. This was generally at the mid-height of the specimen. Once the band was formed, delamination at the splice would result in the snapping of the ring and a slippage in the order of ½" to 1½". The slippage was marked on the specimens by a black ink marker as shown in Figures 5.5 and 5.7. Specimens 3UBA and 5UBC were severed in two, and large chunks of rock could be seen inside the two halves (Figures 5.5 and 5.7). Except for the 1-layer bonded specimens (Figure 5.4), and Specimen 1UBC (Figure 5.3), no other specimen failed by a marked fiber rupture. This was attributed to the bond failure at the splice being the primary cause of failure. Some of the specimens such as 3UBB (Figure 5.5) did not show a clear sign of failure, however, resulted in a considerable drop of the load. It should be noted that the failure was not at all the same as those seen in the past for the filament-wound tubes. It was then concluded that since fiber rupture was not present, the specimens must have failed at loads somewhat lower than their full capacity. This was attributed to the 0° orientation of the fibers, i.e., hoop direction. Also, the short splice length and/or insufficient resin within the splice length could be considered as the cause for the observed mode of failure. The patches of high stress concentration were not as significant as those in the filament-wound tubes such

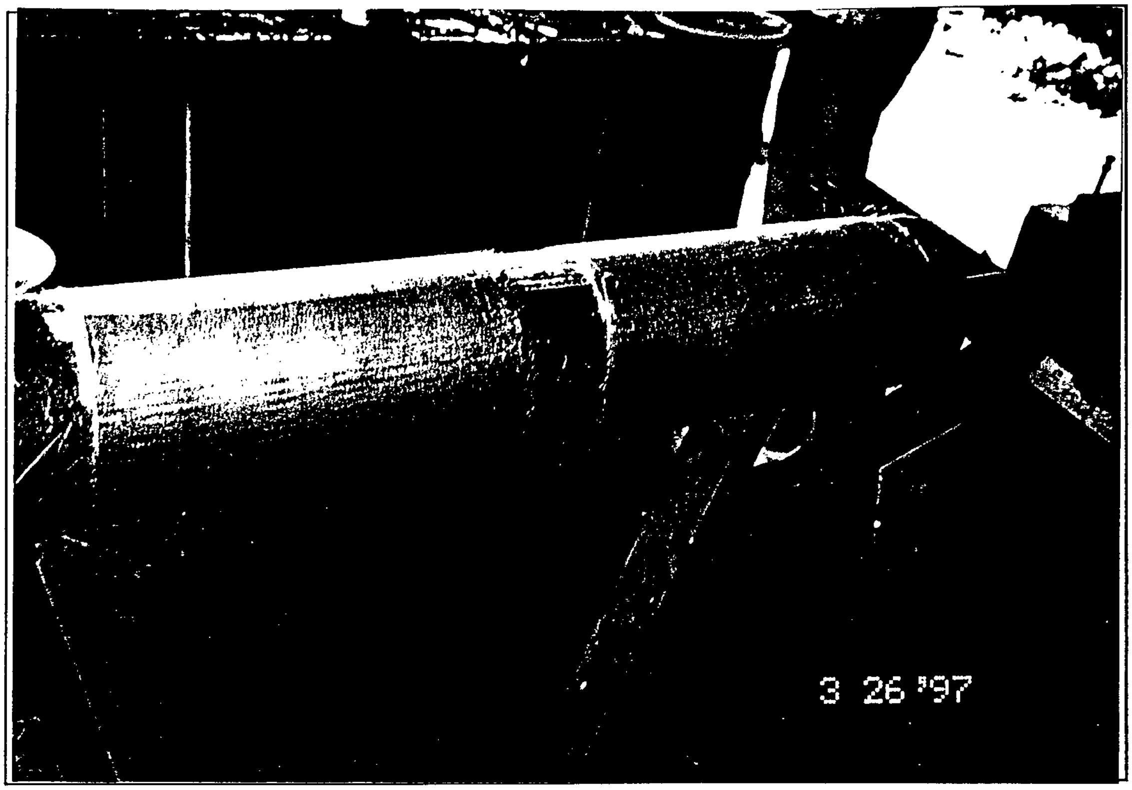

Figure 5.1 Collapsible mandrel with two S-glass tubes

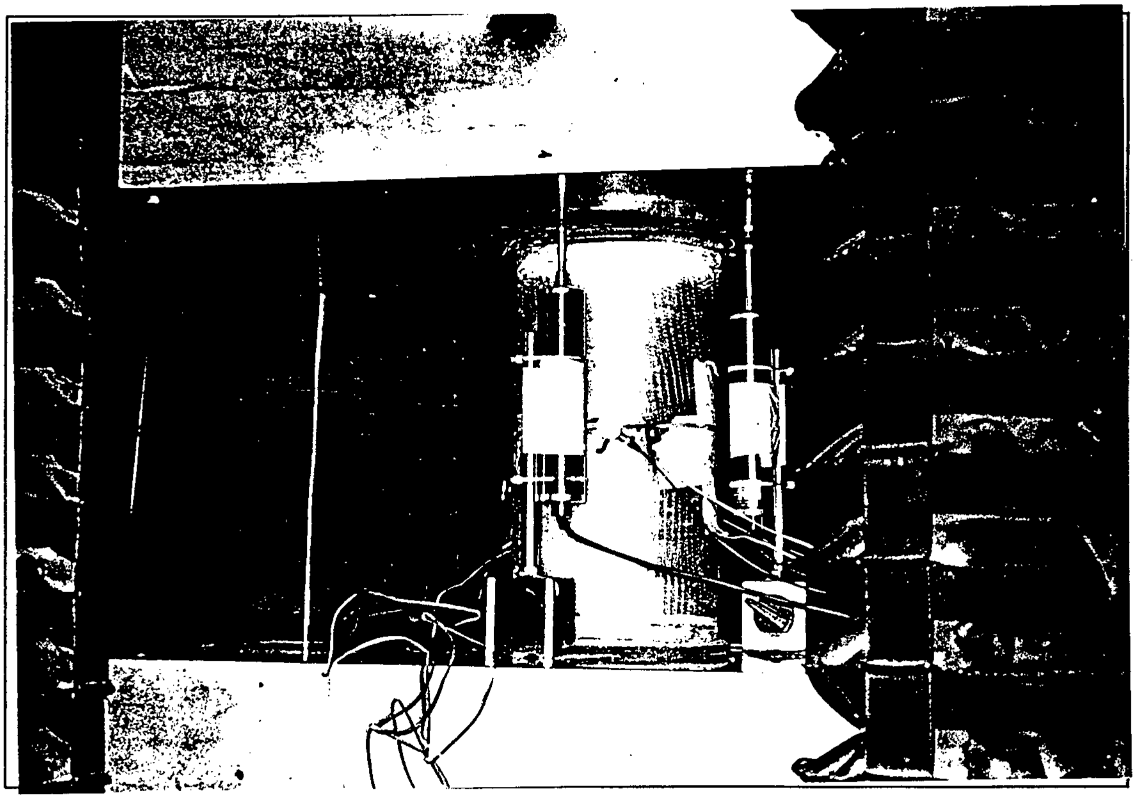

Figure 5.2 Test setup and instrumentation

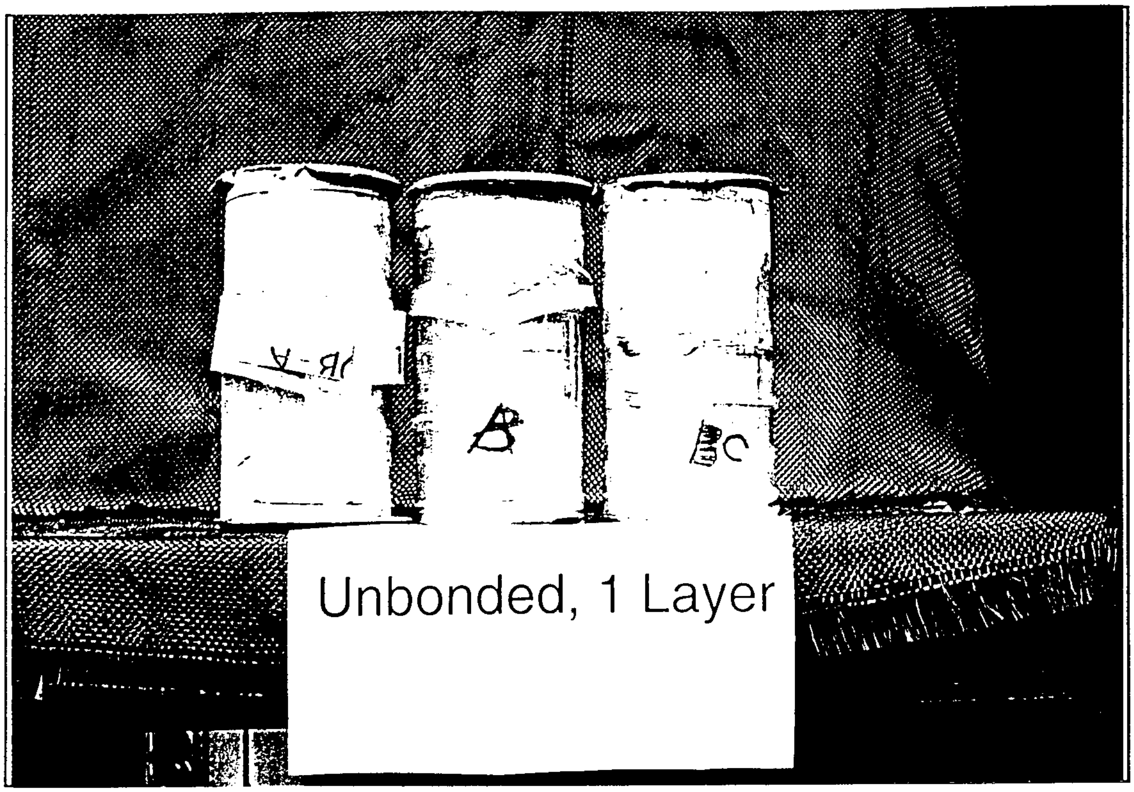

Figure 5.3 Failure of 1-layer unbonded specimens

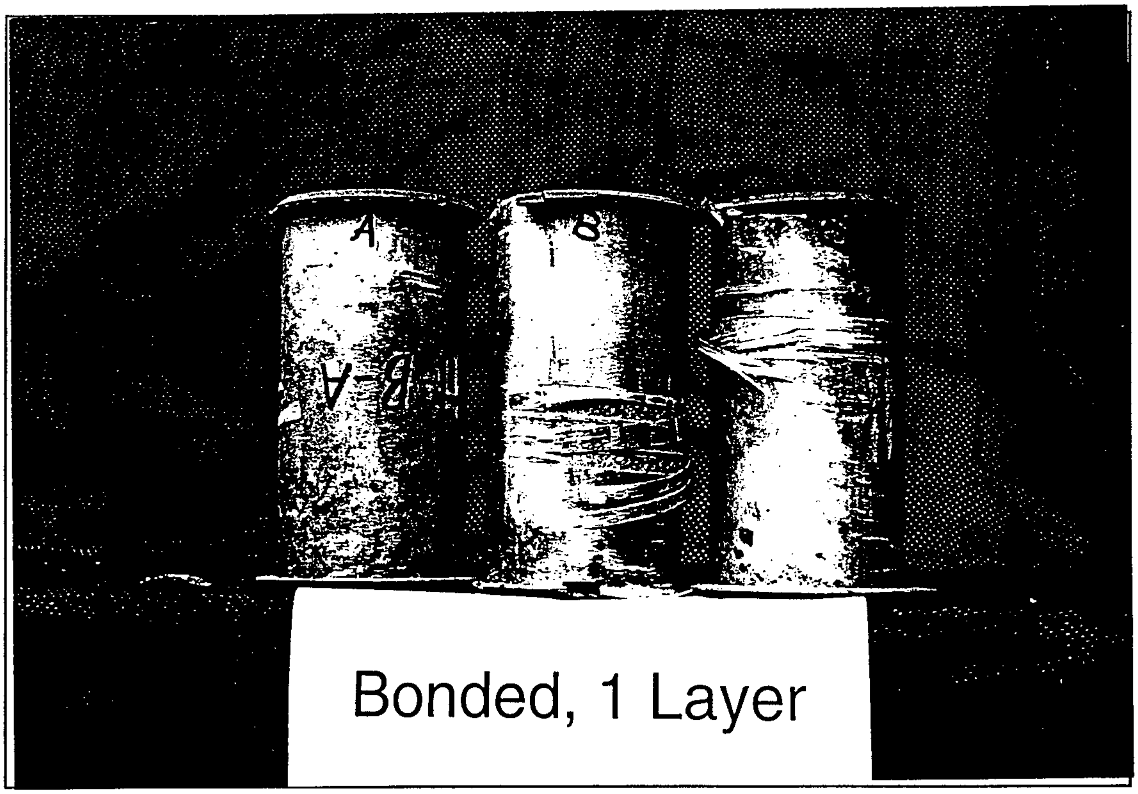

Figure 5.4 Failure of 1-layer bonded specimens

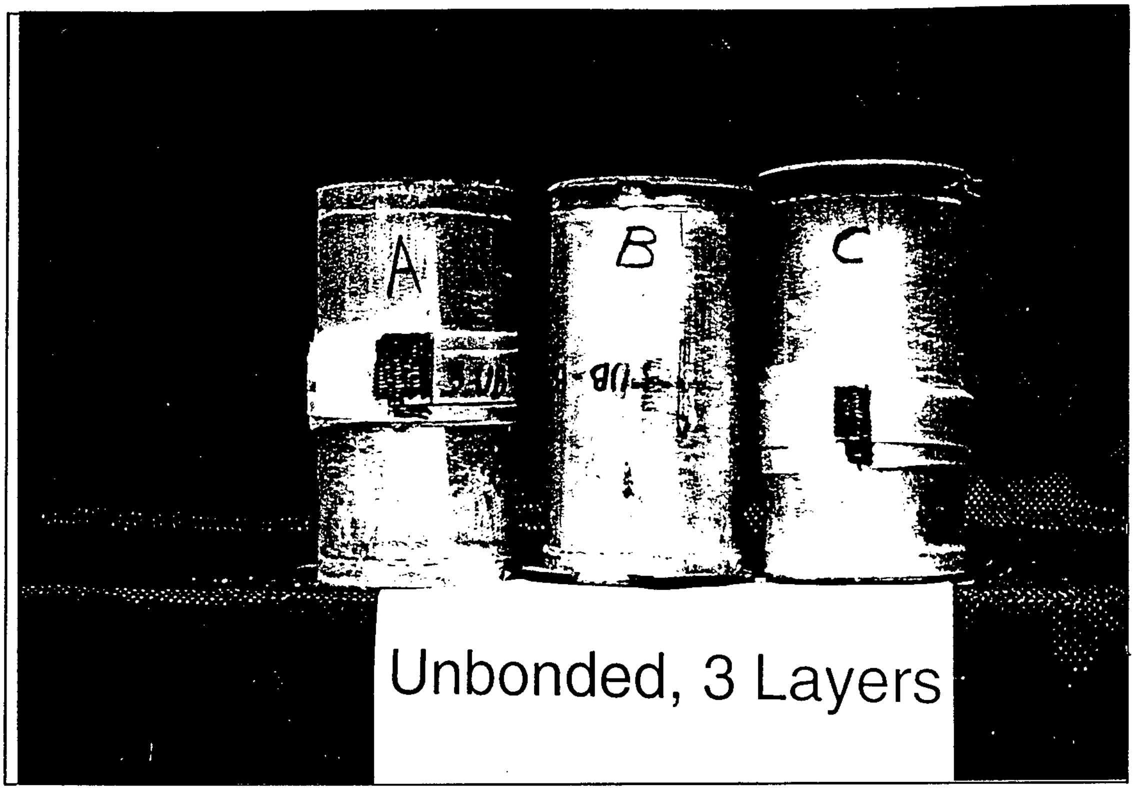

Figure 5.5 Failure of 3-layer unbonded specimens

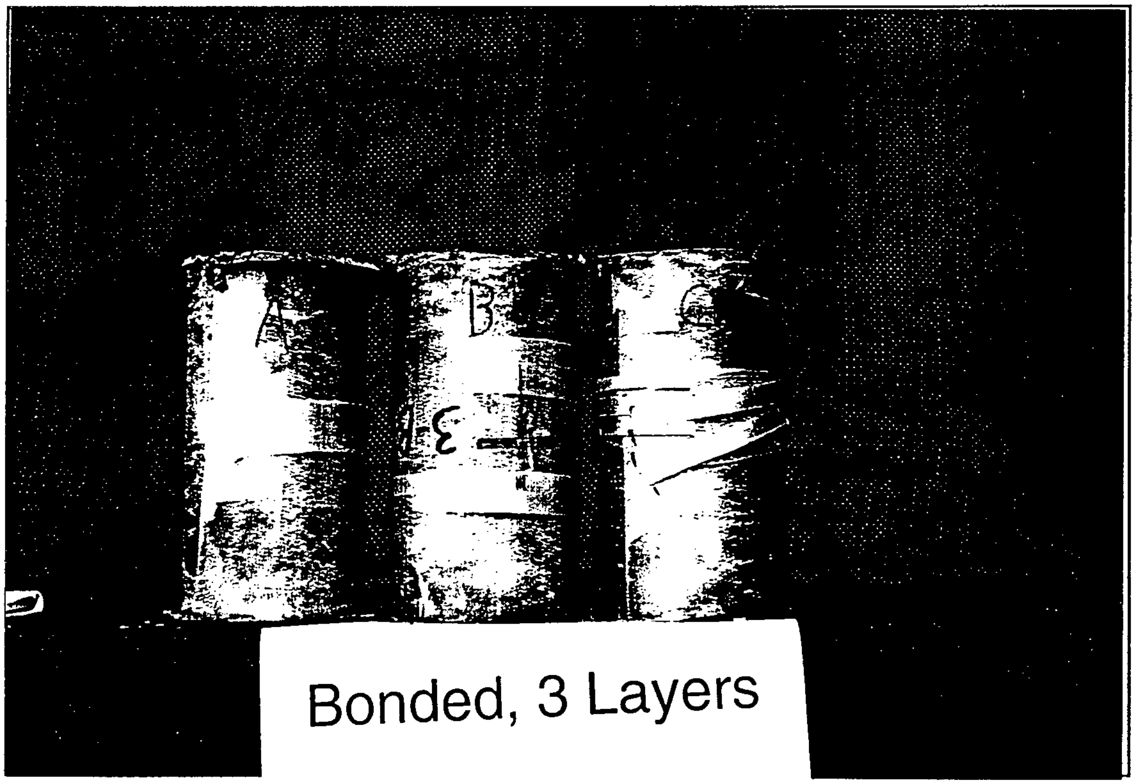

Figure 5.6 Failure of 3-layer bonded specimens

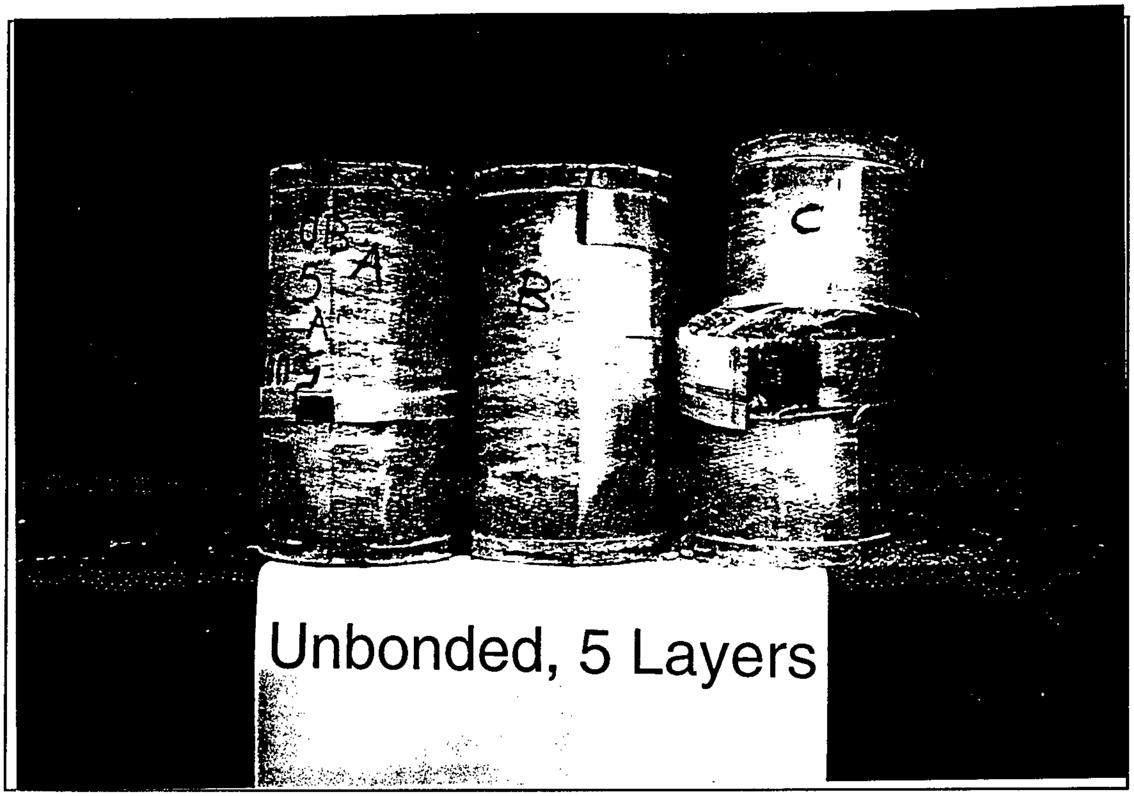

Figure 5.7 Failure of 5-layer unbonded specimens

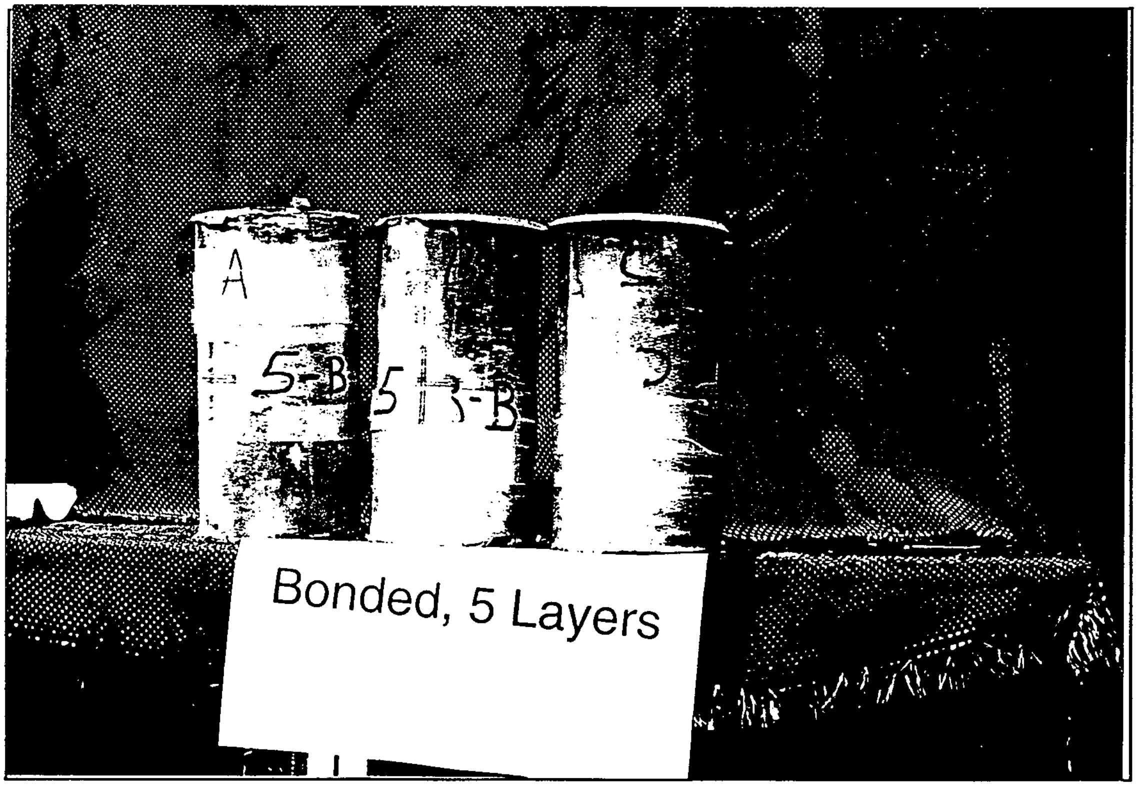

Figure 5.8 Failure of 5-layer bonded specimens

as those reported in Chapter 4, perhaps because of the color of the resin. However, sounds heard during various stages of loading were not much different from those reported in Chapter 4. Failure, while sudden, was physically detectable and predictable. No form of violent failure was observed. Location and extent of failure for each specimen is indicated in Table 5.2, along with the test results.

Table 5.2 Test results for bond effect specimens

Specimen No.	L (in.)	f'_{cu}* (ksi)	f'_{cc}* (ksi)	ϵ_{cu}	ϵ_{ru}	Mode of Failure
Control 1	12.313	4.23			-	-
Control 2	12.313	4.36			-	-
Control 3	12.438	4.38			-	-
1UBA	12.438	4.25	4.50	0.010	-0.018	splice failure, mid-height
1UBB	12.313	4.76	4.94	0.013	-0.019	splice failure + fiber rupture
1UBC	12.125	3.87	5.16	0.015	-0.011	fiber rupture
1BA	12.313	4.47	4.88	0.010	-0.021	fiber rupture
1BB	12.375	3.77	4.81	0.023	-0.023	fiber rupture + splice failure
1BC	12.313	4.14	4.82	0.020	-0.016	fiber rupture + splice failure
3UBA	12.125	9.14		0.027	-0.021	splice failure, split in half
3UBB	12.156	7.11		0.018	-0.009	bond slippage, no other distress
3UBC	12.438	8.51		0.030	-0.015	splice failure, ½" separation
3BA	12.188	9.14		0.027	-0.021	splice failure, 2" band at top
3BB	12.313	9.45		0.030	-0.018	splice failure, two 2" bands
3BC	12.313	9.46		0.028	-0.005	splice failure, 2½" middle band
5UBA	12.438	12.59		0.033	-0.015	splice failure, 1" separation
5UBB	12.250	12.81		0.036	-0.019	splice failure at the top
5UBC	12.188	13.58		0.038	-0.017	splice failure, 2½" separation
5BA	12.188	13.59		0.043	-0.020	splice failure, ½" separation
5BB	12.250	13.38		0.039	-0.021	splice failure, 2" middle band
5BC	12.438	13.99		0.044	-0.019	splice failure, two 2" bands
7UBA	12.000	15.83 ‡		0.037	-0.015	-
7UBB	12.188	16.22 ‡		0.038	-0.020	-
7UBC	12.250	16.07 ‡		0.052	-0.016	-
7BA	12.375	16.24 ‡		0.047	-0.016	-
7BB	12.438	16.12 ‡		0.040	-0.018	-
7BC	12.375	16.14 ‡		0.039	-0.018	-

* f'_{cu} is the ultimate stress while f'_{cc} is the peak stress. This is only reported for the 1-layer specimens that had a descending branch in their stress-strain curves.

‡ The 7-layer specimens did not fail, and these values are only the maximum stresses they sustained.

As indicated earlier, the 7-layer specimens did not fail within the capacity of the testing machine. Therefore, 3 cycles of loading and unloading were applied which did not result in any failure either. To examine the difference between the bonded and unbonded construction, and to examine the status of the concrete core, the jacket was removed from two of the specimens (7UBC and 7BA) by an electric handsaw. Figure 5.9 shows the concrete core for the unbonded tube. The tube separated with no sign of distress. The concrete core, however, had horizontal cracks and split in two halves when dropped on the floor. Figure 5.10, on the other hand, shows that the jacket for the bonded tube does not separate from the concrete core that easily, and in fact as soon as the stresses in the jacket are released, concrete core cracks circumferentially, and the exterior portion of the core remain attached to the tube.

Figure 5.11 shows the stress-strain curves of the bonded and unbonded specimens with 1, 3, 5, and 7 layers. In this figure, axial stress is plotted against axial and radial strains. Each curve is an average of three samples (A, B, and C) with the same type of construction and the same number of layers. The stress-strain curves for the 3,5, and 7-layer specimens have the same bilinear shape as those observed in Phase I (Mirmiran 1997). However, it appears that for the 1-layer specimens, the confinement provided was not sufficient to enhance the strength of the concrete core, as a descending branch is present in their response. The figure shows no marked difference between the response of the bonded and unbonded specimens. The maximum difference appears to be for the 7-layer specimens. Also, note that the stress-strain curves of the 7-layer specimens do not represent the ultimate strength as they did not fail within the capacity of the machine. Figure 5.12 shows the lateral versus axial strains. The maximum difference exists between the bonded and unbonded specimens with 7-layer jackets. Figure 5.13 shows the volumetric strain versus axial strains. It is clear that 5-layer jackets effectively restrain the dilation of concrete core. A similar trend can be seen from the plots of axial stress versus volumetric strains in Figure 5.14. Finally, Figure 5.15 shows the dilation rate versus axial strains. Despite some variations, as the number of layers increases, the peak and ultimate dilation rates both decrease.

Split-disk Coupon Tests

To establish the tensile strength of the jacket, five (5) rings of each tube thickness (1, 3, 5, and 7 layers) were tested by the same split disk method as in Phase I (Mirmiran 1997). The ring specimens were cut by a table saw from an extra tube that was made along with the unbonded tubes of Series 1. All specimens had a nominal width of 1". The actual measurements of all specimens are listed in Table 5.3, along with the test results. Of the five samples for each thickness, only one was instrumented with strain gauges, while for the remainder of the specimens only the load and head movement of the machine were monitored. Tests were conducted at the FDOT Structures Lab on May 23, 1997. Table 5.3 also shows the mode of failure for each specimen. Nearly all specimens, with the exception of the 7-layer rings, split longitudinally at failure. Further evaluation of the results for these tests will be reported separately (Mastrapa 1997) or in the final version of this report once the uniaxial tension tests are completed and compared with the split-disk test results.

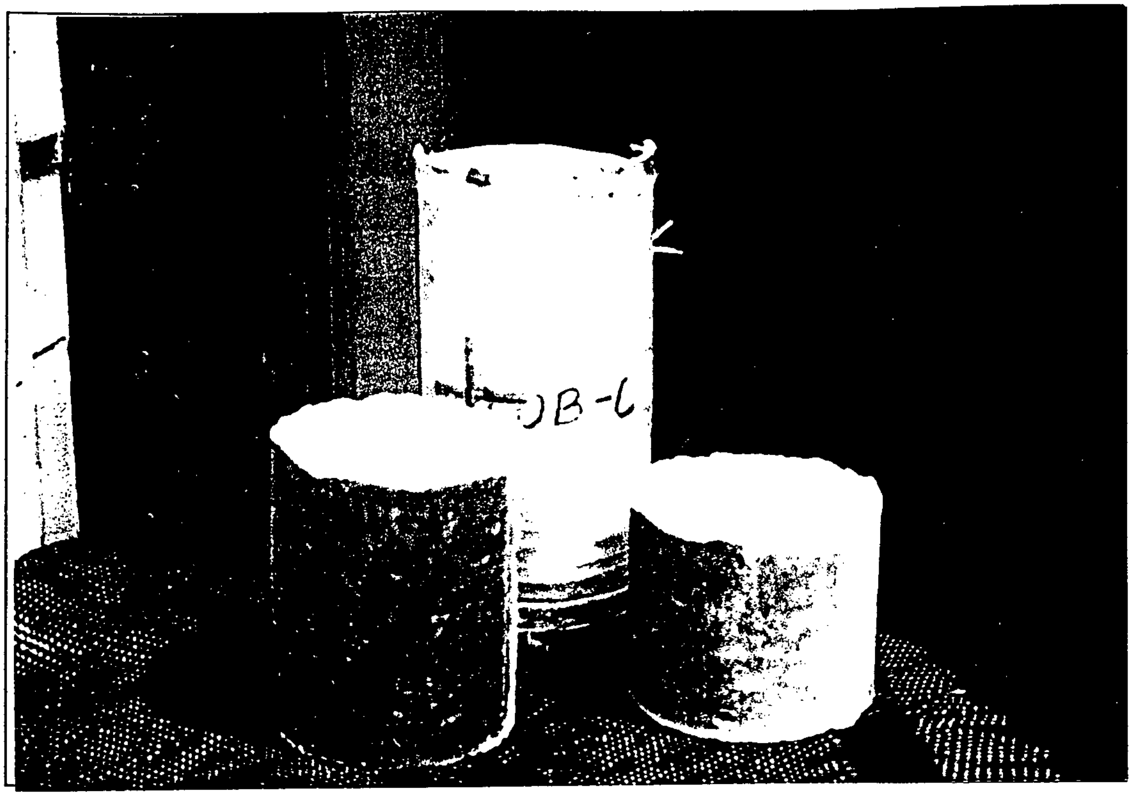

Figure 5.9 A 7-layer unbonded specimen after removal of the jacket

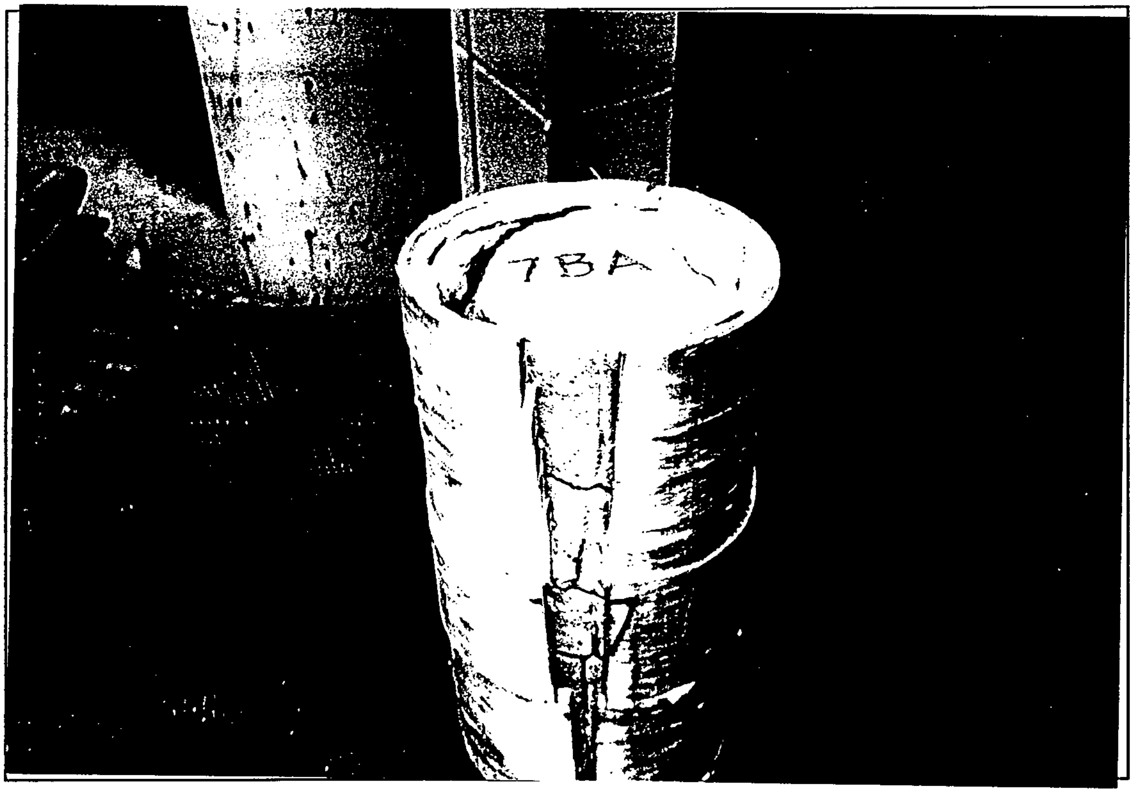

Figure 5.10 A 7-layer bonded specimen after removal of the jacket

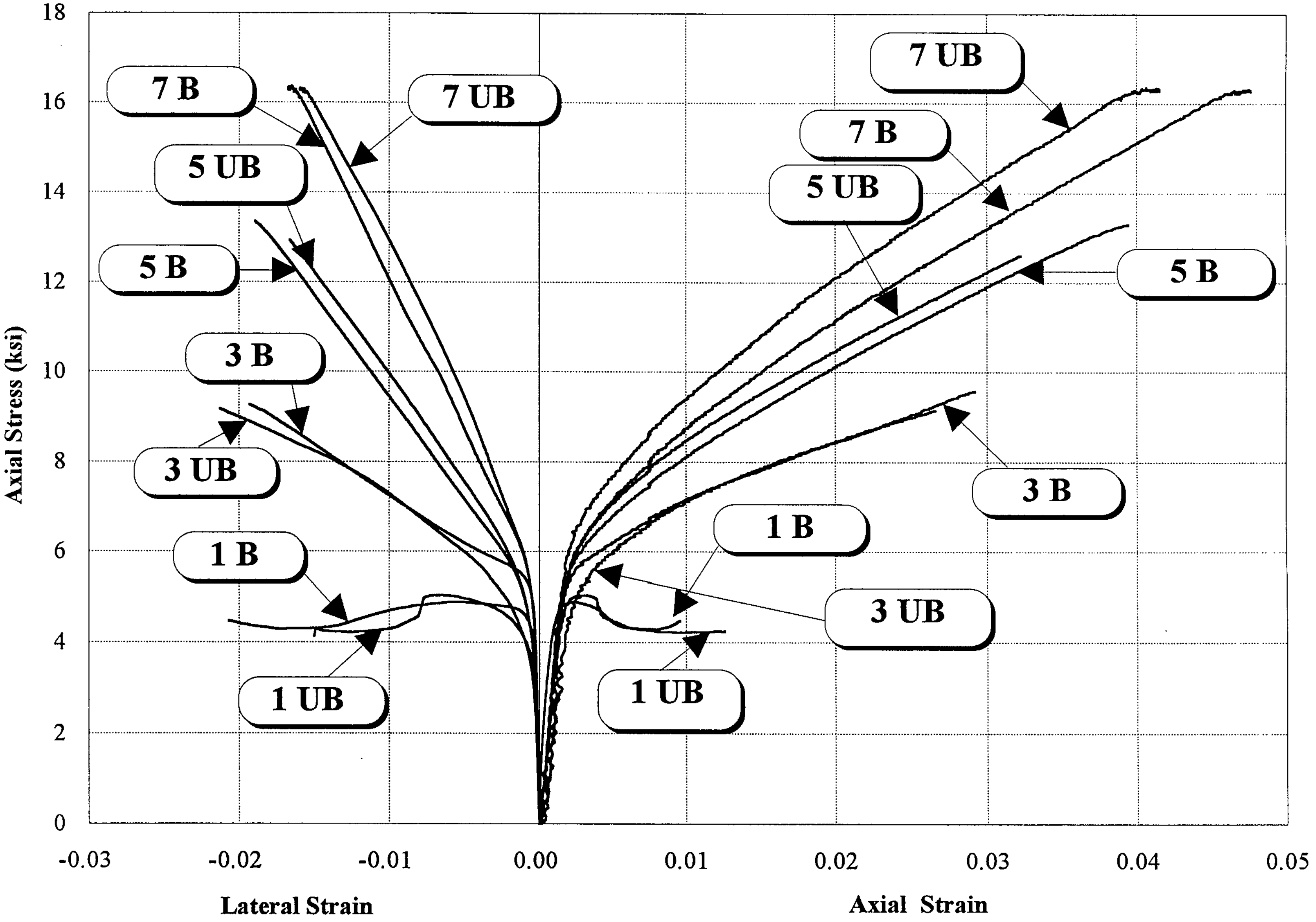

Figure 5.11 Stress-strain curves for bonded and unbonded specimens

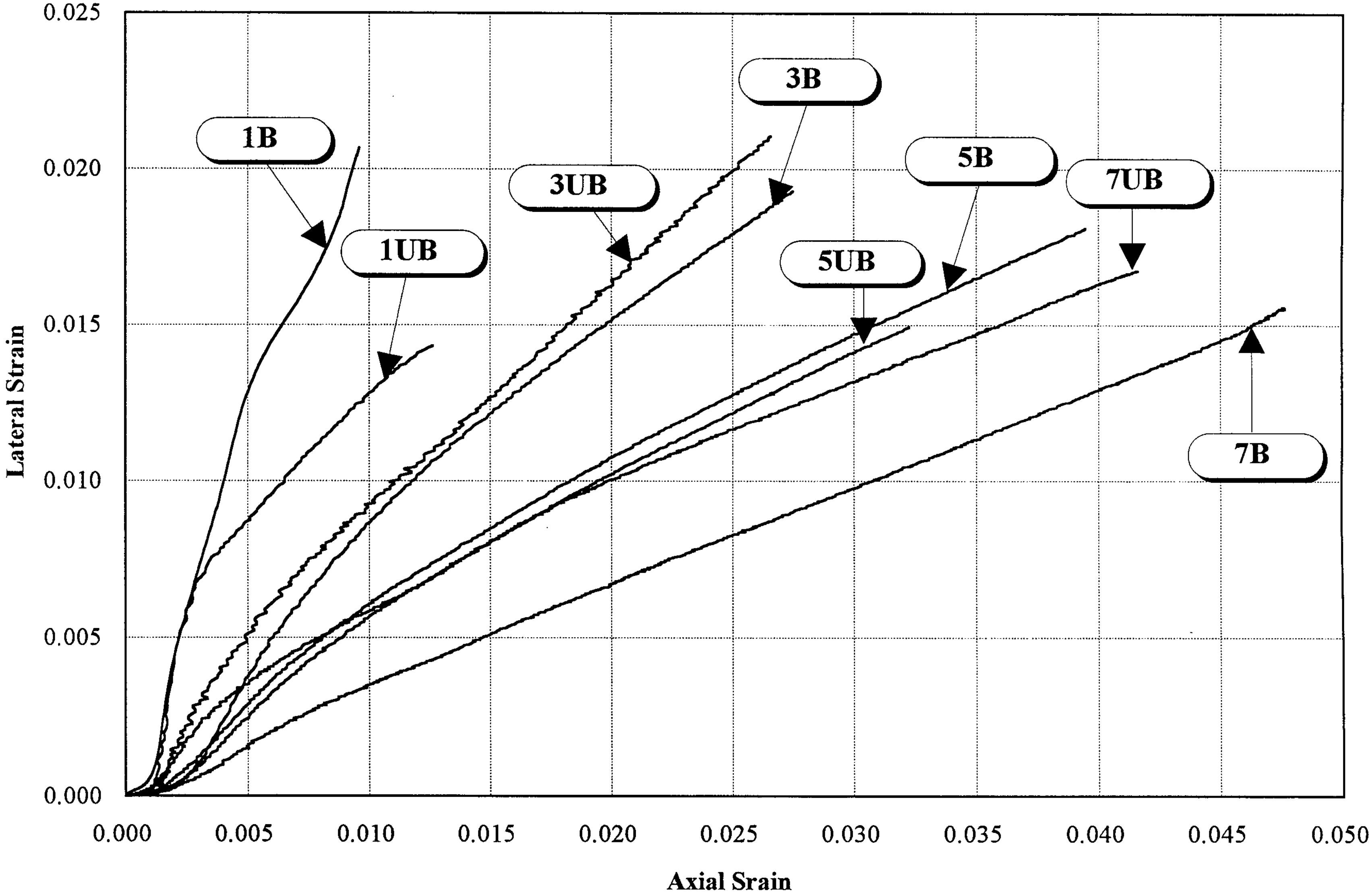

Figure 5.12 Lateral strain versus axial strain

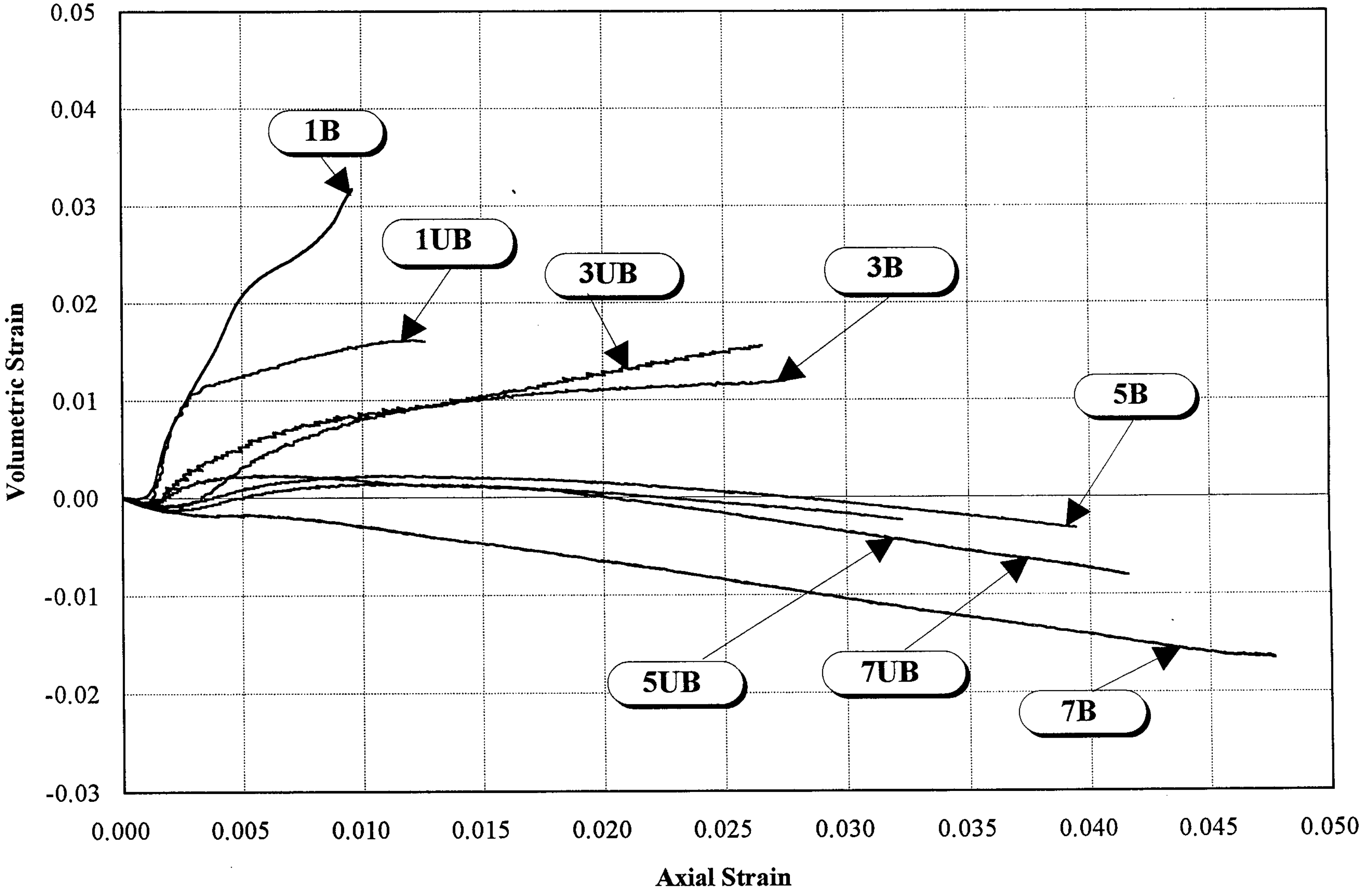

Figure 5.13 Volumetric strain versus axial strain

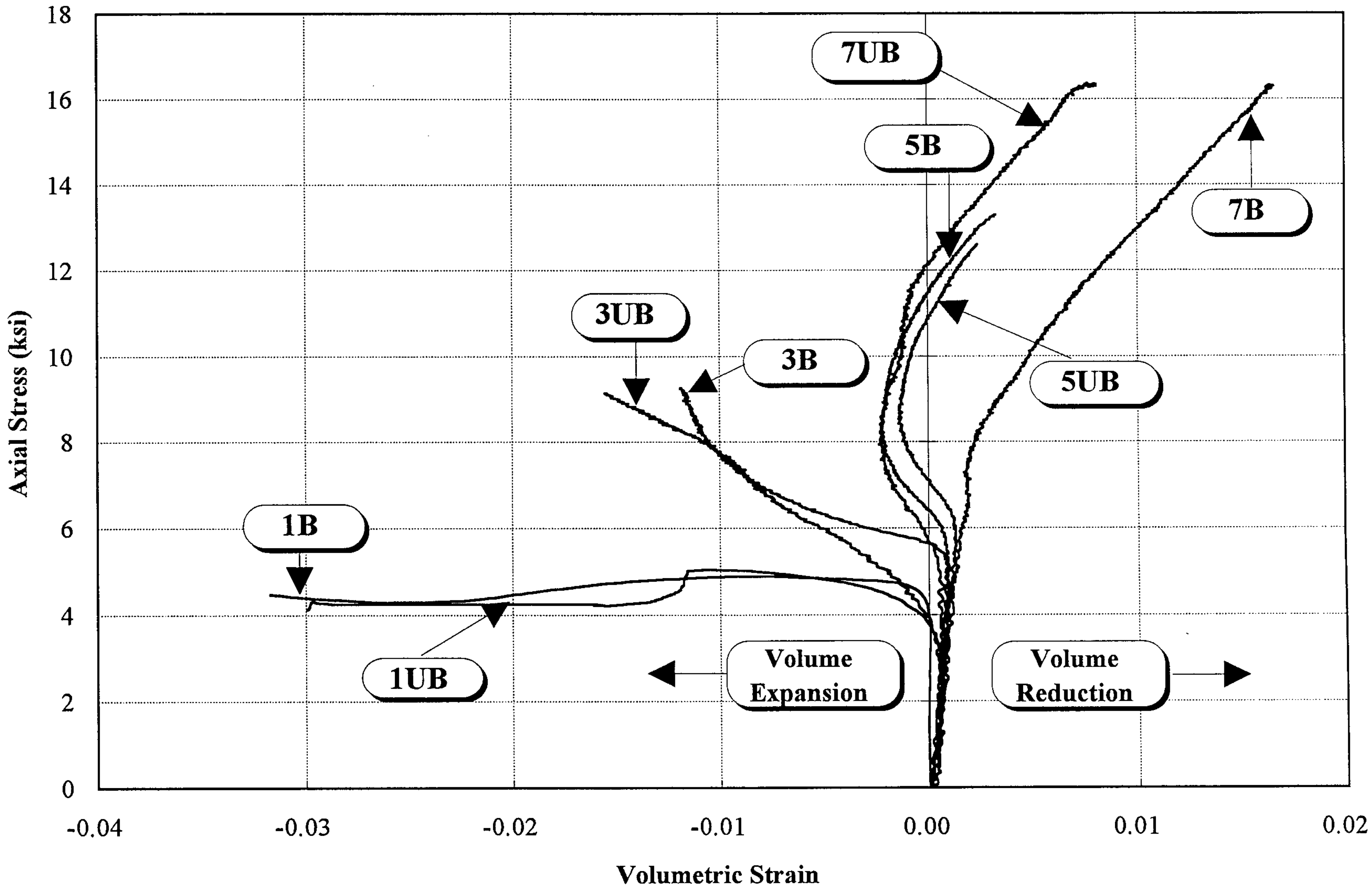

Figure 5.14 Axial stress versus volumetric strain

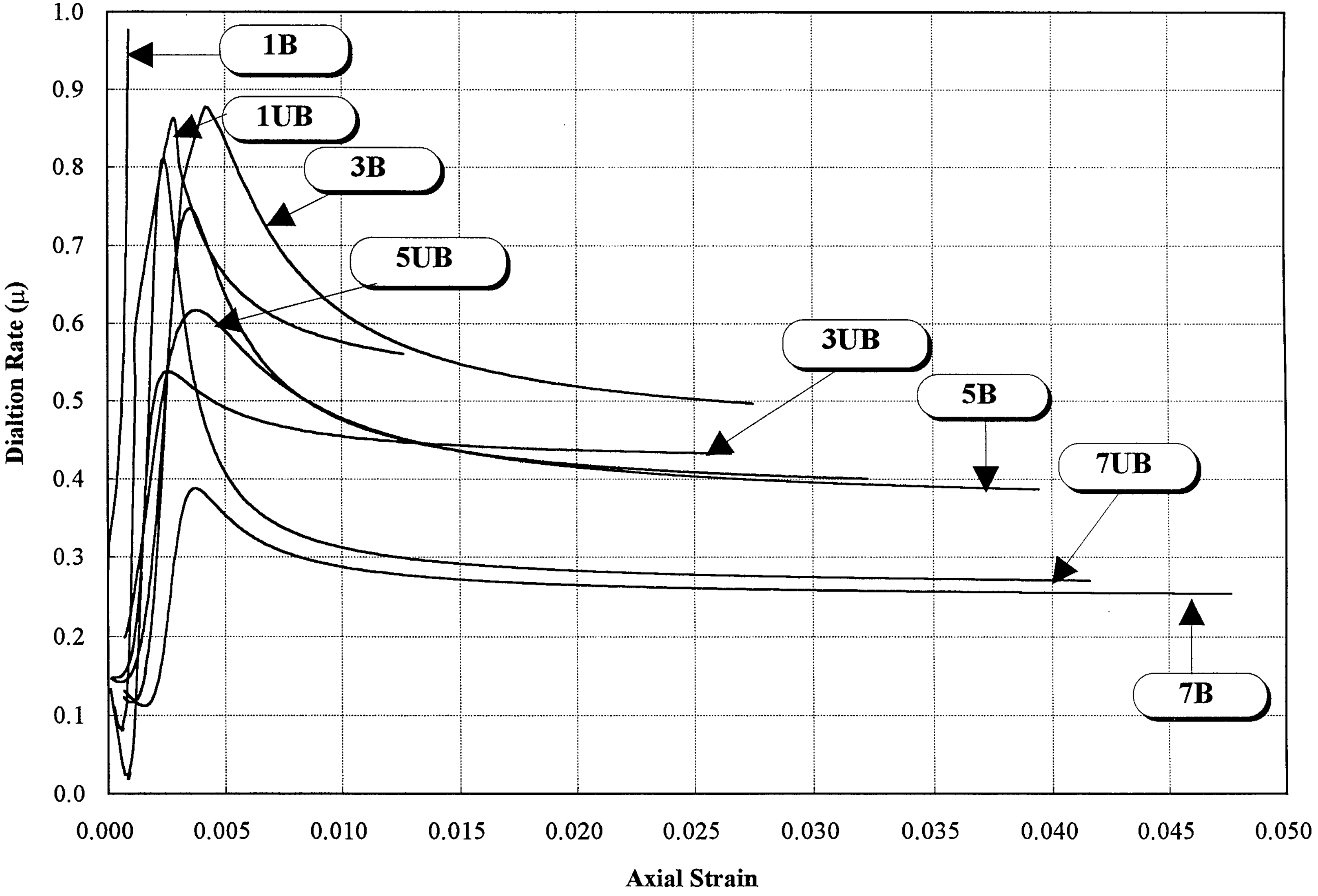

Figure 5.15 Dilation rate versus axial strain

Table 5.3 Split-disk test results

Specimen No.	Width (in.)	Thickness (in.)	Max. Load (kip)	Max. Deflection (in.)	Failure Mode
1-A	0.968	0.025	3.241	0.310	delamination at splice
1-B	0.983	0.028	3.291	0.329	delamination at splice
1-C	0.894	0.028	2.069	0.278	delamination at splice
1-D	0.894	0.028	3.322	0.284	delamination at splice
1-E	0.945	0.027	3.153	0.277	mode of failure not recorded
3-A	1.029	0.068	10.572	0.326	delamination at in/outside splice
3-B	1.025	0.069	9.560	0.331	fiber rupture on west side
3-C	1.013	0.072	13.022	0.382	fiber rupture on west side
3-D	0.978	0.068	10.853	0.308	delamination at splices
3-E	0.990	0.068	10.925	0.345	fiber rupture on west side
5-A	0.996	0.117	21.278	0.409	fiber rupture on east side
5-B	0.982	0.118	21.378	0.410	fiber rupture on east side
5-C	0.981	0.136	17.247	0.333	fiber rupture on west side
5-D	1.010	0.139	23.091	0.423	fiber rupture on east side
5-E	1.007	0.124	20.647	0.402	fiber rupture on west side
7-A	1.008	0.155	29.231	0.479	fiber rupture on west side
7-B	1.006	0.200	30.925	0.359	fiber rupture on west side
7-C	1.003	0.154	25.562	0.354	fiber rupture on east side
7-D	0.999	0.162	27.516	0.440	fiber rupture on east side
7-E	1.009	0.151	25.063	0.393	fiber rupture on west side

Series 2

Since the specimens of Series 1 generally failed at the splice, it was decided to conduct another set of experiments in which the splice will not be the primary source of failure. Since 1-layer specimens failed with no strain hardening, and 7-layer specimens did not fail within the capacity of the testing machine, only the 3- and 5-layer specimens were considered. A total of 8 composite specimens with two types of construction (bonded and unbonded) and two different number of layers (3 and 5) were prepared. For each type of construction and number of layers, two identical samples were prepared for repeatability verification. The specimens were labeled with the letter R (for revised), number of layers (3 or 5), letter B or UB for bonded or unbonded construction, and the sample number (A or B). All specimens were made of the same fabric and resin as those described for Series 1. The only difference being that the layers were made of a continuous roving with a total overlap of 6" which amounted to about 32% of the perimeter of a 6"-diameter cylinder. Therefore, the fabric were cut into 12"x63" for the 3-layer specimens and 12"x101" for the 5-layer specimens. Since some dryness was noticed in the specimens of Series 1, it was decided to increase the amount of resin in the specimens of Series 2. Therefore, the fiber volume fraction and the void ratio for this series were set at 34% and 3%, respectively.

The fabrication process was similar to that of Series 1 with some minor adjustments for the placement of the fabric onto the roller. First, the fabric was placed on a long wax paper, and then the resin was applied and spread on the fabric, while the mandrel was being rolled on to the fabric, and the fabric being wrapped around it. The specimens were left to cure for 24 hours before removing from the mandrel. The concrete mix was designed with a water-to-cement ratio of 0.49 (by weight) for a 28-day compressive strength of 4000 psi, and a slump of 4". The quantity of materials per cubic yard of the mix was: 598.0 lb cement, 293.4 lb water, 1080.9 lb sand, and 1804.2 lb gravel. No additives were used. Concrete was cast on July 9, 1997 at UCF using a single batch made in a 9 cubic-foot rental mixer. Three control cylinders were also made for the strength tests. The slump was measured to be approximately 6". Exposed surface of the specimens were wetted daily for three days, after which, all specimens were brought inside the lab.

The bonded specimens were made much in the same way by rolling the concrete cylinder over the fabric that was cut to the required length based on the desired number of layers. Wrapping is to be performed on August 4, 1997 at the age of 26 days, and the uniaxial compression tests are to be conducted at the FDOT Structures Lab on August 6, 1997 at the age of 28 days. Test procedure and the instrumentation are the same as in Series 1. However, results from this series are reported separately (Mastrapa 1997).

Uniaxial Tension Coupon Tests

It has been established that ring tests (split-disk tests) can cause excessive flexural and torsional stresses which result in some inconsistencies in the determination of the strength and stiffness of coupon specimens. Therefore, it was decided to evaluate the strength and stiffness of the 3 and 5 layer specimens in a uniaxial tension test similar to that reported by Garmestani (1997) for the carbon fiber composite. The method consists of preparing 4 samples of 12"x3" specimens for each of the 3 and 5 layer laminates. Of the 6" length, 3" at each end is a gripping tab that is made of the same material as that being tested. Therefore, the overall thickness at the location of the tabs is three times the thickness at the middle portion which is to be tested. Figure 5.16 shows the specimen-tab geometry for the tension coupon tests. These coupon specimens are to be made on August 4, 1997, and are to be tested in uniaxial tension at the FDOT Structures Lab on August 5 and 6, 1997. Results from these tests are reported separately (Mastrapa 1997).

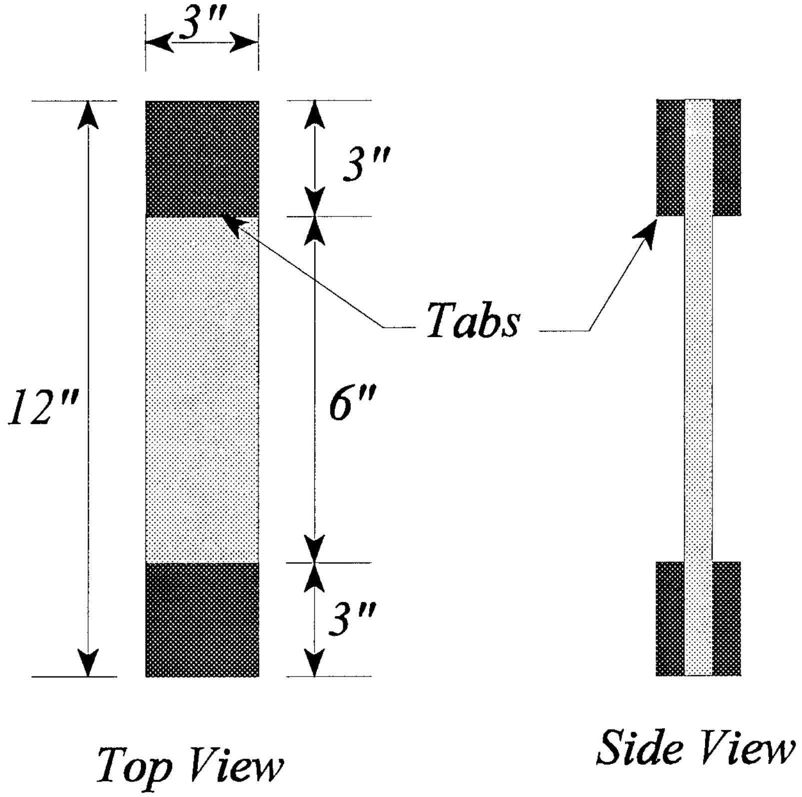

Figure 5.16 Specimen-tab geometry for the tension coupon tests

CHAPTER 6

COST OPTIMIZATION

6.1 Literature Review

When designing a structural member for practical purposes, cost effectiveness is always of paramount concern. While for homogenous members, minimizing the cross-sectional area often results in a more cost-effective design, hybrid members need to be designed with a more detailed optimization scheme. The composite FRP-concrete column is composed of a concrete core cast in an FRP tube with both axial and hoop fibers. For any given axial load and bending moment, a variety of combinations of these materials exist that can satisfy the design requirements. It is important to find the most optimum proportions of concrete, axial fibers, and hoop fibers, based on safety and cost. Since fibers are significantly more expensive than concrete, one might propose to maximize the area of concrete core, while utilizing the minimum amount of fibers. This would make sense if only the materials contributed to the cost of the column. Materials, however, are not the only factor. Weight of the column is also a contributing factor. If the concrete core is made so large as to substantially increase the weight of the column, it could affect cost of other supporting members such as the foundation. The idea then is to create an FRP composite column that promotes cost effectiveness based on two parameters, cost of materials and weight per pound of column.

A small sampling of previous work on optimization of beam-columns is offered here. Kanagasundaram and Karhaloo (1991) developed a program to design reinforced concrete structures for a minimum total cost of concrete, steel, and formwork. The cost function incorporated several design requirements, such as fire resistance, strength, serviceability, and durability. The program provided a feasible range of solutions within the design constraints of Australian standards. Reddy, Gupta, and Singh (1993) developed a two-stage optimization technique. The first stage developed a minimum cost function based on the costs of steel, concrete, formwork and labor. The second stage involved incorporating the cost function with several inputs including specific rules and regulations, purpose of structure, shape, and other design criteria. The program proved to be helpful in providing an optimum solution at the conceptual stage of design. Chakabakarty (1992) addressed the issue of there being many beam dimensions and reinforcement ratios for a given resisting moment. An optimization model, therefore, was developed to give the least cost design of a beam. The model was based on parameters for cost of materials, shuttering and structural requirements. Results showed that there are large variations in cost depending upon the values for the aforementioned parameters. Under Phase I (Mirmiran 1997) the optimum winding angle for concrete-filled FRP columns with and without composite action was studied. It was shown that the optimum winding angle is a function of eccentricity of the applied load, and the bond between the two materials.

6.2 Cost Optimization Program

Two computer models were developed for this study. The first, a sensitivity model, was a spreadsheet module to show theoretical characteristics of FRP-encased concrete columns, and effects of various geometric and material properties on their behavior. The second was a FORTRAN program that modeled the optimization scheme. Following assumptions were made for both models:

1. Perfect bond, i.e., full strain compatibility, exists between the FRP tube and the concrete core. The bond may be provided by, for example, a set of shear connectors;
2. Concrete does not contribute to the tensile strength of the section;
3. Properties for axial fibers under compression are the same as those in tension. This assumption, although not exactly accurate, is a good approximation since axial fibers are prevented from buckling by the concrete core and the hoop fibers; and
4. Any fiber orientation can be effectively resolved into axial and hoop fibers (0° and 90°). This may be accomplished by Classical Laminate Theory (see for example Kargahi 1995).

Both programs were based on Mander's model with an energy balance approach (Mander et al. 1988). While it has become apparent that Mander's model does not provide accurate results for concrete columns confined by fiber composites, for the purpose of cost optimization, it was decided to use the model for its simplicity. It should be noted that University of Arizona and University of California, San Diego have both used this model for their investigations of fiber-wrapped columns. Details of this model can be found in Scherer (1996) and Kargahi (1995).

Sensitivity Model

The primary function of this model was to perform a sensitivity analysis to show how the variations of hoop and axial fiber reinforcements and column diameter affect the moment capacity and curvature of fiber-jacketed columns. The model divides the column cross-section into multiple differential layers and calculates the strain, stress, force, and moment contributions of each layer. The force and moment contributions are then summed to give the axial load and moment capacities of the section. For details of this model and its results, see Scherer (1996).

Optimization Model

An optimization model, written in the FORTRAN language, was developed to find the most cost-effective design solution for a particular axial load and bending moment. The cost is calculated as a function of material usage, and is given in terms of the cost of concrete per unit length of the column. Thus, the total cost for materials (C_M) for any diameter is given by

$$C_M = \frac{\Pi D^2}{4} \left[C_C + (\rho_A + \rho_H) C_F \right] \tag{6.1}$$

where D is the core diameter, ρ_A and ρ_H are the fiber reinforcement ratios in the axial and hoop directions, respectively, and C_C and C_F are costs per unit volume of concrete and FRP, respectively. For hybrid FRP, where axial and hoop fibers are different, the generalized cost formula is given by

$$C_M = \frac{\Pi D^2}{4} \left[C_C + \rho_A C_A + \rho_H C_H \right] \tag{6.2}$$

where C_A and C_H are the costs per unit volume of axial and hoop fibers, respectively. In this study, costs are normalized in terms of cost per unit volume of concrete. Table 6.1 shows the relative material densities and costs for glass and carbon fibers as well as concrete. The data is obtained from a recent study at MIT (Deskovic, Triantafillou, and Meier 1995).

Table 6.1 Relative material density and cost (Deskovic, Triantafillou, and Meier 1995)

Material Data	Concrete	Glass Fibers	Carbon Fibers
Relative Density	24	16	13
Relative Cost / Weight	0.1	18	160

Therefore, normalized cost of fiber composites and concrete in terms of unit volume of concrete can be determined as follows:

$$\begin{aligned} C_C\ (Concrete) &= 1.0 \\ C_F\ (Glass) &= \left(\frac{18}{0.1}\right)\left(\frac{16}{24}\right) = 120 \\ C_F\ (Carbon) &= \left(\frac{160}{0.1}\right)\left(\frac{13}{24}\right) = 867 \end{aligned} \tag{6.3}$$

The optimum design is a function of materials cost as well as weight of the column. As stated previously, if the column becomes extremely large, it could affect the amount of reinforcement needed in a supporting member. A weight penalty function (α) should be added to represent the increased cost due to the weight of the column. The total cost equation (C_T) then becomes

$$C_T = C_M + \alpha W \tag{6.4}$$

where C_M is the cost of materials per linear foot of column, α is the cost per pound per linear foot of column, and W is the combined weight of the concrete and the fibers. The weight penalty function (α), however, is not a constant value, but also depends on the location of the column, type of structure, and type and size of other supporting members. For example, the penalty function for a column on an upper floor of a building is higher than that of the same column on a lower floor. For the flow chart of the program, see Scherer (1995). Input parameters for the program are as follows:

1. Applied axial load and bending moment;
2. Peak strength and corresponding strain for unconfined concrete (f'_{co} and ϵ_{co});
3. Number of layers of concrete for integration;

4. Range of concrete core diameter and hoop and axial fiber reinforcement ratios;
5. Relative costs for hoop and axial fiber reinforcement (C_A and C_H); and
6. Modulus of elasticity and ultimate strength of hoop and axial fibers.

Within the specified range, the program will find for each diameter, all combinations of hoop and axial fiber reinforcements that will resist the applied loads and bending moments, and are the most cost-effective. Calculation of the resisting internal forces and bending moments is done by dividing the cross section into several differential layers as shown in Figure 6.1. The total compressive force in concrete (P_C) is given by

$$P_C = \sum_{i=1}^{n} f_{ci} A_{ci} \tag{6.5}$$

where f_{ci} is the stress in concrete layer *i* found from Mander's stress equation, and A_{ci} is the area of concrete layer *i*. The total force in the axial fiber layers (P_A) is given by

$$P_A = \sum_{i=1}^{n} E_A \epsilon_i A_{Ai} \tag{6.6}$$

where E_A is the modulus of elasticity of the axial fibers, ε_i is the strain in layer *i*, and A_{Ai} is the area of axial fibers in layer *i*. The total force (P_T) in the section is

$$P_T = P_C + P_A \tag{6.7}$$

Moment capacity of the concrete section is given by

$$M_C = \sum_{i=1}^{n} f_{ci} A_{ci} y_i \tag{6.8}$$

where y_i is the distance from the centroidal axis to the center of layer *i*. Moment Capacity in the axial fiber layers is given by

$$M_A = \sum_{i=1}^{n} E_A \epsilon_i A_{Ai} y_i \tag{6.9}$$

The maximum strains in the cross section are controlled for three critical conditions:

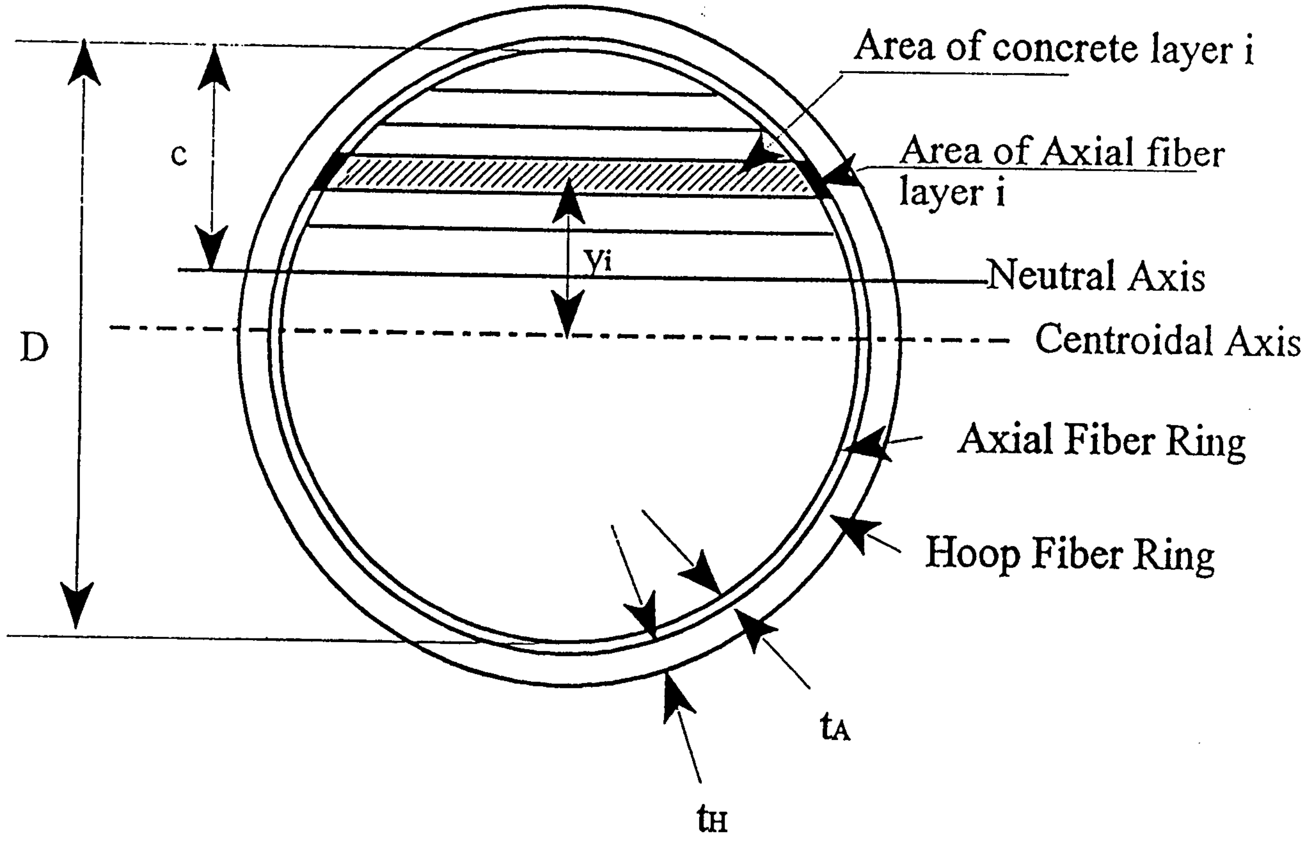

Figure 6.1 Discretization of hybrid section

1. To ensure that axial fibers will not fail in compression, the ultimate strain in confined concrete (ε_{cu}) may not be greater than the ultimate strain in the axial fibers (ε_A).
2. As shown in Figure 6.2, when depth of the neutral axis is less than the radius of concrete core, maximum tensile strains in the jacket will be greater than maximum compressive strains. The failure, is then governed by either tensile fracture of the jacket (ε_A) or compressive crushing of concrete (ε_{cu}).
3. As shown in Figure 6.3, when depth of the neutral axis exceeds the radius of concrete core, tensile fracture will not be governing the failure of the column. Maximum allowable strain, therefore, will be the lesser of ε_{cu} or ε_A on the compressive side.

6.3 Analysis and Discussion

The sensitivity study, among other things, indicated that the effect of axial reinforcement is more pronounced for larger diameter columns. It is recommended that for larger moments, larger diameter columns with moderate amounts of axial reinforcement should be used instead of smaller diameter columns with higher amounts of axial reinforcement. As the diameter of concrete core increases, for each combination of axial and hoop fibers, the moment capacity increases. Also, for any core diameter and hoop fiber thickness, a higher moment capacity is observed with the increase of the axial reinforcement ratio. It is also seen that the change in moment capacity with respect to diameter increases at a higher non-linear rate as the axial reinforcement ratio is increased, irrespective of the thickness of hoop fibers. This is an indicator that the hoop reinforcement is not a major contributing factor to the moment capacity. There is, however, some increase in moment capacity when hoop fiber thickness is increased. The increase comes from the increase in ultimate strain of concrete (ε_{cu}), which in turn increases the amount of axial force in concrete. Axial fibers are then better utilized as the compression and tension fibers are allowed to take more of the applied forces. Finally, as the diameter of concrete core increases, the effect of hoop fibers becomes more significant. For more details on the sensitivity model and its results, see Scherer (1996).

Figure 6.4 shows the interaction diagrams for a concrete core diameter of 60 inch, hoop fiber thickness of ½" and ¼", and axial fiber reinforcement ratio of 1.67%, 3.36%, and 5.06%. Axial loads and bending moments are normalized with respect to the capacity of a composite column with ¼ inch hoop fiber thickness and axial reinforcement ratio of 1.67%. When comparing any two curves that have the same axial reinforcement ratios, it can be seen that the thickness of the hoop fibers is of little consequence in regions near the pure flexure. This is due to the fact that the column is failing in tension and that most of the concrete in the cross-section is in tension. Thus, the concrete is being pulled longitudinally and is shrinking laterally. The only way the confining effects of hoop fibers are put to use is when concrete is compressed against the fibers, activating them. Adding more hoop fibers to concrete in tensile regions becomes a futile effort. When a sufficient amount of axial load is applied, however, increasing the thickness of hoop fibers may prove useful. If one compares two interaction curves with the same axial reinforcement ratios for an axial load ratio of above 0.4, it can be seen that a substantial increase in moment capacity occurs from increasing the hoop reinforcement from ¼" to ½". This is attributed to a compression mode of failure for the column. It is also noted that at balanced failure for a hoop fiber thickness, nearly the same axial load, but higher moment, is observed by increasing the axial reinforcement ratio.

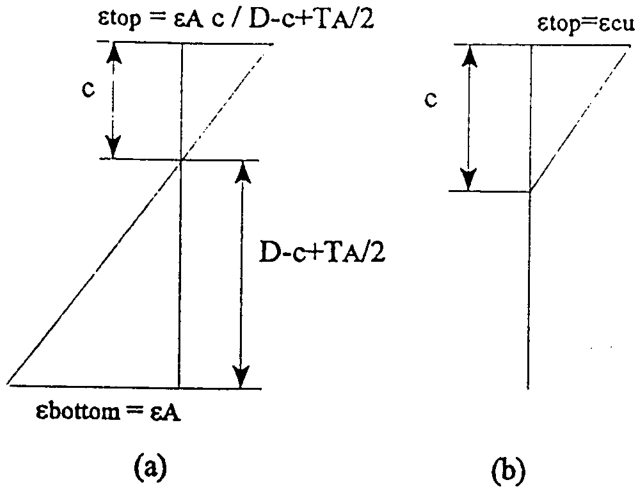

Figure 6.2 Tension control failure in hybrid column

a) Failure in FRP b) Failure in concrete

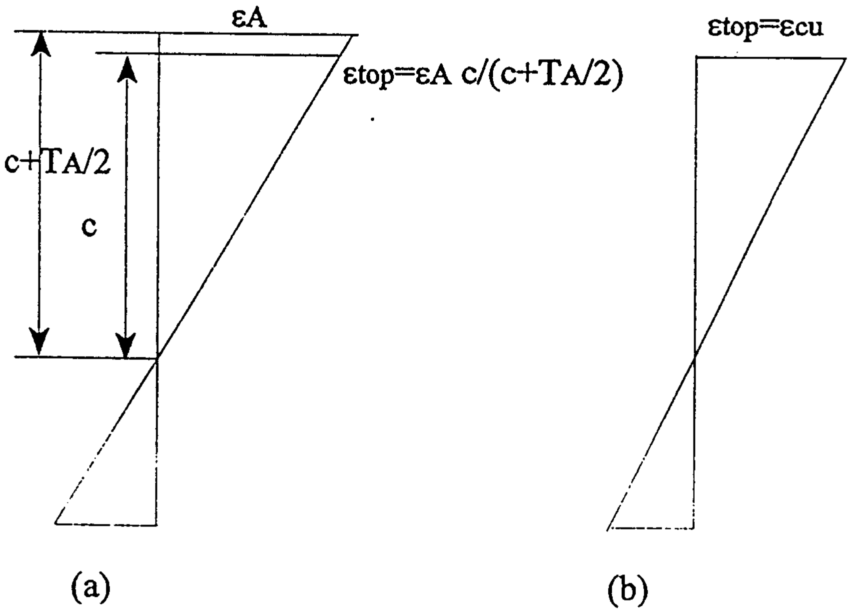

Figure 6.3 Compression control failure in hybrid column

a) Failure in FRP b) Failure in concrete

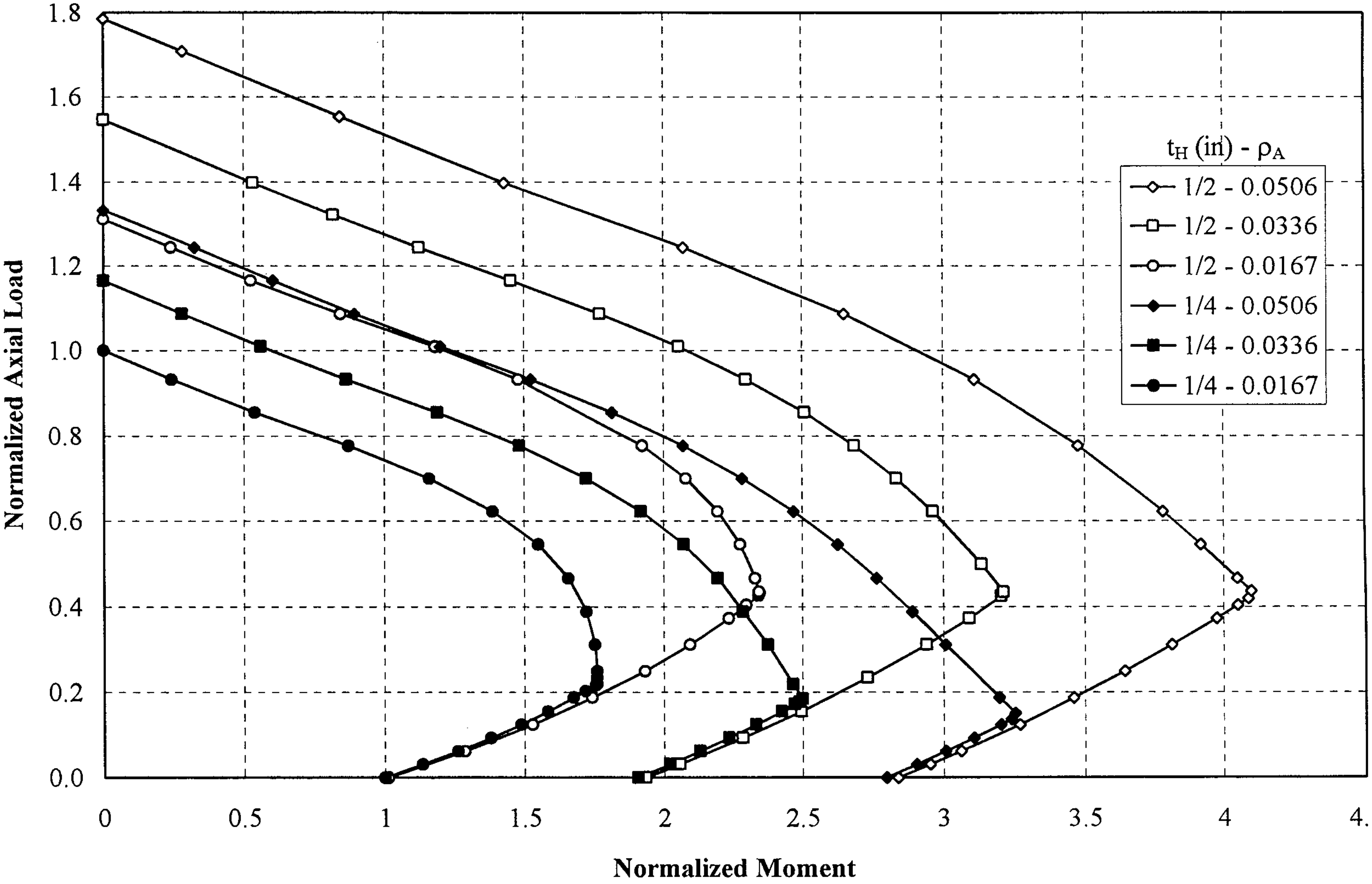

Figure 6.4 Normalized interaction diagrams for hybrid column

Normalized moment-curvature (ϕ) relationships are shown in Figure 6.5 for a core diameter of 60 inch, hoop fiber thickness of ½ inch, and axial reinforcement ratio of 3.36%. In this figure, moments and curvatures have been normalized to those of the balanced condition. Curvature is defined as $\phi = \frac{\epsilon_{top}}{c}$, where ε_{top} is the strain in the top layer of concrete section and c is the depth of neutral axis. Curves represent various axial load levels and are plotted to the point of failure at ultimate curvature (ϕ_{cu}). For pure flexure, bending moment increases linearly with an increase in curvature. The highest bending moment and curvature at failure occurs at the balanced condition where axial fibers and the confined concrete reach their ultimate failure strains at the same time, ε_A and ε_{cu}, respectively. Both moment and curvature are decreased for any other axial load level. For axial loads higher than that of the balanced condition, compression failure occurs. Furthermore, it is clear that as the axial load is increased, a more ductile response can be observed.

Figure 6.6 shows relative material cost versus reinforcement ratio for a 60 and 70 inch diameter column with an axial load and moment capacity of 10,000 kips and 250,000 kip-in. Since concrete is much less expensive than fibers, it is obvious that cost of materials will decrease as the diameter of the concrete core increases. The figure shows, however, that for any one diameter, using hoop fibers in great excess of axial fibers and vice-versa does not lead to an optimum solution. An optimum solution is only achieved by using respectable amounts of both axial and hoop fiber reinforcement. The range of optimum solutions widens as the core diameter is decreased. Figure 6.7 shows relative material cost versus reinforcement ratio for a 58 inch diameter column. Curves are representative of an axial load of 10,000 kips and bending moments of 200,000 and 250,000 kip-in., respectively. The figure shows that as bending moment increases, the optimum solution is achieved by increasing both the axial and hoop fiber reinforcement ratios. Therefore, the moment-to-axial load ratio significantly affects the optimum solution. Both Figures 6.6 and 6.7 show that for optimum solutions, hoop fiber reinforcement ratio is always greater than axial fiber reinforcement ratio. Figure 6.8 shows a schematic plot of relative costs versus column diameter. The figure shows relative cost for materials, added cost due to weight as a function of α, and total cost. Portions of the curves in the shaded regions are outside what eventually would be allowable design fiber reinforcement ratios. The figure clearly shows the effects that weight has on optimum column diameter. As α increases, the general trend is to decrease column diameter and to increase the fiber reinforcement ratios. Figure 6.9 shows relative material, weight, and total costs versus column diameter for various penalty functions at an axial load and moment capacity of 10,000 and 250,000 kips, respectively. Relative material, weight, and total costs for values of $\alpha=1$, 5, and 10 are shown. As in the previous figure, the effect of weight and the penalty function on optimum column diameters is clearly shown. For $\alpha=1$, the optimum solution is to choose the largest column diameter, within the feasible range. As α increases, however, the optimum column diameter is reduced and both hoop and axial optimum reinforcement ratios are increased.

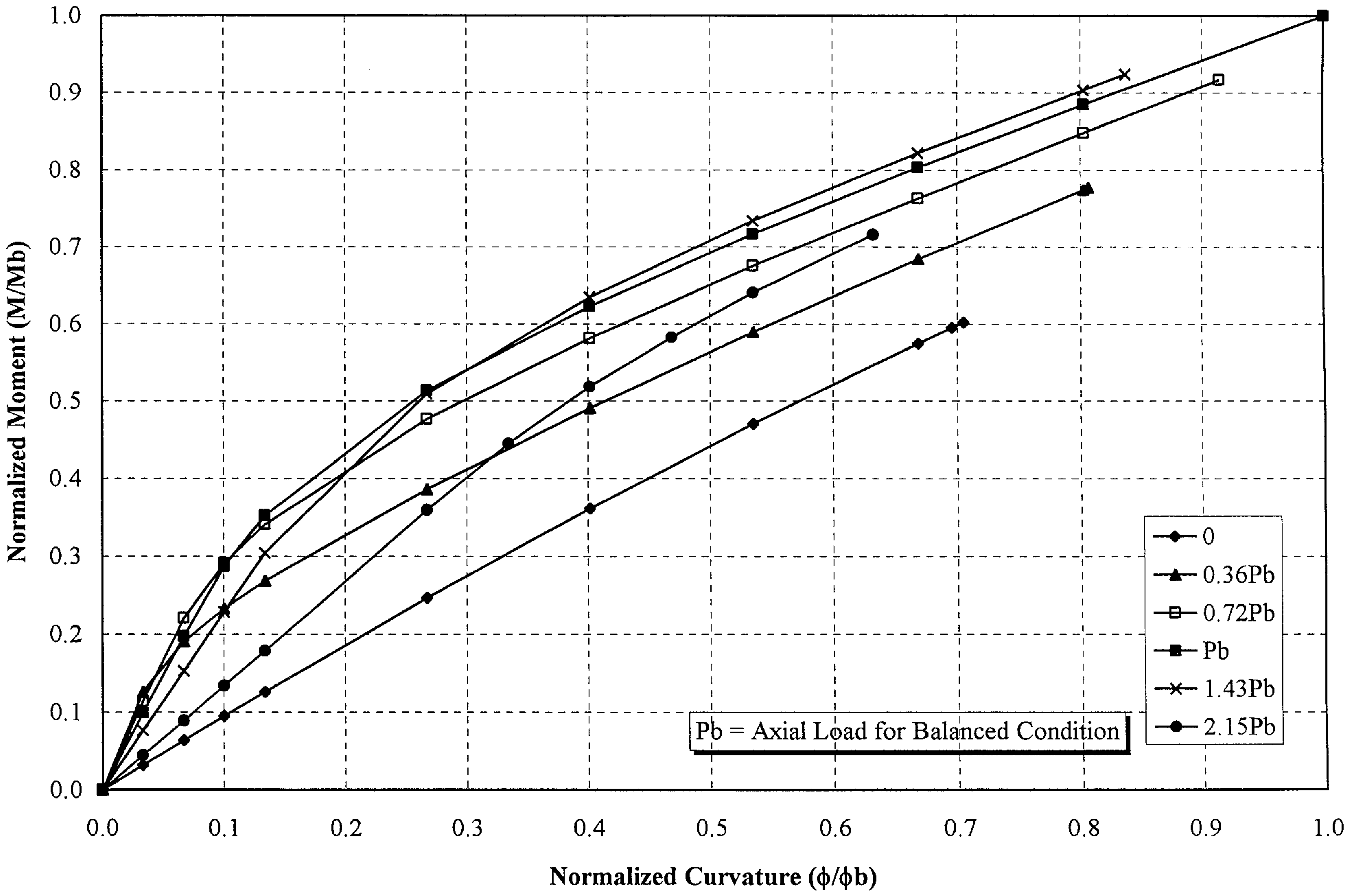

Figure 6.5 Normalized moment-curvature diagrams for a hybrid column

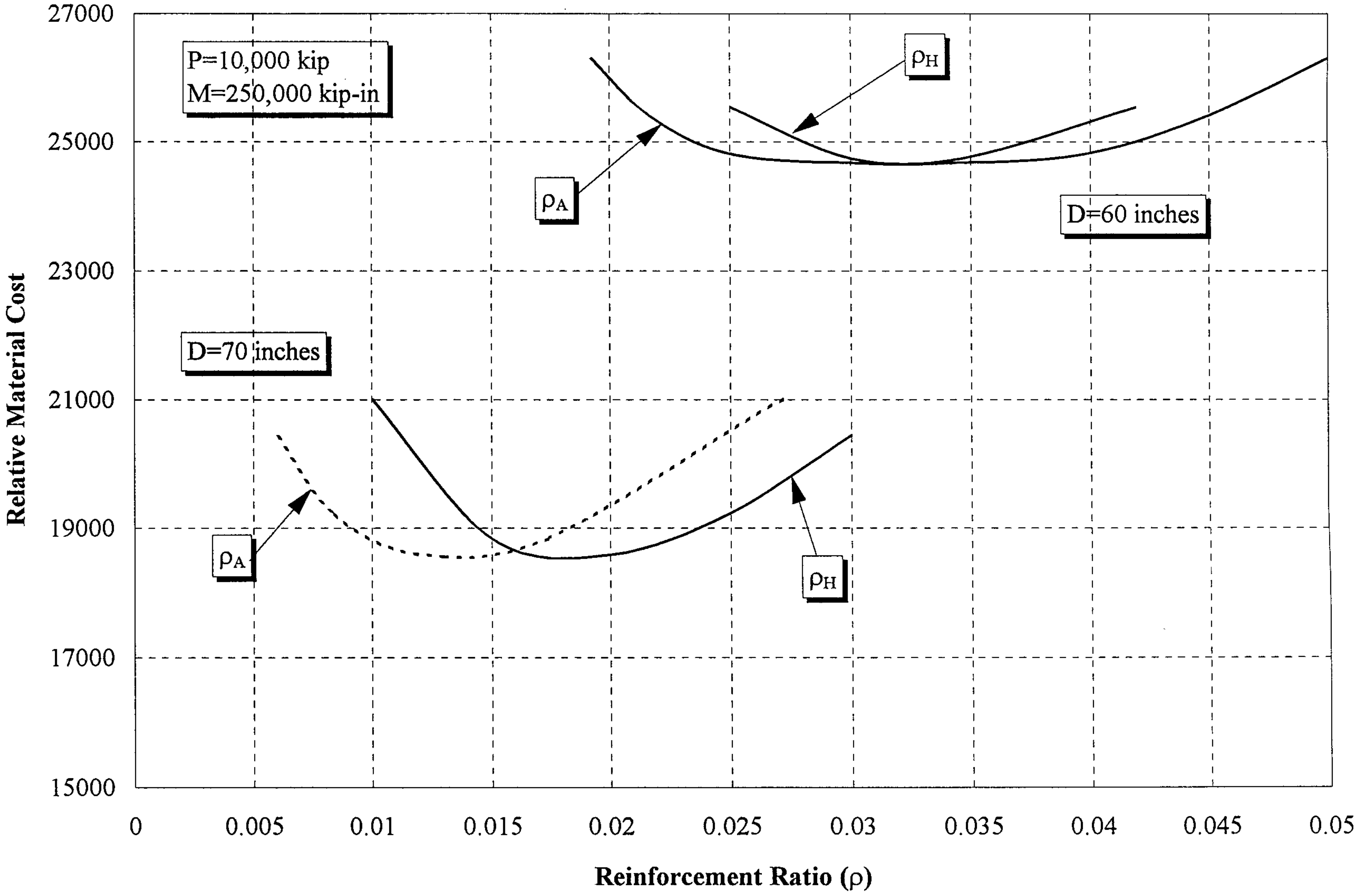

Figure 6.6 Relative material cost versus reinforcement ratio for various core diameters

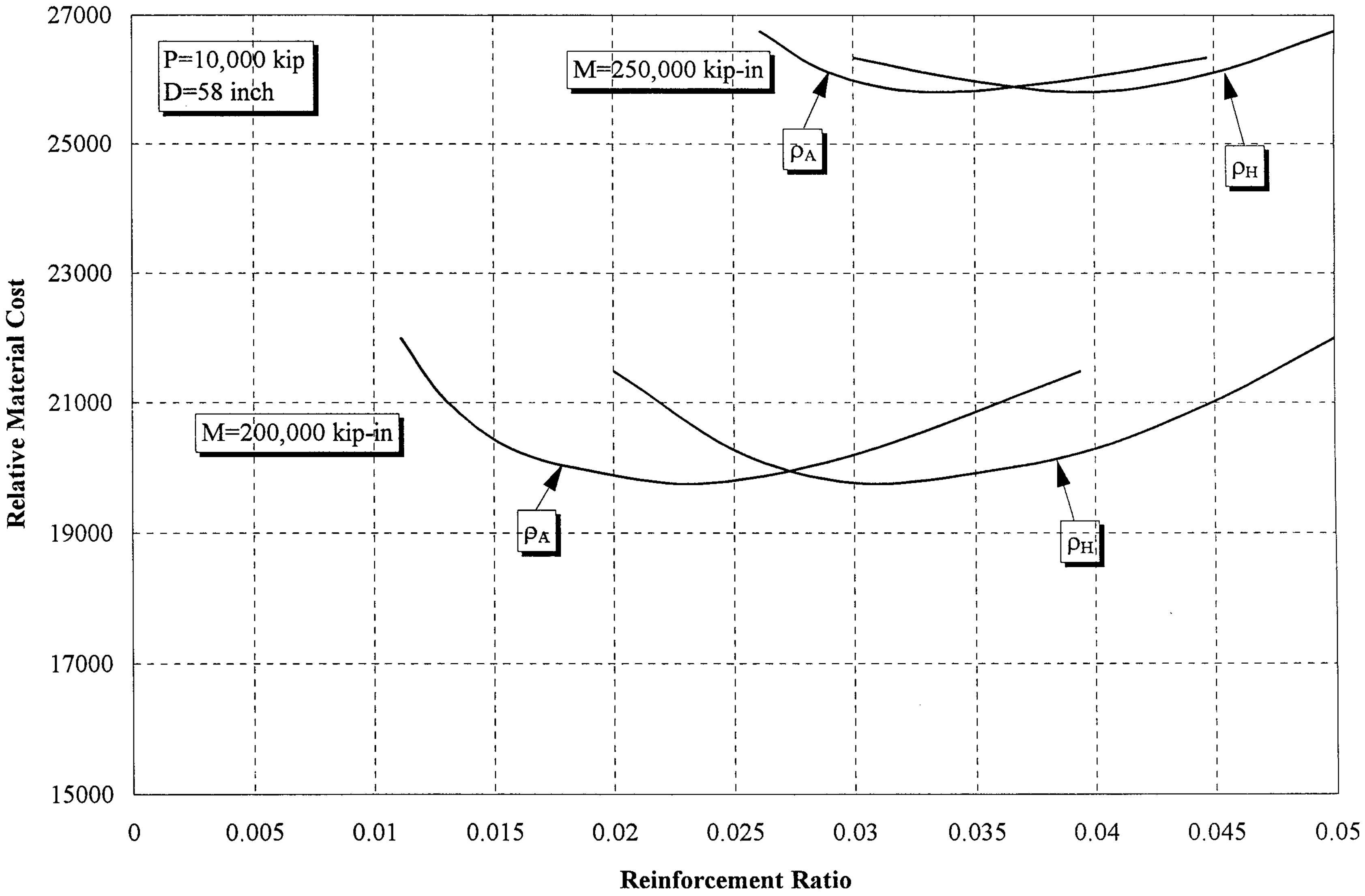

Figure 6.7 Relative material cost versus reinforcement ratio for various bending moments

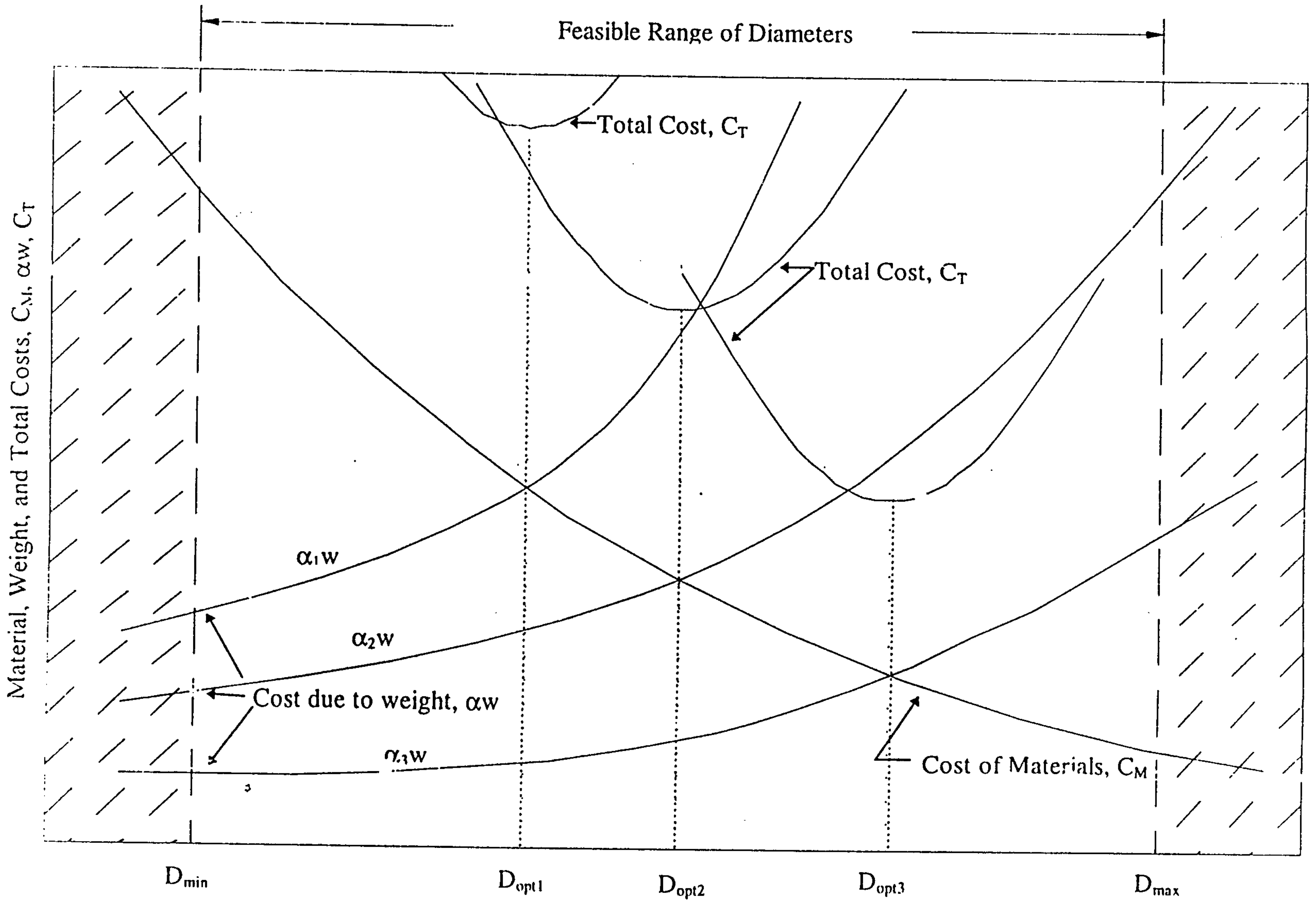

Figure 6.8 Schematic cost optimazation for hybrid columns

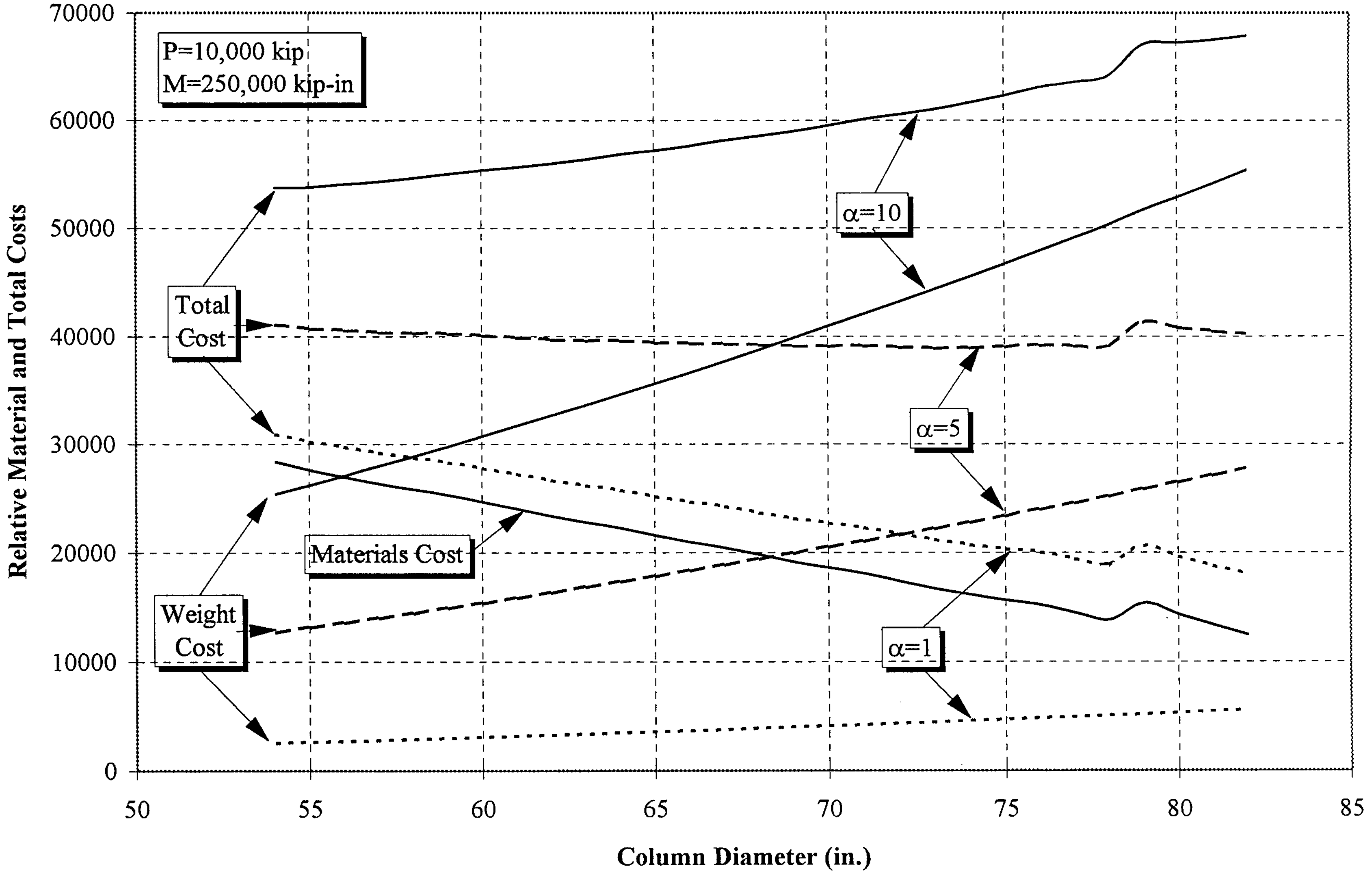

Figure 6.9 Relative total costs versus core diameter for various penalty functions

CHAPTER 7

ACOUSTIC EMISSION

7.1 Literature Review

Acoustic emissions (AE) are transient elastic waves generated by the rapid release of energy from localized sources within a material. When a body suddenly deforms locally and relieves local stresses, a burst of elastic energy is emitted. The elastic strain energy that is released during the deformation process, then propagates through the specimen and can be detected by sensors placed on the surface of the specimen (see Figure 7.1). AE is a powerful test for examining the behavior of materials deforming under stress. With AE equipment one can listen to the sounds of cracks growing, fibers breaking and many other modes of active damage in the stressed materials. Therefore, AE can be used as a non-destructive evaluation (NDE) technique to find defects during structural monitoring. AE techniques have been used in a variety of fields in concrete engineering.

A detailed investigation of the applicability of acoustic emission to concrete was done by McCabe et al. (1976). They conducted tests on concrete under compression, creep and flexural loading, and concluded that a good qualitative assessment of damage and the remaining life of the structure was possible using acoustic emission. Raymond (1984) investigated the application of the AE technique on a prototype model of a masonry tunnel to predict its brittle failure. His research efforts indicated that the AE technique was able to detect crack initiation with an accuracy of up to 90%. Li and Poorooshasb (1986) identified initial and critical damage states in plain and reinforced concrete. They found that acoustic emission from reinforced concrete is different from that of plain concrete, because the amplitude of the events caused by the friction at the steel-concrete interface is higher than those caused by cracking of the concrete. The most useful information obtained from AE wave-forms are the source location and characteristics. Maji and Shah (1988) used AE events to locate the fracture process zone. They showed that the AE event rate could be used to study the crack growth and the crack arrest phenomena. Okamoto (1992) studied crack size development in reinforced concrete structures under cyclic loading using AE principles. Loading tests were performed for an L-shaped rigid frame of reinforced concrete. Results clearly showed that the Kaiser effect is an effective tool for estimating the level of deterioration in concrete structures (see next section for definition of Kaiser effect). Farahat and Ohtsu (1995) investigated the relation between the plastic damage and the AE events in concrete subjected to uniaxial compressive loading. Both undamaged and damaged concrete specimens were tested until complete failure. They found that as the plastic damage increases, the activity of AE signals increases, as well. They also noticed that the degree of non-linearity of the relationship between the plastic damage and AE events depends significantly on the initial deterioration of the concrete specimen.

Using the AE technique for concrete-filed tubes and fiber-wrapped concrete can be very important, since the status of the concrete core is not visible from outside the jacket. In this project, the AE technique is used to examine the behavior of confined concrete for different length-to-diameter (L/D) and diameter-to-thickness (D/t) ratios, and for bonded and unbonded construction methods.

7.2 Characteristics of Acoustic Emission Signals

When an acoustic emission event occurs at a source within a material (due to either deformation or cracking), AE waves propagate through the material and can be detected on the surface by an AE sensor, which then turns the vibrations into electrical signals. Physically, it has been clarified that AE waves consist of P (longitudinal) waves and S (shear) waves, and might further include surface (Rayleigh) waves, reflected waves, diffracted waves and other components. As shown in Figure 7.2, two basic types of AE signals can be detected:

1. Continuous emission is a qualitative description of the sustained signal level produced by rapidly occurring AE events. These are generated by events which occur in a reasonably continuous manner (ASTM E610-82, 1987).

2. Burst emission is a qualitative description of the discrete signal related to an individual AE event occurring within the material, such as that which may occur during crack growth or fracture in brittle materials (ASTM E610-82, 1987).

Figure 7.3 shows the general form of an AE burst and illustrates some of the important AE parameters which are defined below:

- AE event is a local material change giving rise to acoustic emission.
- AE event energy is the total elastic energy released by an emission event, it is essentially the area under the amplitude versus time curve for each burst and it is known as the signal strength.
- AE count is the number of times the AE signal exceeds a preset threshold during any selected portion of a test.
- AE signal amplitude is the peak voltage of the largest excursion attained by the signal wave-form from an emission event.
- AE sensor is a detection device, generally piezoelectric, that transforms the particle motion produced by an elastic wave into an electrical signal.
- AE channel is an assembly of a sensor, preamplifier, filters, secondary amplifier or other instrumentation as needed, connecting cables, and detector or processor.
- Couplant is a material used at the structure-to-sensor interface to improve the transmission of acoustic energy across the interface during acoustic emission monitoring.
- Kaiser effect is the absence of detectable acoustic emission at a fixed sensitivity level, until previously applied stress levels are exceeded (see Figure 7.4).
- Felicity effect is the appearance of significant acoustic emission at a stress level below the previous maximum applied stress (the reverse of the Kaiser Effect). The felicity effect is

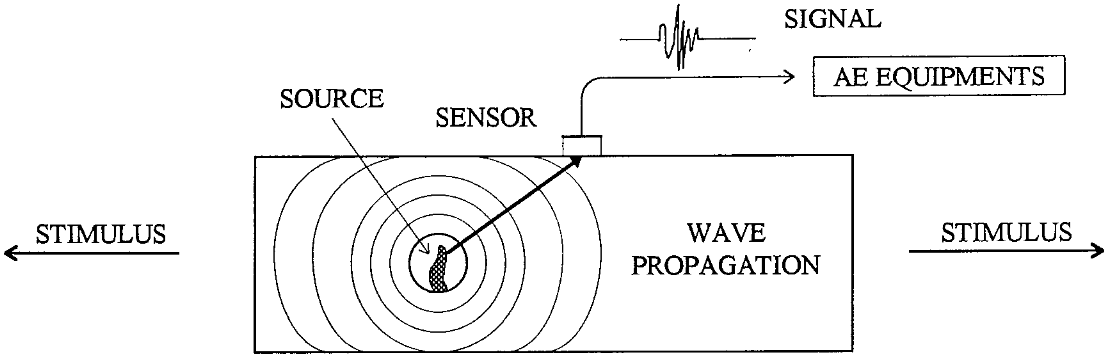

Figure 7.1 Propagation and detection of AE signals

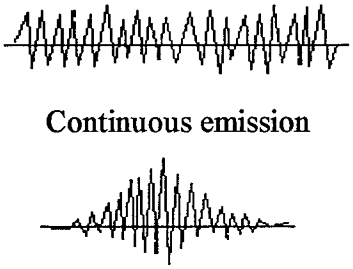

Figure 7.2 Types of acoustic emission signals

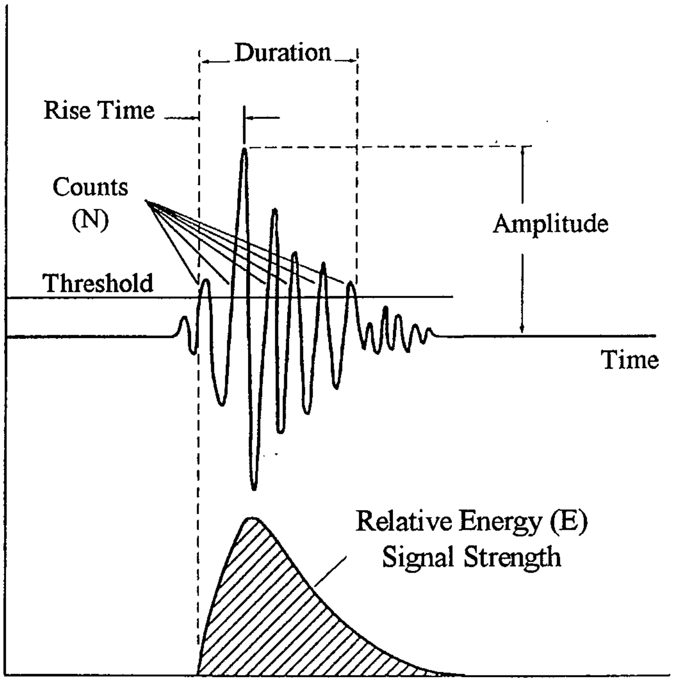

Figure 7.3 Acoustic emission signal features

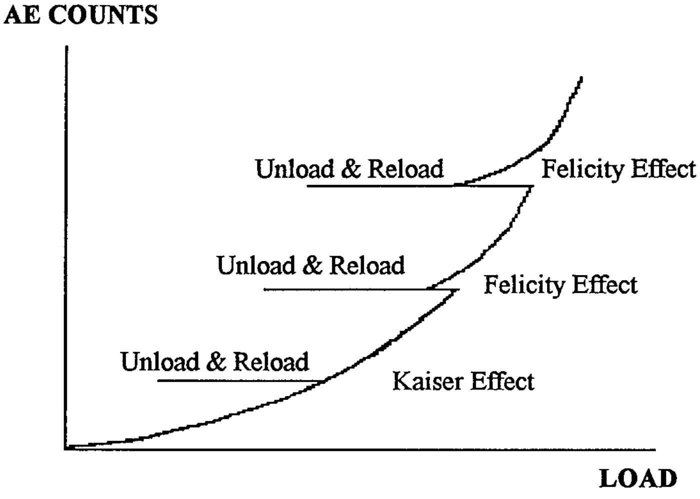

Figure 7.4 Kaiser effect and Felicity effect

especially important in composites (see Figure 7.4).

- Felicity ratio is the ratio between the applied load at which acoustic emission reappears during the next application of loading, and the previous maximum applied load.

Different damage types that can be introduced in composite materials when they are loaded include: reinforcement/matrix debonding, matrix cracking, delamination and reinforcement failure. AE tests are widely considered as the most effective NDE measures for assuring the structural integrity of composite materials, and to help better understand the initiation, growth and interaction of the different damage types. The main AE characteristics of composite materials are as follows:

- Large amounts of AE.
- Large increase in activity (AE rate) before failure.
- At higher stress levels, emission continues during load holds.
- Felicity effect is a good indicator of prior damage.
- AE gives an informative amplitude distribution.
- Friction at damaged surfaces is a major AE source, as well as any new damage.

7.3 Acoustic Emission Tests

AE monitoring was used in conjunction with the load tests on a total of over 50 specimens of both the length effect series and the bond effect series. Details of the specimen layout, test procedure and other relevant information for these two types of specimens were presented in Chapters 4 and 5, respectively.

AE Setup and Instrumentation

Tests were conducted using the AE Digital Signal Processing-32/16 for Mistras-2001, from Physical Acoustics Corp. This is a fully digital, four-channel, computerized acoustic emission system that performs AE wave-form and signal measurement and stores, displays and analyzes the resulting data. Each AEDSP-32/16 board processes two (2) AE channels. The PC computer holds 2 AEDSP boards or 4 channels, however all specimens but one (S6-24-1) were tested using two channels because of the large data storage capacity required. Various aspects of the instrumentation are described below:

- AE Sensors: The single most important factor in the acoustic emission testing is the selection of an AE sensor. This generally depends on the specific application. One type of the general purpose sensors is the R15, that has been used in this test. As shown in Figure 7.5, the two sensors were mounted at the mid-

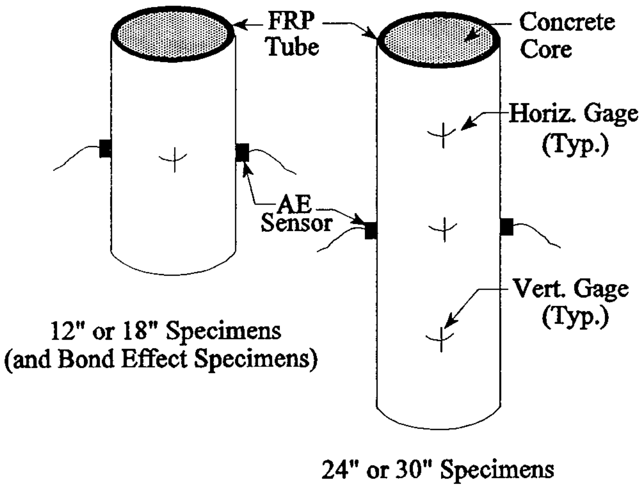

Figure 7.5 Mounting of sensors on the specimens

height of the specimens, opposite from each other. Specimen S6-24-1 is the only one in the entire series that has been tested using four sensors. For this specimen, two sensors (type R15) are at the mid-height, and the other two (type R15I) are at the top and bottom quarters. Figure 7.6 shows the test set up for the Specimen S6-24-1 with four sensors and full instrumentation.

- AE Transfer Coupling: It is essential to fill the air gap between the sensor and the specimen to achieve an efficient coupling of the AE wave energy from the cylinder into the sensor, especially for the curved surfaces such as those on the FRP tubes. These requirements were considered and a high viscous fluid (SLC 70-Krautkramer Branson) was used. The surfaces of the sensor and the specimen were first cleaned and smoothed, allowing for maximum couplant adhesion. Then, a thin layer of the viscous liquid was used to wet both surfaces. The sensor was held against the specimen with some pressure. In order to keep the sensors stationary during the loading process, a rubber-band was used to wrap the two sensors around the specimen.

- Preamplifiers and Connecting Cables: The function of the preamplifier is to increase the strength of the signal to make it more suitable for measurement and transmission. Also the cables from the sensors to the preamplifiers must be as short as possible to eliminate the signal attenuation. In these tests, two 1220A preamplifiers (from Physical Acoustics Corp.) were used. These preamplifiers have the reliability to select high pass, low pass, or bandpass filters, single-ended or differential input, 40 dB or 60dB gain. The gain that was established for these tests was 40 dB of a pre-amplification gain. These preamplifiers were only used with the Type R15 sensors, since the other type (R15I) are integral-preamplifier sensors, which have their preamplifiers built into the sensor case. In addition, the 1220A output and power was supplied by a single conductor 50 ohm coaxial cable with a BNC connector (PAC Model 1234). Figure 7.7 shows one of the specimens with sensors, preamplifiers and cables, prior to loading.

- Digital Hardware Setup: In order to obtain valid and representative acoustic emission (AE) results from the tests, some parameters needed to be adjusted to enhance the sensitivity and capability of detecting smaller signals. Figure 7.8 shows the selected hardware settings for these tests. The parameters that needed to be satisfied consist of the following:

  1. Threshold Level: The hardware design has its ability to choose between fixed and floating thresholds. the floating threshold is used under conditions of high, varying background noise. The threshold level floats above continuous background noise level, going up and down with the noise. Although this gives maximum sensitivity to burst-type emission, it may cost some loss of control, and add complexity in the data interpretation. The threshold was set fixed at a level of 40 dB.

  2. Sample Rate is the rate at which the AEDSP board samples wave-forms on a per second basis. A sample rate of 1 MHz means that one wave-form sample is taken every μsec. All

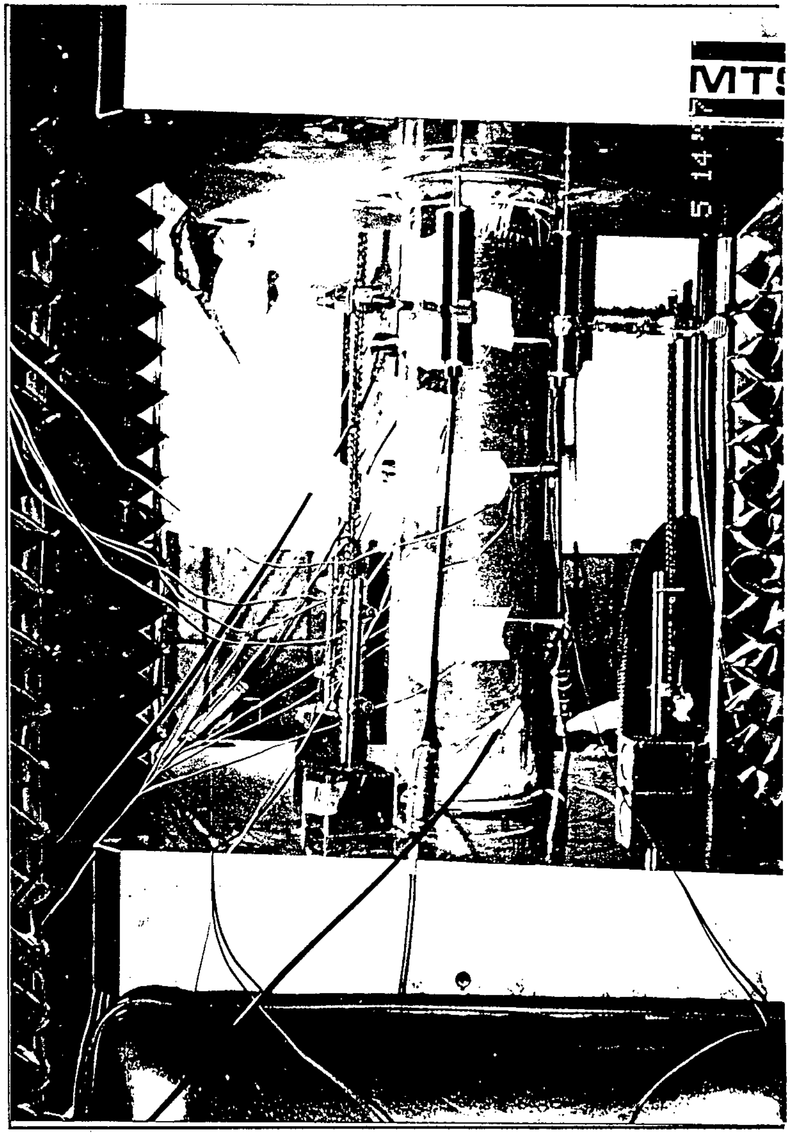

Figure 7.6 Test setup for Specimen S6-24-1 with four sensors prior to loading

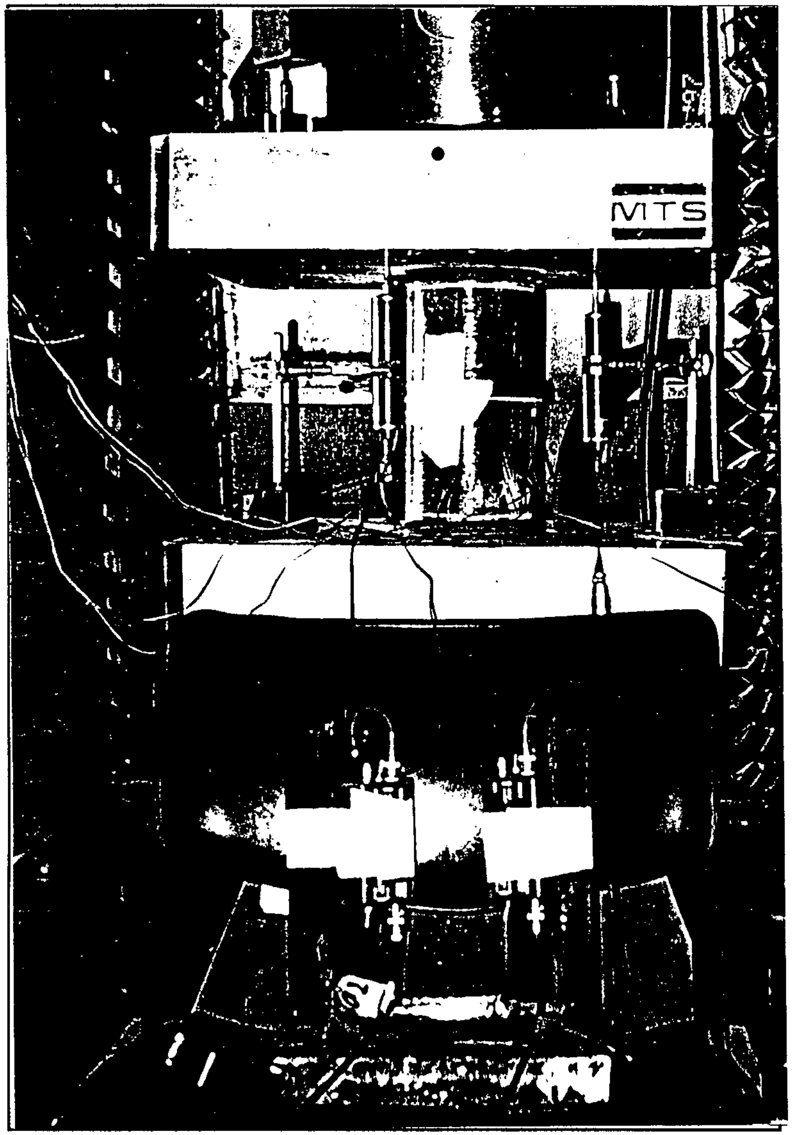

Figure 7.7 Preamplifiers located near the specimen

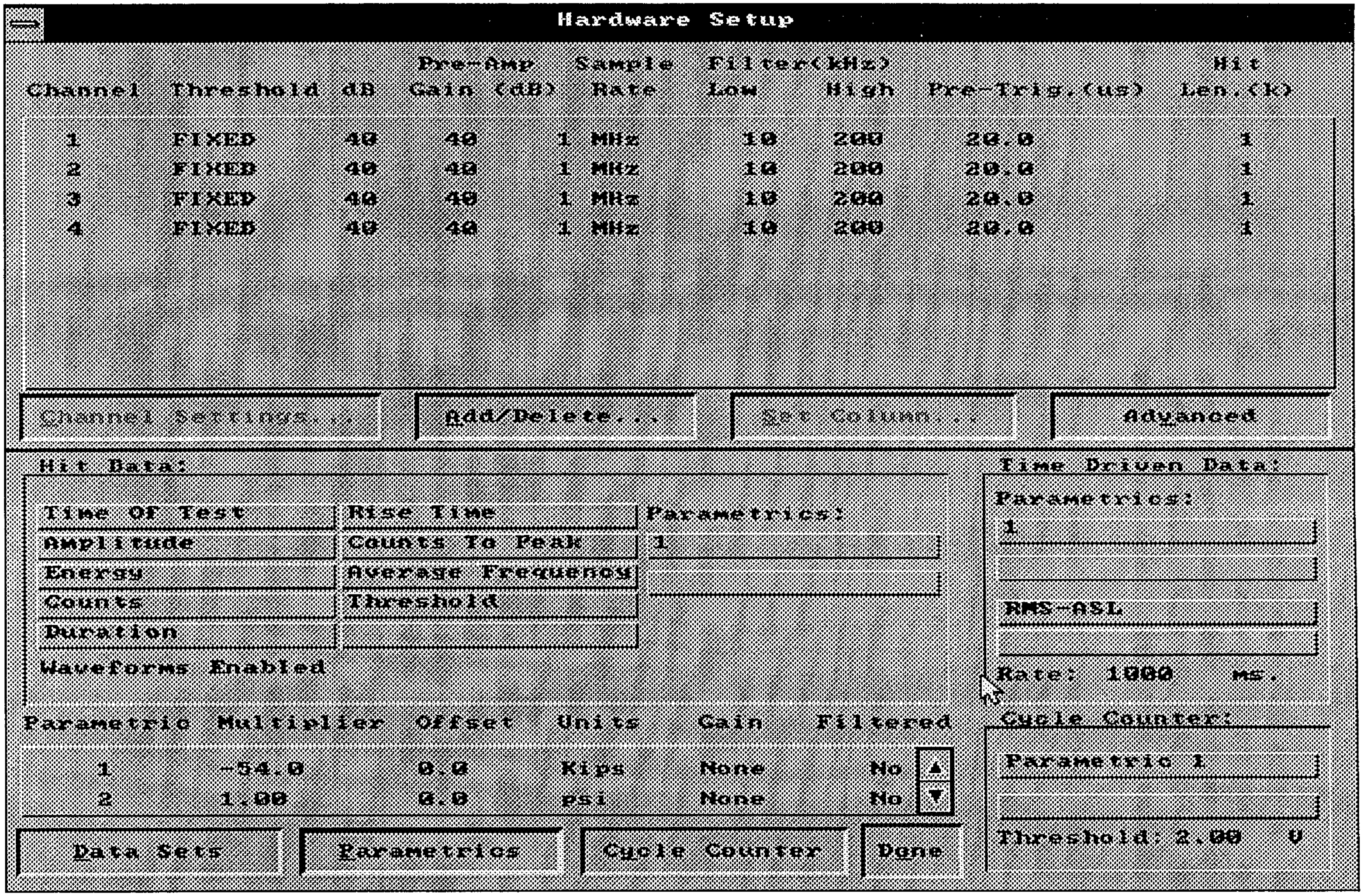

Channel	Threshold	dB	Pre-Amp Gain (dB)	Sample Rate	Filter(kHz) Low	Filter(kHz) High	Pre-Trig.(us)	Hit Len.(k)
1	FIXED	40	40	1 MHz	10	200	20.0	1
2	FIXED	40	40	1 MHz	10	200	20.0	1
3	FIXED	40	40	1 MHz	10	200	20.0	1
4	FIXED	40	40	1 MHz	10	200	20.0	1

Hit Data:

Time Of Test
Amplitude
Energy
Counts
Duration
Rise Time
Counts To Peak
Average Frequency
Threshold

Parametrics:
1

Waveforms Enabled

Time Driven Data:

Parametrics:
1
RMS-ASL

Rate: 1000 ms.

Parametric	Multiplier	Offset	Units	Gain	Filtered
1	-54.0	0.0	Kips	None	No
2	1.00	0.0	psi	None	No

Cycle Counter:

Parametric 1

Threshold: 2.00 V

Figure 7.8 Hardware setup dialog box showing selected hardware settings the 12 and 18 specimens, as well as the 6 layers of the 24 specimens, were tested with sample rate of 4 MHz. For the rest of the specimens, the sample rate was modified to 1 MHz because of the large capacity of the data obtained.

3. Filter: The objective of the filter is to discriminate between different frequencies. It provides constant transmission over any desired range of frequencies, and a high degree of attenuation for all other frequencies. Four analog filter values, for low pass and high pass filters, are available on each active channel. The filter high limit is always calculated by dividing the sample rate by three (3), and selecting the next lowest available filter value.

4. Pre-Trigger: The pre-trigger value tells the software how long to record (in µsec) before the trigger point, which is the point at which the threshold is exceeded. The maximum allowable pre-trigger value is calculated by dividing the hit length by the sample rate in MHz. The hit length determines the size of a wave-form message.

Test Results

It was generally noticed that the sensor closer to the failure point or near the white bands indicated larger amplitude and energy, especially near the end of the test. The AE tests indicated a large increase in the amplitude just before failure of the specimen. Of the various AE parameters, AE energy and number of AE counts were found most useful. It is interesting to note that the frequency content of the composite specimens was in the range of 100 to 400 kHz. Figure 7.9 shows the axial stress versus the cumulative number of AE counts for the control specimen as well as a typical 6, 10, and 14-layer 12" specimen from the length effect series. In the same figure, the corresponding stress-strain response of these specimens are shown for comparison. The figure clearly shows how the number of counts is larger for the thicker jackets. This is a good indication of the degree of confinement provided by the jacket. It is noticed that the curves of stress versus AE counts has the same bilinear shape as those of the stress-strain response. It is also clear that once the concrete core reaches its unconfined strength (at a strain of about 0.002-0.004), the number of counts begins to increase more rapidly. Therefore, the rate of AE counts may provide a good NDE measure for hybrid columns. Another important note that should be mentioned is that all AE curves show a large rate of AE activity during the initial loading, which results in a soft plateau in the beginning of each AE curve. This may be attributed to the presence of air voids in the sulfur capping, and could be corrected the same way as in the stress-strain curves (see Mirmiran 1997). Figure 7.10 shows one of the cyclic tests for a 7-layer S-glass specimen of the bond effect series. One can see that emissions occur significantly at a load level lower than that previously attained. Even during unloading, some minor increases in the energy can be seen which implies the presence of Felicity effect. Therefore, while Kaiser effect is not present for composite columns even at low levels of axial load, Felicity effect during loading and unloading is apparent as one would expect from fiber composites. For more details regarding the AE tests, see El Echary (1997).

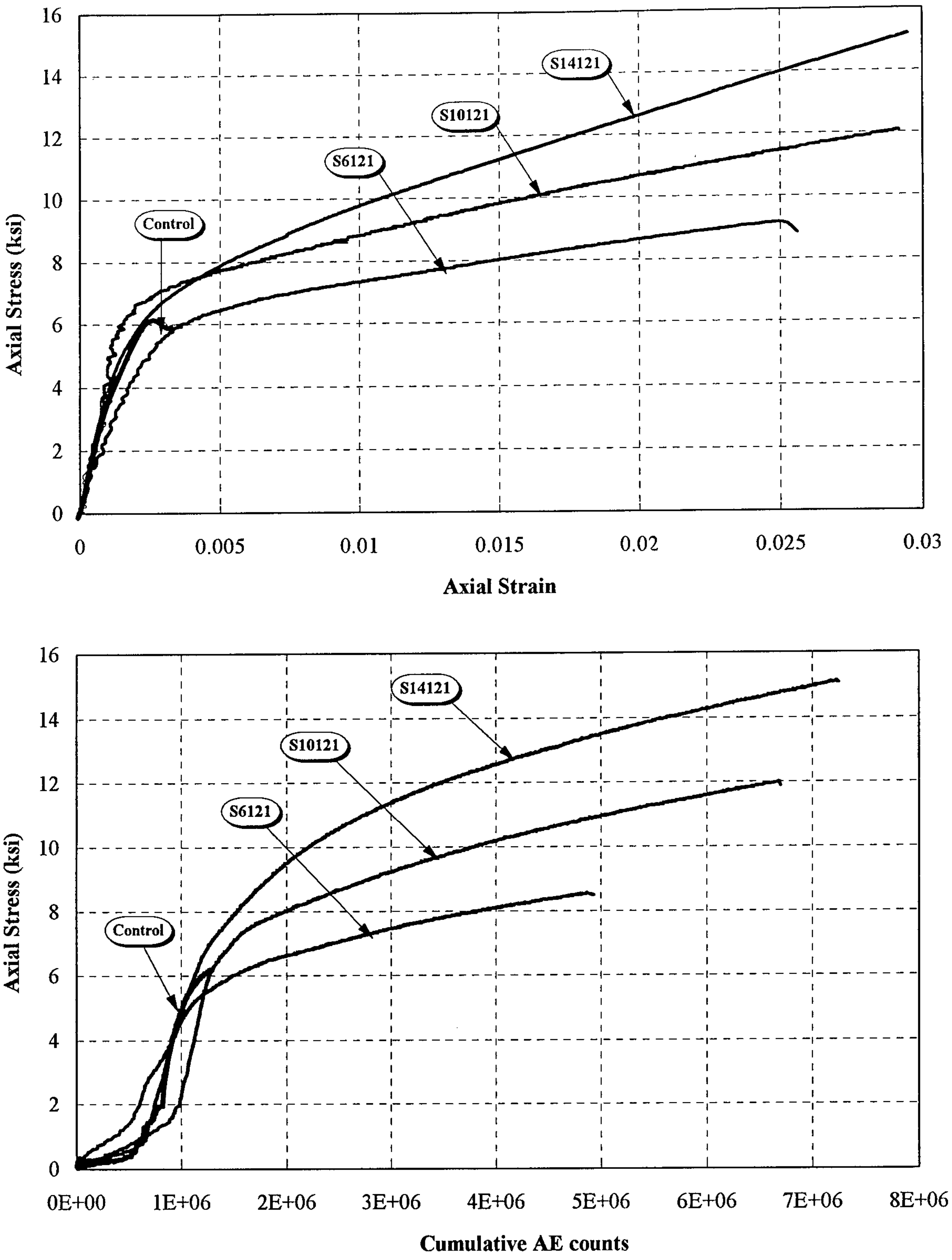

Figure 7.9 Effect of confinement on AE counts

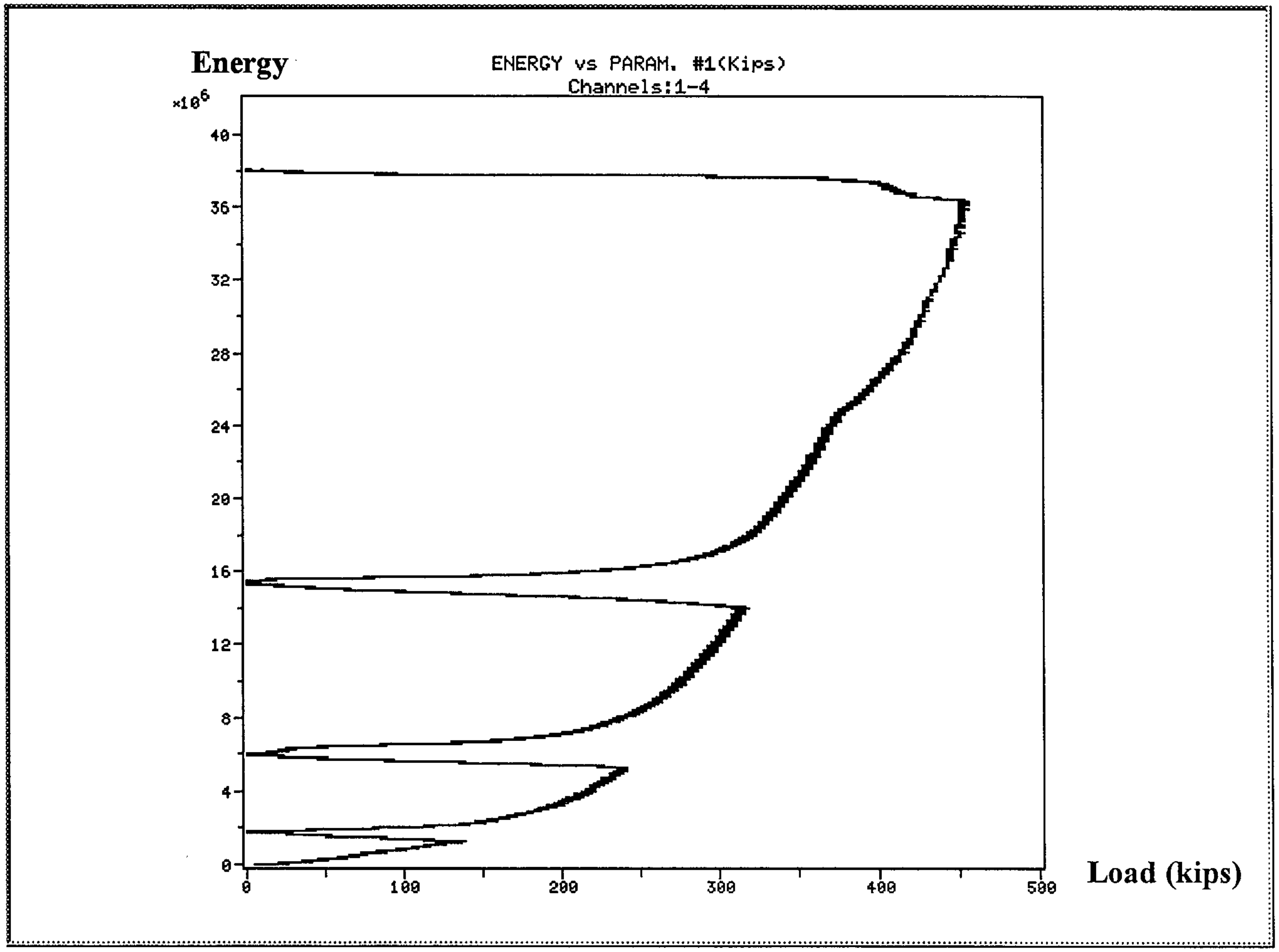

Figure 7.10 Felicity effect for a 7-layer S-glass jacketed concrete specimen

CHAPTER 8

CONCLUSIONS

A series of beam and column tests with a variety of design parameters helped quantify the response of hybrid FRP-concrete columns as related to shear strength, confinement, cross-section, slenderness, and construction bond. It was shown that design of hybrid columns can be optimized for any load combination and core diameter. Finally, effective use of nondestructive methods for FRP-concrete columns was demonstrated. Below summary and conclusion of each component of this project are presented.

Shear Strength of Concrete-Filled FRP Tubes

Two series of beam shear tests with and without shear ribs were conducted on a total of 16 beams. Also, equations for the shear strength of the FRP jacket were proposed and correlated with results from the experiments. The following conclusions were drawn:

- Unless shear ribs are provided, hardly any bond would exist naturally between the FRP jacket and concrete. As a result, slippage would not allow shear to be transferred at the concrete-FRP interface. The tube, however, still somewhat increases the shear strength of concrete by simply containing the cracked section.

- With the shear connectors, the slippage problem was corrected, and the tube increased the strength by at least 6 times the shear strength of unjacketed beams of the same cross section. Also, the ribbed FRP tube proved effective in inhibiting shear failure of the beams.

Effect of Cross Section on Confinement

A total of 9 composite specimens with square section were tested, and results were compared with circular sections of Phase I (Mirmiran 1997), and fiber-wrapped specimens (Rochette 1997). The following conclusions were drawn:

- Square sections are not as effective as circular sections in confining the concrete core, as the strength of concrete is increased only marginally and rather independent of the jacket thickness. However, a post-peak ductility can be expected.

- Failure of the square FRP-encased specimens is accompanied by white patches around the corners, showing stress concentration at the edges. As the corner radius is increased, the confinement effectiveness and the behavior of confined concrete become closer to circular sections. The over-riding parameter in controlling the confinement was shown to be the product of the corner radius and the confining pressure.

Effect of Column Length on Confinement

To evaluate the effects of length-to-diameter (L/D) and diameter-to-thickness (D/t) ratios of the column on confinement of concrete, a total of 24 6"-diameter composite specimens with three different tube thicknesses (6, 10, and 14 layers) and four different lengths (12", 18", 24", and 30") were tested which corresponded to L/D ratios from 2:1 to 5:1. The effect of length on the ultimate strength and ultimate strain of the confined concrete was quantified, though did not seem to be very significant. No slenderness effect in the form of buckling was observed during the tests. The column length did not alter the general behavior of confined concrete such as mode of failure or dilation characteristics of concrete core. Detailed analysis of the data for each specimen indicated that the maximum eccentricity was within 10-12% of the section width. Noting that ACI 318-95 considers a minimum eccentricity of 10% and a strength reduction of 20% for tied columns, the amount of eccentricity and the strength reductions that were noticed for L/D ratios of 2:1 to 5:1 seemed acceptable. It was therefore, concluded that the 12" cylinders should be considered adequate to represent the confinement of concrete sections. Longer specimens possess an inherent eccentricity that results in lower values of the ultimate load. However, the eccentricity is well within the acceptable range, and does not necessarily qualify for any slenderness effect.

Effect of Bond on Confinement

To evaluate the effects of construction bond on confinement, two series of compression tests were conducted. The difference between the two series was mainly in the continuity of the layered shell. In Series 1, the shell was made layer by layer with an overlapped splice of approximately 3" per layer which is about 17% of the perimeter of the 6"-diameter cylinders. For multi-layer specimens, the location of splice would vary from one layer to another. Once tested, specimens of Series 1 failed mainly at the splice of the outermost layer before reaching the ultimate strength of the fiber composite. Therefore, a second series of tests on a smaller number of specimens was planned. Two types of coupon tests were also planned; a split-disk test accompanied specimens of Series 1, while a uniaxial tension test was chosen for Series 2. Results obtained to date indicate that the effect of construction bond on confined concrete is not significant, as long as the biaxial stresses in the jacket are considered properly for the bonded specimens.

Cost Optimization

Optimization studies were carried out to determine the most cost-effective proportions of the hoop and axial fibers for any concrete core diameter in a concrete-filled FRP tube subjected to an axial load and a bending moment. A penalty function was introduced to determine the significance of weight on the total cost of a hybrid column. Parametric studies indicated that:

- ♦ Adding hoop fibers at low axial loads does not increase the capacity of the section.
- ♦ For a specific core diameter, there is only one particular combination of axial and hoop fibers that provides the optimum solution.

- When weight becomes a significant factor, the optimum solution shifts to a lower core diameter and higher hoop and axial fiber reinforcement ratios.

Acoustic Emission

Acoustic emission (AE) tests on over 48 composite specimens, i.e., specimens of the length effect and bond effect, proved to be an efficient non-destructive evaluation (NDE) technique for hybrid columns. Of the various AE parameters, AE energy and number of AE counts can both effectively represent the response of confined concrete. It was noticed that the curves of stress versus AE counts has the same bilinear shape as that of the stress-strain response. It was also clear that once the concrete core reaches its unconfined strength (at a strain of about 0.002-0.004), the number of counts begins to increase more rapidly. Therefore, the slope of stress versus AE counts may provide a good NDE measure for hybrid columns. Finally, it was shown that while Kaiser effect was not present for composite columns even at low levels of axial load, Felicity effect during loading and unloading was apparent as one would expect from fiber composites.

CHAPTER 9

DISSEMINATION OF FINDINGS

The findings of this project have been disseminated through archival journals, conference proceedings, presentations, M.S. theses, doctoral dissertations, and newspaper and magazine articles as listed below by the year of publication. It should be noted that this list is cumulative and includes the updated entries that were reported under Phase I (Mirmiran 1997).

Journal Papers

Mirmiran, A., and Shahawy, M. (1996). "A new concrete-filled hollow FRP composite column." *Composites Part B: Engrg.*, Special Issue on Infrastructure, 27B(3-4), 263-268.

Mirmiran, A., and Shahawy, M. (1997). "Behavior of concrete columns confined by fiber composites." *J. Struct. Engrg.*, ASCE, 123(5), 583-590.

Mirmiran, A., and Shahawy, M. (1997). "Dilation characteristics of confined concrete." *Mech. of Cohesive-Frictional Materials, An International J.*, 2(3), 237-249.

Mirmiran, A., Samaan, M., Cabrera, S., and Shahawy, M. (1997). "Design, manufacture, and testing of a new hybrid column." *Construction and Building Materials*, in press.

Samaan, M., Mirmiran, A., and Shahawy, M. (1997). "Modeling of concrete confined by fiber composites." *Journal of Structural Engineering*, ASCE, Under Review.

Conference Proceedings

Mirmiran, A., and Shahawy, M. (1995). "A novel FRP-concrete composite construction for the infrastructure." *Proc. Structures Congress XIII*, ASCE, Boston, MA, 1663-1666.

Mirmiran, A., and Kargahi, M. (1995). "An innovative FRP-concrete composite construction for seismic regions." *Proc. 2nd Int. Conf. Seismology and Earthquake Engrg.*, Tehran, Iran, 1047-1054.

Mirmiran, A., Kargahi, M., and Shahawy, M. (1995). "FRP-encased concrete columns." *Proc., 2nd Int. Conf. Composites Engrg.*, New Orleans, LA, 509-510.

Mirmiran, A. (1995). "Concrete composite construction for durability and strength." *Proc. Symp. Extending Lifespan of Struct.*, Int. Assoc. for Bridge and Struct. Engrg. (IABSE), San Francisco,

CA, 1155-1160.

Mirmiran, A., Kargahi, M., Samaan, M.S., an Shahawy, M. (1996). "Composite FRP-concrete column with bi-directional external reinforcement." *Proc. 1st. Int. Conf. Composites in Infrastructure*, Tucson, AZ., 888-902.

Shahawy, M., and Mirmiran, A. (1996). "A new FRP-encased bridge pier column." *Proc. 4th National Workshop on Bridge Research in Progress*, Buffalo, N.Y., 325-330.

Shahawy, M., and Mirmiran, A. (1996). "Hybrid columns of FRP and concrete." *Proc. 4th Materials Engrg. Conf.*, ASCE, Washington, D.C., 73-82.

Shahawy, M., and Mirmiran, A. (1997). "Stiffened FRP tubes for hybrid construction." *Proc. 4th Int. Conf. Composites Engrg.*, Hawaii.

Mirmiran, A. (1998). "Length Effects on FRP-Reinforced Concrete Columns." *NSF Sponsored 2nd International Conference on Composites in Infrastructure*, Tucson, AZ.

Presentations

Mirmiran, A. (1994). "Composites for rebuilding the infrastructure." *5th International Conference on Marine Applications of Composite Materials*, Melbourne, FL.

Mirmiran, A., and Shahawy, M. (1995). "Behavior and design of reinforced concrete columns with external shell reinforcement." ACI Spring Convention, Session on *Advances in Reinforced Concrete Column Design*, Salt Lake City, UT.

Samaan, M.S., Mirmiran, A., and Shahawy, M. (1995). "Bridge concrete columns confined by fiber reinforced plastic tubes." ACI Fall Convention, Session on *Research in Progress*, Montreal, Canada.

Mirmiran, A. (1996). "Plastic tubes as permanent formwork and external reinforcement for concrete columns." Florida Department of Transportation Design Conference, Session on *Structural Research*, Orlando, FL.

Samaan, M., Mirmiran, A., and Shahawy, M. (1997). "Hybrid FRP-concrete columns." International Composites Expo, Composites Institute, *Student Poster Session*, Nashville, TN.

Mirmiran, A. (1997). "Concrete-filled plastic tubes for piles and pile splices." Florida Department of Transportation Design Conference, Session on *Structural Research*, Orlando, FL.

Master Thesis

Kargahi, M. (1995). "Fiber reinforced plastic (FRP) shell as external reinforcement for concrete columns." *M.S. thesis*, University of Central Florida, Orlando, FL.

Monte, J.C. (1995). "Structural applications of fiber reinforced composites." *M.S. thesis*, University of Central Florida, Orlando, FL.

Scherer, M.E. (1996). "Design optimization and behavior of concrete-filled FRP tubes." *M.S. thesis*, University of Central Florida, Orlando, FL.

Cabrera, S. (1996). "Shear strength and seismic performance of concrete-filled FRP tubes." *M.S. thesis*, University of Central Florida, Orlando, FL.

El Echary, H. (1997). "Length effect on behavior of concrete columns confined by fiber composites using acoustics emission." *M.S. thesis*, University of Central Florida, Orlando, FL.

Mastrapa, J.C. (1997). "Effect of bonded and unbonded construction on confinement with fiber composites." *M.S. thesis*, University of Central Florida, Orlando, FL.

Pico, O. (1997). "Confinement effectiveness of square FRP tubes in hybrid columns." *M.S. thesis*, University of Central Florida, Orlando, FL.

Ph.D. Dissertation

Samaan, M. (1996). "Behavior of concrete-filled FRP tubes." *Dissertation proposal*, University of Central Florida, Orlando, FL.

Samaan, M. (1997). "Analytical and experimental investigation of FRP-concrete composite columns." *Ph.D. thesis,* University of Central Florida, Orlando, FL.

Reports

Mirmiran, A. (1997). "Analytical and experimental investigation of reinforced concrete columns encased in fiberglass tubular jackets and use of fiber jacket for pile splicing." *Final Report*, Florida Department of Transportation, Contract No. B-9135, Tallahassee, FL.

Mirmiran, A. (1997). "FRP-concrete composite column and pile jacket splicing - phase II." *Final Report*, Florida Department of Transportation, Contract No. B-9895, Tallahassee, FL.

Featured Articles

"Engineering Professor bridges gap in technology." (1995). *The Central Florida Future*, 28(21), 3.

"Researchers develop plastic support for bridges." (1995). *The UCF Report*, 18(8), 1 and 5.

"Building better bridges." (1996). *The Knight Engineer Magazine*, 1(1), 11.

"Patented design for bridges brings in National Science grant." (1996). *The UCF Report*, 19(5), 5.

"Plastic proves to be golden for one UCF professor." (1996). *The Central Florida Future*, 29(16),

1-2.

"Hybrid FRP-concrete columns ." (1997). FRP International (to appear).

REFERENCES

Abdel-Halim, M.A.H., and Abu-Lebdeh, T.M. (1989). "Analytical study for concrete confinement in tied columns." *J. Struct. Engrg.*, ASCE, 115(11), 3036-3054.

ACI Committee 318. (1995). *Building code requirements for structural concrete.* ACI 318-95, American Concrete Institute.

Ahmad, S.H. (1981). "Properties of confined concrete under static and dynamic loads." *Ph.D. thesis*, University of Illinois at Chicago Circle, Chicago, IL.

Ahmad, S.H., Khaloo, A.R., and Irshaid, A. (1991). "Behavior of concrete spirally confined by fiberglass filaments." *Mag. Concr. Res.*, 43(156), 143-148.

Ahmad, S.H., and Mallare, M.P. (1994). "A comparative study of models for confinement of concrete by circular spirals." *Mag. Concr. Res.*, 46(166), 49-56.

Ahmad, S.H., and Shah, S.P. (1982). "Stress-strain curves of concrete confined by spiral reinforcement." *ACI J.*, 79(6), 484-490.

Almusallam, T.H., and Alsayed, S.H. (1995). "Stress-strain relationship of normal, high-strength and lightweight concrete." *Magazine of Concr. Research*, 47(170), 39-44.

Al-Sulaimani, G., Sharif, A., Basunbul, I., Baluch, M. and Ghaleb, B. (1994). "Strengthening of Initially Loaded Reinforced Concrete Beams Using FRP Plates." *ACI Struct. J.*, 91(2), 458-464.

Al-Sulaimani, G., Sharif, A., Basunbul, I., Baluch, M. and Ghaleb, B. (1994). "Shear Repair for Reinforced Concrete by Fiberglass Plate Bonding." *ACI Struct. J.*, 91(3), 458-464.

ASTM E610-82. (1987). "Standard definitions of terms relating to acoustic emission." *American Society for Testing and Materials*, ASTM, Philadelphia, 2.03.

Ballinger, C., Maeda, T., and Hoshijima, T. (1993). "Strengthening of reinforced concrete chimneys, columns and beams with carbon fiber reinforced plastics." *Proc. Int. Symp. Fiber-Reinforced-Plastic reinforcement for Concrete Structures*, Nanni, A., and Dolan, C.W., ed., ACI, SP 138, 233-247.

Bavarian, B., Shively, J., Ehrgott, R., and Di Julio, R. (1996). "External support of concrete structures using composite materials." *Proc. 1st Int. Conf. Composites in Infrastructure*, Saadatmanesh, H., Ehsani, M.R., ed., Tuscon, AZ., 917-928.

Bjerkli, L., Tomaszewicz, A., and Jensen, J.J. (1990). "Deformation properties and ductility of high-strength concrete." *Proc.,* Second International Conf. On High-Strength Concrete, ACI SP 121, 215-238.

Cabrera, S. (1996). "Shear strength and seismic performance of concrete-filled FRP tubes." *M.S. thesis*, University of Central Florida, Orlando, FL.

Chai, Y.H. (1991). "Steel jacketing of circular reinforced concrete bridge columns for enhanced flexural performance." *Ph.D. thesis*, University of California, San Diego, CA.

Chai, Y.H., Priestley, M.J.N., and Seible, F. (1991). "Seismic retrofit of circular bridge columns for enhanced flexural performance." *ACI Struct. J.*, 88(5), 572-584.

Chai, Y.H., Priestley, M.J.N., and Seible, F. (1994). "Analytical model for steel-jacketed RC circular bridge columns." *J. Struct. Engrg.*, ASCE, 120(8), 2358-2375.

Chajes, M.J., Januszka, T.F., Mertz, D.R., Thomson, T.A., and Finch, W.W. (1995). "Shear Strengthening of Reinforced Concrete Beams Using Externally Applied Composite Fabrics." *ACI Struct. J.*, 92(3), 295-303.

Chakabakarty, B.K. (1992). "Models for optimal design of reinforced concrete beams." *Computers and Structures*, 42(3), 447-451.

Cedolin, L., Crutzen, Y.R.J., and Deipoli, S. (1977). "Triaxial stress strain relationship for concrete." *J. Engrg. Mech. Div.*, ASCE, 103(3), 423-439.

Chen, W.F. (1982). *Plasticity in reinforced concrete*. McGraw-Hill Book Co., New York, N.Y.

Chen, W.F., and Chen, C.H. (1973). "Analysis of concrete-filled steel tubular beam-columns." *Memoirs*, International Association for Bridge and Struct. Engrg. (IABSE), 33(II), 37-52.

Considere, A. (1906). "Resistance a la compression du beton arme et du bet frette." *Experimental Researches Reinforced Concrete*. New York, N.Y.

Demers, M., and Neale, K.W. (1994). "Strengthening of concrete columns with unidirectional composites sheets." *Proc.*, Developments in Short and Medium Span Bridge Engineering Conf., 895-905.

Deskovic, N., Triantafillou, T.C., and Meier, U. (1995). "Innovative design of FRP combined with concrete: short term behavior." *J. Struct Engrg.*, ASCE, 121(7), 1069-1078.

El Echary, H. (1997). "Length effect on behavior of concrete columns confined by fiber composites using acoustics emission." *M.S. thesis*, University of Central Florida, Orlando, FL.

Elwi, A.A., and Murray, D.W. (1979). "A 3D hypoelastic concrete constitutive relationship." *J. Engrg. Mech. Div.*, ASCE, 105(4), 623-641.

Farahat, A., and Ohtsu, M. (1995). "Evaluation of plastic damage in concrete by acoustic emission." *J. Materials in Civil Engrg.*, ASCE, 148-153.

Fardis, M.N., and Khalili, H. (1981). "Concrete encased in fiberglass-reinforced plastic." *ACI J.*, 78(6), 440-446.

Fardis, M.N., and Khalili, H.H. (1982). "FRP-encased concrete as a structural material." *Magazine of Concrete Research*, 34(121), 191-201.

"Florida, Oregon protect bridge substructures." (1991). *Civil Engrg.*, 61(10), 18-19.

Fyfe, E.R. (1995). "Testing and field performance of the high strength fiber wrapping system." *Proc. Structures Congress XIII*, ASCE, Boston, MA., 603-606.

Gardner, N.J., and Jacobsen, E.R. (1967). "Structural behavior of concrete filled steel tubes." *ACI J.*, 64(7), 404-413.

Garmestani, H. (1997). "Mechanical and microscopy analysis of carbon fiber reinforced polymeric matrix composite materials." *Final Report*, Florida Department of Transportation, Contract No. B-9949, Tallahassee, FL.

Ge, H., and Usami, T. (1996). "Cyclic tests of concrete-filled steel box columns." *J. Struct. Engrg.*, ASCE, 122 (10), 1169-1170.

Hajjar, J.F., and Gourley, B.C. (1996). "Representation of concrete-filled steel tube cross-section strength." *J. Struct. Engrg.*, ASCE, 122(11), 1327-1336.

Harries (1997). *Private correspondence*. Lehigh University, Bethlehem, PA.

Harmon, T.G., and Wang, H.H. (1996). "Behavior of composite confined concrete under cyclic loading." *Proc.*, 41st International SAMPE Symp., Anaheim, CA., 975-989.

Hobbs, D.W. (1974). "Strength and deformation properties of plain concrete subjected to combined stress." *Tech. Rept. 42.497*, Part 3, Cement Concrete Assoc., London, U.K.

Hollaway, L. (1993). *Polymer Composites For Civil and Struct. Engrg.* Blackie Academic & Professional.

Heinz, R. (1993). "Plastic Piling." *Civil Engrg.*, 63(4), 63-65.

Hunaiti, Y.M. (1991). "Bond strength in battened composite columns." *J. Struct. Engrg.*, ASCE, 117(3), pp. 699-714.

Jones, R.M. (1975). *Mechanics of Composite Materials.* Hemisphere Publishing Corporation.

Jin, L., Saadatmanesh, H., and Ehsani, M.R. (1994). "Seismic retrofit of existing reinforced concrete columns by glass-fiber composites." *Proc. Materials Engrg. Conf.*, ASCE, 758-763, New York, N.Y.

Kanagasundarum, S., and Karhaloo, B.L. (1991). "Minimum cost design of reinforced concrete structures." *Computers and Structures*, 41(6), 1357-1364.

Kargahi, M. (1995). "Fiber reinforced plastic (FRP) shell as external reinforcement for concrete columns." *M.S. thesis*, University of Central Florida, Orlando, FL.

Knowles, R.B., and Park, R. (1969). "Strength of concrete filled steel tubular columns." *J. Struct. Div.*, ASCE, 96(10), 2565-2587.

Kurt, C.E. (1978). "Concrete-filled structural plastic columns." *J. Struct. Div.*, ASCE, 104(1), 55-63.

Lahlou, K., Aïtcin, P.C., and Chaallal, O. (1992). "Behavior of high-strength concrete under confined stresses." *Cement & Concrete Composites*, 14, 185-193.

Li, L., and Poorooshasb, H.B. (1986). "Characteristics of acoustic emission from reinforced concrete." *Progress in acoustic emission III*, The Japan Society of NDI, 522-528.

Li, M.W. (1992). "Parametric study of concrete columns strengthened with composite straps." *M.S. thesis*, University of Arizona, Tucson, AZ.

Lu, Y.Q., and Kennedy, D.J.L. (1994). "The flexural behavior of concrete-filled hollow structural sections." *Canadian J. Civil Engrg.*, 21(1), 111-130.

Karabinis, A.I., and Kiousis, P.D. (1994). "Effects of confinement on concrete columns: plasticity approach." *J. Struct. Engrg.*, ASCE, 120(9), 2747-2767.

Kupfer, H., Hilsdorf, H.K., and Rusch, H. (1969). "Behavior of concrete under biaxial stresses." *ACI J.*, 66(8), 656-666.

Madas, P., and Elnashai, A.S. (1992). "A new passive confinement model for the analysis of concrete structures subjected to cyclic and transient dynamic loading." *J. Earthquake and Struct. Dynamics*, 21, 409-431.

Maji, A., and Shah, S. (1988). "Process zone and acoustic emission measurements in concrete." *Experimental Mechanics*, 28, 27-33.

Maji, A.K., and Sahu, R. (1994). "Acoustic emissions from reinforced concrete." *Experimental Mechanics*, 379-388.

Malhotra, V.M., and Carino, N.J. (1991). *CRC Handbook on Nondestructive Testing of Concrete.* CRC Press.

Mallick, P.K. (1988). *Fiber reinforced composites: materials, manufacturing and design.* Marcel Dekker, Inc., New York, N.Y.

Mander, J.B., Priestley, M.J.N., and Park, R.J.T. (1988). "Theoretical stress-strain model for confined concrete." *J. Struct. Engrg.*, ASCE, 114(8), 1804-1826.

Mander, J.B., Priestley, M.J.N., and Park, R.J.T. (1988). "Observed stress-strain behavior of confined concrete." *J. Struct. Engrg.*, ASCE, 114(8), 1827-1849.

Mastrapa, J.C. (1997). "Effect of bonded and unbonded construction on confinement with fiber composites." *M.S. thesis*, University of Central Florida, Orlando, FL.

McCabe, M., et al. (1976). "Acoustic emission behavior of concrete laboratory specimens." *ACI J.*, 73(4), 367-371.

McKenna, J.K. and Erki, M.A. (1994). "Strengthening of Reinforced Concrete Flexural Members Using Externally Applied Steel Plates and Fibre Composite Sheets--A Survey." *Canadian J. Civil Engrg.*, 21, 16-24.

Meier, U., and Kaiser, H. (1991). "Strengthening of structures with CFRP laminates." *Proc. Spec. Conf. Adv. Composites Mat. in Civ. Engrg. Struct.*, ASCE, 224-232.

Miller, R.K., and McIntire, P. (1987). *Acoustic Emission Testing.* Vol 5 of Nondestructive Testing Handbook, American Society for Nondestructive Testing (ASTM).

Mirmiran, A. (1997). "Analytical and experimental investigation of reinforced concrete columns encased in fiberglass tubular jackets and use of fiber jacket for pile splicing." *Final Report*, Florida Department of Transportation, Contract No. B-9135, Tallahassee, FL.

Mirmiran, A. (1995). "Concrete composite construction for durability and strength." *Proc. Symp. Extending Lifespan of Struct.*, Int. Assoc. for Bridge and Struct. Engrg. (IABSE), San Francisco, CA, 1155-1160.

Mirmiran, A., and Kargahi, M. (1995). "An innovative FRP-concrete composite construction for seismic regions." *Proc. 2nd Int. Conf. Seismology and Earthquake Engrg.*, Tehran, Iran, 1047-1054.

Mirmiran, A., Kargahi, M., Samaan, M.S., an Shahawy, M. (1996). "Composite FRP-concrete column with bi-directional external reinforcement." *Proc. 1st. Int. Conf. Composites in Infrastructure*, Tucson, AZ, 888-902.

Mirmiran, A., Kargahi, M., and Shahawy, M. (1995). "FRP-encased concrete columns." *Proc., 2nd Int. Conf. Composites Engrg.*, New Orleans, LA, 509-510.

Mirmiran, A., Samaan, M., Cabrera, S., and Shahawy, M. (1997). "Design, manufacture, and testing of a new hybrid column." *Construction and Building Materials*, (in press).

Mirmiran, A., and Shahawy, M. (1995). "A novel FRP-concrete composite construction for the infrastructure." *Proc. Structures Congress XIII*, ASCE, Boston, MA, 1663-1666.

Mirmiran, A., and Shahawy, M. (1996). "A new concrete-filled hollow FRP composite column." *Composites Part B: Engrg.*, Special Issue on Infrastructure, 27B(3-4), 263-268.

Mirmiran, A., and Shahawy, M. (1997). "Dilation Characteristics of Confined Concrete." *Mech. of Cohesive-Frictional Materials, An International J.*, 2(3), 237-249.

Mirmiran, A., and Shahawy, M. (1997). "Behavior of Concrete Columns Confined by Fiber Composites." *J. Struct. Engrg.*, ASCE, 123(5), 583-590.

Muguruma, H., Nishiyama, M., Watanabe, F., and Tanaka, H. (1992). "Ductile behavior of high-strength concrete columns confined by high strength transverse reinforcement." *Proc.*, ACI International Conf., Hong Kong, ACI SP 128-54, II, 877-891.

Nanni, A. (1995). "Concrete Repair with Externally Bonded FRP Reinforcement." *Concrete Int.*, 22-26.

Nanni, A., and Bradford, N.M. (1995). "FRP-jacketed concrete under uniaxial compression." *Constr. and Bldg. Materials*, 9(2), 115-124.

Newman, K., and Newman, J.B. (1971). "Failure theories and design criteria for plain concrete." *Proc. Int. Civil Engrg. Mater. Conf. on Struct., Solid Mech. and Engrg. Design*, Wiley Interscience, New York, N.Y., 936-995.

Ohtsu, M. (1996). "The history and development of acoustic emission in concrete engineering." *Magazine of Concrete Research*, 321-330.

Okamoto, T., et al. (1992). "Discrimination of cracking and estimation of cracking width developed in reinforced concrete structures by acoustic emission." *Proc. 4th Int. Symp. on Acoustic Emission* *from Composite Materials*, Seattle, 139-146.

Okamoto, T., Maeno, T., Hisatoku, T., Kaneta, K., and Nishizawa, H. (1989). "An experimental study on rectangular steel tube columns infilled with ultra-high strength concrete cast by centrifugal force." *Proc. 3rd Int. Symp. Tubular Structures*, Lappeenranta, Finland, Elsevier Applied Science, New York, N.Y., 364-371.

Orito, Y., Sato, T., Tanaka, N., and Watanabe, Y. (1987). "Study on the unbounded steel tube structure." *Proc., Int'l. Conf. Composite Construction in Steel and Concrete*, ASCE, 786-804.

Picher, F. (1995). "Confinement of concrete cylinders with unidirectional carbon epoxy components". *M.S. Thesis*, University of Sherbrooke, Quebec, Canada.

Picher, F., Rochette, P., and Labossiere, P. (1996). "Confinement of concrete cylinders with CFRP." *Proc. 1st Int'l. Conf. Composites in Infrastructure*, Saadatmanesh, H., Ehsani, M.R., ed., Tuscon, AZ., 829-841.

Pico, O. (1997). "Confinement effectiveness of square FRP tubes in hybrid columns." *M.S. thesis*, University of Central Florida, Orlando, FL.

Pollock, A.A. (1997). *Notes for SNT-TC-1A qualification/certification level 2 course for acoustic emission personnel.* Physical Acoustics Corporation, Huntsville, AL.

Popovics, S. (1973). "Numerical approach to the complete stress-strain curves for concrete." *Cement and Concrete Research*, 3(5), 583-599.

Priestley, M.J.N., Seible, F., Xiao, Y., and Verma, R. (1994). "Steel jacket retrofitting of reinforced concrete columns for enhanced shear strength - part 1: theoretical considerations and test design." *ACI Struct. J.*, 91(4), 394-405.

Priestley, M.J.N., Seible, F., Xiao, Y., and Verma, R. (1994). "Steel jacket retrofitting of reinforced concrete columns for enhanced shear strength - part 2: test results and comparison with theory." *ACI Struct. J.*, 91(5), 537-552.

Prion, H.G.L., and Boehme, J. (1994). "Beam-column behavior of steel tubes filled with high strength concrete." *Canadian J. Civil Engrg.*, 21(2), 207-218.

Priestley, M.J.N., Seible, F., and Fyfe, E.R. (1992). "Column seismic retrofit using fiberglass/epoxy jackets." *Proc. 3rd NSF Workshop on Bridge Engrg. Research in Progress*, La Jolla, CA., 247-251.

Rangan, B.V., and Joyce, M. (1992). "Strength of eccentrically loaded slender tubular columns filled with high-strength concrete." *ACI Struct. J.*, 89(6), 676-681.

Raymond, M.C. (1984). "Application de l' emission acoustique pour le controle en genie civil." *Revue d' Acoustique*, 70, 151-157.

Reddy, R.R., Gupta, A., and Singh, R.P. (1993). "Expert system for optimum design of concrete structures." *J. of Computing in Civil Engrg.*, 7(2).

Richard, R.M., and Abbott, B.J. (1975). "Versatile elastic-plastic stress-strain formula." *J. Engrg. Mech.*, ASCE, 101(4), 511-515.

Richart, F.E., Brandzaeg, A., and Brown, R.L. (1929). "Failure Of plain and spirally reinforced concrete in compression." *Bul. 190*, Engrg. Experiment Station, University of Illinois, Urbana, IL.

Richardson, T. (1987). *Composites, A Design Guide.* Industrial Press, Inc.

Ritchie, P.A., Thomas, D.A., Le-Wu, L., and Connelly, G.M. (1991). "External Reinforcement of Concrete Beams Using Fiberglass Reinforced Plastics." *ACI Struct. J.*, 88(4), 490-500.

Rochette, P. (1997). "Confinement of short square and rectangular columns with composite materials." *M.S. Thesis*, University of Sherbrooke, Quebec, Canada.

Rochette, P., and Labossiere, P. (1996). "A plasticity approach for concrete columns confined with composite materials." *Adv. Composite Mater. in Bridges and Struct.*, M.M. El-Badry, (Ed.), Canadian Society for Civil Engineering, 359-366.

Saadatmanesh, H., Ehsani, M.R., and Li, M.W. (1994). "Strength and ductility of concrete columns externally reinforced with fiber composite straps." *ACI Struct. J.*, 91(4), 434-447.

Saadatmanesh, H. and Eshani, M.R. (1991). "RC Beams Strengthened with GFRP Plates, I: Experimental Study." *J. Struct. Engrg.*, ASCE, 117(11), 3417-3433.

Saatcioglu, M., and Razvi, S.R. (1992). "Strength and ductility of confined concrete." *J. Struct. Engrg.*, ASCE, 118(6), 1590-1607.

Samaan, M. (1996). "Behavior of concrete-filled FRP tubes." *Dissertation Proposal*, University of Central Florida, Orlando, FL.

Samaan, M. (1997). "Analytical and experimental investigation of FRP-concrete composite columns." *Ph.D. thesis,* University of Central Florida, Orlando, FL.

Samaan, M., Mirmiran, A., and Shahawy, M. (1997). "Modeling of Concrete Confined by Fiber Composites." *Journal of Structural Engineering*, ASCE, Under Review.

Scherer, M.E. (1996). "Design optimization and behavior of concrete-filled FRP tubes." *M.S. thesis*, University of Central Florida, Orlando, FL.

Scott, B.D., Park, R.J.T., and Priestley, M.J.N. (1982). "Stress-strain behavior of concrete confined by overlapping hoops at low and high strain rates." *ACI J.*, 79(1), 13-27.

Scribner, C.F. (1986). "Reinforcement buckling in reinforced concrete flexural member." *ACI J.*, 83(6), 966-973.

Seible, F., and Karbhari, V. (1996). "Advanced composites for civil engineering applications in the united states." *Proc. 1st Int. Conf. Composites in Infrastructure*, Saadatmanesh, H., and Ehsani, M.R., ed., Tuscon, AZ., 21-37.

Shahawy, M., and Mirmiran, A. (1996). "A new FRP-encased bridge pier column." *Proc. 4th National Workshop on Bridge Research in Progress*, Buffalo, N.Y., 325-330.

Shahawy, M., and Mirmiran, A. (1996). "Hybrid Columns of FRP and Concrete." *Proc. 4th Materials Engrg. Conf.*, ASCE, Washington, D.C.

Shahawy, M., and Mirmiran, A. (1997). "Stiffened FRP Tubes for Hybrid Construction." *4th International Conference on Composites Engineering*, Hawaii, Accepted.

Sheikh, S.A., and Uzumeri, S.M. (1980). "Strength and ductility of tied concrete columns." *J. Structural Div.*, ASCE, 106(5), 1079-1102.

"The status of the nation's highways, bridges, and transit: conditions and performance." (1993). *Rept. of the Secretary of Transportation to the U.S. Congress.*

Steputat, C. (1993). "Acoustic Emission Spectra of Steel & Fiber Reinforced Concrete Beam Specimens as induced by static loading." *M.S. thesis*, University of Central Florida, Orlando, FL.

Tia et al. (1990). "Field and laboratory study of modulus of rupture and permeability of structural concretes in Florida." *Rept.*, Univ. of Florida, Gainesville, FL.

Triantafillou, T.C. (1994). "New fiber reinforced plastic structural elements in combination with concrete." *Proc. 1st. Int. Conf. Composites Engrg.*, Hui, D., ed., 987-988, New Orleans, LA.

Tsai, S.W. (1988). *Composites Design.* Think Composites, Dayton, OH.

Usami, T., and Ge, H. (1994). "Ductility of concrete-filled steel box columns under cyclic loading." *J. Struct. Engrg.*, ASCE, 120(7), 2021-2040.

Wevers, M. (1997). "Listening to the sound of materials: acoustic emission for the analysis of material behaviour." *NDT & E Int.*, 30, 99-106.

Xiao, Y., Martin, G.R., Yin, Z., and Ma, R. (1996). "Seismic retrofit of reinforced concrete bridge columns using a prefabricated composite wrapping system." *Proc. 1st Int. Conf. Composites in Infrastructure*, Saadatmanesh, H., and Ehsani, M.R., ed., Tucson, AZ., 903-916.

Yong, Y., Nour, M.G., and Nawy, E.G. (1988). "Behavior of laterally confined high-strength concrete under axial loads." *J. Struct. Engrg.*, ASCE, 114(2), 332-352.

Zahn, F.A., Park, R., and Priestley, M.J.N. (1989). "Strength and ductility of square reinforced concrete column section subjected to biaxial bending." *ACI J.*, 86(2), 123-131.

Reproduced by NTIS

National Technical Information Service
Springfield, VA 22161

This report was printed specifically for your order from nearly 3 million titles available in our collection.

For economy and efficiency, NTIS does not maintain stock of its vast collection of technical reports. Rather, most documents are printed for each order. Documents that are not in electronic format are reproduced from master archival copies and are the best possible reproductions available. If you have any questions concerning this document or any order you have placed with NTIS, please call our Customer Service Department at (703) 605-6050.

About NTIS

NTIS collects scientific, technical, engineering, and business related information — then organizes, maintains, and disseminates that information in a variety of formats — from microfiche to online services. The NTIS collection of nearly 3 million titles includes reports describing research conducted or sponsored by federal agencies and their contractors; statistical and business information; U.S. military publications; multimedia/training products; computer software and electronic databases developed by federal agencies; training tools; and technical reports prepared by research organizations worldwide. Approximately 100,000 *new* titles are added and indexed into the NTIS collection annually.

For more information about NTIS products and services, call NTIS at 1-800-553-NTIS (6847) or (703) 605-6000 and request the free *NTIS Products Catalog,* PR-827LPG, or visit the NTIS Web site **http://www.ntis.gov**.

NTIS
Your indispensable resource for government-sponsored information—U.S. and worldwide

NTIS does not permit return of items for credit or refund. A replacement will be provided if an error is made in filling your order, if the item was received in damaged condition, or if the item is defective.

U.S. DEPARTMENT OF COMMERCE
Technology Administration
National Technical Information Service
Springfield, VA 22161 (703) 605-6000